Kingston University London
Department of Mechanical engineering

Development of Nanoengineered Coatings for Leading Edge Protection of Wind Turbine Blades

by

Arash Dashtkar

MSc Mechanical Engineering

A dissertation submitted to the Faculty of Science Engineering and Computing in partial fulfilment of the requirements for the degree of Doctor of Philosophy in Mechanical Engineering.

March 2022

Dedication

This thesis is dedicated to my parents.

To my father; I am sure I will find good mentors through my life but my father will always be my inspiration because he gave me the greatest gift anyone could give another person, he believed in me. Today, concluding this chapter of my life I can look myself in to the mirror and see his face, knowing I am honouring him once again.

To my mother; I have the grit to push through the challenges that are in my way and live a meaningful life because my mother made me the person that I am today. Thank you for always being there for me and making more sacrifices than can even be counted so that I could pursue my dreams and become a man that you can be proud of.

Declaration

I **Arash Dashtkar** hereby certify that I had personally carried out the work presented in this thesis entitled “Development of Nanoengineered Coatings for Leading Edge Protection of Wind Turbine Blades” except where otherwise indicated and acknowledged. The work presented is original and has been carried out under my supervisor Associate Professor Homayoun Hadavinia.

Signature:

Arash Dashtkar

Date: 17 February 2022

List of published papers in journals and conferences

1. A Dashtkar, N Frost-Jensen Johansen, L Mishnaevsky Jr., NA Williams, Shadi W. Hasan, Vijay S. Wadi, Alessio Silvello, Homayoun Hadavinia, Graphene/sol gel modified polyurethane coating for wind turbine blade leading edge protection: Properties and performance, *Polymers and Polymer Composites* **2022,** Vol 30, 1-18 **(J).**

2. N Frost-Jensen Johansen, L Mishnaevsky, A Dashtkar, NA Williams, Søren Fæster, Alessio Silvello, Irene Garcia Cano, Homayoun Hadavinia, Nanoengineered graphene-reinforced coating for leading edge protection of wind turbine blades, *Coatings* **2021,** 11(9), 1104 **(J).**

3. A Dashtkar, H Hadavinia, J Barros-Rodriguez, N Williams, M Turner, S Vahid, Quantifying damping coefficient and attenuation at different frequencies for graphene modified polyurethane by drop ball test, *Polymer Testing* **2021,** Vol 100, 107267 **(J).**

4. Arash Dashtkar, Homayoun Hadavinia, Jose Barros Rodriguez, Neil A Williams, Samireh Vahid, Characterising Damping Coefficient and Attenuation of Graphene Modified Polyurethane Nanocomposites by Drop Ball Test, 2nd International Symposium on Leading Edge Erosion of Wind Turbine Blades, Technical University of Denmark, Denmark, February **2021 (C)**.

5. A Dashtkar, H Hadavinia, MN Sahinkaya, NA Williams, S Vahid, F Ismail, Matthew Turner, Rain erosion resistant coatings for wind turbine blades – A review, *Polymers and Polymer Composites* **2019,** 27 (8), 443–475 **(J).**

6. Arash Dashtkar, Homayoun Hadavinia, Mehmet Sahinkaya, Neil A Williams, Samireh Vahid, Chemical Surface Functionalization of Multi-walled Carbon Nanotubes (MWCNTs), Nano World Conference, Paris, France, March **2019 (C)**.

Acknowledgements

I would like to express my sincere appreciation to my first supervisor Dr Homayoun Hadavinia, and supervisory team Dr Neil Williams and Dr Samireh Vahid, for their great support during my PhD. Their help and knowledge have been fundamental for completing the work presented in this thesis. Specially Dr Hadavinia who was supporting me at all time, not only academically, but also for life, thanks to him for all of the lessons he had taught me. Thanks to Dr Jose Barros Rodriguez for helping in damping analysis.

I would like to thank Dr Leon Mishnaevsky and Dr Nicolai Frost-Jensen Johansen from Technical University of Denmark for helping in erosion testing. Professor Shadi W. Hasan and Dr Vijay S. Wadi from Khalifa University of Science and Technology, and Professor Irene Garcia Cano and Dr Alessio Silvello from Universitat de Barcelona for their collaboration in this project.

I would also like to thank Dr Fanya Ismail, CEO and Founder of SGMA Company for providing sol-gel material and Mr Stephen Gormley, Managing Director of Covestro Company for providing polyurethane material for my research.

My sincere thanks to all my colleagues in Kingston University London for their helpful support on experimental works, especially Dean Wells who always provided me friendly support and useful training to use different equipment, Alex Vine, Shaun Don, and Wendy Brosnan.

I thank my loving family for their continuous support, and for helping me both emotionally and spiritually, specially my sister Parastoo.

Last but not least, I would like to thank my wife and love of my life, Shaghayegh. She has been extremely supportive throughout my PhD study and she stood by me patiently during these years and I am always indebted to her countless sacrifices.

Abstract

This research is focused on developing rain erosion resistant coatings for leading edge of the wind turbine blades. One of the critical problems of wind turbine blades is erosion of its leading edge. Leading edge erosion (LEE) will degrade the aerodynamic performance of the wind turbines by increasing the drag force and decreasing the lift force. Past studies showed that the annual energy production (AEP) of the wind turbine can be reduced by up to 25% due to LEE. Hence, applying an erosion resistant coating to the wind turbine blades is necessary. Elastomeric polyurethane (PU) has been used for LEE protection. The approach of this research is to use PU and enhance its the mechanical properties by introducing carbon nanoparticles (CNPs) multi-walled carbon nanotubes (MWCNT) and graphene nanoplatelets (GNP) and also increase the hydrophobicity of the PU by introducing silica-based sol-gel (SG).

Initially the effect of the environmental temperature on mechanical properties of the pure PU was studied by performing tensile tests at different temperatures and strain rates. It was found that increasing the temperature decreases the tensile properties of the pure PU and increasing the strain rate will increase these properties.

For optimising mixing parameters of CNPs in PU, PU was modified by CNPs at three different mixing speeds and three different mixing durations. Tensile tests were performed on these nanocomposites, and the optimum mixing duration (18 minutes) and speed (8000 rpm) where nanocomposite materials showed the highest mechanical performance were established.

The optimum weight percentage of nanoparticles loading was also required. The PU was modified at different CNPs loading and the tensile tests were performed on pure and modified PUs. The results of the tensile tests showed that PU with 0.5wt% of MWCNTs and PU with 0.5wt% of GNP-COOH loading resulted in the highest amount of Young's modulus, UTS, elongation at break and modulus of toughness. Other CNPs such as GNP-NH_3 and combined GNP-COOH/CNT and GNP-NH_3/CNT were also investigated. The results showed that modifying PU with GNP-COOH at 0.5wt% loading gives the best tensile properties. Finally, the hydrophobicity of the coating was improved by adding silica-based sol-gel to the GNP modified PU. The water contact angle (CA) experiments showed that modifying PU with GNP and SG increased the CA of neat PU from 56 degree to 110 degree for PU+GNP+SG while the free surface energy reduced from 114.6 mJ/m^2 to 50 mJ/m^2.

The cyclic compression tests were carried out and the results revealed that the maximum stress at maximum strain of 0.5 for PU is 107.9 MPa, for PU + GNP is 77.4 MPa and for PU + GNP

+ SG is 71.5 MPa. This indicates PU + GNP + SG experiences the least stresses during cyclic compressive loading. Tearing test results showed that the PU + GNP nanocomposite has the highest tearing strength and PU + GNP + SG has the highest elongation at break. The PU + GNP + SG nanocomposite has much higher value for Young's modulus (95%), tensile strength (115%), modulus of toughness (124%) and elongation at break (102%) relative to the neat PU at room temperature. In addition, the tearing energy for both modified PU nanocomposites was higher than the neat PU (137% increase for PU + GNP and 148% increase for PU + GNP + SG).

In addition to the mechanical tests, water absorption test was carried out for a period of six months to analyse the amount of the water that can be absorbed by developed materials and the effect of absorbed water on the tensile properties of the coating materials were identified. Experimental results showed that after six months, the weight of the pure PU, PU+GNP and PU+GNP+SG increased by 4%, 3.7% and 3.6%, respectively. The results showed that absorbing water by PU decreases the tensile properties of the material.

Microstructural analysis of the developed PU coatings by FTIR, field emission scanning electron microscope (FESEM) and energy-dispersive X-ray spectroscopy (EDX) were carried out and the detailed results are presented in this thesis.

Finally the developed coatings were tested for anti-erosion performance using the single point impact fatigue testing (SPIFT) technique. It is demonstrated that graphene / silica reinforced PU coating can provide better erosion protection with substantial longer time before material loss than non-reinforced PU.

Table of Contents

List of Figures

List of Tables

Nomenclature

Abbreviations

AEP	Annual Energy Production
ASTM	American Society for Testing and Materials
CA	Contact Angle
CNT	Carbon Nanotubes
CNP	Carbon Nanoparticles
DMA	Dynamic Mechanical Analysis
DPS	Degree of hard segment
DSA	Drop Shape Analyser
EDX	Energy Dispersive X-Ray
EL	Elongation at Break
EMA	Experimental Modal Analysis
FESEM	Field Emission Scanning Electron Microscopy
FGSs	Functionalized graphene sheets
FTIR	Fourier Transform Infrared Spectroscopy
GFRP	Glass Fibre Reinforced Polymer
GNP	Graphene Nanoplatelets
GO	Graphene oxide
GONPs	Graphite oxide nanoplatelets
HDPE	High-density polyethylene
HPA	High Pressure Air
IDT	Initial Decomposition Temperature
LE	Leading Edge
LEE	Leading Edge Erosion
LER	Leading Edge Roughness
MWCNT	Multi-Walled Carbon Nanotube
PET	Polyethylene terephthalate
PTFE	Polytetrafluoroethylene
PVC	Polyvinyl chloride
RET	Rain Erosion test
SOD	Stand-off Distance
SPIFT	Single Point Impact Fatigue Test
SSET	Stationary Sample Erosion Test
TGA	Thermal Gravimetric Analysis
UHMWPE	Ultra-high molecular weight polyethylene

UTS	Ultimate Tensile Strength
USLE	Universal Soil Loss Equation
WARER	Whirling Arm Rain Erosion Rig

Greek letter

γ_L^T	Water surface tension
tan δ	Damping coefficient
θ	Contact angle
ξ_i	Damping ratio
$\dot{\varepsilon}$	Strain rate
$\boldsymbol{\varepsilon}^{\boldsymbol{r}}$	Residual strain
ε_{max}	Maximum strain
η	Material loss factor
ψ	pseudo-determinant

Symbols

C	Damping
C0	Acoustic velocity
C_b	Coefficient of hydrogen bonded urethane
C_f	free urethane
d	Density
d	Specimen thickness
DI	Deionised Water
E	Young's Modulus
E'	Storage modulus
E''	loss modulus
Ed	Damage Depth
EL	Elongation at break
f_s	frequency
f-GNP	Functionalized graphene
H	Humidity
Ip	Incubation Period
K	Stiffness
M	Mass
MG	Modified Graphite
mV	Maximum voltage
N	Cycle
PU	Polyurethane
Rd	Damage Depth Rate

RT	Room Temperature
SG	Sol-Gel
t	Time
t	Cool-down time
T	Modulus of toughness
T	Temperature
T_g	Glass temperature
T_s	Tearing Strength
U_0	Substrate Speed
Vm	Erosion rate
v	Velocity
vi	Impact velocity
vr	Rebound velocity
y(t)	Deformation vector
ΔE	Change in kinetic Energy
ΔG_{SL}	Surface free energy

Chapter 1 Introduction

1.1 Motivation and Scope

Erosion has been reported after two years of operations in some wind turbine blades which are usually made of glass fibre reinforced polymer (GFRP) [1, 2]. Inspection of 201 blades in 67 wind turbines operated by EDP Company showed that erosion occurred at the leading edge of 174 blades, which is around 87% of inspected blades [3]. Modern and large wind turbines are affected less by particle erosion in comparison with the small turbines. The reason may be the increased influence of the blade flow field towards a deviation of the incoming particles [4]. It was noted that offshore wind farms are subjected to more intense particle erosion than the majority of in land installations. The main causes of blade damage were identified as sand grains and raindrops, other impactors such as insects and hailstones do not have a significant effect on the erosion of wind turbine blade [4]. LE erosion causes an increase in surface roughness of the blade and thereby an increase in the air flow boundary layer thickness over the aerofoils on the blade when it is operating. The increased boundary layer thickness causes an increased drag coefficient and a decreased lift coefficient, and thus reduces the aerodynamic performance, particularly at higher angles of attack [5]. The consequence is severe losses in energy production. It has been reported that eroded blades in wind turbine can reduce Annual Energy Production (AEP) by as much as 25% [6, 7]. Coating the blade against erosion using appropriate materials can drastically reduce these losses and hence is of great interest.

Due to the impact of erosion on the operation of wind turbine blades they need to be monitored during their lifespan, however, the health monitoring process of a blade surface is time consuming and costly. During the monitoring process, wind farm needs to be shut down and then photographed from the ground. The location, depth and roughness of the damaged areas are the main aspects that are monitored as they affect the aerodynamic performance of the blade [8].

Liquid impingement erosion is important primarily where the target body moves at high speeds and collides with liquid drops that are moving much slower as is the case for wind turbine blades. Due to the higher blade speed at the outer part of the blades, erosion mostly appears at the LE in this area (**Figure 1-1**). For this reason, maintenance of the leading edge of the blade is not only recommended but it is essential if blades are expected to reach their life expectancy (20-25 years).

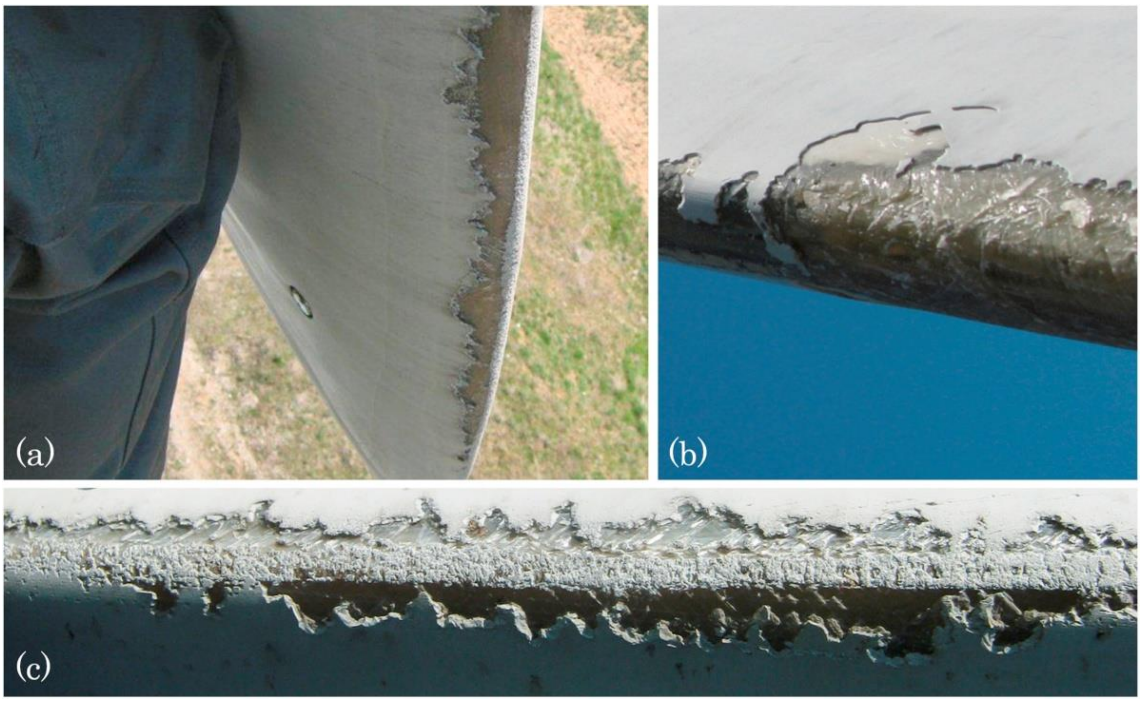

Figure 1-1 (a) Eroded wind turbine blade tip [9], (b) detail of eroded LE [10] and (c) close-up of eroded LE [9]. Reprinted from Ref. [11] with the permission of Elsevier Publishing. Reprinted from O'Carroll et al. [10] with the permission of Elsevier publishing. LE: leading edge.

Leading Edge Erosion (LEE) of wind turbine blades caused by the impact of rain, dust, salty vapour, hail stones and insects, reduces the lifetime of the blades. This in turn results in a loss in Annual Energy Production (AEP) by the turbines. AEP loss depends on different factors, such as degree of erosion, aerodynamic profile of blade, type of turbine and wind speed. Potential AEP losses of between 4.5-25% (depends on the degree of erosion, which means higher degree of erosion causes more AEP reduction) have been reported by Sareen [5], losses from 2% to 3.7%, (depending on the extent of damage at the leading edge), have been reported by Han *et al* [3]. Sandia National Laboratories [12] estimated the AEP losses as 5-8%. Kruse, *et al.* [13] simulated the aerodynamic performance of a NACA 63_3-418 aerofoil and showed up to 35% reduction in lift and 90% reduction in glide ratio for the specified angle of attacks ranges.

Leading edge erosion of the wind turbine blades can cause water ingress, with water entering the blades through surface defects due to erosion resulting in degradation to the constituent components of the blades. Water absorption by the resin will increase the weight of the composite structure causing imbalances and an increase in wind turbine vibrations [14]. In some studies, instead of water, rubber balls are used to impact specimen surfaces [15, 16].

The erosive force of rainfall is expressed as rainfall erosivity [17]. Rainfall erosivity considers the rainfall amount and intensity and is most commonly expressed as the R-factor in the

Universal Soil Loss Equation (USLE) model and its revised version (RUSLE). Estimation of the potential erosion caused by rain at specific wind farm sites is more challenging at sea than at land due to the limited available precipitation data. Over land, the rainfall erosivity for soil degradation has been assessed from 1541 precipitation stations in all European Union (EU) Member States and Switzerland, with temporal resolutions of 5 to 60 min [17, 18]. The map on rainfall erosivity in Europe at 500m spatial resolution assessed by European Soil Data Centre (ESDAC) is shown in **Figure 1-2** [17]. This database is valuable for the production of a rain erosion map for wind turbines where precipitation, wind speed and turbine characteristics such as tip speed would be input [19].

In order to understand the details of erosion process and characterise the failure mechanism, numerical models of rain droplet impact simulations are necessary [20].

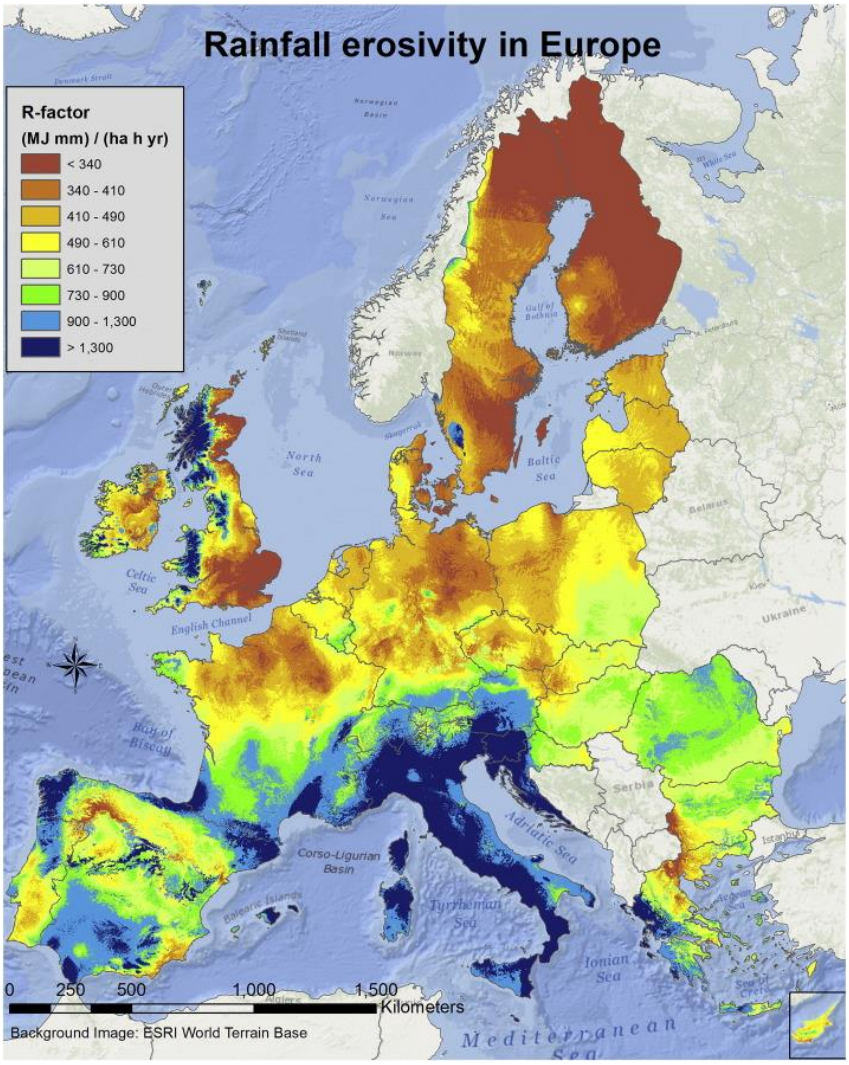

Figure 1-2 Rainfall erosivity in Europe at 1 km grid cell resolution. Reprinted from Ref. [17] with the permission of Elsevier Publishing.

Improving mechanical properties of PU including the fracture toughness and tearing strength, increasing the damping coefficient for absorbing the impact energy of the rain droplet and increasing the hydrophobicity of the coating to absorb lesser amount of the rainwater were important criteria for designing new coating materials. Previous studies [21, 22] showed that GNP has capability to enhance key mechanical properties such as UTS, modulus of toughness, fracture toughness and tearing strength and silica can improve the hydrophobicity of the polymers. Hence in this project the PU elastomer is modified by GNP and SG.

The scope of this project is development of nanoengineered rain erosion resistant coatings materials with higher erosion resistant than neat polyurethane elastomer for protection of leading edges of wind turbine blades by modifying PU elastomer with graphene nanoplatelets (GNP) and silica-based sol-gel (SG). Various mechanical tests will be carried out on the developed coating materials and the microstructures of the coatings will be characterised. The hydrophobicity of the coatings will be identified by water contact angle measurement. Finally, the erosion durability of the developed coatings will be measured by the robber ball impact erosion tests, investigating the thermal effect on erosion as well as microscopic analysis of the damaged coatings.

1.2 Problem Definition

It is reported that leading edge erosion (LEE) is the most common type of damage observed on wind turbine which adversely affect the turbine annual energy production (AEP). LEE of wind turbine blades caused by the impact of rain, dust, salty vapour, hailstones, and insects, reduces the lifetime of the blades and this in turn results in a loss in AEP by the turbines. The percentage loss in AEP depends on the degree of damage severity of the blade leading edge, and the tip speed which varies with blade size. This AEP loss is reported by various studies between 4.5-25% [23]. It is known that operations and maintenance of the wind turbine is costly, for instance for a 750-kW turbine, the maintenance cost might be 25-30% of the overall energy generation cost which can be even increased by adding repair cost to it [23]. Unfortunately, it is very difficult to predict the cost of repairing the blade as it is highly dependent on the type of repair solution, but usually repairing the blades does not perform per turbine which means that always there are running turbines with eroded LE.

In conclusion, erosion of the LE of wind turbine will increase the maintenance and repair cost in one hand and decrease the annual energy production of the wind turbine in the other hand.

1.3 Aim and Objectives

The aim of this project is to develop nanoengineered rain erosion resistant polyurethane coatings to protect the leading edge of wind turbine blade. The PU is modified with different CNPs and with silica-based sol-gel to have better mechanical and hydrophobicity performance. The developed coating must have substantial improvement in lifetime relative to the base material.

1.3.1 Project Objectives

- Analyse the performance of the pure polyurethane in different temperature and strain rate.
- Optimising the parameters of mixing carbon nanoparticles in pure polyurethane.
- Analyse the effects of adding different percentage of multi-walled carbon nanotubes (MWCNTs) on tensile properties of pure polyurethane.
- Analyse the effects of adding different percentage of functionalized GNP-NH_3 on tensile properties of pure polyurethane.
- Analyse the effects of adding different percentage of functionalized GNP-COOH on tensile properties of pure polyurethane.
- Analyse the effects of adding different percentage of hydrophobic silica-based sol-gel on tensile properties of PU+GNP-COOH.
- Material characterization of the developed coating materials.
- Analyse the tearing performance of the developed coating materials.
- Performing impact erosion testing using a Single Point Impact Fatigue Tester (SPIFT) method.

1.4 Layout of Thesis

A comprehensive investigation on developing an Nanoengineered Graphene-Reinforced rain erosion resistant coating for leading edge of wind turbine blade in this thesis as six different chapters described as follows:

Chapter 1: A brief background, motivation, scope and problem definition of this research, aims and objectives and importance of this research study are highlighted.

Chapter 2: This chapter looks at past literatures of related works for development of rain erosion resistant coatings. In addition, different techniques of rain erosion test,

different techniques of applying coating on wind turbine blades, and fundamentals about polyurethane and sol-gel materials are discussed.

Chapter 3: In this chapter in the first part material preparation method is explained. After that material characterization using FTIR, TGA, DMA, water contact angle and scanning electron microscopy was performed, and the results of pure polyurethane were compared with those of developed coating materials (PU+GNP) and (PU+GNP+SG).

In second part mechanical tests tensile, compression and tearing tests were performed to measure the mechanical properties of the pure and developed coating materials. In this part initially tensile test was done on pure PU at different temperature and strain rate. After that optimum mixing parameters of carbon nano particles in PU was established. This has been done by adding different carbon nanoparticles loading to PU and performing tensile tests to find the type and amount of the CNP which gave the best mechanical properties for developed coating materials. Afterward, compression and tearing tests were done on pure PU and developed coating materials and the results are compared. In the last part of this chapter water absorption studies was done on pure PU and developed PU nanocomposites by submerging the specimens in water over six months period. Tensile tests were performed on dogbone specimens at various time intervals to find the effect of water absorption on mechanical properties and the amount of water absorption was measured on cubic specimens submerged in water together with dogbone specimens in water tank.

Chapter 4: In this chapter drop ball tests were performed for measuring the amount of energy transmitted to the substrate. This has been done by dropping a steel ball on the upper surface of the specimen and recording the voltage from a piezoelectric located at the lower surface of the specimen by an oscilloscope. The results from drop ball tests are analysed by SVD-QR method, and the damping ratio of each material was calculated. At the last section of this chapter resilience tests was performed to analyse the amount of rebound energy by using motion capture system.

Chapter 5: In this chapter first, cool down time for pure PU coating was determined and based on that the required interval between shooting of the rubber ball in the Single Point Impact Fatigue Tester (SPIFT) were determined. After that SPIFT tests were performed at two different impact speeds of 150 m/s and 173 m/s. Energy dissipation and the extend of the heat affected are measured using thermographic infrared camera. The time to crack initiation, delamination and material loss are determined. At the end of the SPIFT tests SEM images of cross sections of specimens are obtained to compare the pattern of crack growth in different coating materials.

Chapter 6: This chapter presents the concluding remarks of this research and make recommendations for future works. A brief summary of the findings is presented.

Chapter 2 Literature review

2.1 Liquid erosion parameters

There are several parameters that affect erosion by liquid droplets. These parameters are: speed of impact, impact angle, droplet size, liquid density, acoustic velocity, cyclic properties of materials, hardness and geometrical aspects.

Impact speed: To explain the relationship between the erosion rate and impact speed, equation (2.1) can be used, which is derived from dimensional analysis [24].

$$V_m = cV^4 d^3 n_m \qquad (2.1)$$

Where V_m is erosion rate and c is a constant. The erosion rate V_m can be evaluated from Eq.(2.1) by using the experimental data of the droplet velocity *V*, the droplet diameter d and the number of impinging droplets n_m and c constant is determined to meet the experimental erosion rate at different position of test specimen along the spray axis [24]. The droplet velocity can be measured by particle image velocimetry, its diameter by shadowgraph technique and the number of impinging droplets in a unit area can be counted by a sampling probe [24, 25, 26]. Recently, the influence of the liquid film on the erosion rate is found to be the other influential droplet parameter. The thickness of the liquid film is an important factor for quantitative prediction of erosion rate [27, 26]. Generally, the erosion rate is directly proportional to the droplet size [28]. Different sizes of droplet cause different erosion damage, the difference is more significant for lower velocities. To analyse the effect of the droplet size on the erosion phenomena, two aspects should be considered. First, the same volume of water should impinge the samples and second, samples should be tested at speeds higher than the threshold speed to damage. Although droplet size and shape have an effect on the impact velocity, impact pressure is independent of the droplet size or shape [28]. Increasing the impact frequency of the water droplet also increases the damage depth rate and decreases the incubation period [29].

Impact angle: Impact angle is the angle between the direction of the water motion and the target surface [30]. The effect of the impact angle can be neglected if the incubation period for crack formation is short enough [31]; but if the incubation period is not short enough, the amount of volume loss will be different for different impact angles and the highest volume loss will be at a 90° angle of attack.

Initial surface condition: A slightly roughened surface will erode faster than a smooth surface. So the constant rate of erosion at the terminal stage for rougher surface can be realized in a shorter time period than for a smooth surface [32, 26].

Mechanical properties of the surface: Although hardness is the most common property that determines erosion damage, yield strength, modulus of elasticity, wear resistance, ultimate rebound resilience, and fracture toughness are the other factors that have an influence on erosion damage.

Temperature: Both the environmental temperature and liquid drop temperature have an effect on the erosion damage. The erosion rate will increase at higher temperatures due to the reduction in the viscosity of the liquid.

2.2 Liquid erosion mechanism of the blades

Failure due to liquid impact of water droplets which causes damage in the form of pitting or peeling over time is divided into two regimes.

Water droplet inlet: When the contact edge travels across the surface of the target at a velocity (Vc) greater than the velocity of shock wave (C) propagating into the water drop, the initial damage occurs (**Figure 2-1**). This damage happens because of the water hammer pressure which can be up to several MPa. This pressure can introduce initial cracks in the coating which can lead to the second stage of erosion mechanism (shear stress) [33].

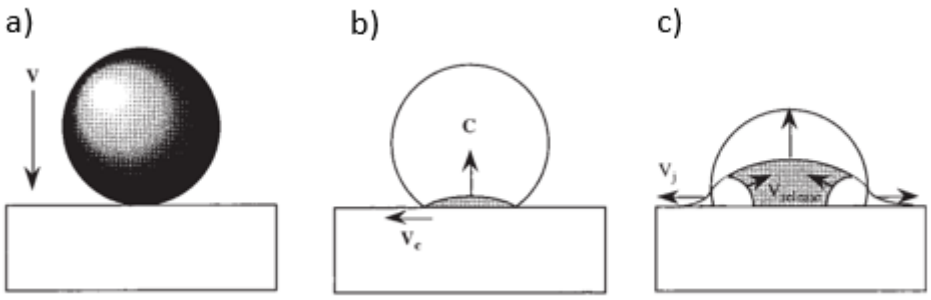

Figure 2-1 Sequence of liquid impact from initial impact through to release of high pressure: (a) at impact; (b) where water drop is compressed due to lack of free surface; (c) after shock wave has overtaken contact edge allowing decompression and jetting; dark regions in (b) and (c) represent area of compressed fluid. Reprinted from Jackson and Field [33].

To calculate the shock wave velocity into the water drop, the following equation can be used for impact velocity up to 1000m/s:

$$C = C_0 + kV \tag{2.2}$$

where C_0 is acoustic velocity, V is the droplet impact velocity and value for k is approximately 2.

Lateral jets: After the first stage, the water trapped in the compressed region can escape and generate water flow across the surface producing a high velocity sideways jet of fluid [34]. The velocity of the lateral jet is greater than the impact velocity and can cause material loss and extension of cracks (**Figure 2-2**).

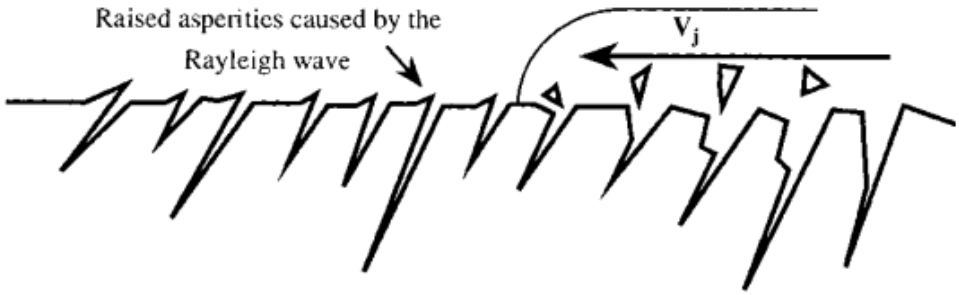

Figure 2-2 Damaging effects of lateral jetting; left hand side damaged by Rayleigh wave only; as lateral jetting crosses surface it tears off asperities it collides with. Reprinted from Jackson and Field [33].

Droplet after shockwave overtakes contact edge and generates a free surface which allows the compressed region to be released. From this free surface, three types of waves propagate into the water droplet to reduce the water hammer pressure. This incompressible pressure can be calculated by following equation [35]:

$$P_w = \rho CV = \rho V(C_0 + kV) \tag{2.3}$$

where ρ is the water density 1000 kg/m^3, C is the shock wave velocity and v is the droplet impact velocity as before. As an example, water impacting at 500 m/s gives an impact pressure of about 1250 MPa. The stagnation pressure of continuous jet acting at this speed calculated from $\rho V^2/2$ is about one tenth of this value [28].

Compression, shear and Rayleigh are the three stress waves, which play critical roles in the erosion process (**Figure 2-3**). The compression wave is the fastest one, whereas the shear wave is slower. The compression wave has small effect on causing the damage. The Rayleigh wave is the one, which interacts with the surface cracks. This wave has both vertical and horizontal components. The vertical component penetrates into the depth of the surface and it depends on the impact velocity and radius of the drop. The total impact energy, divided between these three waves is: Rayleigh wave (67.4%), shear wave (25.8%) and compression wave (6.9%). Stress reflections oscillate repeatedly through the coating and substrate structure until they dampen out and the energy of the initial shockwave is reduced [36].

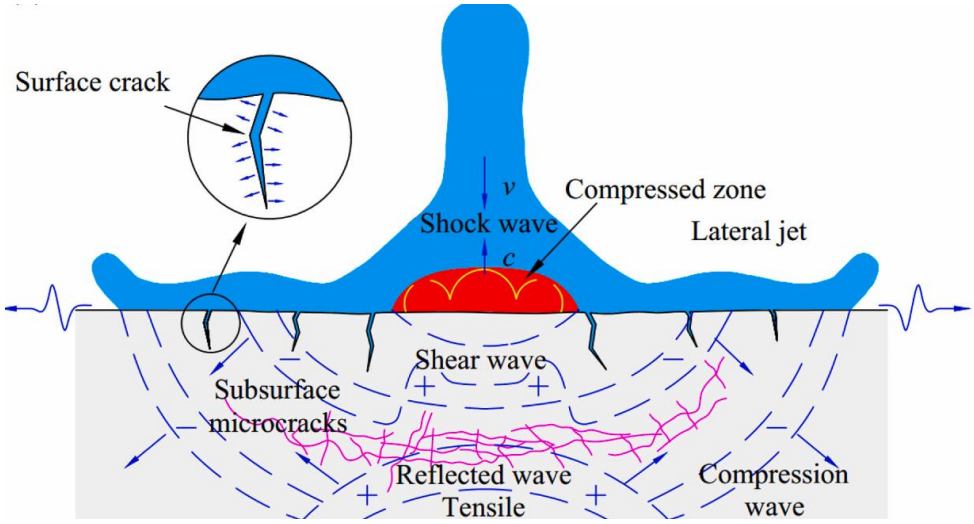

Figure 2-3 Different types of stress waves generated as a results of water droplet impact [37].

Spalling and lateral delamination between two coatings can be expected because of mismatch of the physical properties of both materials. In another word when an elastic wave reaches a free surface or interface between solids having different physical properties, the resultant wave can cause material failure [38, 36].

The process of liquid erosion occurs in the following stages:

- Incubation stage; where the surface remains unaffected and there is no record of significant mass loss (**Figure 2-4**). This stage may not appear if the impact conditions are severe enough to cause material loss for a single impact.
- Acceleration stage; during which rate increases rapidly to a maximum
- Maximum rate stage; where the erosion rate remains (nearly) constant
- Deceleration (or attenuation) stage; where the erosion rate declines to (normally) 1/4 to 1/2 of the maximum rate
- Terminal (or final steady-state) stage; in which the rate remains constant once again indefinitely. However, in some cases the erosion rate can continue to decline or fluctuate. Also, for some brittle materials, the rate can increase once again in what is called a “catastrophic stage” [28].

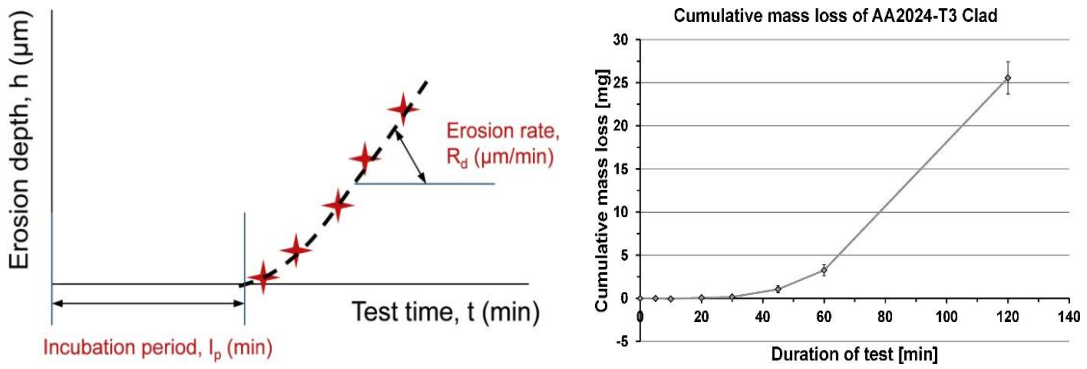

Figure 2-4 Incubation period and the stage with a constant erosion rate [39] (right), cumulative mass loss [40] (left)

Generally surface erosion in the turbine blade gradually expanded from the pressure side near the stagnation point to the suction side and the depth and width of the erosion increases in section closer to the tip [3].

2.3 Evaluation of erosion damage

Damage caused by rain erosion can be evaluated by analysing the erosion depth and incubation period.

Erosion depth: It is the local volume of damage per small area and it can be calculated by equation (2.4)

$$E_d = R_d\ (t - I_p) \tag{2.4}$$

Where E_d is damage depth in (mm), R_d is damage depth rate in (mm/s), t is the time and I_p is the incubation period in second [26].

Incubation period: all the materials exhibit an incubation period where no damage is observed up to a certain level of exposure to rain impact, but beyond this period of exposure, erosion damage increases rapidly [41, 35]. The amount of erosion damage per unit mass of droplets can be calculated by using the following equation:

$$E = \frac{R_d}{F_{req}.\rho(\pi.\frac{d^3}{6})} \tag{2.5}$$

Where E is the erosion damage per unit mass of droplets (mm^3kg^{-1}), R_d is damage depth rate in (mm/s), F_{req} is the impact frequency of the water droplet (number mm^2s^{-1}) and d is the diameter of the water droplet [29].

2.4 Erosion prevention systems

Erosion by liquid impingement can be reduced by a lower impact velocity, a decrease in normal component of the velocity (e.g. “tilting” the surface), smaller droplet size, shorter operation times under severe conditions, more resistant materials and the application of a shielding layer. One of the effective method to protect the wind turbine blades against the erosion is using an erosion resistant coating [23]. There are two common techniques to produce an effective surface coating, in-mould application and post-mould application. For the in-mould application, a surface coating layer of material similar to the matrix material is added to the surface of the blade as part of the moulding process. In the case of post-mould application, a surface coating is applied after the moulding process by different methods of coating [42]. It should be kept in mind that using the coating to protect the leading edge of the blades from the rain erosion will change the shape of the initial aerofoil section slightly which can have effect on the aerodynamic performance of the turbine; but this effect is negligible in comparison with the effects of the eroded blade on the performance of the turbine [6, 43].

Materials are coated for a number of reasons such as to: make a substrate biocompatible, increase a material’s thermal, mechanical or chemical stability, increase the wear resistance, improve the durability, decrease friction, inhibit corrosion or change the overall physicochemical and biological properties of the material [44]. As leading edge of the blade is the most sensitive area of the wind turbine, protective layers such as tape or paintable and elastic coating are used for mitigating leading edge erosion of the blades. These layers absorb the impact energy without crack formation. The ability of a coating to absorb and distribute the energy from an impact can vary and this is expressed by the impact frequency [1].Current blade coating systems typically consist of a putty layer which is applied for filling pores in the composite substrate, a primer to secure good adhesion of the subsequent coat and a flexible topcoat usually from a polyurethane-based formulation [1]. If leading edge protection has not been applied during the manufacturing process, leading edge erosion can occur within two years of operation. A rough estimation suggests 50% of new large wind turbines are specified with a blade rain erosion resistant coating [8]. There is a variety of procedures for coating including: vapour deposition, chemical milling, layer-by-layer coating, dip coating and sol–gel coating technique [44]. The development of new coatings, which can protect the leading edge of the blades against the erosion, is a topic of current research. Super hydrophobic coating using nanoparticles embedded in a resin [45], hydrophobic coating with anti-icing capability

[46]and ceramic coating materials with a high-erosion resistance [2] are some of these coating which are used in the industry to protect the leading edge of the wind turbine blades.

2.5 Design of liquid impact testing apparatus

There are two methods for performing accelerated rain erosion tests; one method uses a whirling arm, which carries the specimens and rotates them under an artificial rain field produced by nozzles or needles [40] and in the other method a high velocity stream or jet of water is fired onto a stationary test specimen [47, 48]. The two methods are generally similar, one of the differences between these methods is the active/passive impact mode between water droplets/jet and test specimens [1] and another difference is that the continuous jet produces stagnation pressure, whereas the discrete impacts in liquid droplet impingement produce much larger shockwave pressures.

2.5.1 Critical parameters for design

Stand-off Distance (SOD): The distance between the nozzle and the specimen surface has a significant effect on the erosion rate (See **Figure 2-5**).

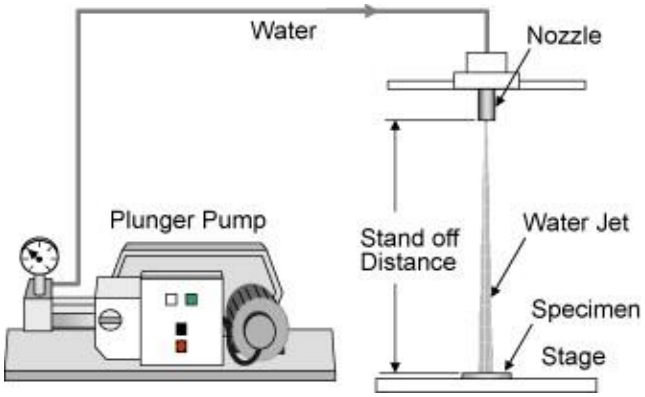

Figure 2-5 Schematic illustration of a testing apparatus. Reprinted from Oka and Miyata [2] with the permission of Elsevier Publishing.

The damage depth rate will decrease for very short or very long SOD. If the distance is too short (less than the intact length), it will cause negligible material removal because, in the short SOD the water that hits the surface forms a water column instead of water droplet. It is known that water droplet impact is more damaging than the impact of an intact fluid stream [30, 38, 49]. Intact length is the minimum distance from the nozzle over which the liquid jet is still connected [50, 51, 52]. The effect of the SOD on the erosion volume can be explained in four steps. As can be seen in **Figure 2-6**, erosion starts immediately after the incubation period and is then followed by the acceleration, maximum rate, deceleration and terminal erosion stages [28].

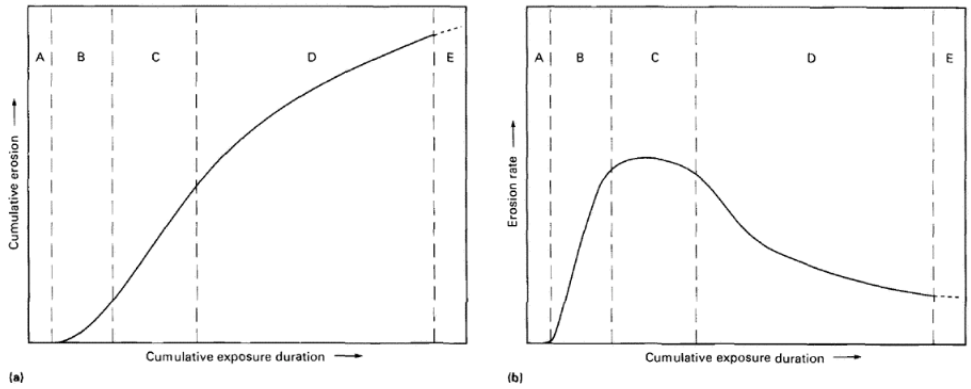

Figure 2-6 Characteristic erosion versus time curves. (a) Cumulative erosion (mass or volume loss) versus exposure duration. (b) Corresponding instantaneous erosion rate versus exposure duration. The following stages have been identified: (A) incubation stage (B) acceleration stage (C) maximum rate stage (D) deceleration stage; and (E) terminal or final steady-state stage, if assumed to exist. Reprinted from Heymann [28].

The decrease of the erosion rate far from the nozzle can be explained by the decrease in the droplet velocity; however, the decreased erosion rate in the near field of the nozzle is because of the influence of the liquid film over the specimen (**Figure 2-7**).

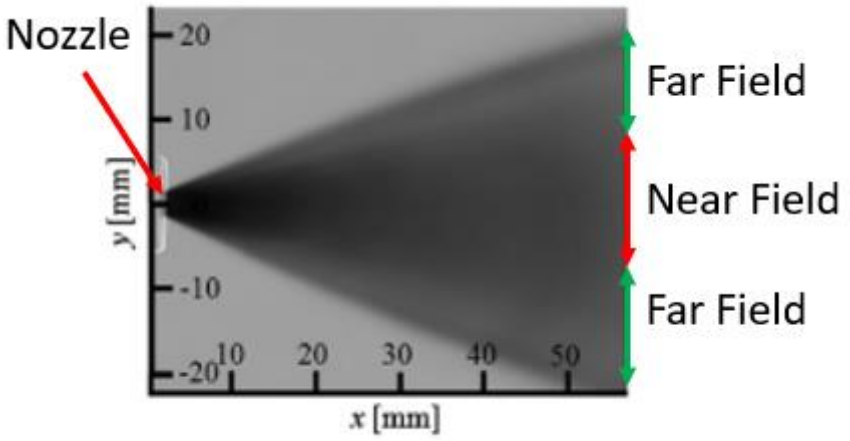

Figure 2-7 Near filed and far field from the nozzle [24].

It is proven that the maximum pressure on the solid surface due to the impingement of a droplet of diameter 100µm is damped down by 10% because of the presence of a liquid film with 2.5µm thickness over the solid material [49]. Furthermore, the erosion in the near field of the nozzle is higher than the erosion rate in the far field of the nozzle, which is due to the higher local flow rate in this area [24].

Impact angle: As explained before the maximum rate of mass loss will happen at an impact angle of 90^{o} [50, 31].

Testing time, nozzle diameter, droplet size and impact velocity are the other important parameters that need to be well-defined when designing a liquid erosion testing machine.

2.5.2 Whirling arm based system

This type of apparatus has been used for the study of liquid droplet impingement erosion by droplets having a diameter larger than 1mm [51]; moving the sample is good way to simulate the impact taking place when a moving object is exposed to a rainfall. The well-known rig which is used for this method is the whirling arm. In the following some of the previous designed systems are explained.

The Whirling Arm Rain Erosion Rig (WARER) was designed and built by University of Limerick [40]. It consists of a rotating arm that carries the sample on the tip of itself (**Figure 2-8**). In this machine, water droplets are introduced into the test chamber through 36 blunt dispensing needles with an internal diameter of 0.15 mm [40].

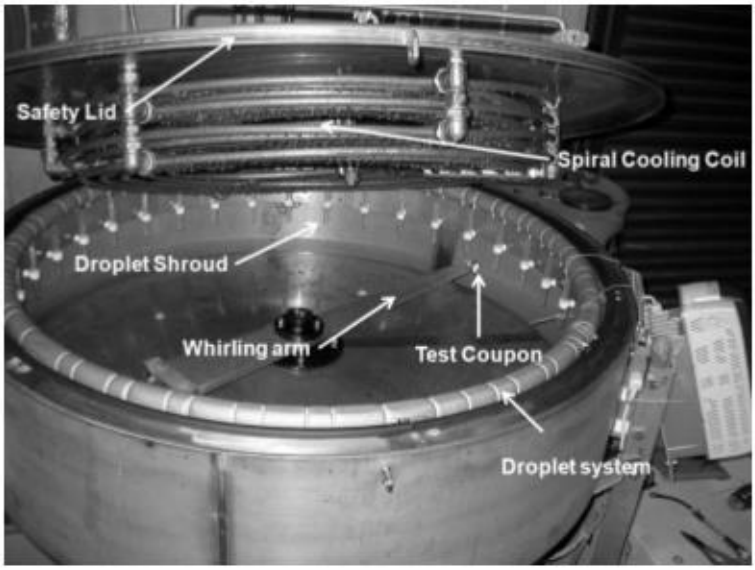

Figure 2-8 WARER at University of Limerick. Reprinted from Tobin et al. [40] with the permission of Elsevier Publishing.

SAAB is another erosion testing facility (**Figure 2-9**); designed in the 1960s it has a prominent history in the field of rain erosion [41]. The sample is placed on a rotating arm at a radius of 2.19 m. The system is able to simulate impact speeds of up to 300 m/s. This system also is able to vary the droplet size and rainfall rate.

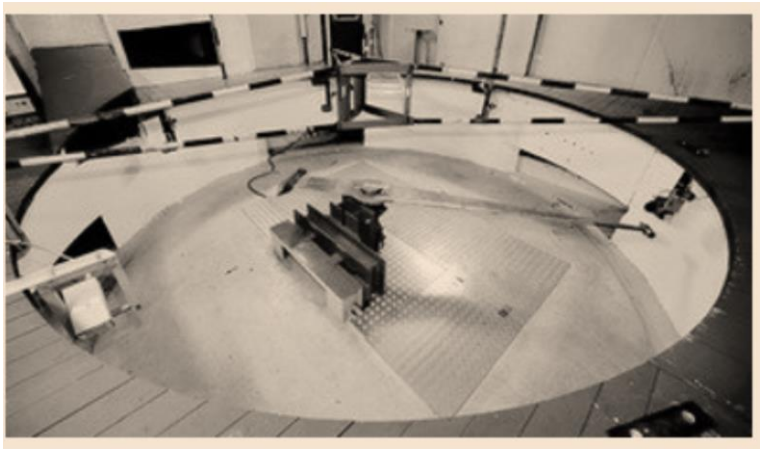

Figure 2-9 SAAB rain erosion test facility. Reprinted from Tobin et al. [41].

Zhang, et al. [1] designed a laboratory water jet setup to analyse the liquid erosion of blade coatings. In this machine 22 coated panels can be placed on the rotating wheel with the diameter of 52 cm and speed range of 126-160 m/s, **Figure 2-10**. In this system, the distance between the nozzle orifice and the sample surface was kept at 10 cm and erosion evaluated by inspecting samples every half an hour. The rainfall intensity is 30-35 mm/h and the water droplet size is 1-2 mm.

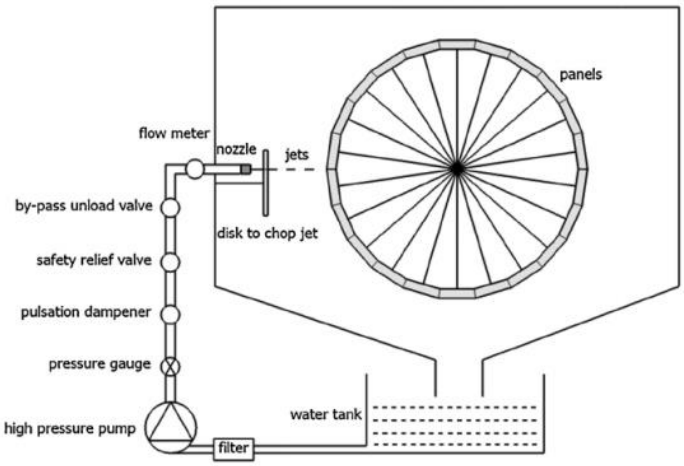

Figure 2-10 Water jet erosion rig. Reprinted from Zhang et al. [1] with the permission of Elsevier Publishing.

2.5.3 Stationary sample erosion test (SSET)

This apparatus allows the study of the liquid droplet impingement erosion for smaller droplets with diameters in the order of few hundreds of micrometres [24]. This method is simple, economic and reliable (**Figure 2-11**). The specimen is fixed and water hits the surface of the specimen through a water jet nozzle.

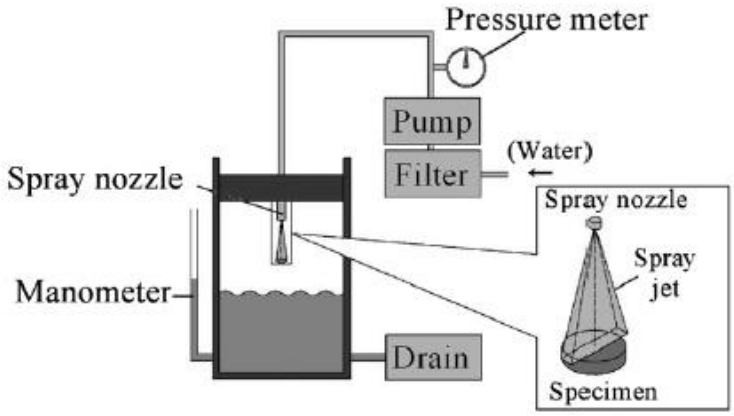

Figure 2-11 Experimental apparatus for liquid impingement erosion by high speed spray. Reprinted from Fujisawa et al. [24] with the permission of Elsevier Publishing.

Grundwürmer et al. [53] used SSET water jet for liquid erosion testing (see **Figure 2-12**). The SSET unit was setup with fixed SOD of 300mm between the nozzle and sample surface, impact angle of 90^{o} and droplet diameters starting from 0.3mm down to below 0.1mm. The water jet was moved across the sample surface at two different feed speeds: 0.017 and 0.25m/s resulting in exposure times of 4.8 and 0.32s per water jet crossing.

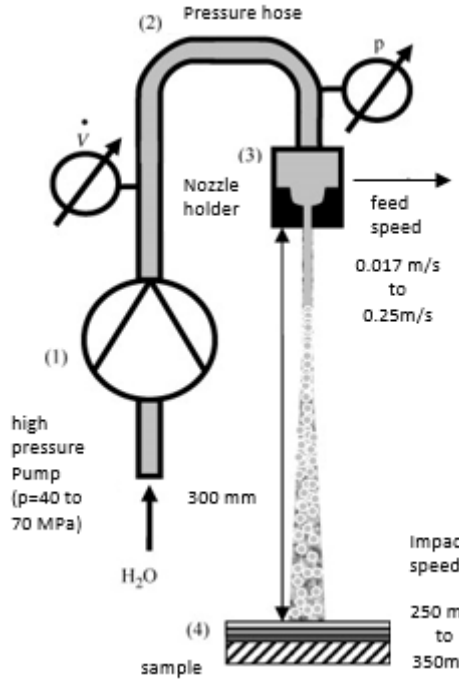

Figure 2-12 Stationary sample erosion test. Reprinted from Grundwürmer et al. [53] with the permission of Elsevier Publishing.

Fujisawa et al. [25] designed an experimental apparatus for water droplet impingent testing (**Figure 2-13**). They setup two different units for their experiments, one unit with a 0.8mm diameter nozzle, SOD of 270mm with the nozzle pressure of 16MPa and the other unit with

the same nozzle but SOD of 480mm and nozzle pressure of 28MPa, for both units the impact angle was 90° [25].

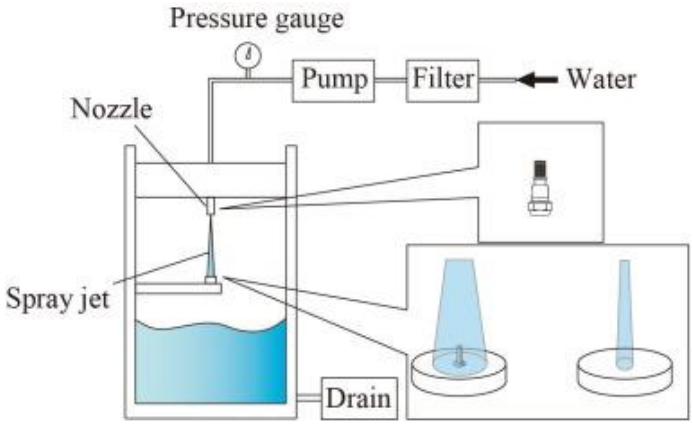

Figure 2-13 Experimental apparatus for LDI erosion. Reprinted from Fujisawa et al. [25] with the permission of Elsevier publishing. LDI: liquid droplet impingement.

Pulsating Jet Erosion (PJET) is an erosion test facility in which a high pressure water jet is forced through a nozzle of 0.8mm diameter and is subsequently cut into individual water jets by a rotating disk (**Figure 2-14**). This system can provide different impact velocity and impact frequency as well [40, 47].

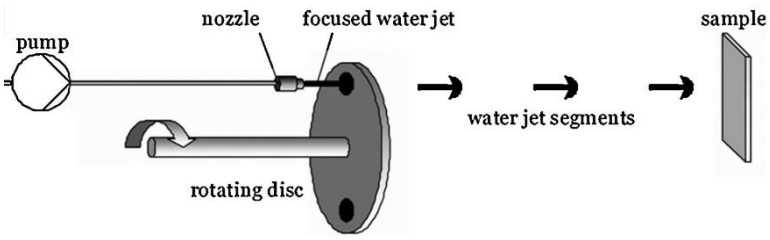

Figure 2-14 Principle of PJET test method. Reprinted from Tobin et al. [40] with the permission of Elsevier Publishing. PJET: pulsating jet erosion

2.6 Polyurethane (PU)

2.6.1 History of polyurethane

Polyurethane discovered first in 1937 by Otto Bayer and his co-workers in laboratories of Farben in Leverkusen, Germany. By passing time, different types of polyurethanes were produced and introduced to the market; for instance, in 1952 polyisocyanates were used commonly in industry, between 1952-1954 due to the advantages of polyether polyols, such as: cheaper price, easier material handling procedure and better hydrolytic stability, it is decided to use it instead of polyester in the structure of polyester-polyisocyanate system. In 1956 first polyether polyol was produced by polymerising tetrahydrofaran by Du Pont and introduced as polytetramethylene ether-polyglycol (PTMG). Following to that in 1957, BASF produce polyalkykene glycols. In 1960 another form of polyurethane was introduced which

was flexible polyurethane foams and the rigid foam was also produced in 1967 [54]. During years, different combination and reactions were tested and the potential new applications were explored based on the properties of the outcome product. Currently polyurethane play a large role in everyday life in a different number of applications. There is a significant grow in interest of using PU due to the simple synthesis method, variety of applications and superior properties of this material. Tendency to elastic deformation of the polyurethane, makes it able to absorb impact energy of erodent particles with minimal damage which make this material a good candidate to use as rain erosion resistant coating; on the other hand, softness and high deformability of PU increase the impact time of the particles which results in reducing the impact force and stresses and finally reduce the erosion [55]. For instance, one of the applications of using polyurethane is to use it as a wear protection for oil pipe, where the particles are freely moving along the fluid stream and suddenly impacting the surface of the pipe due to the flow turbulences and cause wear at low impact angle. There are few items which indicate the end-use application of PU, such as, type, position and structure of the isocyanate as well as the hydrogen bonding [54]; for instance it is shown that using IPDI as isocyanate gives an PU with product with higher stability and also shorter hydrogen bond provides stronger bonds [56, 57]. Some of the polyurethane applications can be seen in **Figure 2-15**:

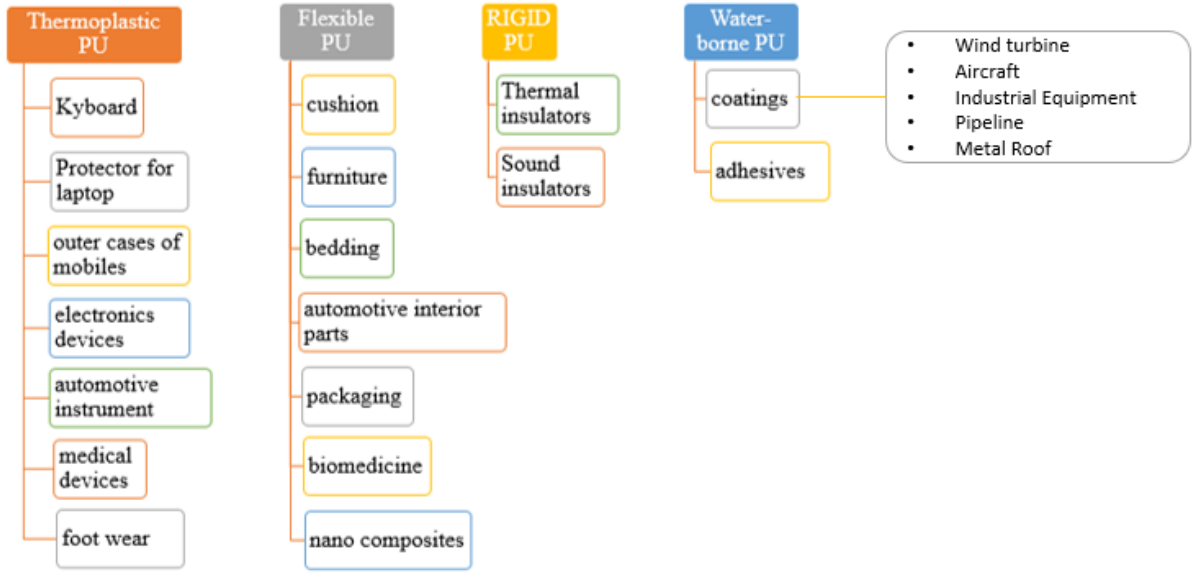

Figure 2-15 Different applications of polyurethane.

2.6.2 Polyurethane structure

Polyurethanes are created through an exothermic reaction between an isocyanate with a polyol in the presence of additives. Diisocyanates are key raw materials involved in the synthesis of polyurethane; these materials are characterized by N=C=O group and are highly reactive

alcohols. Two types of isocyanates are mainly used to synthesise polyurethane, which are toluene diisocyanate (TDI) and polymeric isocyanate (IPDI). TDI is formed by adding nitrogen group on toluene and then reacting them with hydrogen and IPDI is created from phosgenation reaction of aniline-formaldehyde polyamines. **Figure 2-16** shows the isocyanate TDI and **Figure 2-17** shows isocyanate IPDI.

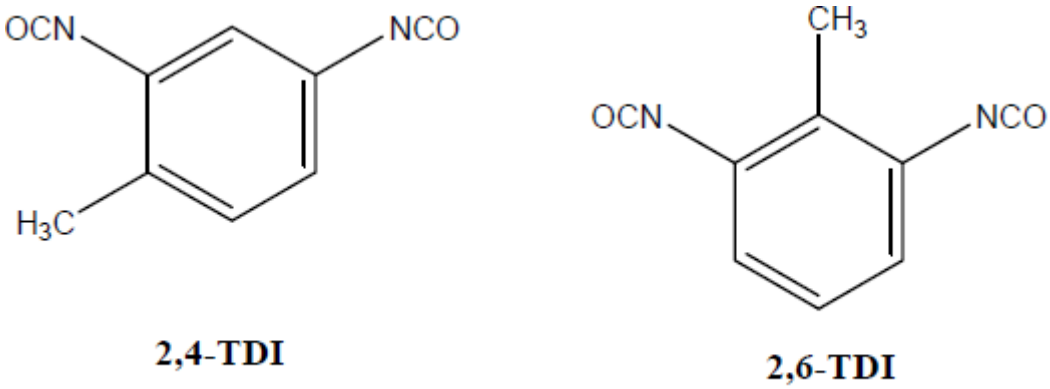

Figure 2-16 TDI isocyanate [54].

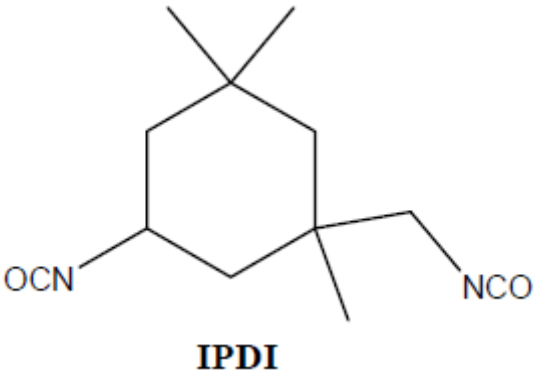

Figure 2-17 IPDI isocyanate [54].

As mentioned before another component of polyurethane is polyol which is an organic compound, containing more than two hydroxyl or alcohol group. To protect polyurethane from external damages such as heat, oxidation and light, additives are used during the manufacturing process of polyurethane. For example, to protect PU from oxidation hindered phenols are used as additive or to protect PU from light hydroxybenzotriazole is used.

Polyurethanes have good tensile strength, compression strength, impact resistance, abrasion resistance and tear strength. In comparison with rubber, PU has higher abrasion resistance, higher tear resistance, higher load bearing capacity and more resistance to radiation. In comparison with metals, PU is lighter, has higher abrasion resistance, higher corrosive resistance, higher flexibility, higher resistance to impact and higher resilience [58]. In

comparison with plastics, PU has higher impact resistance, better elastic memory, higher abrasion resistance, higher resilience, and better radiation resistance. It is shown that thermoplastic polyurethane (TPU) are suitable material for erosion resistant coating [59]; these materials have good corrosion resistance, good adhesion to the substrate and lighter weight than metallic protections [60].

2.6.3 Polyurethane derived coatings

Polyurethane coatings applied in the interest of erosion resistance, including that of rain, are already common practice in both aerospace and wind turbine applications. Polyurethane topcoats exhibit such high resistance against rain erosion which can be used in both on-shore and off-shore large-scale wind turbines [40]. One of the reasons that make polyurethane a good candidate for rain erosion resistant coating is due to its unique mechanical properties; Polyurethane has excellent water, oil, and corrosion resistance, high elasticity and dampening, and good adhesion to other materials [61]. Also, it has very light weight in compare to the metallic materials, easy to apply and then reduce the cost of application in comparison to other methods. As there is no standardized test procedure for erosion protection coating for wind turbine blades; it is hard to say that which application method of PU is the best.

One of the ways of applying polyurethane coating on the leading edge of wind turbine blade is introduced by material company 3M, which is called two-component polyurethane tape [62]. This method has some advantages and some disadvantages; for example, one of the advantages is the ease of use, which can be done by being adhered to the edge of the wind turbine blade in a single layer of tape. On the other hand, failing to absorb a significant amount of impact energy, time consuming and costly procedure of maintain, repair and replacing the tape and also increasing the drag coefficient of the blade are some of the disadvantages of this method which makes this method limited to use only in smaller scale of wind turbines [63]. As mentioned before other method of applying polyurethane to the surface of wind turbine blade is via spray or painting the leading edge of blade. In this method first primer applied on the substrate and then covered by topcoat composed of polyurethane (**Figure 2-18**).

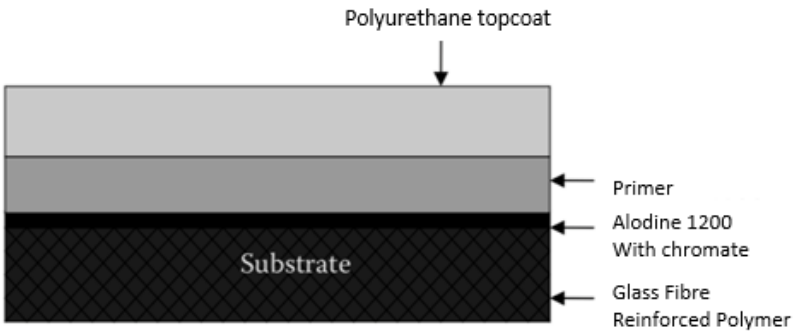

Figure 2-18 Typical Aerospace Coating System [64].

In this method the primer coat has the function of providing adhesion between the polyurethane top coat and the substrate layer composed of composite materials [64]. Procedure of applying spray coating can be seen in **Figure 2-19**. However, it should consider that reapplication process of this sprayed or painted on topcoat is not as simple as reapplying the tape forms of polyurethane, it is extremely costly, especially in the case of off-shore wind farming.

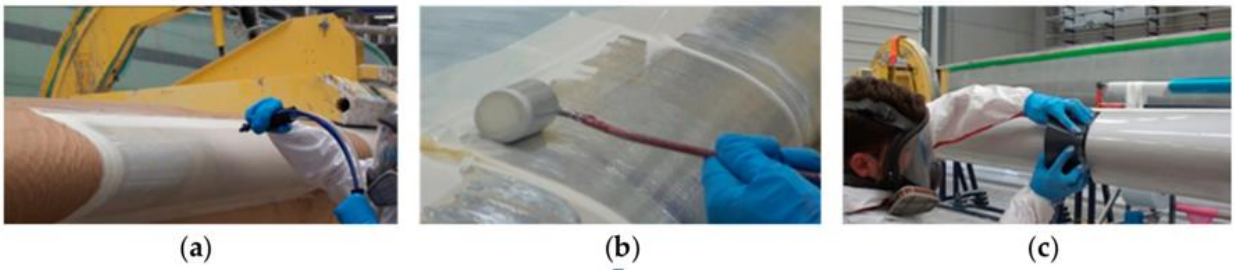

Figure 2-19 Leading Edge Protection Application Procedures, (a) spray, (b) roller, (c) trowel [65].

2.6.4 Polyurethane modified nanoparticles

Adding nano-sized reinforcing particle to polymers is one of the common ways to improve the required properties of pure PU. Various studies showed that among various nanomaterials, carbon nanoparticles (CNPs) can improve toughness, tensile strength, Young's modulus, hardness, modulus of stiffness and thermal conductivity of PU. During droplet impact some energy absorbed and dissipated in the coating. A higher thermal conductivity distributes and dissipates the generated heat more effectively.

As can be seen in **Figure 2-20** development of nanoparticle-filled polymer systems is the core of the roadmap with the development of technology to tailor both nanoparticle–polymer interfaces and nanoparticle dispersions [64].

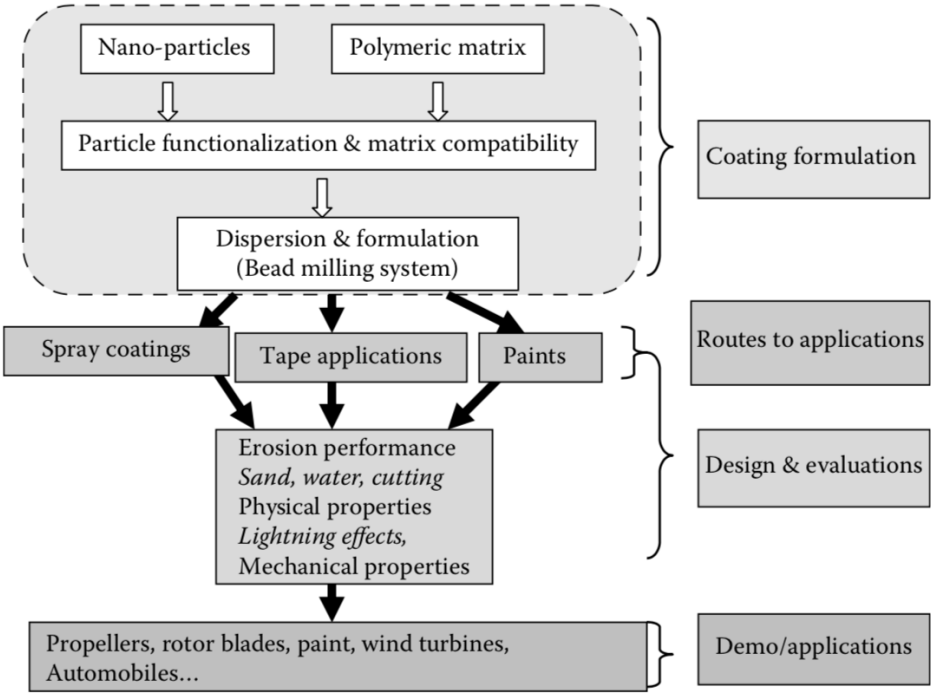

Figure 2-20 A Proposed Nanocomposite Coating Technology Roadmap [64].

There is no standardized way to mix carbon nanoparticles and polyurethane, so many methods must be reviewed. Papers can be found that detail different ways to create these nanocomposite materials, but only few actually involve polyurethane in particular. One of the difficulties in developing a proper mixing procedure is the dispersion of the carbon nanoparticles within the polyurethane matrix and thus deterioration of polyurethane properties [66]. In the past, several researchers have reported how the mechanical properties and erosion resistance of PU elastomers can be improved by addition of various nanoparticles. Malaki et al. [67] reported a 29% improvement in the erosion resistance of polyurethane coatings with the addition of 6wt% of fumed nanosilica. Petrović et al. [68] made polyurethane nanocomposite with nanosilica filler concentration ranging from 0 to 50wt%. They showed the coefficient of thermal expansion decreased with increasing nanosilica content. At 40wt% nanosilica concentration, the tensile strength was increased 300%. Elongation at break continuously increased with increasing nanosilica content, reaching an increase of 600% at 50wt%. Chung, et al. [69] prepared hybrid PU/silica composites using a sol-gel reaction between tetraethyl orthosilicate (TEOS) and triethoxysilyl groups (TESPI) grafted onto PU. The UTS sharply increased from the cross-linking of the grafted silica at low TEOS concentrations but decreased with the increase of TEOS content as the excess silica inhibited cross-linking: UTS of 15.2 MPa (PU without TEOS and TESPI) increased to 59.6 MPa at 12.5mmol of TEOS and 2.5mmol of TESPI (290% increase). The tensile strain results suggested that sol-gel cross-linking did not

disturb the PU chain stretching. Syamsundar et al. [70] studied erosion wear resistance of PU coatings modified with boron carbide (B_4C) or silicon carbide (SiC) nanoparticles and compared the results with neat PU. They found the optimum nanoparticles loading with B_4C was 20wt% and 10wt% for SiC, beyond these loadings the performance deteriorated. Mills et al. [71] modified PU coatings with 5 and 10wt% of nano-silica and found that with a 5wt% loading, ionic resistance was significantly increased due to the polymer network reinforcement and water absorption was reduced. Kotnarowska et al. [72] reported that the type of nanofiller and its size significantly affected the erosion resistance of polyurethane coatings. The greatest erosion resistance was obtained for PU modified with silica having the smallest filler grain. Pokharel *et al.* [73] manufactured PU nanocomposites by in-situ polymerization using pristine graphene nanoplatelets (GNPs), graphene oxide (GO), and functionalized graphene sheets (FGSs). The PU nanocomposites with a 2wt% loading of GO or FGS showed significantly higher Young's modulus. than the one modified with GNPs. Tarasov, et al. [74] analysed effect of fullerene, GO and their mixture (15/85 ratio) on cross-linked PU urea elastomer for filler loading of 0.01wt% to 0.1wt%. Addition of fullerene resulted in 10% decrease in the Young's modulus at 0.1wt% filler loading, while GO increased Young's modulus by 10% relative to the neat PU. For the fullerene/GO blend, a weak negative synergetic effect on tensile strength was observed. However, the use of fullerene/GO additive demonstrated a well-pronounced positive synergetic effect resulted in a 20% growth of Young's modulus for 0.01 wt% loading of fullerene/GO and in a 30% growth at 0.1 wt% loading. Low concentration of fullerene or GO additives decreased the resistance of the PU composite to spall fracture by more than 15% and 30%, respectively. This is caused by introduction of the hard particles in homogeneous structure of the PU which generated numerous additional nuclei of fracture, causing at lower tensile stress. Xia and Song [66] studied polyurethane–carbon nanotubes (single- and multi-walled) composites prepared by in-situ polymerization with 0.5, 1 and 2wt% CNT. The highest tensile strength was with PU modified with 2wt% single-walled CNT at 9.11 MPa. Tayfun, et al. [75] prepared 0.5, 1, 1.5 and 2wt% CNT reinforced thermoplastic polyurethane (TPU) composites by melt-mixing. The highest improvement of 41% in UTS was obtained for 0.5wt% nitric acid-treated CNT and the highest increase of 150% in Young’s modulus was achieved at 1wt% of CNT loading. Guo et al. [76] used multi-walled CNTs (MWCNTs) for reinforcement of PU by the combination of in-situ polymerization and solution-casting approach. Compared with neat PU, incorporation of 1.0wt% loading of MWCNTs into PU matrix significantly improved the Young’s modulus, stress-at-break and the elongation-at-break by about 90%, 500%, and 75%, respectively. Kumar, et al. [77] synthesized PU with 1 to 10wt% MWCNTs

using a two-step solution mixing films and compression moulding of the thin films. The results of quasi-static nanoindentation tests showed elastic modulus and hardness have been continuously improved by increasing MWCNT loading and increased 124% and 53%, respectively, for 10wt% MWCNTs loading. The fracture resistance has also improved by 52% for 7wt% MWCNTs loading. Li, et al. [77] used various loading of acid-treated MWCNTs for reinforcement of polyisobutylene (PIB) /polyethylene glycol (PEG)-based polyurethane nanocomposites (PIGNTs). The test results showed that the mechanical properties of PIGNTs were significantly enhanced at fairly low MWCNT loading. A 126% improvement of UTS is achieved at 0.3 wt% MWCNT loading. Additionally, the PIB/PEG-based PU and PIGNTs exhibit excellent damping properties (tan $\delta > 0.3$) in a wide range of temperature from −60 to 35°C. Qiao et al. [78] developed hydrophobic polydimethylsiloxane-based polyurethanes (Si-PUx) with hydroxypropyl polydimethylsiloxane (H-PDMS). They showed that the cavitation erosion resistance of Si-PUx coatings improved with an increase in the H-PDMS content. The cumulative mass loss of Si-PUx with 12.5wt% H-PDMS was 2.96 mg without any visible holes and cracks on the surface after 80 h testing. Eivazi Zadeh et al. [79] prepared neat PU and PU/CNT composites containing 0.05%, 0.1%, 0.5%, and 1% wt% CNTs by electrospinning. The highest increase in toughness (4.5 times) and stiffness (3.5 times) relative to neat PU was achieved with 0.5wt% CNT. In addition, although the existence of CNTs did not affect the contact angle significantly, it increased the hydrophilicity of PU to a maximum at 0.1wt% CNTs. Moghim et al. [80] studied thermoset polyurethane reinforced with 0.05–5wt% loading of multi-walled CNT, prepared using a solution casting method. Modulus of elasticity, tensile strength and toughness of PU strongly affected by the amount of CNTs loading and tensile strength of PU was enhanced about 122% with 1 wt% CNTs loading. Alberto et al. [81] tested PU resin films reinforced with few-layered graphene (FLG) nanoparticles and observed an improvement of over 100% in the abrasion resistance, 25% increase in the coefficient of static friction and a 200% increase in the coefficient of dynamic friction. Rihayat et al. [82] used a polyether polyol in the production of a PU by reaction with an isocyanate. The clay was treated with cetyltrimethyl ammonium bromide (CTAB) and octadodecylamine (ODA) and the resulting organoclay was intercalated in the PU. Tensile strength and elongation at break of the PU/clay nanocomposites increased with increasing clay content. The largest increase of 166% in tensile strength and 600% in elongation at break achieved with 5wt% loading of ODA modified clay. Chung et al. [83] modified graphite (MG) powder with particle size <20 μm and covalently linked them to a polyurethane backbone. The hydroxyl content (-OH) of the MG is

an important factor for linking graphite to the PU. The ultimate tensile stress increased up to 436%, and the maximum strain increased by 1744% compared to the linear polyurethane.

2.7 The sol–gel technique

Over the last few decades, the sol–gel techniques have been used for production of a variety of mixed–metal oxides, nanomaterials and nanoscale architectures, nanoporous oxides, and organic-inorganic hybrids. The sol–gel processing is the most convenient manufacturing method because of its simplicity, good mixing of starting materials, relatively low reaction temperature and easy control of chemical composition of the end product. Sol–gel synthesis is utilized to fabricate advanced materials in a wide variety of forms: ultrafine powders, thin film coatings, porous or dense materials.

The sol–gel technique is a wet-chemical technique that can produce polymeric networks of hybrid organic/inorganic materials that can be used as composite coatings. These composite materials which produced by sol–gel techniques have the properties of organic polymers such as flexibility and the properties of inorganic materials such as hardness at the same time. In a sol–gel, solid particles are suspended in a liquid to form a colloidal solution (*sol*) that acts as the precursor to an integrated network (*gel*) of either discrete particles or a polymer network [52]. The hardness and the flexibility of the sol–gel derived coating can be adjusted by the amount of inorganic-rich compounds as well as by the degree of cross linkage, for example increasing the Non-cross linking organic groups will increase the flexibility of the coating.

The sol–gel process enables the deposition of films and coatings of thicknesses from 0.01-5 μm. The properties of sol–gel derived coatings can be engineered at the molecular level for optimum physical and chemical behaviour, providing control over adhesion, hydrophobicity, permeability, texture, morphology, optical properties and other characteristics [84].

For enhancement of resistance to liquid erosion, the hybrid network provides sufficient mechanical stability to avoid cracks caused by droplet impact and is also flexible enough to absorb the kinetic energy of droplets [53]. The most promising coatings for commercial applications made using the sol–gel technique are Organically Modified Ceramics (ORMOCER) and Organically Modified Silica (ORMOSIL) [85]:

(i) Organically Modified Ceramics (ORMOCER) is inorganic-organic composites on a molecular or nano level. The inorganic backbone may be synthesized alkoxides or soluble oxides. Organic components can be introduced through the formation of carbon–silicon bonds, covalent bonds or through electrostatic interactions (i.e. ionic bonding). Introduction of organic polymeric chains leads to a second type of network; this network

can be chemically linked to the inorganic backbone or act as an interpenetrating network. Properties of the materials can be varied by changing stochiometries, reaction conditions and processing. Their applications run from thermoplastic materials (e.g. sealing) to brittle coatings (hard coatings) [86]. The basic properties of ORMOCER® which make them very attractive materials for coating applications are their transparency, their good adhesion to various substrates, their chemical stability and their good abrasion resistance due to the inorganic structures in ORMOCER® [87].

(ii) Organically Modified Silica (ORMOSIL), the silica surface consists of two types of functional groups, siloxane (Si–O–Si) and silanol (Si–OH). Thus, silica gel modification can occur via the reaction of a particular molecule with either the siloxane (nucleophilic substitution at the Si) or silanol (direct reaction with the hydroxyl group) functions. Reaction with the silanol group constitutes the most common modification pathway. There are three main methods in which functional groups are attached to the silica surface [2]: (i) reaction of organosilanes or other organic molecules and silica surface functions, (ii) chlorination of the silica surface followed by reaction of the Si-Cl with an appropriate reactant (e.g. amine or alcohol), (iii) via sol–gel methodology followed by post-modification, wherever necessary [88].

2.7.1 Advantages of sol- gel technique over traditional techniques

There are several coating methods in the industry, some of them are expensive because of expensive equipment (e.g. plasma spraying), some of them produce low quality coatings (e.g. flame spraying), some methods are not practical to coat the internal surface of the small cylindrical (e.g. high velocity oxygen fuel spraying) and some of them are time consuming and so challenging to produce thin film (e.g. powder coating technique). On the other hand, purely inorganic coating materials are very expensive coatings and they have poor adhesion to substrate due to the difference in thermal expansion coefficient between the coating materials and substrate.

Sol–gel technique is an alternative to traditional coating techniques which makes it possible to produce organic-inorganic hybrid coating [89, 90]. In this method individual coating layers are limited to less than 0.5 μm to prevent cracking and coating failure during thermal processing as a result of trapped organics within the coating [91] which has negligible additional weight on the substrate. By sol–gel method it is possible to produce coating layer which is thick enough for corrosion protection as well [92]. In this method having the ability to use different silane precursors allows modification of the properties of the gel [93]. Control of stochiometries

allows control of the hardness and the amount of non-cross linking organic groups determines the flexibility of the coating.

In addition, in sol–gel technique mixing is done at the molecular level, so the coating has high purity and uniformity. Sol–gel coatings are normally performed at relatively low temperature, so there is no need to reach the melting point, the method is more energy efficient than other methods of coatings that require temperature approaching melting point of materials [94, 95], temperature can be as low as room temperature up to a maximum of 500 ℃ , which is the upper limit for the temperature stability of the organic groups [96].

This technique (sol–gel) has some disadvantages as well; one of them is the high permeability of the coating and the difficulty in controlling the porosity, which is important as erosion resistance is strongly linked to porosity of the coatings [97]. Shrinkage of the wet gel during curing process can also cause crack formation in the coating structure and finally the sol–gel method is highly substrate-dependent, primarily due to limitations imposed by thermal expansion mismatch between the coating and substrate [92].

Sol–gel process has four steps:

a. Preparation of a stable suspension of colloidal particles (sol) in a liquid.
b. Depositing the solution on the surface by one of a variety depositing methods and produces the coating.
c. Polymerization of the sol through the removal of the stabilizing components and produce a gel in a state of a continuous network.
d. Heat treatments to pyrolyze the remaining organic or inorganic components and form an amorphous or crystalline coating.

The reactions in the sol–gel process depend on the parameters such as: nature and concentration of alkoxides, amount of water added, type of the catalyst used, sequence of adding components, mixing schedule and temperature.

2.7.2 Techniques for deposition of sol–gel coatings

Dip Coating Technique is a process where the substrate, which needs to be coated, is immersed in a liquid and then withdrawn with a well-defined withdrawal speed. This process is performed under controlled temperature and atmospheric conditions (**Figure 2-21**). In this technique, two parameters control the thickness of the coating: the viscosity of the liquid and the angle between the substrate and liquid surface. This method is suitable for coating the curved surfaces like bulbs, eyeglass lenses and bottles.

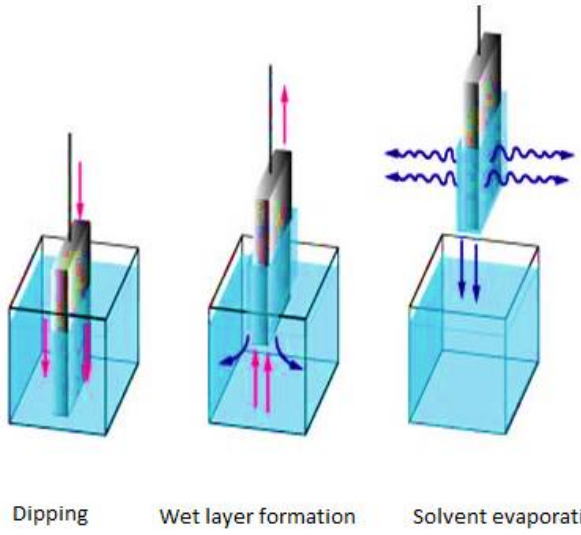

Figure 2-21 Dip coating process. Reprinted from Attia et al. [95].

Spin Coating Technique:

Spin coating is an incredibly effective technique for producing high quality, uniform thin films. In this technique, the substrate spins around an axis, which should be perpendicular to the coating area (**Figure 2-22**).

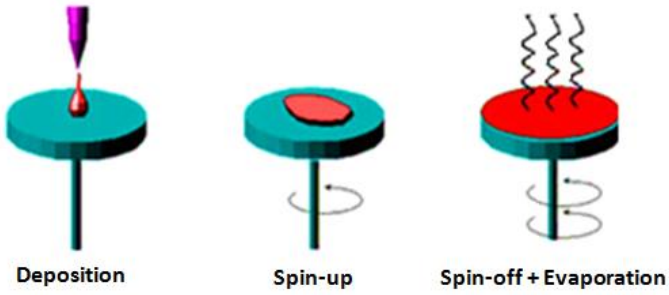

Figure 2-22 Spin coating process. Reprinted from Attia et al. [95].

This technique has four steps: deposition of the sol, spin up, spin off and gelation by solvent evaporation. In comparison with the dip-coating method, spin coating technique can produce homogeneous thin coatings, even for non-planar substrates. A model is presented for the description of thin films prepared from solution by spinning; using only the centrifugal force, linear shear forces, and uniform evaporation of the solvent [98].

Flow Coating Process:

In this method the coating liquid is poured over the substrate. The thickness of the coating depends on the angle of inclination of the substrate, the coating liquid viscosity and the solvent evaporation rate. In this technique usually after the coating, spinning the substrate helps to generate a more homogeneous coating, otherwise the thickness of the coating will increase from the top of the substrate to the bottom (**Figure 2-23**).

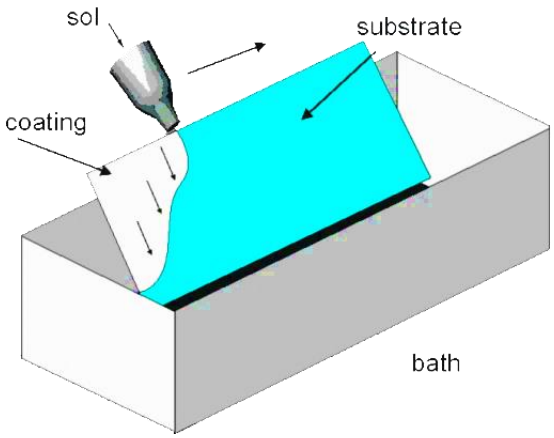

Figure 2-23 Sol- Gel, flow coating technique. Reprinted from Attia et al. [95].

Capillary Coating Technique:

In previous four methods there is some wastage of the coating liquid, e.g. in the spray coating, 100% overspray is done [95], while in dip coating and flow coating only 10% to 20% of the coating liquid is used in the fabrication of the final coating. This waste can be overcome using the capillary technique, **Figure 2-24**. In this method, the substrate is held upside down by the help of a chuck and then a tubular dispersal unit is moved gently under the surface of the substrate and deposits the coating liquid on to the surface. A solution reservoir collects the excess of fluid and pumps it back into the system to ensure that the deposition of the solution is continuous during the process [95].

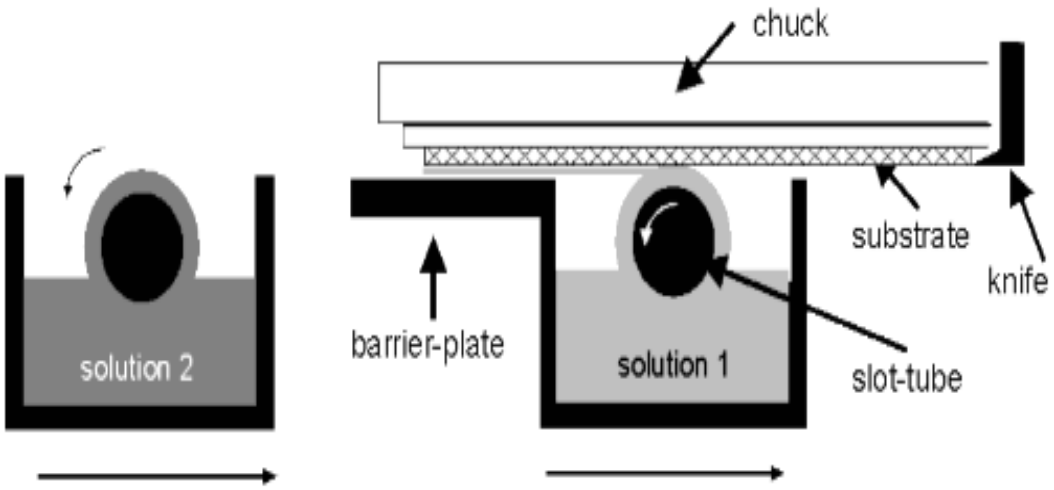

Figure 2-24 Sol–gel capillary coating technique. Reprinted from Attia et al. [95].

2.7.3 Sol–gel applications

Sol–gel coatings are considered as potential candidates to substitute environmentally unfriendly chromate surface treatments for metallic substrates. These coatings are used for different purposes as explained below.

Wear resistant coating: This technique is used to manufacture erosion, corrosion and abrasion resistant coatings to protect substrates such as wind turbine blades, aeronautic structures, submarine body, low-carbon structures and mild steel industrial components [52, 53, 94].

Hydrophobic coating: Coatings with water repellent properties are being increasingly used to serve as protective coatings on windows, car windshields, solar panels, building exteriors, wind turbine blades and other large outdoor surfaces. Sol–gel technology is the preferred route to produce such coatings; for instance Dou et al. [99] developed a single-layer hydrophobic antireflective SiO_2 coating prepared by sol–gel method with 300nm thickness, 97% transmittance and large static water contact angle of 130.6° to improve the optical performance of the optical system efficiency by restrain the absorption of the moisture in the air.

Anti-fog coating: The sol–gel process are also used to produce hydrophilic coatings on glass materials by dispersing the water across the surface and preventing aggregated water molecules to be seen as a droplet and produce fog. There are variety of applications for these glasses e.g. optical lenses, eyeglasses, bathroom mirrors, covers for headlights and vehicle windows.

Self-cleaning coating: This coating has many applications in different industries like textiles, paints, window glasses and cements. This coating saves the costs of cleaning and also increases the duration of woven products. The self-cleaning coating can be hydrophobic or hydrophilic.

Antimicrobial coating: This coating is important to reduce the presence of bacteria on different surfaces that people touch in their daily life, For example, using silver-titanium dioxide nano-coating in subway train interiors reduces the presence of bacteria by up to 60% [100].

Anti-stain coating: This coating has wide applications in different industries such as textile, construction, automotive and electronic because of stain-resistant and hydrophobic characteristics. Anti-stain coatings are hydrophobic coating and they are able to decrease the attachment of the foreign particles to the surface. In this area using organic- inorganic hybrid systems are attractive because they can improve the quality of the coating. For example polyimide/silica hybrid anti- stain coating which synthesized by sol–gel method has characteristics such as hydrophobic, hydrophilicity and optical transparency [100].

Self-healing coating: One of the most important problems with the polymer composites in structural applications is the formation of micro cracks. From engineering point of view, the ability to repair micro cracks can increase the lifetime, safety and durability of a structure. Self-healing materials are able to repair and recover structural ability after damage. Self-healing can be done in a form of capsule or vascular which are different in term of the damage volume that can be healed, repeatability of the healing process and the recovery rate for each approach [100].

2.8 Sol–gel with additive carbon nanotubes and graphene nanoparticles

In sol–gel coatings, the hardness and mechanical resistance can be increased by adding nanoparticle reinforcement to the coating [53]. Many researchers have developed different methods of dissolving the additive nanoparticles in an appropriate solvent and then made hybrid materials, which take advantage of the exceptional material properties of the nanoparticles. As a result, they improved the mechanical, thermal and electrical properties of the coating.

In this section, the review is focused on previous works on using carbon nanoparticles (CNPs), specifically carbon nanotubes (CNTs) and graphene for improving the erosion resistance of coatings.

In the last two decades, many researchers have investigated nanomaterials, with diameters less than 100 nm, as additives in the manufacturing of coatings [21]. There is a variety of nano-

materials interesting properties. Among them, one of the most promising is carbon nanoparticles (CNPs) [101], with their attractive properties, such as nanoscale diameter, high aspect ratio, low-weight, high electrical conductivity, and extraordinary mechanical, optical, and thermal properties. Carbon nanotubes (CNTs) and graphene have attracted much attention in the last decade. Many investigations have shown that a small amount of these nanomaterials resulted in a dramatic improvement in the electro-mechanical properties of their composite materials. However, due to their agglomeration or tangled coils as a result of strong van der Waals interactions, functionalisation of carbon nanoparticles is essential in achieving proper dispersion in polymer matrices and obtaining outstanding electro-mechanical properties.

Figure 2-25 displays the number of published research papers recorded on Scopus containing the word carbon nanotubes, CNT and graphene from 2010 to 2017. It is clear that in recent years, more attention is devoted to graphene and the ratio of Graphene/CNT published works in 2017 is 2.27 while the number of CNT published work is stabilized around 5300 articles.

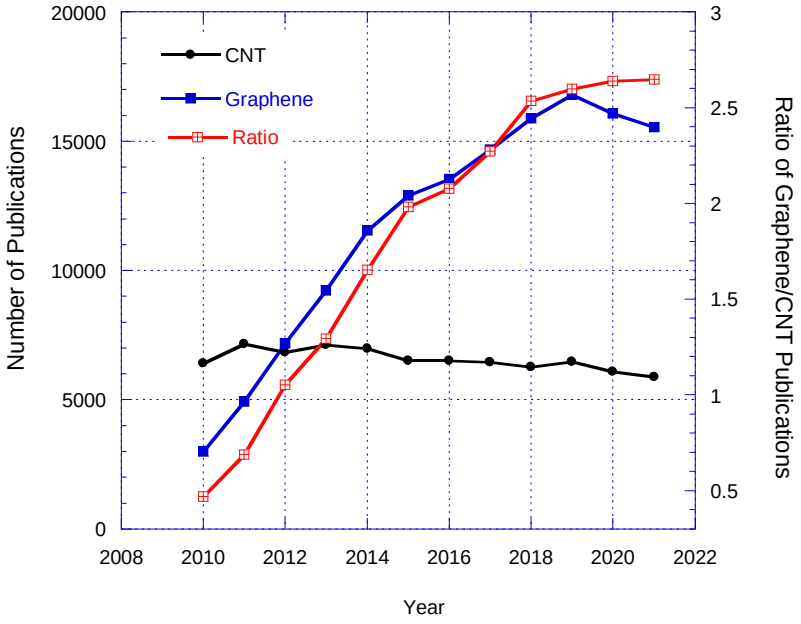

Figure 2-25 Number of publications with titles including “carbon nanotubes” and “graphene”.

2.8.1 Carbon nanotubes (CNTs)

CNTs are allotrope of carbon and have a long one-dimensional cylindrical tube shape of carbon atoms [102]. Carbon nanotubes are classified as single-walled (SWCNTs) originally reported in 1993 [103], and multi-walled (MWCNTs) first discovered in 1991 both by Iijima [104]. SWCNTs are created by rolling a single layer of graphite into a seamless cylinder. SWCNTs have two separate regions, side-wall of the tube and its end cap. The transmission electron microscope (TEM) images of a SWCNT and a MWCNT are shown in **Figure 2-26** [105].

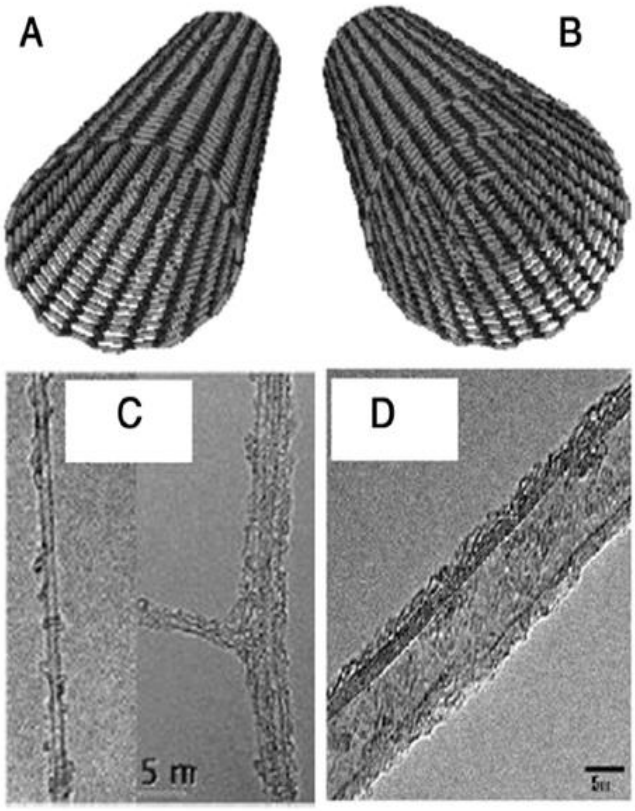

Figure 2-26 Schematic structure of (a) SWCNT and (b) MWCNT. The TEM images of a (c) SWCNT and (d) MWCNT. Reprinted from Eatemadi et al. [105] with the permission of Springer Publishing. TEM: transmission electron microscopy; SWCNT: single-walled carbon nanotube; MWCNT: multi-walled carbon nanotube.

In the SWCNT structure, covalent bonds are acting like a beam element between the carbon atoms, resisting stretching, bending and torsion [106]. The morphology of SWCNT is classified according to the way that the single layer of graphite sheet (hexagonal structures) is wrapped into a cylindrical tube and capped with half shape of fullerene structure [107]. The orientation and magnitude of chiral vector $C = na_1 + ma_2$ in graphene sheet defines the morphology of carbon nanotubes where (n, m) are integers and for (n, 0) makes zig-zag, for (n, n) makes armchair and for (n, m) makes chiral [108]. The diameter of a carbon nano tube can be calculated from below equation:

$$d = \frac{a}{\pi}\sqrt{m^2 + mn + n^2} = 0.783\sqrt{m^2 + mn + n^2} \quad (2.12)$$

where $a = 1.42\sqrt{3}$ Å corresponds to the lattice constant in the graphite sheet (the C-C sp^2 bond length is 1.42 Å). m and n are a pair of indices that describe the chiral vector.

On the other hand, MWCNTs consist of multiple layers of graphene that form concentric tubes. Depending on the number of layers, the inner diameter varies from 0.4 nm up to a few nanometres and the outer diameter varies from 2 nm up to 30nm. Also the distance between

the graphene layers is approximately 0.34 nm to 0.39 nm [105]. MWCNTs can be found in two structural models; Russian doll model which is when a carbon nanotube contains another nanotube inside it with a smaller diameter than the outer one and Parchment model is the one when a single graphene sheet is wrapped around itself manifold like a rolled up scroll of paper [105].

CNTs have high tensile strength and are as strong as a carbon-carbon bond. In **Table 2-1** the material properties of SWCNTs and MWCNTs are compared with graphene and stainless steel [109].

CNTs are used in many different areas including the fabrication of flat panel displays, gas storage devices, toxic gas sensors, lithium batteries, advanced polymer matrices, lightweight composites, conducting paints and electronic nanodevices, etc.

Table 2-1 Comparison of CNTs and graphene material properties with stainless steel.

Material property	**SWCNT**	**MWCNT**	**Graphene**	**Stainless Steel**
Young's modulus (TPa)	1-5	0.2-0.9	125	0.186-0.264
Tensile strength (GPa)	13-53	63-150	150	0.38-1.55
Thermal conductivity (W/m K @RT)	3500	3180	5000	16-24
Electrical conductivity (S/m @RT)	10^7		10^8	1.45×10^6
Thermal stability	up to 2800 °C in vacuum		500 °C	

2.8.2 Graphene

Graphene is a two-dimensional allotrope of carbon which is only one carbon atom thick and arranged in a hexagonal lattice [102], first discovered in 2004 [110]. Graphene is super strong, about 200 times stronger than steel, and has a very high stiffness. It is believed that graphene and CNTs are two of the toughest materials ever tested to date [111]. Graphene is highly transparent, extremely light and an excellent conductor of heat and electricity. Graphene has the highest thermal conductivity of all carbon allotropes and it can carry heat better than any other material [110]. It is possible to stretch the graphene by 25% of its original length without any breakage happening in its structure. Because of the superior mechanical properties of the graphene, it is used to produce hybrid composites which are stronger, tougher, thinner and also lighter than the existing composites. Graphene is also used to increase the electrical conductivity of the composites as well [111].

2.8.3 Functionalization of CNPs

When introducing the individual CNPs into a polymer matrix, it is important to achieve thorough dispersion of the CNPs and strong interfacial interactions between the CNPs and the host polymer matrices. However, due to strong van der Waals forces, it is difficult to disperse CNTs and graphene into the matrix. Therefore, surface functionalisation (chemically adding functional group to the surface of the carbon nano particles) of CNPs is required in the fabrication of nanocomposite coatings.

Usually after purification of CNTs, to increase the solubility of the CNTs further chemical treatments are needed. These chemical treatments are called surface modification of CNTs which increases the solubility of the CNTs in most organic and aqueous solvent [112]. Different methods for functionalising CNPs have been developed **Figure 2-27**. These methods include chemical, mechanical, electrochemical, and irritation reactions. Using these methods, the carbon surface can be activated for subsequent interaction with the host matrix through covalent bonding or non-covalent interactions [113]. Covalent functionalisation is done by directly binding heteroatoms or functional moieties to the carbon lattices by chemical modification. Amino-functionalisation of CNTs enhances the activity of the CNT as both modifier and cross linker to form covalent bonding with host polymer matrix.

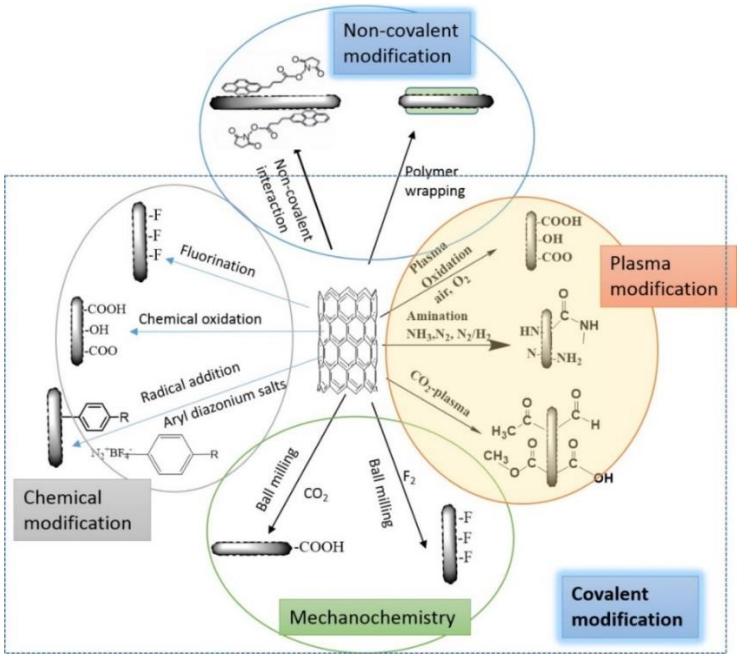

Figure 2-27 Different surface functionalisation methods for CNPs. Reprinted from Alam et al. [113] with the permission of Elsevier Publishing. CNT: carbon nanotube.

The functionalisation efficiency can be characterised and quantified using a range of analytical techniques, including: X–ray photoelectron spectroscopy (XPS), thermo-gravimetric analysis

(TGA), Raman spectroscopy, Fourier transform infrared spectroscopy (FTIR), transmission electron microscopy (TEM), scanning electron microscopy (SEM), atomic force microscopy (AFM), X–ray diffraction (XRD), contact angle measurement and Brunauer- Emmett-Teller (BET) surface area measurements. TGA is commonly used for quantitative determination of grafting molecules bound to the surface of nanomaterials [114]. High residual char content is representative of a high amount of carbon skeleton while the mass losses can be related to the mass of grafted molecules. The extent of functionalisation can be determined using the following equation [115]:

$$R = \frac{x/M_a}{1-x/M_C} \times 100\% \qquad (2.13)$$

where R is the graft ratio, x is the weight loss of the CNP, M_a and M_C are the atomic weight of carbon and molecular weight of the grafting molecule, respectively.

In chemical oxidation functionalization, the distribution and the nature of the functional groups on the surface of CNTs are highly dependent on the type of oxidant used. As can be seen in the **Figure 2-28**, different oxidants affect the distribution of functional groups on the surface of MWCNTs [116]. MWCNTs oxidised with $(NH_4)_2S_2O_8$, H_2O_2 and O_3 yielded higher concentrations of carbonyl and hydroxyl functional groups while HNO_3, H_2SO_4/HNO_3 and $KMnO_4$ formed higher fractional concentration of carboxyl groups [116]. However, such modification is detrimental to the intrinsic optical, electrical and thermal conductivity properties of CNTs.

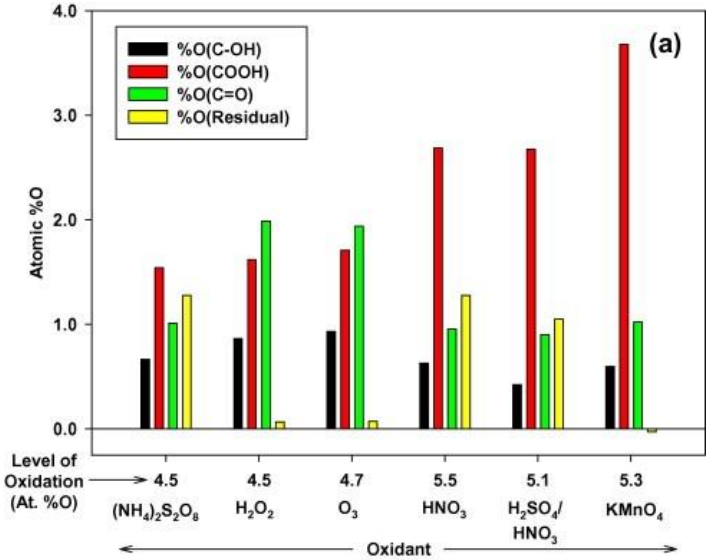

Figure 2-28 Influence of the oxidant on the distribution of oxygen-containing functional groups on the surface of MWCNTs. Reprinted from Wepasnick et al. [116] with the permission of Elsevier Publishing. MWCNT: multi-walled carbon nanotube.

In the **Table 2-2** some of these chemical oxidation techniques and their procedure are summarised.

Table 2-2 Summary of different oxidation procedures to functionalize MWCNTs.

Source	**Oxidant**	**Procedure**
Rosca et al. [112]	HNO_3	0.2g MWCNTs were dispersed for 30min in 100ml HNO_3 and heated under reflux. Then the sample was filtered in a membrane filter and washed to neutral pH and dried at 120℃ for 12h.
Smith et al. [117]	HNO_3	100mg of MWCNTs were sonicated in 200ml of 70% HNO_3 for 1h and then the mixture was heated under reflux for 1.5h at 140℃.
Domun et al. [118]	HNO_3	0.1g of MWCNTs were dispersed in 100ml of HNO_3 (70%) and heated under reflux at 135℃ for 24h. Then the mixture was filtered and dried in vacuum at 40℃.
Hiura et al. [119]	$KMnO_4$	100mg of MWCNTs were sonicated in 200ml of 0.5M $KMnO_4$ for 30min. The MWCNT/ $KMnO_4$ mixture was then heated under reflux for 5h at 150℃. After cooling down the reaction to the room temperature, 10ml of concentrated HCl was added to dissolve the MnO_2 by product.
Blanchard et al. [120]	H_2SO_4/HNO_3 (3:1)	H_2SO_4 and HNO_3 were combined in 3:1 ratio to create the solution with a final volume of 8ml. 100mg MWCNTs were added to this solution and the mixture was heated to 70℃ for 8h without stirring.
Arabi [121]	H_2SO_4/HNO_3 (4:1)	5g of MWCNT were dispersed in 400ml sulfuric acid and 100ml nitric acid in a glass vial and placed in an ultrasonic bath for 3h. Ice was then added to the mixture stored for 24h at ambient

		temperature. Afterward the mixture was neutralised and dried at 60℃.
Kathi et al. [72]	H_2SO_4/HNO_3 (3:2)	3g of MWCNTs were dispersed in 300mL of concentrated H_2SO_4/HNO_3 solution at 50 °C and stirred for 20h. The solution was filtered and remaining solid particles washed with water and acetone. Then f-MWCNTs were dried under vacuum at 100 °C for 24h. After that about 0.050 g of f-MWCNTs was dispersed in 50mL of ethanol via ultrasonication for 30min.
Peng et al. [122]	H_2O_2	100mg MWCNTs were added to 15ml of 30% H_2O_2 and the mixture heated to 70℃ for 4 days with continuous stirring. Every 24h, 1-5 ml of 30% H_2O_2 was added to the solution for the volume lost due to the evaporation.
Kirk JZ et al. [123]	$(NH_4)_2S_2O_8$	50mg MWCNTs were added to 50ml of piranha solution (4:1 96% H_2SO_4: 30% H_2O_2) and stirred for 4h at 80℃.

Amine-functionalised CNTs may be covalently bonded to polymer matrices, such as polyepoxides, polyimides, and polyamide [124]. Amine-functionalised graphene CNTs have been used as reinforcing agents, cross linkers and in catalysis, and play multiple functions in epoxy composites [125].

Functional groups can be created on the carbon surface as a consequence of mechanical grinding and shearing. Ball-milling exfoliates graphite into multi-layer carbon nanoplatelets [126] and breaks MWCNT agglomerates under certain treatment conditions (e.g. duration, temperature, and organic modifiers), generating functional groups on the carbon surface. Similar levels of dispersion of MWCNTs were found for those treated by ball-milling for 20 min with those treated with concentrated acids for 120min, but the MWCNTs were highly shortened after ball-milling [127].

The edges of graphene nanoplatelets (GNPs) can be functionalised by ball-milling of graphite in the presence of hydrogen, carbon dioxide, sulfur trioxide and/or carbon dioxide/sulfur

trioxide. The amount of functional groups formed was around 65–87 wt%, determined from TGA at 800°C in nitrogen. From Raman spectroscopy, the intensity ratios I_D/I_G of the D–band (1350 cm^{-1}) to G–band (1584 cm^{-1}) were in the range 0.79–1.50 [128], indicating a significant size reduction in platelet size due to mechanochemical cracking and edge distortion.

In addition to the wet-chemistry and mechanochemistry methods, cold plasma, especially low-pressure plasma treatments have become one of the key technologies for surface modification of materials. The highly energised gas species of the plasma can penetrate and break covalent bonds to a depth of several nanometres. The activated surface can then readily react with the excited gas species to form functional groups. The level of surface functionalisation is determined by the gas type and treatment parameters such as pressure, power input, flow rate and time [129].

Different plasmas can introduce different functional groups onto the surface, as shown in **Figure 2-29** [113]. For surface modification, a variety of inert gases such as oxygen-containing gases including O_2, CO_2 and H_2O; nitrogen-containing gases including NH_3 and N_2, as well as other gases such as H_2, Ar, P and He have been investigated. Fluoro– or hydrocarbon containing gases such as BF_3, CF_4, styrene, allylamine, acrylic acid or maleic anhydride can induce plasma polymerisation reactions to form pinhole free polymer nanocoatings on the surface. Ammonia, sometimes in a mixture with other gases (N_2, Ar, O_2, CF_4), is often used as precursor to introduce amine functionality to CNPs to enhance hydrophilicity and biocompatibility [129]. Oxygen plasma treatment can generate oxygen-containing functional groups such as –COOH, C=O, -OH, C–O–C, and $–CO_3$ on the surface of carbon, providing a reaction platform for further interaction with polymers. Ammonia, N_2, and N_2/H_2 plasmas introduce primary, secondary and tertiary amines, as well as amides [130].

Figure 2-29 Possible functional groups formed via plasma modification of CNPs. Reprinted from Alam et al. [113] with the permission of Elsevier Publishing. CNP: carbon nanoparticle.

Several chemical procedures have been developed to obtain dispersible functionalised graphene. One of the most effective is the covalent attachment of functionalities to pristine graphene) [22]. The main advantage of this method is increasing the dispersibility of graphene sheet in organic solvents which is an important move toward formation of nanocomposite materials with graphene. For instance by functionalization, allows the addition of chromophores, which can help improve conductivity [131]. Covalent bonds can be formed by reaction between free radicals or dienophiles and C=C bond of pristine graphene or between organic functional groups and the oxygen groups of graphene. **Figure 2-30** shows different graphene covalent functionalisation methods.

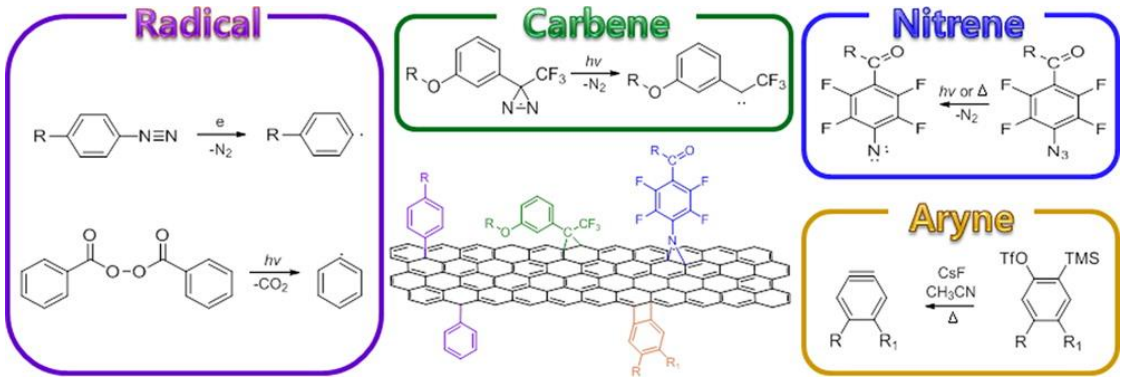

Figure 2-30 Graphene covalent functionalisation methods. Reprinted from Park et al. [132] with the permission of ACS Publishing. ACS: American Chemical Society.

For example, nitro-phenyls functionalisation of the graphene sheet has been achieved via radical chemistry, **Figure 2-31**.

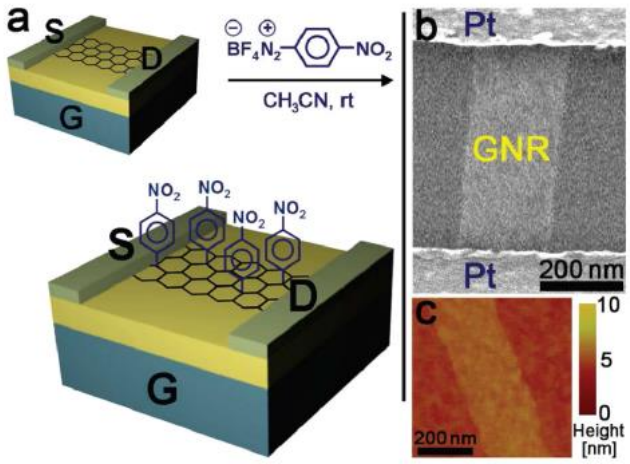

Figure 2-31 Chemical doping of graphene with 4-nitrophenyl groups: (a) schematic representation; (b) SEM image of a graphene nanoplatelet between Pt electrodes; (c) AFM image of a fragment of a monolayer graphene. Reprinted from Sinitskii et al. [133] with the permission of ACS Publishing. SEM: scanning electron microscopy; ACS: American Chemical Society; AFM: atomic force microscopy.

Another alternative is using carbene precursors to functionalize the graphene sheet [134], Chloroform and diazirine as carbine precursors have been used to functionalise graphene oxide.

Nitrenes have also been used in the functionalization of graphene sheet. Graphene sheets were reacted with Boc-protected azidophenylalanine in ODCB. The product was determined to have 1 phenylalanine substituent per 13 carbons (**Figure 2-32**).

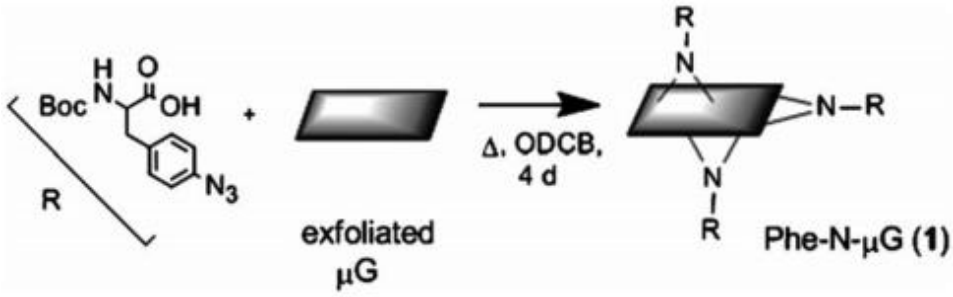

Figure 2-32 Nitrene addition to graphene sheets using Boc-protected azidophenylalanine. Reprinted from Strom et al. [135] with the permission of RSC Publishing. RSC: Royal Society of chemistry.

In this method, the degree of functionalization is dependent on the amount of nitrene added to the reaction mixture (**Figure 2-33**).

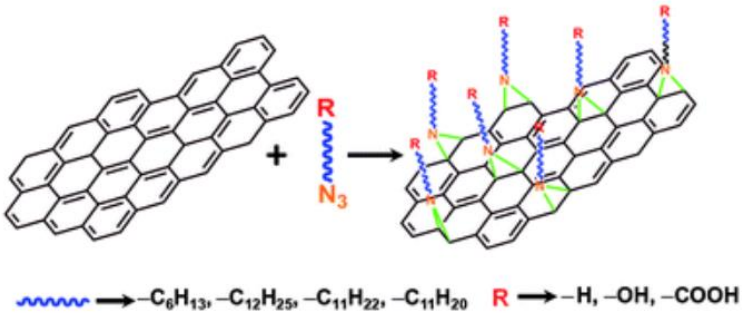

Figure 2-33 The reaction of alkyl nitrenes with graphene sheets. Reprinted from Vadukumpully et al. [136] with the permission of RSC Publishing. RSC: Royal Society of chemistry.

In general, covalent modification breaks the extended conjugation of π-electrons in graphene, resulting in band gap opening and change in conductivity, Also added functional groups to the surface of the graphene sheet will control the chemical properties of the graphene and allows further conjugation of additional molecules and materials to the graphene; beside that covalent modification can improve their solubility and ability to be processed [132].

Chapter 3 Materials and Methods

3.1 Introduction

In this chapter in the first part material preparation method is explained. After that material characterization using FTIR, TGA, DMA, water contact angle and scanning electron microscopy was performed, and the results of pure polyurethane were compared with those of developed coating materials (PU+GNP) and (PU+GNP+SG).

In second part mechanical tests tensile, compression and tearing tests were performed to measure the mechanical properties of the pure and developed coating materials. In this part initially tensile test was done on pure PU at different temperature and strain rate. After that optimum mixing parameters of carbon nano particles in PU was established. This has been done by adding different carbon nanoparticles loading to PU and performing tensile tests to find the type and amount of the CNP which gave the best mechanical properties for developed coating materials. Afterward, compression and tearing tests were done on pure PU and developed coating materials and the results are compared.

In the last part of this chapter water absorption studies was done on pure PU and developed PU nanocomposites by submerging the specimens in water over six months period. Tensile tests were performed on dogbone specimens at various time intervals to find the effect of water absorption on mechanical properties and the amount of water absorption was measured on cubic specimens submerged in water together with dogbone specimens in water tank.

3.2 Materials

Polyurethane with its nanomodified nanocomposites are used in this work to make the leading edge (LE) protection coating. The best carbon nanoparticle for this study is selected based on the tensile properties of the PU modified with, GNP-COOH, GNP-NH_3, MWCNTs, hybrid of GNP-COOH+MWCNTs and hybrid of GNP-NH_3+MWCNTs was investigated and based on the results GNP-COOH was selected for further work.

The three coating materials are pure polyurethane (PU), graphene modified polyurethane (PU+GNP) and Graphene + Sol gel modified polyurethane (PU+GNP+SG).

The two component polyurethanes system BAYTEC® 9005 60A MF Polyol with viscosity of 800-1600 mPa.s and specific gravity of 1.01-1.04 and the DESMODUR® B9 M10 polyisocyanates crosslinkers with viscosity of 120-200 mPa.s and specific gravity of 1.21-1.23

were supplied by Covestro. The mixing ratio by weight of polyol to hardener is 100:37 and it cures at room temperature.

The as received functional graphene nanoplatelets material HDPlas™ GNP–COOH having carboxyl groups at their surfaces by a "split plasma" treatment in oxygen by the manufacturer. The plasma functionalisation is a low temperature, low energy, dry process, with no effluent disposal, and is benign to the structure of the raw material. The functional groups were only attached to the edges, dislocation sites and defects. The average lateral dimensions is between 0.3-5 μm and typical f-GNP thickness of <0.5 nm, bulk density of 215 kg/m^3 and specific surface area of ~25 m^2/g. The individual graphene sheets are approximately 0.335 nm thick with an aspect ratio of ~85 [137].

Hydrophobic silica-based sol-gel P029™ was supplied by Sol-Gel Materials & Applications (SGAM), Gillingham, UK and contains 15% Si.

3.3 Material preparation

3.3.1 Preparation of PU material

BAYTEC® 9005 60A MF polyol (100 g) was mixed with DESMODUR® B9 M10 polyisocyanates (37 g) at room temperature (25°C) for 3 minutes using a homogeniser at 8000 rpm. The mixture was then placed into a degassing chamber for 4 minutes, poured into a designed mould for specific test and left for 1 hours to be cured at room temperature.

3.3.2 Preparation of PU + GNP material

Polyurethane/graphene composites can be prepared by blending or in-situ polymerisation approaches. In this work the in-situ polymerization of PU/f-GNPs was carried out by directly mixing GNP–COOH (wt%) with polyol (100 g) at room temperature (25°C) and mixed using a homogeniser at 8000 rpm for 18 minutes, subsequently DESMODUR® B9 M10 polyisocyanates (37 g) was added to the mixture and stirred for 1 minute and poured into the mould. The functionalised graphenes act as chemical crosslinkers in PUs. The mixture was ready for moulding various test coupons.

3.3.3 Preparation of PU + GNP + SG material

The in-situ polymerization of PU/f-GNPs was carried out by directly mixing hydrophobic silica-based solution (wt%) with the DESMODUR® B9 M10 polyisocyanates (44 g) and then the mixture was added to the mixture of PU + f-GNP (same preparation method as above),

stirred for 1 minute using a homogeniser at 8000 rpm before being ready for moulding various test coupons.

3.4 Material characterization

3.4.1 FTIR test

Fourier transform infrared (FTIR) spectroscopy is a technique which is used to obtain infrared spectrum of absorption, emission and photoconductivity of solid, liquid and gas [138]. This test measures the energy required to initiate molecular vibration in a sample [139, 140]. As covalent bonds are not static, when they absorb energy, they start vibrating in either stretching the bond or bending the bond, which means any compound possessing covalent bonds will absorb certain frequencies of electromagnetic radiation from the infrared region of the electromagnetic spectrum. As different molecules absorb different sets of energies and have different IR spectra, then FTIR is an important tool for studying the composition of polyurethane in molecular bonds. This method has advantages as fast and easy analytical method to provide the results in seconds. To perform this test, small amount of material is required and generally simple or no sample preparation is required for this test. FTIR can be applied to different type of materials such as, liquid, semi liquid, solids, powder and gases [139, 140]. In this part of study, FTIR was used to analyse the presence of key functional group of developed erosion resistant coatings. In the polyurethane N=H and the C=O are the significant bonds which represent the urethane and carbonyl linkage; amount of the free N=H will give us the amount of the cross-linking present and the C=O bond gives details about the portion of the C=O in the urethane linkage [139].

Perkin Elmer Spectrum one – FTIR spectrometer with attenuated total reflectance (ATR) attachment using spectrum version 5.0.1 control and processing software was used to scan the samples in the range of 4000 – 500 cm^{-1} with a resolution of 4 cm^{-1}. Using ATR gave the opportunity to use the samples for FTIR test without preparation. The samples were cut to the dimensions 1mm × 1mm × 1mm and they were put on the crystal. Then the arm was placed over the solid sample to compress it to the crystal and the test was started. The crystal was cleaned after each test to optimise the reflection of the light.

3.4.2 TGA tests

Thermogravimetric Analysis (TGA) is a test which can measure the amount of weight loss in sample as a function of temperature [141]. By performing this test, behaviour such as composition, decomposition reactions, decomposition temperatures, purity and absorbed

moisture content can be measured. This analysis can be done under a changing gas flow or a stable condition. Although TGA is a good technique to understand the temperature range of the material in which they are stable and the range in which decomposition occurs, but some parameters such as sample size, heat transfer rate can add some limitation to it. For instance, for large samples (>50 mg), heating rates within the sample are not rapid enough and poor heat transfer create radial gradient. In this test, linear heating rate was used to analyse the amount of the sample weight loss, and to have a better resolution of the transitions, it was decided to use the temperature rate of 10℃ per minute [142]. TGA tests were performed to analyse the effect of silica-based sol-gel on the weight loss behaviour of the PU up to 900℃ temperature range.

For this experiment METTLER TOLEDO was used with up to 50 million resolution points continuously. This machine is able to determine the weight change of 0.1μg to 5g samples. This machine is equipped with STAR^e which is one of the most complete and comprehensive thermal analysis software for TGA analysis. Temperature can be increased at heating rate of 10° per min up to 900℃ and weight-loss versus temperature curves is obtained. For these experiment small pieces of each developed coating materials were cut and weighted and then they were placed in the sample pans of the equipment.

3.4.3 DMA tests

Dynamic Mechanical Analysis (DMA) was used to measure the mechanical properties of viscoelastic materials as a function of temperature or frequency when the materials are deformed under the action of a periodic force or displacement. This test can provide viscoelastic properties such as tan δ, storage modulus E' and loss modulus E'' It is known that density of cross link in polyurethane structure has significant effect on the damping properties of the material which can be investigate by measuring tan δ value [143, 144]. tan δ is a measure of how well a material dissipates energy and it is calculated using below equation:

$$tan\ \delta = \frac{E''}{E'} \tag{3.1}$$

DMA test was performed for PU, PU+GNP and PU+GNP+SG. Specimens were manufactured with the dimension of 30mm × 3mm × 3mm. **Figure 3-1** shows the DMA 1 STAR System (Mettler Toledo). To analyse the behaviour of the damping factor against the temperature

change, the samples were cooled down below its glass transition temperature and after that the temperature ramping started. To reach to below the glass transition temperature of the PU (around -20℃), liquid nitrogen was used to cool down the samples up to -70℃ and then it was gradually increased to maximum temperature of 60℃.

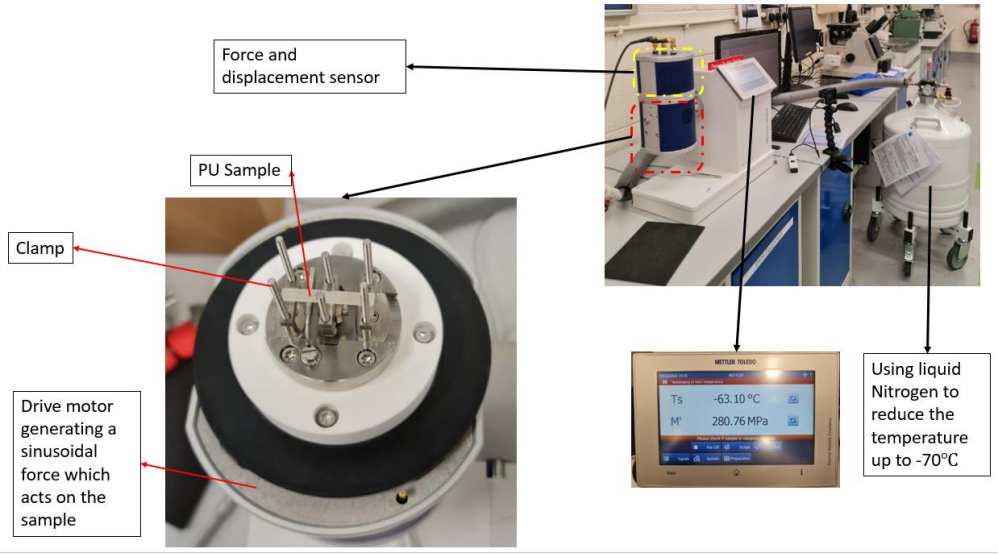

Figure 3-1 DMA 1 STAR System (Mettler Toledo) Equipment.

3.4.4 Contact angle measurement

Liquid repellency is a very important property of coatings; when a drop of water is placed on a material surface, it will spread on the surface, this phenomenon depends on the intermolecular interactions between the solid and the liquid. By measuring water contact angle, it is possible to have a correct understanding of the wettability of the material. Coating can be divided into two groups: a) hydrophobic which shows the water contact angles greater than 90° and b) hydrophilic which shows the water contact angles less than 90° (see **Figure 3-2**) [145]. Complete wetting of the material surface is achieved when the contact angle is zero. Superhydrophobic surfaces are highly hydrophobic, i.e., extremely difficult to wet and the contact angles of a water droplet on a superhydrophobic material exceed 150°. These surfaces have a low surface energy [146]. Materials with low surface energy such as polymers are harder to wet.

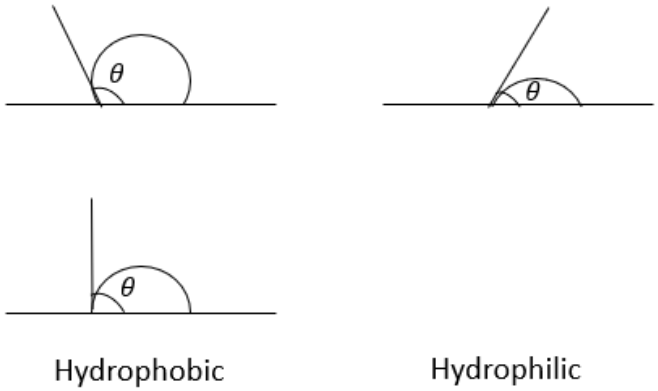

Figure 3-2 Water contact angle difference in hydrophobic and hydrophilic materials [145].

Contact angles (CA) are commonly used to describe surface wettability [147]. There are two ways of measuring the contact angles:

- Statically
- Dynamically

For measuring the water contact angle, water is dropped on the sample surface, then by using a camera, pictures of the droplet are obtained. The image provides the height (h) and width (d) of the water droplet on the surface and then contact angle θ can be calculated (see **Figure 3-3**) [148].

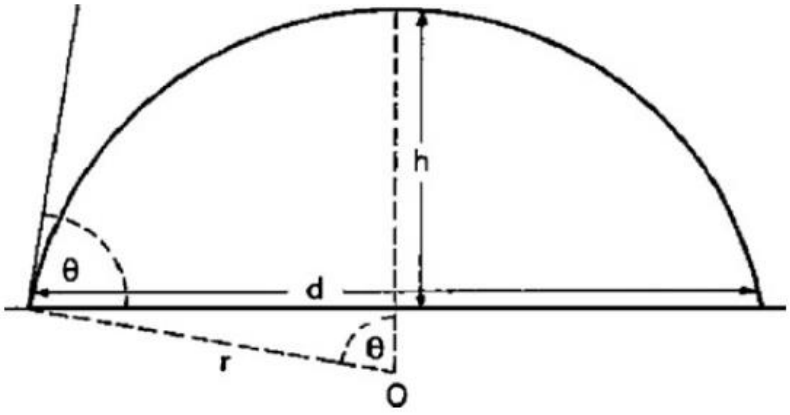

Figure 3-3 Water droplet dimensions for contact angle calculation [148].

Static contact angle: In this method the droplet is produced before the measurement and has a constant volume during the measurement. In this method the contact angle will not remain constant; interactions at the boundary surface can cause the contact angle to change considerably with time (**Figure 3-4**).

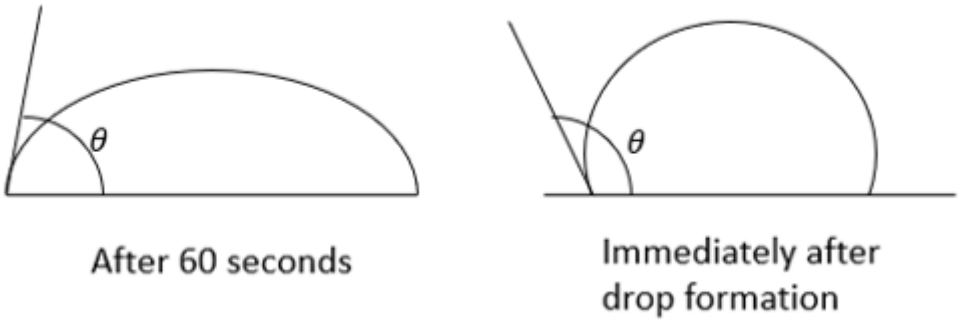

Figure 3-4 Variation of the contact angle with time.

Interaction at the boundary surface can be:

- Evaporation of the drop liquid.
- Absorption of the water by the testing material
- Migration of surfactants from the solid surface to the liquid surface.
- Chemical reactions between the solid and liquid.
- The solid being dissolved or swollen by the liquid.

One of the advantages of this method is that the needle does not remain in the drop during the measurement, preventing the drop from being distorted. Certain materials which do not show a fully rigid surface such as rubber are better being tested with static measurements because of a frequently poor reproducibility of the dynamic contact angle.

Dynamic contact angle: Dynamic contact angle is measured while the drop is being enlarged or reduced. In this method the boundary surface is being constantly newly formed during the measurement. There are two types of dynamic contact angle: (i) advancing angles (contact angles measured on increasing drops) and (ii) receding angles (contact angle measured on reducing drops). In this method a boundary is not formed instantaneously but requires some time before a dynamic equilibrium is established. Hence, the selected flow rate should not be too high, otherwise the contact angle will be measured at a boundary which has not been completely formed. Also flow rate should not be too slow as the time effects mentioned before will then play a role.

For this experiment cubic specimen with the dimension of 40×40×15mm was used. Static water contact angle of the three coatings, i.e. PU, PU+GNP and PU+GNP+SG, are measured. Three specimens were made from each material and five repeat tests were conducted and then the

average water contact angle was calculated. The duration of CA measurement for each droplet was 6000 ms.

Experimental set up

DSA30 water contact angle measurement device was used to measure the contact angle. The principle of this device is in such a way that the droplet is placed on a sample located on a table, then the drop is illuminated from one side and a camera at the opposite side records an image of the drop (**Figure 3-5**). The static deionised (DI) water contact angles (CA) for PU, PU+GNP and PU+GNP+SG coatings were measured for 6000 ms after application of the water droplet (Sessile drop method) with a Krüss GmbH' Drop Shape Analyzer (DSA) machine using 5 µL DI water droplets ejected from a micro-syringe in order to study the changes in the surface water amphiphobicity.

The surface free energy ($-\Delta G_{SL}$) was calculated using the Young-Dupre equation [149]:

$$-\Delta G_{SL} = (1 + \cos\theta) \cdot \gamma_L^T \qquad (3.2)$$

where γ_L^T is the water surface tension (72.8 $mJ{\cdot}m^{-2}$), and θ is the measured DI water contact angle.

Figure 3-5 DSA30 contact angle measurement device.

3.4.5 Scanning electron microscopy (SEM)

The PU and the modified PU nanocomposites surface morphology was examined using Field Emission Scanning Electron Microscopy (FESEM), with Quanta- FEG-250 model. All samples were cleaned with pressurised air followed by ethanol washing to remove any adsorbed particles. The samples were coated with 10-15 nm of platinum to inhibit charging and improve the secondary electron signal, allowing for better imaging of the samples. All FESEM samples were mounted on SEM stubs using carbon tape with adhesive sides and the images were taken at 75 to 5000 magnification at 5 kV. Energy-dispersive X-ray spectrometer (EDX) with acceleration voltage (10-15 kV) was used to study the elemental composition of neat PU and their nanocomposites.

3.5 Mechanical testing

In this section mechanical properties of the PU, PU+GNP and PU+GNP+SG was analysed by performing tensile test to calculate the Young's modulus, elongation at break, ultimate tensile strength and modulus of toughness; also to investigate the compressive behaviour of each material a compression test was performed at different temperature and different strain rate and residual strain was calculated; beside that hardness tests was done to analyse the hardness properties of each material and at the end tearing test was done to calculate the tearing strength and tearing energy.

3.5.1 Tensile tests

In this part of the study first the tensile properties of the neat polyurethane (BAYTEC+DESMODUR) were investigated. The objectives of this part were to understand the behaviour of the neat PU at room and at elevated temperature. After that multi-walled carbon nanotubes (MWCNTs) were used to optimise the mixing procedure of carbon nanoparticle in the PU; for this reason 0.5wt% of MWCNTs was dispersed in PU at three different mixing speeds and for three different mixing durations. After establishing the optimum mixing procedure, different weigh percentage of MWCNTs were dispersed in the PU and the tensile test was performed to analyse the mechanical properties of each sample to realise the best amount of weight percentage that should be added to the PU to enhance the mechanical properties of the pure PU. In the next part two types of functionalised GNP were added to the PU to see the effect of adding graphene on the mechanical properties of the pure PU. In the following different weight percentage of the GNP-COOH were added to the PU and then the tensile tests were performed to compare the mechanical properties of samples with

each other. At the end, the hydrophobic silica base Sol-Gel was added to the pure PU and GNP modified PU and the results of the tensile test were analysed.

Manufacturing of Tensile test specimens

Neat PU specimens were manufactured according to the method mentioned in section 3.2.1 (see **Figure 3-6**).

Figure 3-6 a) Mixture of the PU and isocyanate after stirring, b) in the vacuum degassing chamber, c) after degassing process.

A mould for casting uniaxial tensile tests coupon was manufactured from Aluminium. The dogbone specimen dimensions are according to BS EN ISO 527-2:2012 (Type 1BA geometry) (**Figure 3-7**). After degassing process, the mixture was gently poured into the mould and left for an hour to be cured at room temperature (**Figure 3-8**); Tests were carried out 24 hours after casting the specimens.

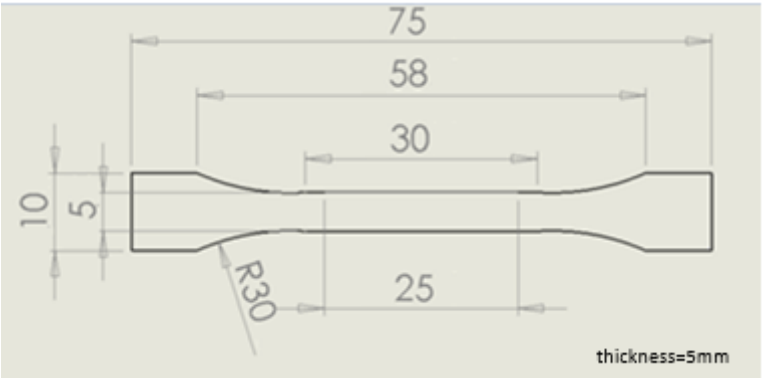

Figure 3-7 Dimension of dogbone specimen based on BS EN ISO 527-2:2012 (Type 1BA geometry).

Figure 3-8 Casting of tensile test pure polyurethane specimens.

Manufacturing carbon nanoparticles modified PU specimens

For dispersing of carbon nanoparticles (CNPs) in the neat PU, specified CNPs loading (wt %) was mixed with PU using a high speed homogeniser as mentioned before (**Figure 3-9**). Speed of homogeniser and mixing duration are the parameters which were studied to optimise the mixing procedure of CNPs in the PU matrices.

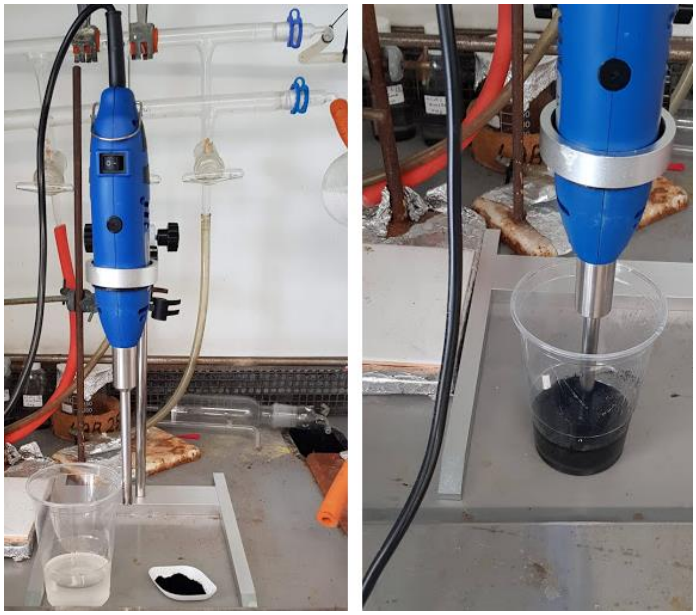

Figure 3-9 Mixing the as received MWCNTs with the neat PU using a homogeniser.

Samples of cured specimens in the mould are shown in **Figure 3-10**.

Figure 3-10 Curing dogbone specimens of PU+0.5 wt% MWCNTs nanocomposite at room temperature

Manufacturing silica-based sol-gel PU+GNP+SG specimens

Procedure of manufacturing these specimens was explained in section 3.2.3.

3.5.2 Compression tests

The compression tests were carried out using Zwick/Roell universal testing machine fitted with a 25 kN load cell. An extensometer was used to record the compression of the specimens. The extensometer was connected to the machine with a specially designed fixture. In the compression tests, the crosshead speed was set at 2.1, 10.5 and 21 mm/min (equivalent to strain rate of 0.01, 0.05 and 0.1 s^{-1}) and at each strain rate, the tests were performed at three different temperatures 25°C (RT), 50°C and 70°C using an in-situ heating chamber during compression. For each case three specimens were tested.

Manufacturing of Compression test specimens

For this test, cylindrical samples with the diameter of 12mm and thickness of 3mm were manufactured according to the work by Qi and Boyce [150]. To eliminate potential buckling, the sample height to diameter ratio was set to be less than 1. In addition, to reduce the contribution of friction due to the interaction with the

compression platens, Teflon sheets were placed between the sample and the platens and the initial height/diameter ratio were set to be greater than 0.5. First a sheet of material of about 3mm in thickness was manufactured by pouring the PU or modified PU into a machined aluminium mould; after curing and removing the PU sheet from the mould, a die cutter with

hydraulic press machine was used to cut the specimens with the required shape and dimensions, (**Figure 3-11, Figure 3-12 and Figure 3-13**).

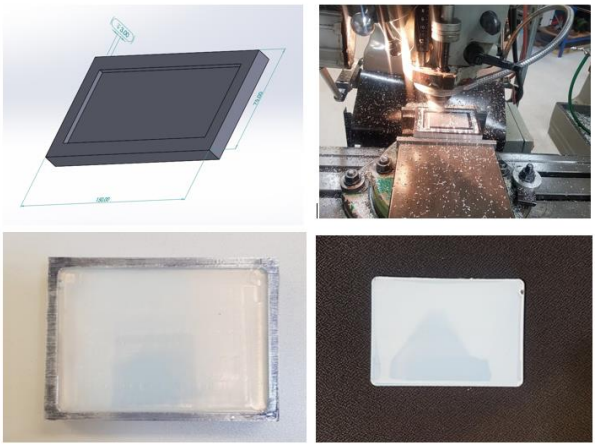

Figure 3-11 Manufacturing the Aluminium mould.

Figure 3-12 Using die cutter to cut the PU sheet.

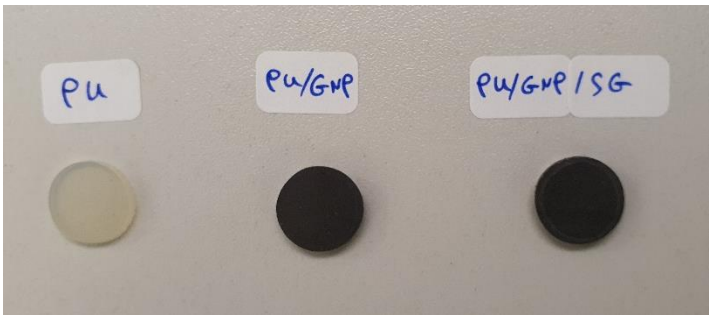

Figure 3-13 Compression test samples.

3.5.3 Hardness tests

It is known that increase in hardness will results in better resistance to penetration and therefore increase the erosion resistance and reduce the erosion rate [151]. For that reason, it is important to analyse the hardness properties of the neat PU and modified PU. In this pat Hardness test were carried out using a Durometer 0-100 HD (**Figure 3-14**). Samples were manufactured in the dimension of 5×5×5mm. For each samples three different points were tested and then the average was presented as the hardness of the sample. Hardness is a dimensionless quantity can

be varied from 0 (soft) to (100) hard; if the indenter completely penetrates the samples a reading of 0 is obtained and if no penetration occurs, a reading of 100 results.

Figure 3-14 Durometer 0-100 HD.

3.5.4 Tearing tests

Angle tear strength test specimens with a nick were made according to the ISO 34-1:2015 tearing test standard [152]. The tests were performed at standard laboratory temperature (23℃ ± 2℃) to measure the force required to propagate a pre-nick cracked specimen. Tearing tests were performed with a Zwick/Roell universal testing machine fitted with a 50kN load cell. The tests were operated without interruption at a constant rate of travel until the test piece breaks. The crosshead speed was kept at 500 mm/min ± 50 mm/min and the applied forces and crosshead movement were recorded during the test. For each type of material, three specimens were tested.

The measured tear strength indicates the resistance to the propagation of a defect, such as a nick in the specimen. In the angle tear test, the force required to tear a specified test piece along the nick already made in the test piece is measured. For calculating the tearing strength (T_s), the maximum force required to extend the nick cut during tearing is divided by the thickness of the specimen (d).

$$T_s = \frac{F_{max}}{d} \text{ (kN/m)} \tag{3.3}$$

Manufacturing of tearing test specimens

The tearing test specimens were made by the moulding method. A suitable mould was made by the CNC machining of resin tooling boards (**Figure 3-15**). After removing the specimens from the mould, a sharp razor blade was used to cut a sharp nick at the point of stress concentration in the tear test specimens according to the ISO 34-1:2015 standard. The razor blade (cutting tool) was clamped in a plane perpendicular to the surface of the specimen and no lateral movement was permitted during introduction of the nick into the specimens [152]. The blade was wetted with soap solution prior to nicking. The depth of the nick was 1mm ± 0.2mm at the apex of the internal angle of the test specimen. The tearing force and crosshead displacement were recorded during crack propagation. Three specimens were tested for each material.

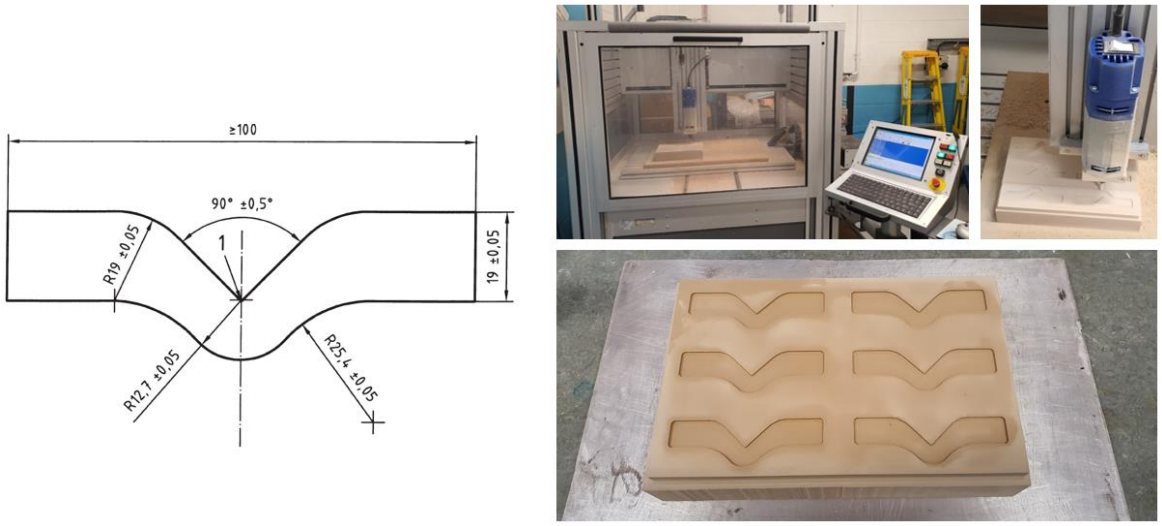

Figure 3-15 Process of mould manufacturing for preparation of tearing test specimens by CNC machining of resin tooling board.

3.6 Environmental effect

3.6.1 Water absorption tests

The water absorption of the three coating materials (PU, PU+GNP and PU+GNP+SG) was experimentally studied and the effects of the water absorption on the tensile properties of the materials were investigated. It was desired to understand the extent of changes in mechanical properties of the PU and modified PU coatings by water absorption and how these changes affect the functionality of the coatings.

Manufacturing water absorption test specimens

Two different sets of specimens were manufactured. The first set was round samples for measuring the amount of water absorption by each material over a 6 months period in immersion in water. The second set was dogbone specimens. These were also immersed in water and tensile tests were carried out on these specimens after certain period of water immersion and then tensile mechanical properties were obtained.

Test specimens were manufactured according to the D570-98 standard in the form of a disk 50.8mm in diameter and 3.2mm in thickness. First, a sheet of material was manufactured in the thickness of 3.2mm and then a die cutter was to cut the round disk specimens with the diameter of 50.8mm (**Figure 3-16**). The samples manufactured for each type of materials are shown in **Figure 3-17**. The specification and numbering code of the samples for water absorption tests are summarised in **Table 3-1**.

Figure 3-16 Manufacturing specimens for the water absorption **tests**.

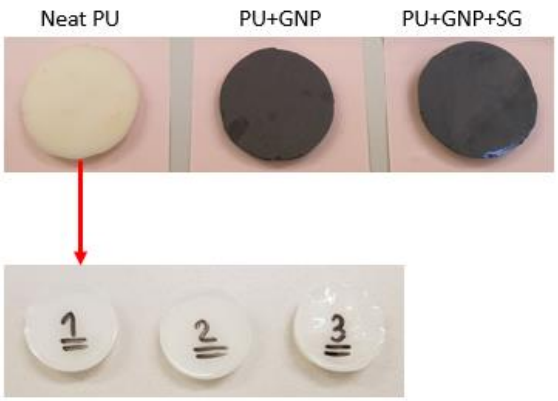

Figure 3-17 Samples for water absorption experiment.

Table 3-1 Samples specification and numbering code for water absorption.

Sample Specification	**Sample code**
Neat Polyurethane	$PU1_{wat}$
Neat Polyurethane	$PU2_{wat}$
Neat Polyurethane	$PU3_{wat}$
PU+0.5 wt% GNP	$PU+GNP1_{wat}$
PU+0.5 wt% GNP	$PU+GNP2_{wat}$
PU+0.5 wt% GNP	$PU+GNP3_{wat}$
PU+0.5 wt%GNP+1wt%SG	$PU+GNP+SG1_{wat}$
PU+0.5 wt%GNP+1wt%SG	$PU+GNP+SG2_{wat}$
PU+0.5 wt%GNP+1wt%SG	$PU+GNP+SG3_{wat}$

The dogbone tensile test samples were manufactured by casting method. As can be seen in the **Figure 3-18**, the coating materials were poured into the mould and left at room temperature (25°C) for 1 hour to cure. Coding of the samples can be seen in the Table 3-2.

Figure 3-18 Manufacturing the tensile test samples.

Table 3-2 Samples specification and numbering code for water absorption.

Sample Specification	Sample Code
Neat Polyurethane	$PU1_{wat\text{-}ten}$
Neat Polyurethane	$PU2_{wat\text{-}ten}$
PU+0.5 wt% GNP	$PU+GNP1_{wat\text{-}ten}$
PU+0.5 wt% GNP	$PU+GNP2_{wat\text{-}ten}$
PU+0.5 wt%GNP+1wt%SG	$PU+GNP+SG1_{wat\text{-}ten}$
PU+0.5 wt%GNP+1wt%SG	$PU+GNP+SG2_{wat\text{-}ten}$

Experimental set up

All samples were immersed completely in a water tank and kept in the similar environmental condition for six months (**Figure 3-19**). During this period according to the specific time frame, samples were taken out from the water tank for testing. Round samples weighted and returned back to the water tank immediately while dogbone specimens weighted and tensile test were carried out immediately to analyse the effects of water absorption on tensile properties of the coating material after specified exposure to water immersion.

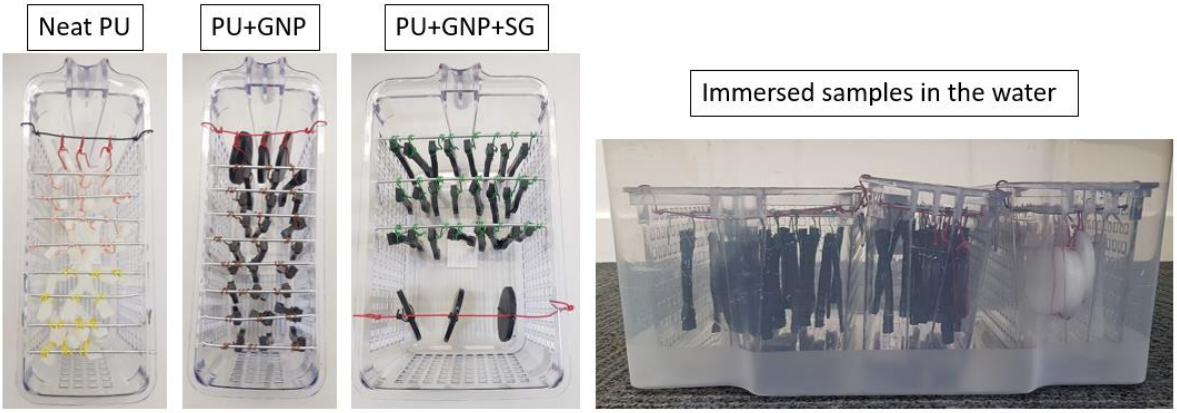

Figure 3-19 Immersing the samples completely into a water tank.

The specimens were weighted after 24 hrs, 48 hrs, 1 week, 2 weeks, 1 month, 2 months, 3 months and final measurement were taken after 6 months. Each time that the samples were taken out from the water tank, to make sure that the environmental condition is as stable as before, temperature and PH of the water and also humidity of the air were measured (**Figure 3-20**).

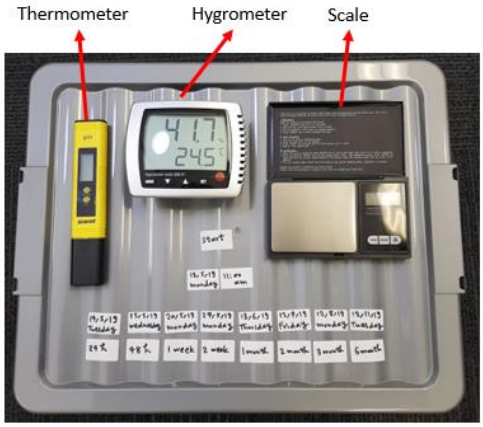

Figure 3-20 Measuring the environmental parameter that could affect the experiment.

The tensile tests on water absorbed dogbone specimens were carried out using a Zwick/Roell universal testing machine fitted with a 50kN load cell. The crosshead speed was set at

120mm/min (equivalent to strain rate of 0.05 s^{-1}) and then tensile tests were performed at room temperatures 25°C. For each sample, the Young's modulus (E), UTS, elongation at break EL (%) and modulus of toughness (T) were evaluated.).

.

3.7 Results and Discussion

In this section all the results related to material characterization analysis, mechanical tests and environmental effects analysis are discussed in detail.

3.7.1 FTIR Results

Results of FTIR analysis is an FTIR spectrum which shows the intensity and frequency of sample absorption in two -dimensional plot; X axis of the graph shows the wave length and Y axis shows the percentage of the light which is transmitted. Each functional group in a molecule has a characteristic IR band for absorption and the intensity of the absorption is related to the concentration of the component [153]. **Figure 3-21** shows the FTIR spectra of PU, PU+GNP, and PU+GNP+SG. All three FTIR spectra displayed characteristic peaks due to the key functional groups of polyurethane: N-H stretch at 3250 cm^{-1}, C-H stretches in 2950-2800 cm^{-1} region and a carbonyl group stretch at 1700 cm^{-1}. By comparing the FTIR results of the PU and GNP modified PU, it can be seen that both materials showed exactly the same behaviour as expected. The reason is that because pure PU has carbon in its structure and if the mixing procedure of GNP in PU was sufficient enough and GNP dispersed homogenously in PU and create hydrogen bonding with PU backbone chain successfully, then the trend of the FTIR should be as same as pure PU. By looking at the fingerprint region (1500-500 cm^{-1}) the only significant difference observed between PU and the modified PU is an additional peak around 800 cm^{-1} in the spectrum of PU+GNP+SG. This attributed to the symmetric stretching vibration of a Si-O-Si [154] and it can be explained due to the introducing silica-based sol-gel to the structure of modified PU. As a result of this experiment it can be seen that Pu and GNP modified PU has the same behaviour from wave absorption point of view and GNP/SG modified PU has an extra pick around 800 cm^{-1} which is related to the silica-based sol-gel. The general scheme for the preparation of PU nanocomposites and their interaction with the GNP is presented in **Figure 3-22** Carboxyl functionalised GNP create hydrogen bonding with the PU backbone chain, and hence stronger interface of GNP and PU backbone chain, resulting in improvement in mechanical properties of PU.

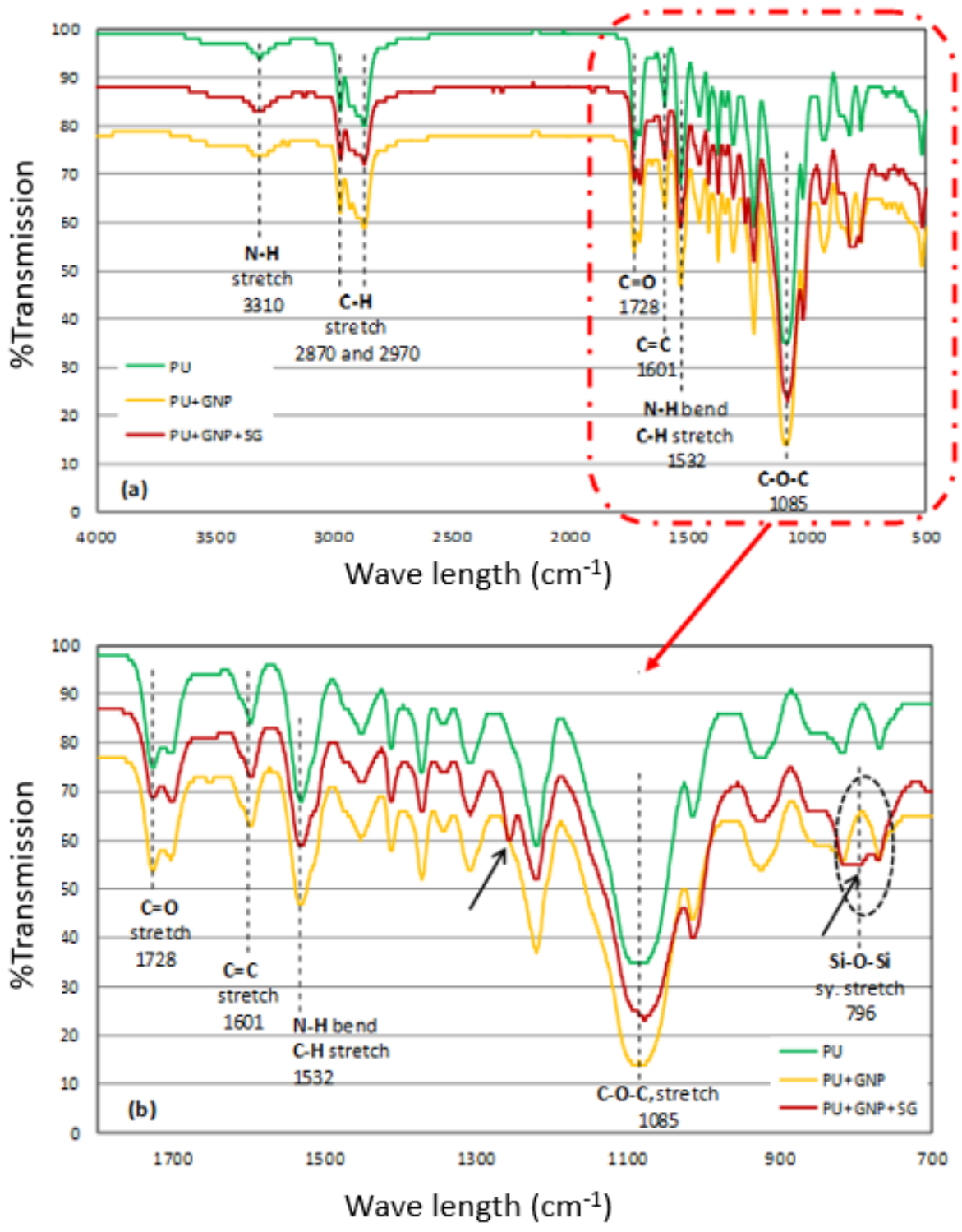

Figure 3-21 FTIR spectra of PU, PU+GNP and PU+GNP+SG at wavenumber range of (a) 4000–500 cm^{-1} and (b) 1800–700 cm^{-1} [155].

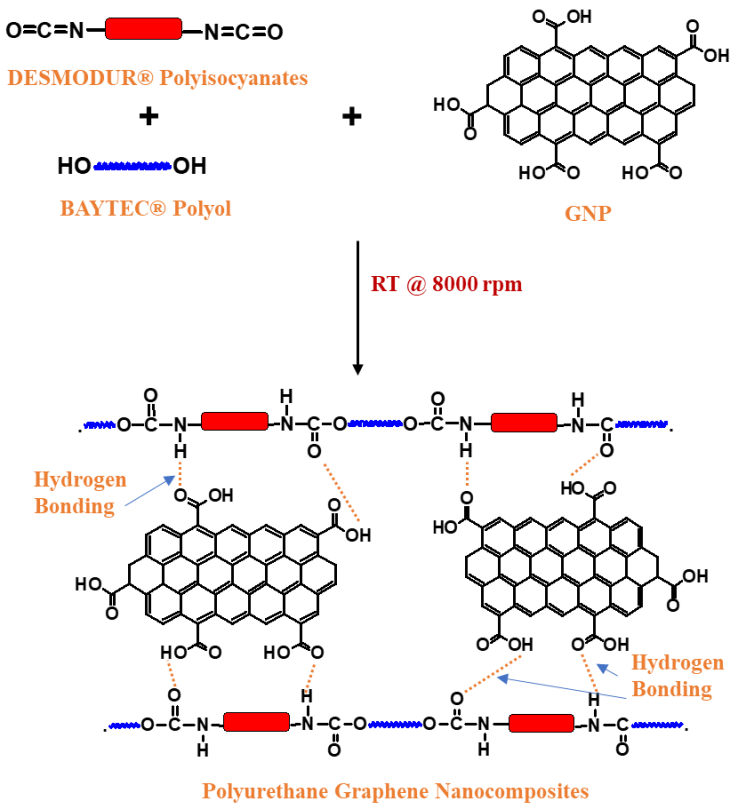

Figure 3-22 General Scheme for the preparation of PU and its GNP composites [155].

3.7.2 TGA tests results

The thermal stability of pure PU, graphene modified PU and GNP/hydrophobic silica-based modified PU was investigated using TGA and the results are presented in **Figure 3-23**. Higher initial decomposition temperature (IDT) of PU+GNP samples shows the higher thermal stability of this material. Dense network between the GNP nanoparticles and PU hinders the out-diffusion of decomposed products and thereby increase its overall thermal stability. By looking at the results of the TGA, it can be seen that although there is 1wt% sol-gel in PU+GNP+SG samples, but the IDT of this material is approximately the same as the pure PU. This is because the GNP like PU is mainly made up of organic carbon material. As can be seen in **Figure 3-23** , all samples show similar behaviour up to 280 °C, after that there is a significant weight loss for all samples up to 500 °C which can be explained by decomposition of the urethane bond in the PU structure and also weight loss of COOH group attached to the surface of the graphene [156]. Another point which should be considered is the difference in weight loss for PU+GNP+SG and the other two materials at the beginning of the test in the temperature range of 20 °C to 280°C. In this temperature range, PU+GNP+SG showed around 2% less weight loss in comparison to the other two materials. This is due to the hydrophobicity character of the PU+GNP+SG material which absorbs less moisture than the other two

materials. The negative weight loss for PU and PU+GNP+SG is due to the experimental error. First test was done for PU+GNP sample and the weight at the end of the test is zero which is correct. The TGA was run without placing any samples for few minutes to make sure that machine ready for the next test, however, it is apparent the duration was not enough in this case. The second and third tests were carried out after the first test and it is possible small amount of residuals remained in the TGA chamber.

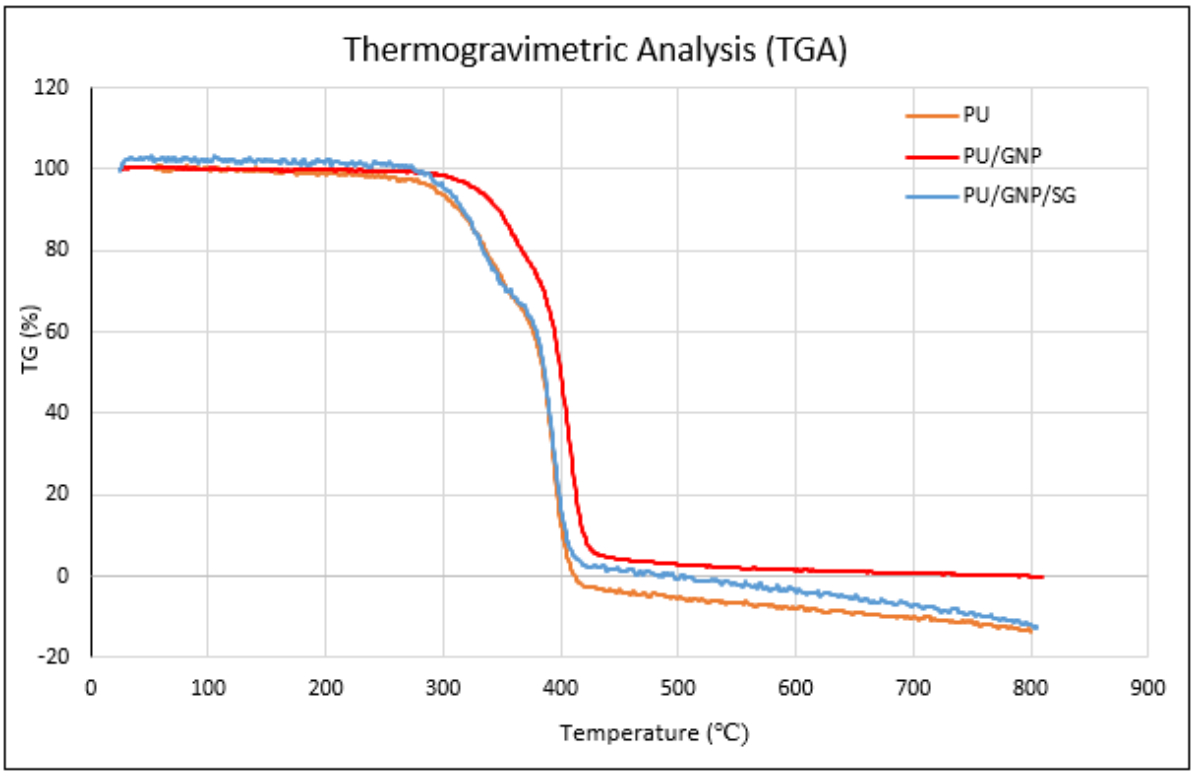

Figure 3-23 TGA curves of PU, PU/GNP and PU/GNP/SG samples.

3.7.3 DMA tests results

DMA test can be done in different modes: tension, torsion and bending. For polymer materials tension mode is the common method to analyse the viscoelastic properties. To perform the DMA test it is required first to do the amplitude sweep test to find the linear viscoelastic range (LEV). It is important to make sure that all tests were done in elastic region before destroying the structure of the samples. In this study ramping temperature DMA tests were performed in tension mode with cooling/heating rate of 3°C min^{-1} to measure the variation of damping coefficient with temperature and identify the glass transition temperature. The tests were carried out with strain-controlled mode under vibration amplitude of $5\mu m$ and frequency of 10Hz. **Figure 3-24** shows variation of the damping factor (tan δ) versus temperature for PU, PU+GNP and PU+GNP+SG. For all samples at low temperature tan δ is low as materials are

hard, and then by increasing the temperature it reached to the maximum value at the glass transition temperature which is around−20℃. After that by increasing the temperature, it starts decreasing. In addition, by looking at the shape of the peak for three materials in **Figure 3-24**, PU with lowest stiffness in comparison to the other two materials shows a broad peak and PU+GNP with the highest stiffness shows a sharp peak.

DMA test shows that adding 0.5wt% graphene to the PU decreases the cell size and also increases the cross-link density which results in increasing the damping capacity at the glass transition range [157]. This topic will be analysed in more details in Chapter 4.

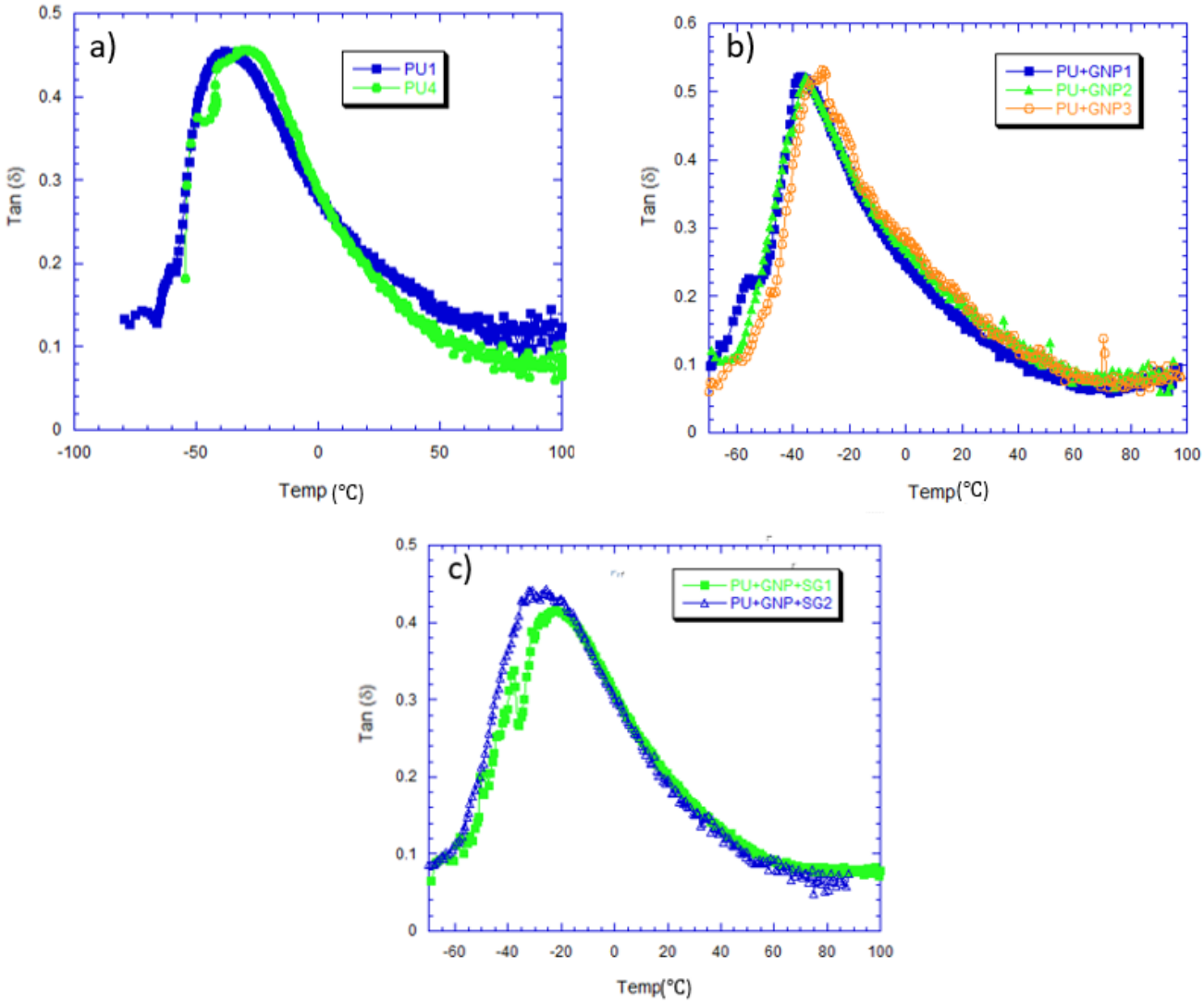

Figure 3-24 Variation of the damping factor (tan δ) versus temperature for a) PU, b) PU+GNP and c) PU+GNP+SG.

3.7.4 Water droplet contact angle and surface energy measurement results

The variation of water contact angle (CA) with respect to time for PU and its nanocomposites are presented in **Figure 3-25**. The results show that the water CA of PU is from 56° to 57°. This indicates the slightly hydrophobic property of the neat PU. The low hydrophobicity of PU is due to the presence of a large number of surface polar urethane functional groups which can interact with polar water molecules. However, addition of f-GNP nanoparticles to the PU increased hydrophobicity (CA from 70° to 80°). The two-dimensional f-GNP nanoparticles possess a high surface area and are highly hydrophobic due to grapheme's non-polar nature and only a small concentration of carboxylic groups at the edges. The small addition of 0.5 wt% of f-GNP covers a large surface area within PU matrix and improves the overall hydrophobicity. By looking at the **Figure 3-25** it can be seen that for the GNP-PU samples the water contact angle decreased for the first 1500 ms and then became constant, the reason can be explained due to the porosity of one of the samples which means that for that particular sample the GNP didn't dispersed in PU completely homogeneous and left some porosity on the surface (take into account that the presented contact angle is the average contact angle of five samples). Further, the addition of hydrophobic silica along with f-GNP significantly contributes to the increase in the overall hydrophobicity of the coating. The CA of PU increased from 56° to around 110° with the addition of 0.5wt% f-GNP and 1wt% hydrophobic silica. The hydrophobic functionalized silica improves the compatibility as well dispersibility in the PU matrix. The silica nanoparticles are easily adsorbed on the graphene surface which further improves their dispersibility as observed in the elemental mapping shown in **Figure 3-26**. The addition of hydrophobic nanoparticles (0.5wt% GNP + 1wt% sol-gel) and their homogeneous dispersion enhance the hydrophobicity of the PU matrix.

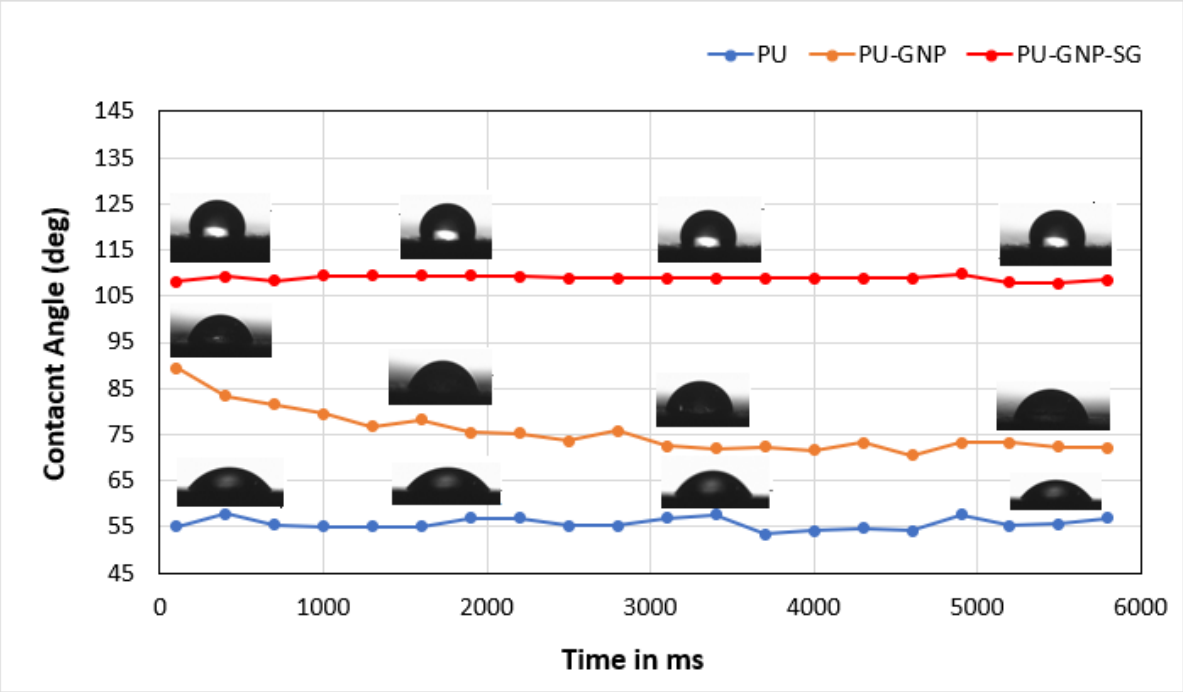

Figure 3-25 The comparison of static DI water contact angle (CA) of the GFRP surfaces coated with PU, PU+GNP and PU+GNP+SG at different interval of time.

Moreover, the surface free energy, which was determined from the initial static DI CA values, followed an opposite trend when compared to the static DI CA. The calculated surface free energy of pure PU was around 114.55 $mJ{\cdot}m^{-2}$, however, with the addition of the *f*-GNP into the PU the surface energy decreased to 73.36 $mJ{\cdot}m^{-2}$. Furthermore, the addition of hydrophobic silica significantly reduced the surface free energy to 50.06 $mJ{\cdot}m^{-2}$ in the PU+GNP+SG material. The decrease in surface free energy suggests the superior water repellency of the PU modified coatings which could improve the weather resistant property.

3.7.5 SEM results

FESEM images of the PU and its composites are presented in **Figure 3-26** together with energy-dispersive X-ray spectroscopy (EDX) and elemental mapping of the samples. The SEM images of PU and PU+GNP clearly indicate that the incorporation of f-GNP into the PU polymer did not significantly alter the surface morphology and there were no appreciable evidences of graphene sheets appearing on the surface, suggesting the homogeneous dispersion of f-GNP in the PU matrix. This could be due to the strong interaction of f-GNP carboxylic groups with the urethane functional groups in PU via hydrogen bonding as shown in **Figure 3-22**. The strong hydrogen bonding leads to the uniform dispersion of f-GNP and can avoid leaching of graphene sheets out of the PU matrix over time. Interestingly, PU+GNP+SG

displayed a smoother surface than PU and PU+GNP. This could be due to the in-situ polymerization technique adopted in the preparation of PU+GNP+SG. The silica particles are initially well dispersed in the polyisocynates and are then transferred to the f-GNP-polyol mixture to initiate the polymerization; thus, the polymerization initiates around the silica and f-GNP nanoparticles, which facilitates the strong interactions between the nanoparticles and polymer chains. This in turn prevents the aggregation of nanoparticles and helps the homogeneous dispersion of nanomaterials within the PU matrix. Moreover, research has shown that grafting hydrophobic moieties onto the silica surface can enhance the silica's miscibility with polymer components due to its reduced hydrophilicity and enhanced interfacial interaction with the PU matrix [158, 159]. Furthermore, the presence of carboxylic groups on f-GNP can improve the dispersibility via hydrogen bonding. The uniform and continuous dispersion of silica nanoparticles in the PU matrix was further confirmed in the EDX and elemental mapping, as shown in **Figure 3-26**.

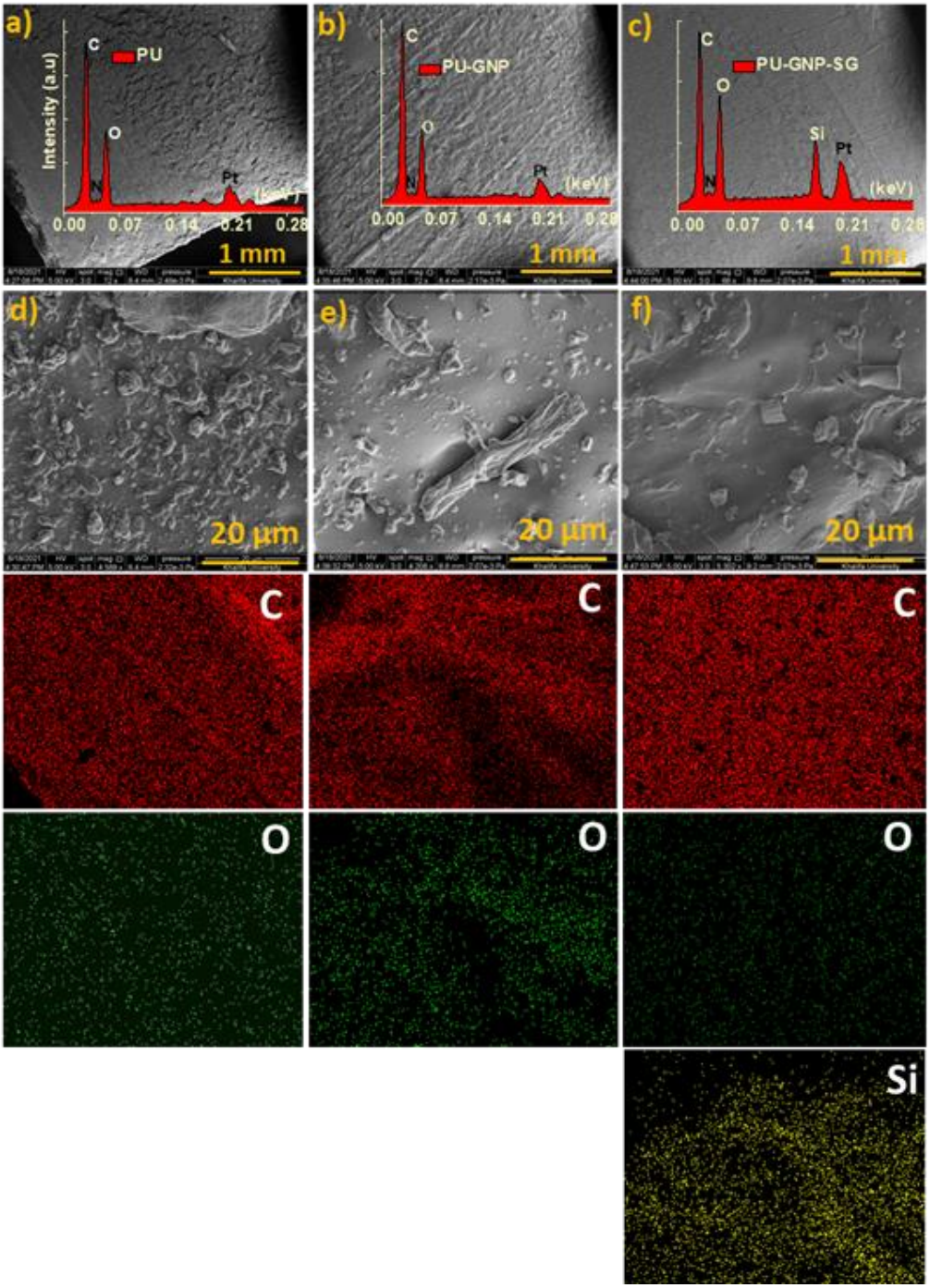

Figure 3-26 The FE-SEM of top surface of (a, d) PU, (b, e) PU+GNP and (c, f) PU+GNP+SG, at different magnification. Insight image on (a) to (c) shows the corresponding EDX mapping and the bottom columns correspond to the respective elemental mapping [155].

3.7.6 Tensile tests results

Initially, the tensile properties of the neat polyurethane were investigated to understand the performance of the neat PU at room and at elevated temperature. The optimised mixing procedure of CNPs in the PU was established by dispersing MWCNTs in PU at three different mixing speeds and for three different mixing durations. It was found that mixing at 8000 rpm for 18 minutes using a homogenizer gave the most homogenous mixture with little damage to

the structure of carbon nanoparticles (CNPs). After establishing the optimum mixing procedure, different loading of f-MWCNTs and f-GNP were dispersed in the PU and the tensile tests were carried out and the optimum MWCNTs and GNP loading for achieving the best mechanical properties of the nanocomposites was determined. Then the mixture of hybrid MWCNTs+ GNP was added to the PU to analyse the mechanical properties. Finally, hydrophobic silica-based sol-gel (SG) was added to the modified PU+GNP and the results of the tensile tests for this PU nanocomposite were obtained.

3.7.6.1 Tensile properties of the neat PU

The tensile tests were carried out using a Zwick/Roell universal testing machine fitted with a 50kN load cell. The crosshead speed was set at 2.1, 10.5 and 21 mm/min (equivalent to strain rate of 0.01, 0.05 and 0.1 s^{-1}) and at each strain rate, tensile tests were performed in-situ at three different temperatures 25 (RT), 50 and 70°C using heating chamber (**Figure 3-27**).

The Young's modulus (E), ultimate tensile strength (UTS), elongation at break EL (%) and toughness (T) were evaluated at each temperature and strain rate. For each case three specimens were tested for statistical evaluation. The specimen codes are presented in Table 3-3.

The tests were carried out at three different temperatures and strain rates and the results are summarised in Table 3-4.

(a) (b)

Figure 3-27 (a) Universal tensile test (b) Heating chamber for in-situ tensile testing at high temperature.

Table 3-3 Tensile test conditions and specimens' number.

Temperature	Strain rate $\dot{\varepsilon}$ (s^{-1})	Specimen Code
25°C	0.01	PU-SR0.01-T25- 1 to 3
	0.05	PU-SR0.05-T25- 1 to 3
	0.1	PU-SR0.1-T25- 1 to 3
50°C	0.01	PU-SR0.01-T50- 1 to 3
	0.05	PU-SR0.05-T50- 1 to 3
	0.1	PU-SR0.1-T50- 1 to 3
70°C	0.01	PU-SR0.01-T70- 1 to 3
	0.05	PU-SR0.05-T70- 1 to 3
	0.1	PU-SR0.1-T70- 1 to 3

Table 3-4 Tensile properties of the neat BAYTEC+DESMODUR polyurethane at different temperature and strain rate.

Temp.	$\dot{\varepsilon}$ (s^{-1})	Specimen Code.	Young's modulus (MPa)		UTS (MPa)		EL (%)		T (kJ/m^3)	
25°C	0.01	PU-SR0.01-T25-1	1.92	1.83 ±0.05	18	17.4 ±0.3	616	657 ±32	8756	8832 ±425
		PU-SR0.01-T25-2	1.82		16.8		676		8445	
		PU-SR0.01-T25-3	1.76		17.4		680		9295	
	0.05	PU-SR0.05-T25-1	2.2	2.13 ±0.05	22.5	21.56 ±0.45	740	659 ±68	11745	10301 ±1130
		PU-SR0.05-T25-2	2.1		20.6		632		9675	
		PU-SR0.05-T25-3	2.1		21.6		604		9485	
	0.1	PU-SR0.1-T25-1	2.4	2.07 ±0.3	27.3	26.50 ±4.5	728	769 ±51	12929	13302 ±2235
		PU-SR0.1-T25-2	1.8		21.6		752		11254	
		PU-SR0.1-T25-3	2.0		30.6		829		15724	
50°C	0.01	PU-SR0.01-T50-1	1.7	1.60 ±0.1	12.9	11.67 ±0.95	384	387 ±4	6945	6255 ±534
		PU-SR0.01-T50-2	1.6		11.1		392		5943	
		PU-SR0.01-T50-3	1.5		11		384		5877	
	0.05	PU-SR0.05-T50-1	1.8	1.80 ±0.1	10	13.67 ±4.5	332	422 ±84	5898	6670 ±944
		PU-SR0.05-T50-2	1.9		12		436		6326	
		PU-SR0.05-T50-3	1.7		19		500		7786	
	0.1	PU-SR0.1-T50-1	2.0	2.00 ±0.1	12	14.00 ±3	420	472 ±56	5591	6937 ±1603
		PU-SR0.1-T50-2	2.1		12		464		6424	
		PU-SR0.1-T50-3	1.9		18		532		8797	
70°C	0.01	PU-SR0.01-T70-1	1.6	1.27 ±0.25	3.3	2.70 ±0.6	168	161 ±26	1405	1255 ±117
		PU-SR0.01-T70-2	1.1		2.7		132		1171	
		PU-SR0.01-T70-3	1.1		2.1		184		1189	
	0.05	PU-SR0.05-T70-1	1.6	1.73 ±0.1	6	6.50 ±0.5	300	301 ±2	3043	3209 ±196
		PU-SR0.05-T70-2	1.8		7		304		3434	
		PU-SR0.05-T70-3	1.8		6.4		301		3152	
	0.1	PU-SR0.1-T70-1	2	1.90 ±0.1	9	8.87 ±0.3	328	324 ±4	4675	4609 ±87
		PU-SR0.1-T70-2	1.9		8.5		320		4502	
		PU-SR0.1-T70-3	1.8		9.1		325		4650	

The true strain-stress results at different strain rate are shown in **Figure 3-28** and at different temperature are shown in **Figure 3-29**. The corresponding engineering strain-stress can be seen in Appendix A.1

.

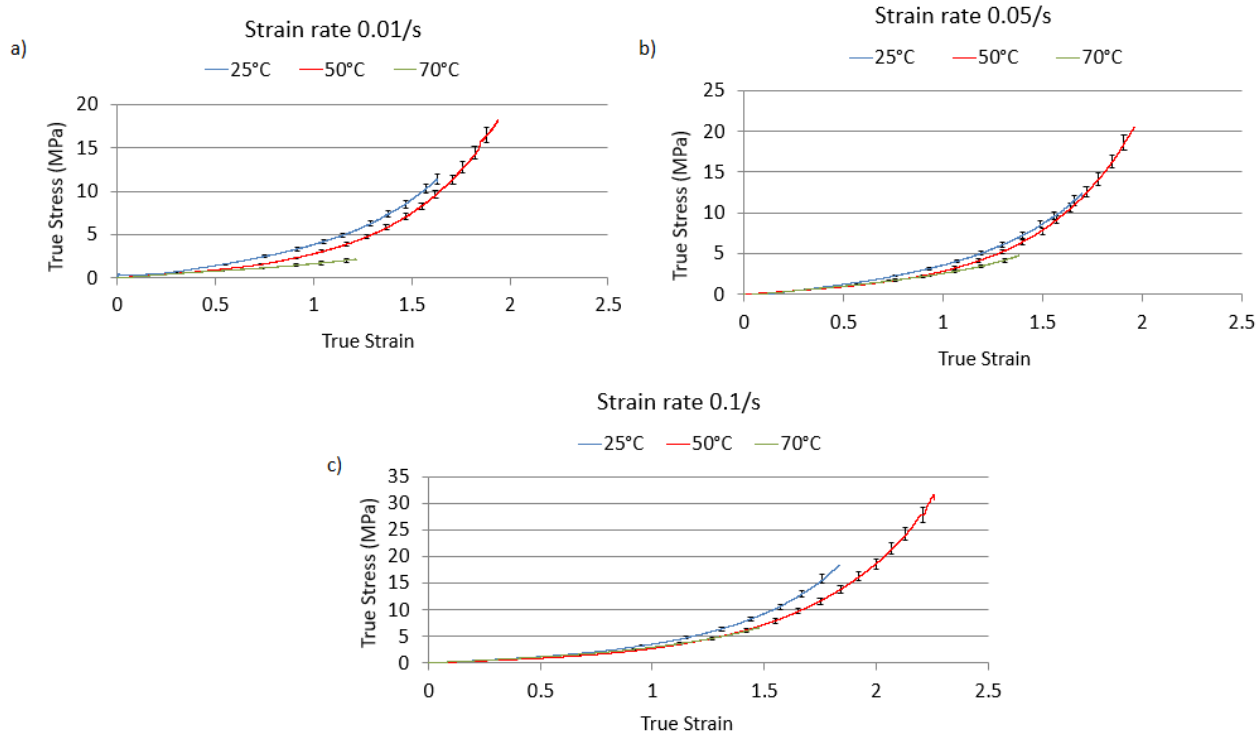

Figure 3-28 True strain-stress for neat PU at strain rate of (a) 0.01 s^{-1}, (b) 0.05 s^{-1} and (c) 0.1 s^{-1} and at RT, 50 and 70°C.

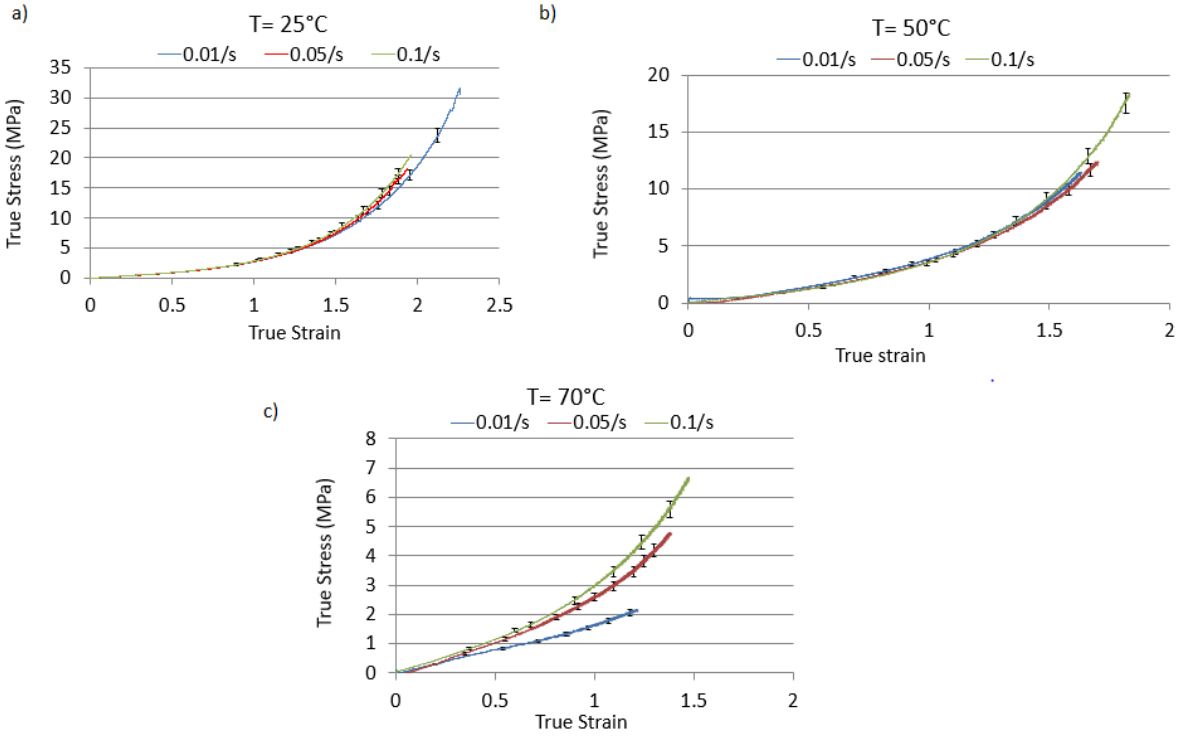

Figure 3-29 True strain-stress for neat PU at temperature of (a) 25 °C, (b) 50 °C and (c) 70 °C.

Effect of temperature and strain rate on Young's modulus of PU

Variation of Young's modulus versus strain rate at different temperatures is shown in **Figure 3-30**. The results show that by increasing the strain rate from $0.01s^{-1}$ to $0.1s^{-1}$, the Young's modulus has increased at all three different temperatures. At 25°C (RT), by increasing the strain rate from 0.01 $s^{-1}$to 0.05 s^{-1}, the initial Young's modulus increased 14.7% but after that by increasing the strain rate to $0.1s^{-1}$, the Young's modulus remains constant. However, the Young's modulus at 50°C and 70°C has continuously increased by increasing the strain rate.

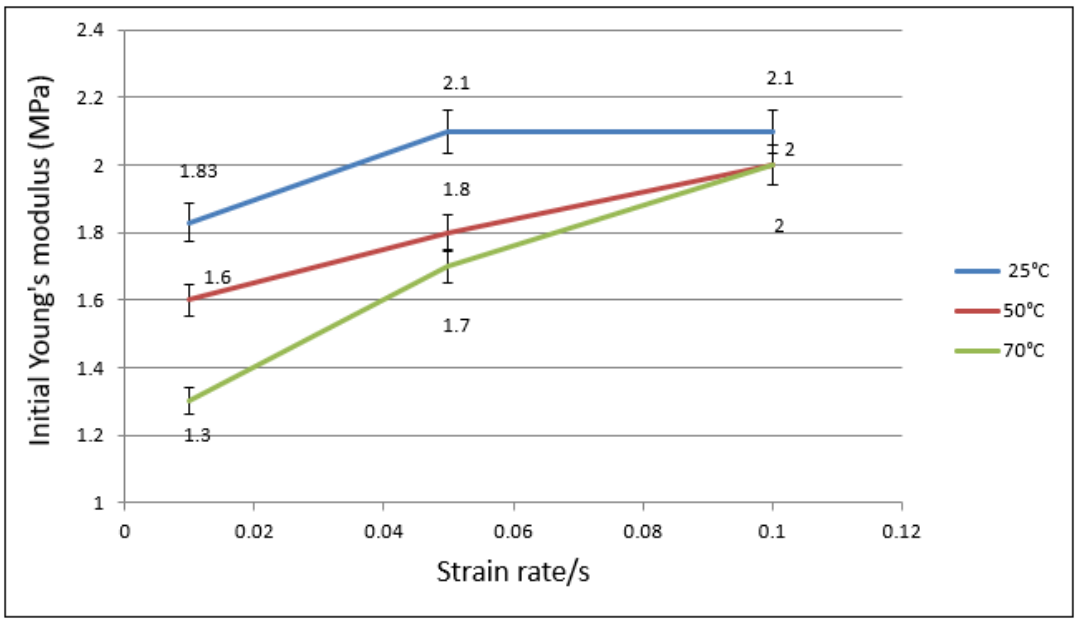

Figure 3-30 Young's modulus of the neat PU versus strain rate at three different temperatures.

Effect of temperature and strain rate on elongation at break of PU

The elongation at break for the neat PU at three different strain rates and temperature showed that by increasing the strain rate, the elongation at break has been increased at all three temperatures (**Figure 3-31**). However, at the same strain rate, increasing the temperature decreases elongation at break. As can be seen in the **Figure 3-31**, at the strain rate of $0.01s^{-1}$, by increasing the temperature from 25°C to 70°C, the elongation at break is decreased by 308% and at the strain rates of 0.05 and 0.1, EL is decreased by 118% and 147%, respectively.

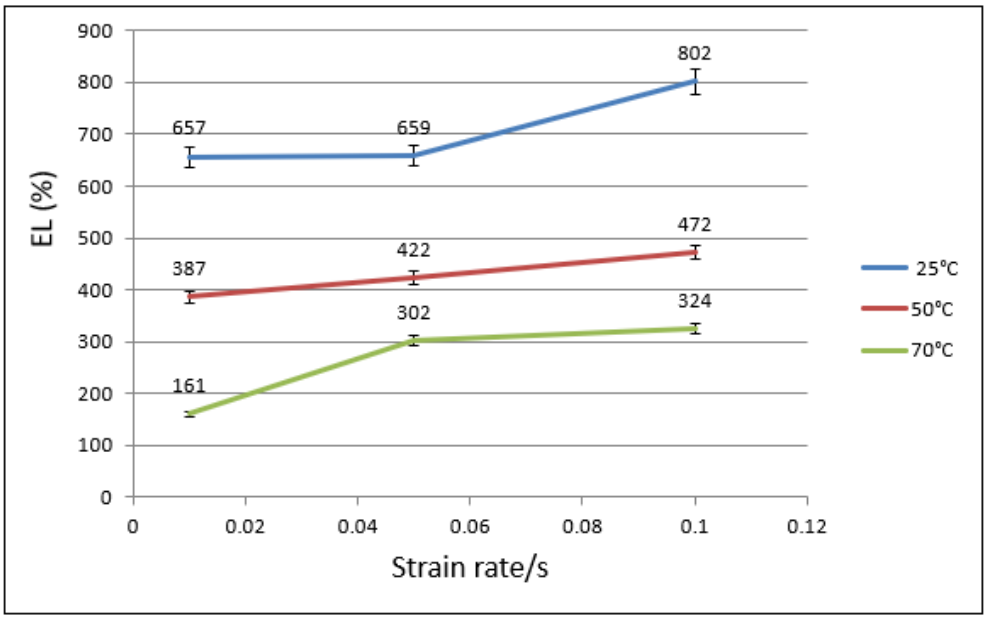

Figure 3-31 Elongation at break of the neat PU versus strain rate at three different temperatures.

Effect of temperature and strain rate on UTS of PU

The UTS is expected to increase at higher strain. Effect of increasing the strain rate at different temperature on the UTS of the neat PU is shown in **Figure 3-32** By increasing the strain rate from $0.05s^{-1}$ to $0.1s^{-1}$ at temperature of 25°C, the UTS is increased by 23%, but at the temperature of 50°C, the UTS increased only by 2% and at 70°C it is increased by 34% (Figure 3-32).

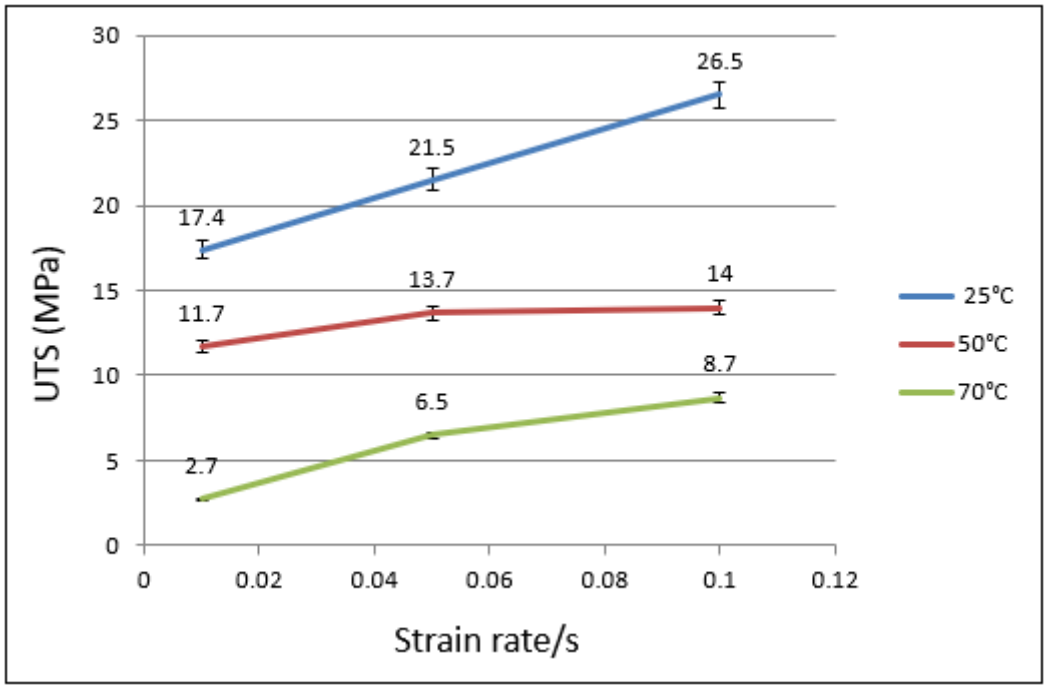

Figure 3-32 Ultimate tensile strength of the neat PU versus strain rate at three different temperatures.

Effect of temperature and strain rate on modulus of toughness of PU

The modulus of toughness is calculated by measuring the area under the strain-stress curve. The effect of temperature and strain rate on the modulus of toughness of the neat PU is shown in **Figure 3-33**. Generally, the modulus of toughness has been increased by increasing the strain rate at all temperature and the highest increase occurred at room temperature. However, at the same strain rate, by increasing the temperature, the modulus of toughness decreases, as less energy is required to break the samples. At lower temperature and higher strain rate, more energy is required to break the samples therefore, maximum modulus of toughness achieved at room temperature and at strain rate of $0.1s^{-1}$ which is $13302kJ/m^3$ and the lowest value of $1255kJ/m^3$ was seen at strain rate of $0.01s^{-1}$ at 70°C.

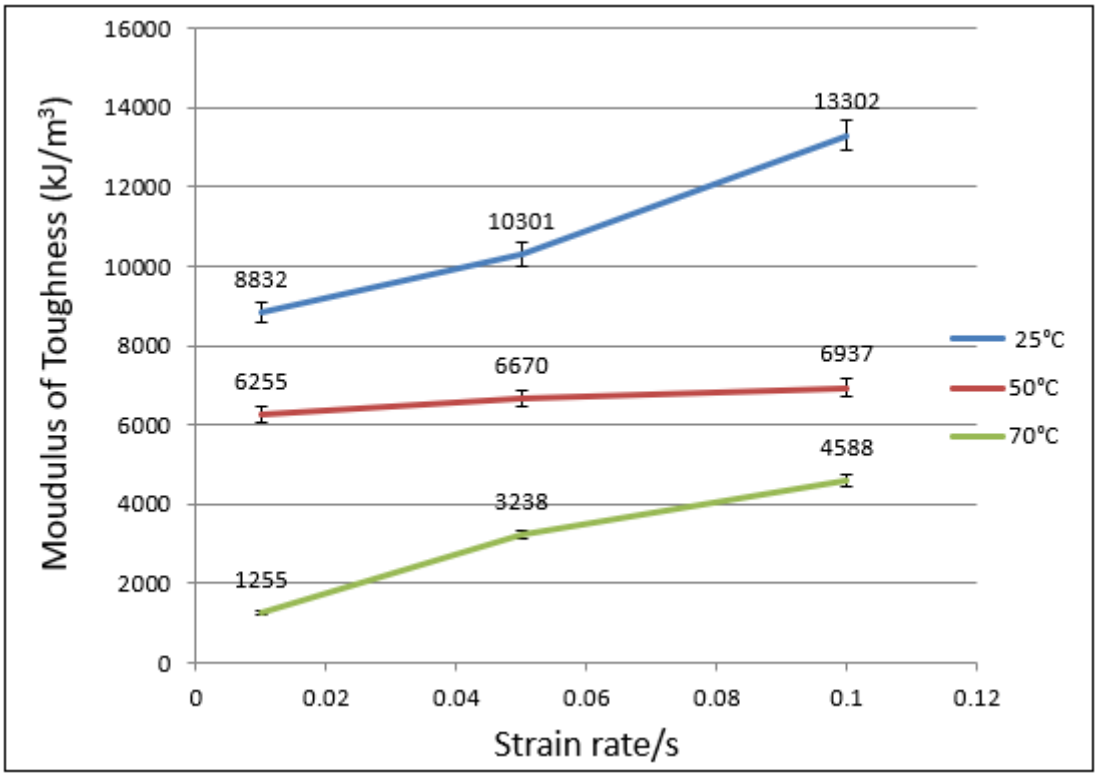

Figure 3-33 Modulus of toughness of the neat PU versus strain rate at three different temperatures.

In summary, these results show that at higher strain rate the material becomes stiffer and at higher temperature at constant strain rate the material becomes softer. This trend is also staying the same for UTS and modulus of toughness. Therefore, in hot climate by losing the stiffness, the performance of the coating material most likely deteriorates.

3.7.6.2 Optimising mixing procedure of CNPs and PU using MWCNTs

After analysing the effect of temperature and strain rate on neat PU, 0.5wt% MWCNTs was added to PU at three different mixing speed and three different mixing duration to optimise the mixing parameters; then tensile test was performed at 25°C and the strain rate of $0.05s^{-1}$ to establish the effect of the mixing duration and speed on the mechanical properties of the nanocomposite. The results of tensile tests are summarised in **Table 3-5**.

Table 3-5 Tensile properties of the PU+0.5wt% MWCNTs nanocomposite at different mixing duration and speed.

Mixing Speed (rpm)	Mixing duration (min)	Specimen Code	Young's modulus (MPa)		UTS (MPa)		EL (%)		T (kJ/m^3)	
8000	6	0.5%CNT/PU-RPM8-D6-1	3.1	3.13 ±0.05	18.44	23.38 ±4	448	537 ±68	9137	11404 ±1752
		0.5%CNT/PU-RPM8-D6-2	3.2		26.6		584		12435	
		0.5%CNT/PU-RPM8-D6-3	3.1		25.1		580		12640	
	12	0.5%CNT/PU-RPM8-D12-1	3.2	3.03 ±0.2	23.1	23.33 ±0.8	558	555 ±44	11673	11709 ±757
		0.5%CNT/PU-RPM8-D12-2	3.1		24.2		598		12485	
		0.5%CNT/PU-RPM8-D12-3	2.8		22.7		510		10971	
	18	0.5%CNT/PU-RPM8-D18-1	2.9	2.97 ±0.1	23.6	25.83 ±4	600	646 ±68	12032	13397 ±1978
		0.5%CNT/PU-RPM8-D18-2	3.1		23.1		604		12173	
		0.5%CNT/PU-RPM8-D18-3	2.9		30.8		736		15987	
12000	6	0.5%CNT/PU-RPM12-D6-1	3.4	3.40 ±0	21.5	21.60 ±0.1	468	421 ±36	10777	10534 ±204
		0.5%CNT/PU-RPM12-D6-2	3.4		21.7		399		10456	
		0.5%CNT/PU-RPM12-D6-3	3.4		21.6		396		10370	
	12	0.5%CNT/PU-RPM12-D12-1	3.4	2.93 ±0.7	23.9	22.47 ±3	528	524 ±21	11945	11606 ±1565
		0.5%CNT/PU-RPM12-D12-2	3.4		25		544		13002	
		0.5%CNT/PU-RPM12-D12-3	2.0		18.5		502		9873	
	18	0.5%CNT/PU-RPM12-D18-1	2.3	2.40 ±0.1	24.3	23.60 ±0.65	648	650 ±4	12483	12506 ±38
		0.5%CNT/PU-RPM12-D18-2	2.4		23		656		12555	
		0.5%CNT/PU-RPM12-D18-3	2.5		23.5		648		12480	
15000	6	0.5%CNT/PU-RPM15-D6-1	4.1	3.80 ±0.3	23.5	21.40 ±4.8	460	436 ±88	12135	10607 ±2399
		0.5%CNT/PU-RPM15-D6-2	3.6		25.2		512		12243	
		0.5%CNT/PU-RPM15-D6-3	3.7		15.5		336		7445	
	12	0.5%CNT/PU-RPM15-D12-1	2.3	2.43 ±0.2	17.3	21.17 ±5.7	484	529 ±48	9079	10994 ±2668
		0.5%CNT/PU-RPM15-D12-2	2.6		28.7		580		14415	
		0.5%CNT/PU-RPM15-D12-3	2.4		17.5		524		9488	
	18	0.5%CNT/PU-RPM15-D18-1	2.2	2.26 ±0.1	20.8	20.60 ±1.1	602	628 ±44	11602	12362 ±2259
		0.5%CNT/PU-RPM15-D18-2	2.4		21.6		685		15000	
		0.5%CNT/PU-RPM15-D18-3	2.2		19.4		598		10483	

Tensile test results of true strain-stress for PU+ 0.5wt% MWCNT nanocomposite at various mixing speed are shown in **Figure 3-34** and at various mixing duration are shown in **Figure 3-35**.

The corresponding results of engineering strain-stress can be seen in Figure A.3 and A.4 in Appendix A.2.

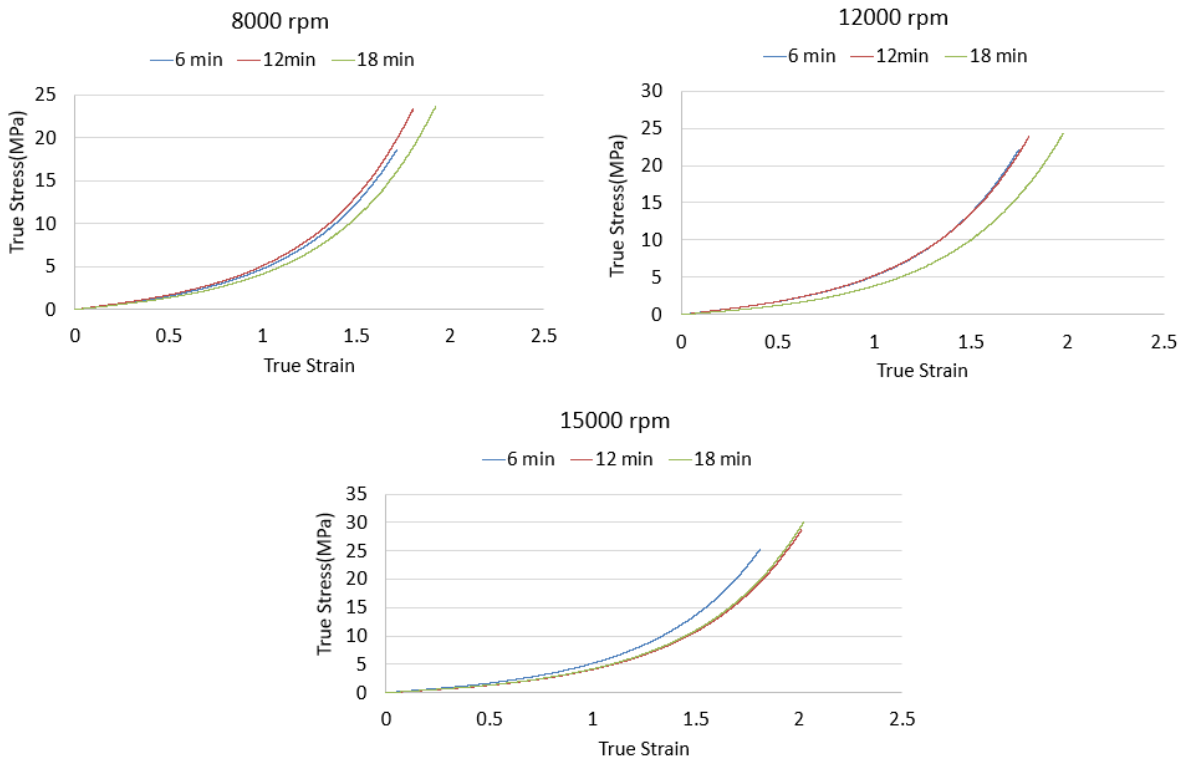

Figure 3-34 True strain-stress for PU+ 0.5 wt% MWCNTs at different speed.

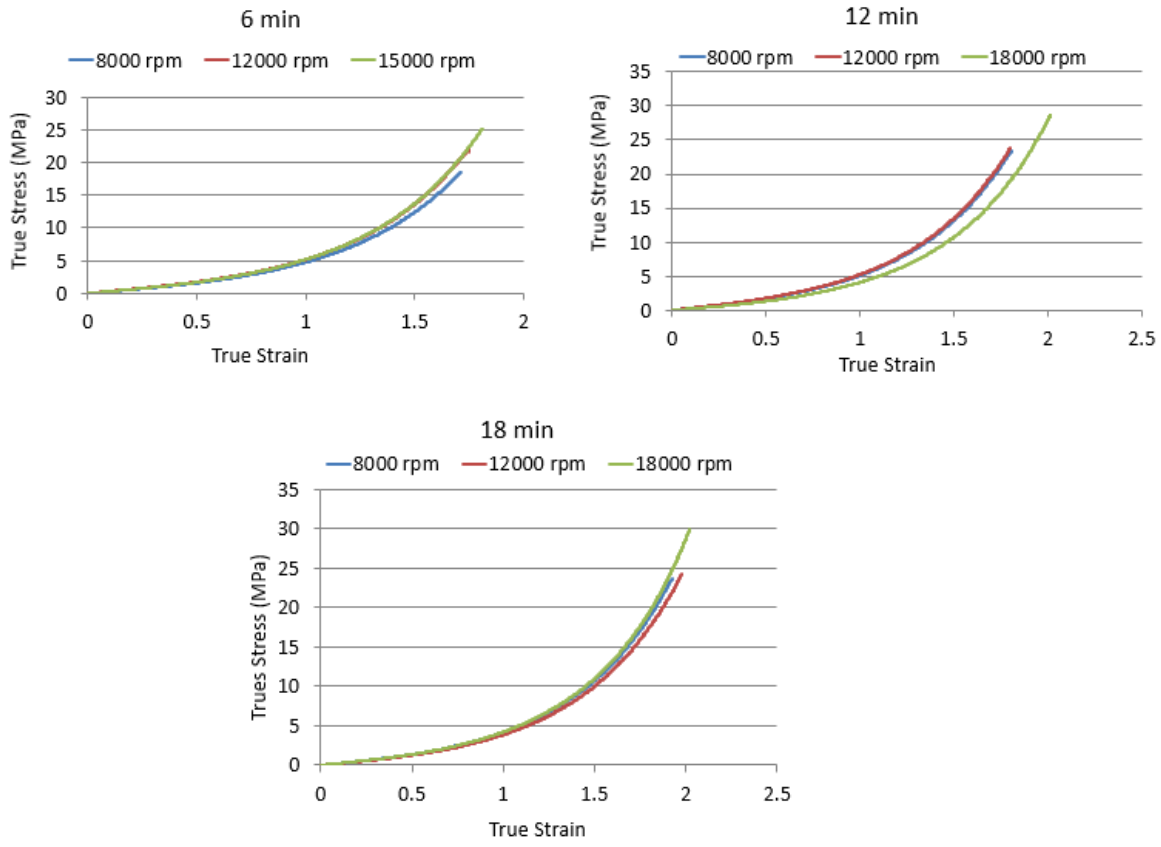

Figure 3-35 True strain-stress for PU+ 0.5wt% MWCNTs at different mixing time.

Young's modulus, elongation at break, UTS and modulus of toughness of various specimens are extracted from **Figure 3-34** and **Figure 3-35.**

Effect of speed and mixing duration on Young's modulus of PU + MWCNTs

Figure 3-36 shows variation of Young's modulus versus mixing duration of MWCNT/PU nanocomposite at 3 different mixing speeds. It can be seen that by increasing the speed of mixing, the Young's modulus is decreasing as the duration of mixing increases from 6 min to 18 min. By increasing the mixing duration from 6min to 18min, the Young's modulus is dropped by 3% at the speed of 8000 rpm, 41% at the speed of 12000rpm and 65% at the speed of 15000rpm.

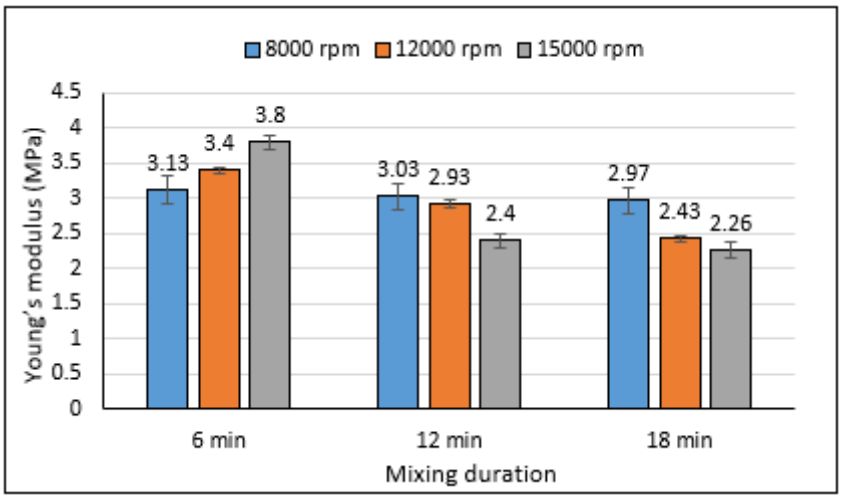

Figure 3-36 Young's modulus of the PU+0.5wt% MWCNTs versus time at different mixing speed at strain rate of 0.05 s^{-1}.

Effect of speed and mixing duration on elongation at break of PU + MWCNTs

Figure 3-37 shows the effect of the speed and duration of mixing on the elongation at break of MWCNT/PU nanocomposite. The results show that by increasing the mixing speed the elongation at break decreases, but at any mixing speed increasing the duration of mixing increases the elongation at break (**Figure 3-37**).

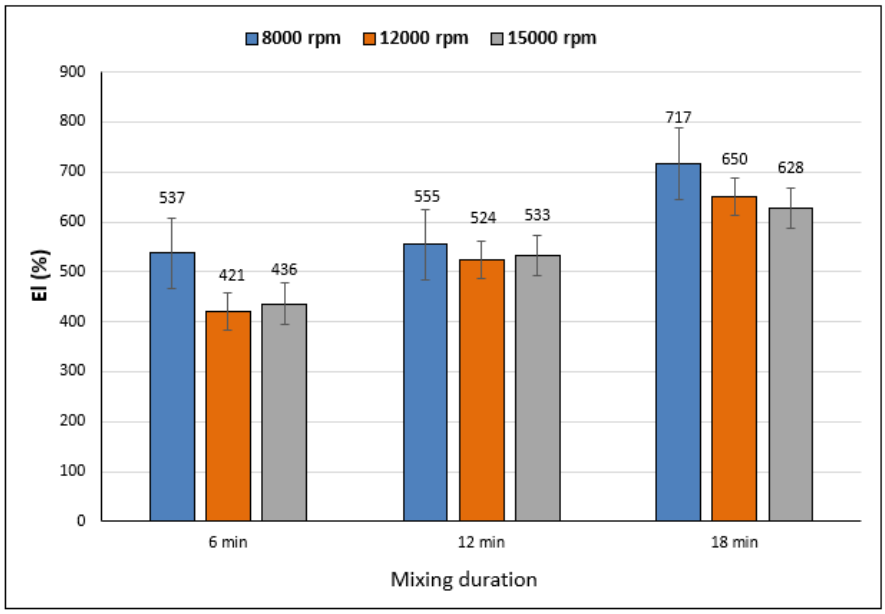

Figure 3-37 Elongation at break of the PU+0.5wt% MWCNTs nanocomposite versus time at different mixing speed at strain rate of 0.05 s^{-1}.

Effect of speed and mixing duration on UTS of PU + MWCNTs

Figure 3-38 shows the effect of the speed and duration of mixing on ultimate tensile strength of MWCNT/PU nanocomposite. The UTS is decreased by increasing the mixing speed at any specific duration. However, at the speed of 8000rpm and 12000rpm, the UTS is increased by increasing mixing duration; but at 15000rpm the UTS slightly decreased as the mixing duration is increased. The highest value for UTS achieved was 25.8MPa at the lowest mixing speed (8000rpm) for mixing time of 18 min. The lowest UTS achieved was 21MPa at the highest mixing speed (15000rpm) for the shortest mixing time of 6min.

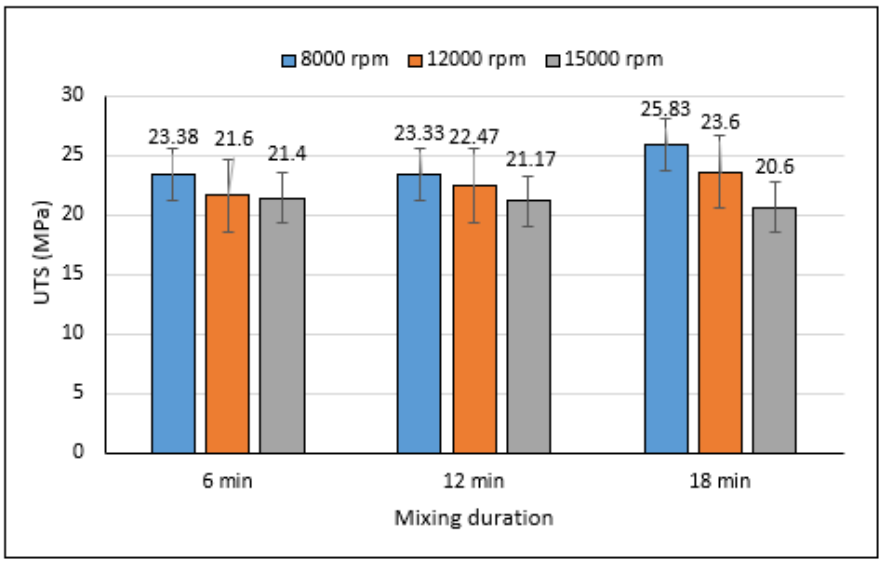

Figure 3-38 Ultimate tensile strength of the PU+0.5wt% MWCNTs versus time at different mixing speed at strain rate of $0.05s^{-1}$.

Effect of speed and mixing duration on modulus of toughness of PU + MWCNTs

From **Figure 3-39** it can be seen that modulus of toughness is increased by increasing the mixing duration and it is decreased by increasing the mixing speed. The highest value of the modulus of toughness of $13397kJ/m^3$ is obtained at the lowest speed (8000rpm) with the longest mixing duration (18min).

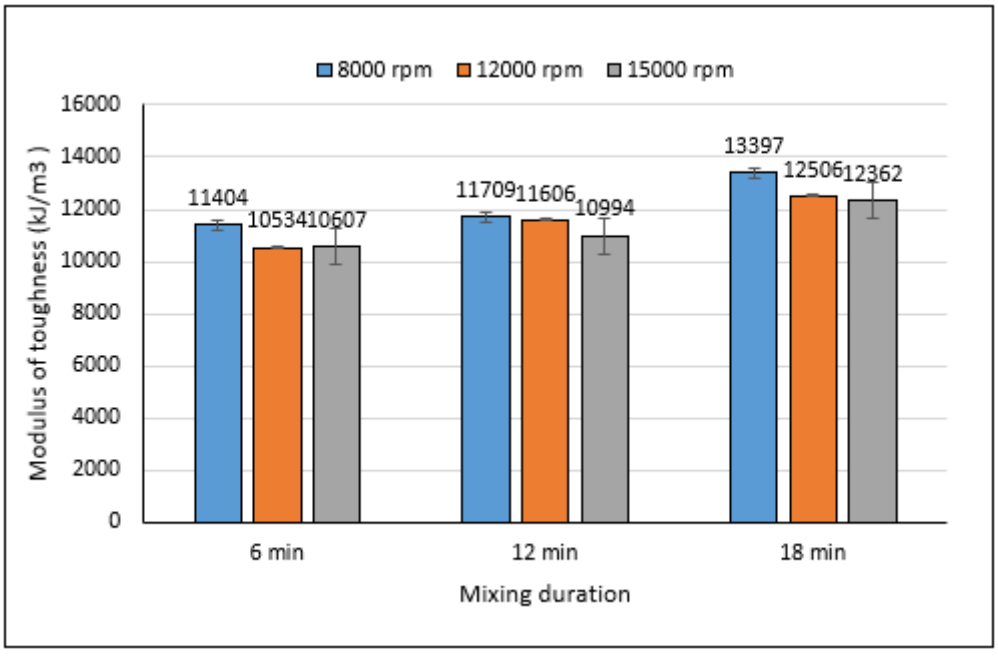

Figure 3-39 Modulus of toughness of the PU+0.5wt% MWCNTs nanocomposite at versus mixing duration and at different mixing speed at strain rate of $0.05\ s^{-1}$.

3.7.6.3 Analysing the effect of adding different MWCNTs loading on tensile properties of PU

In this section different loadings of the CNTs (0.1, 0.2, 0.3, 0.5 and 1wt%) were added to the PU using the established optimum mixing parameters. The tensile properties of the nanocompaoite was analysed and the optimum loading of CNTs was established.

Tensile tests were conducted at room temperature and strain rate of $0.05s^{-1}$. The results of initial Young's modulus, UTS, percentage of elongation at break EL (%) and modulus of toughness (T) are summarised in **Table 3-6**.

Table 3-6 Tensile properties of the modified PU with different weight percentage of CNTs.

Specimen Code	**Young's modulus (MPa)**		**UTS (MPa)**		**EL (%)**		**T (kJ/m^3)**	
Neat PU-RPM8-D18-1	0.98	0.99 ±0.01	6	6.83 ±0.65	303	341 ±29	2914	3442 ±407
Neat PU-RPM8-D18-2	1		7.3		358		3685	
Neat PU-RPM8-D18-3	1		7.2		361		3727	
0.1% CNT/PU-RPM8-D18-1	0.97	0.99 ±0.04	15.87	14.99 ±0.89	608	581 ±26	7934	7335 ±581
0.1% CNT/PU-RPM8-D18-2	0.96		15		577		7299	
0.1% CNT/PU-RPM8-D18-3	1.03		14.1		557		6773	
0.2% CNT/PU-RPM8-D18-1	1.3	1.29 ±0.01	17.91	17.59 ±0.46	626	607 ±20	9584	9096 ±471
0.2% CNT/PU-RPM8-D18-2	1.29		17		587		8643	
0.2% CNT/PU-RPM8-D18-3	1.29		17.86		608		9060	
0.3% CNT/PU-RPM8-D18-1	3.1	2.98 ±0.12	22.7	22.4 ±1.25	629	629 ±8	9682	9315 ±796
0.3% CNT/PU-RPM8-D18-2	2.86		21		622		8336	
0.3% CNT/PU-RPM8-D18-3	2.97		23.5		637		9927	
0.5% CNT/PU-RPM8-D18-1	2.9	3.01 ±0.1	23.6	25.8 ±3.85	600	646 ±68	12032	13397 ±1978
0.5% CNT/PU-RPM8-D18-2	3.1		23.1		604		12173	
0.5% CNT/PU-RPM8-D18-3	2.9		30.8		736		15987	
1% CNT/PU-RPM8-D18-1	2.6	2.63 ±0.15	23.8	23.6 ±2.5	409	415 ±31	10857	10777 ±907
1% CNT/PU-RPM8-D18-2	2.5		26		449		11644	
1% CNT/PU-RPM8-D18-3	2.8		21		387		9831	

The engineering strain-stress results at different weigh percentage of CNTs are shown in **Figure 3-40**.

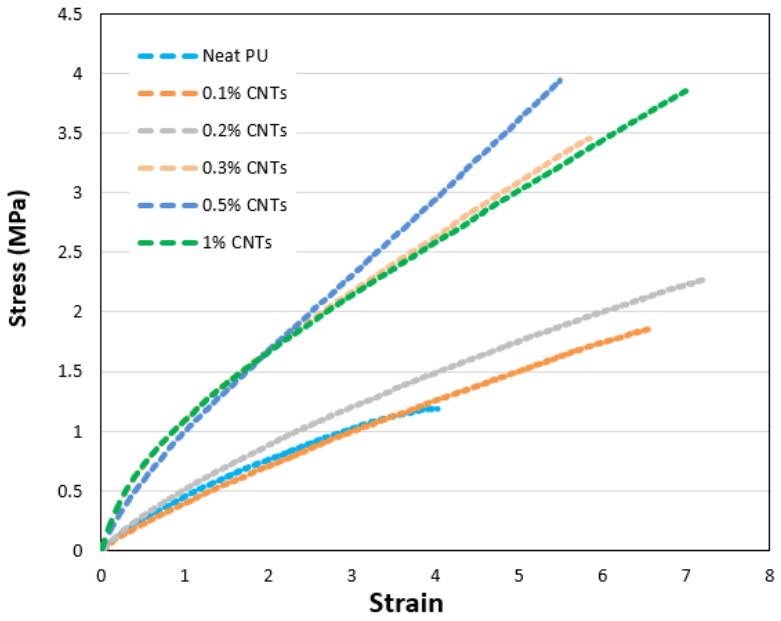

Figure 3-40 Engineering strain-stress for modified PU with different weigh percentage of CNTs at RT and strain rate of $0.05s^{-1}$.

Effect of MWCNTs loading on Young's modulus of PU

Young's modulus, elongation at break, UTS and modulus of toughness of various samples are extracted from strain-stress diagram shown in **Figure 3-40**.

Young's modulus for the modified PU at different CNTs loadings is shown in **Figure 3-41**. The results show that by increasing the loading of CNTs from 0.1 to 0.5wt%, the Young's modulus has increased up to the CNTs loading of 0.5%, and then it decreased at 1% CNT loading. At 0.5wt% loading of CNTs, the Young's modulus of PU is increased by 203%.

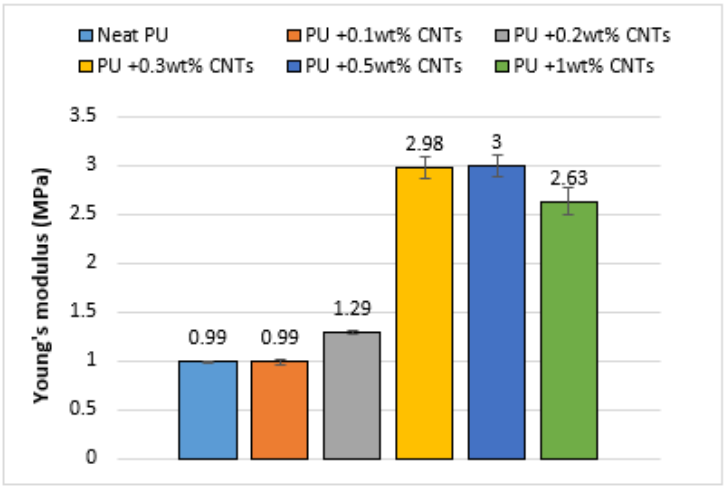

Figure 3-41 Young's modulus of the modified PU with different weight percentage of CNTs.

Effect of MWCNTs loading on elongation at break of PU

The elongation at break for the modified PU at different CNTs loading showed that by increasing CNTs loading from 0.1 to 0.5%, the elongation at break has been increased (**Figure 3-42**). However, by increasing the CNTs loading from 0.5 to 1%, the elongation at break was decreased by 9.3%.

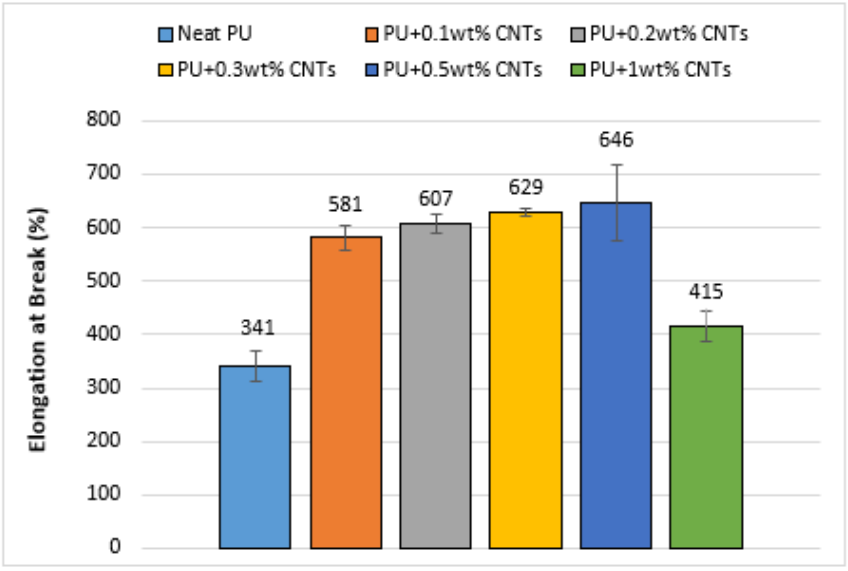

Figure 3-42 Elongation at break of the modified PU with different weight percentage of CNTs.

Effect of MWCNTs loading on UTS of PU

Effect of CNTs loading on the UTS of pure PU is shown in **Figure 3-43**. By increasing CNTs loading from 0.1 to 0.5% the UTs has been increased by 57.4%. Further increase in CNTs to 1wt%, decreased the UTS.

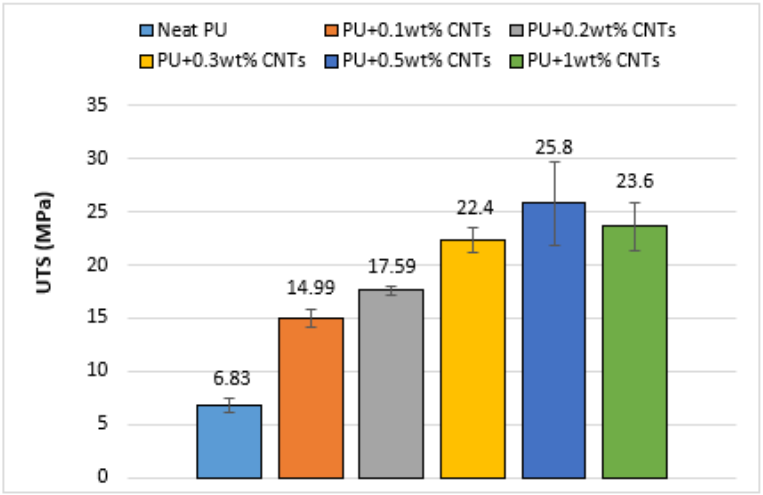

Figure 3-43 Ultimate tensile strength of the modified PU with different weight percentage of CNTs.

Effect of MWCNTs loading on modulus of toughness of PU

Figure 3-44 shows that the modulus of toughness is increased by increasing CNTs loading from 0.1 to 0.5% by 82.6%. However, the modulus of toughness is decreased for CTNs loading of 1wt% by 24.3%.

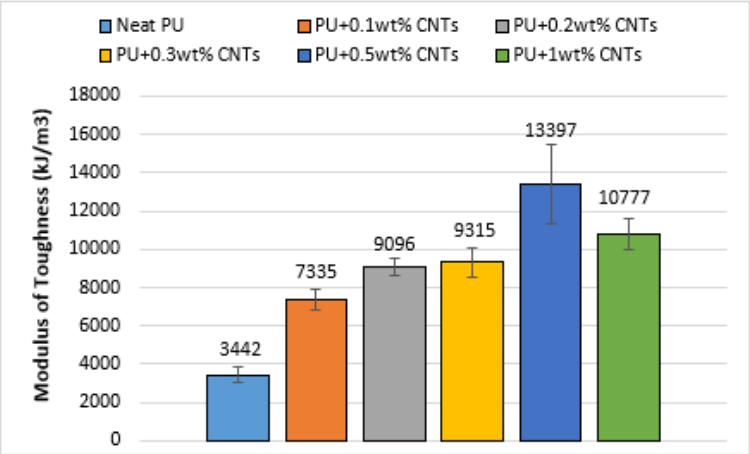

Figure 3-44 Modulus of toughness of the modified PU with different weight percentage of CNTs.

3.7.6.4 Analysing the effect of adding different wt% of GNP-COOH on tensile properties of PU

The PU was modified with 0.1, 0.2, 0.3, 0.5 and 1wt% loading of carboxyl functionalised graphene (GNP-COOH). Tensile tests were carried out at room temperature (25°C) and 0.05s^{-1} strain rate in order to determine the optimum loading of the graphene. The engineering strain-stress results for different GNP loading are shown in **Figure 3-45**. The PU+GNP nanocomposite with GNP loading of 0.5wt% displayed the best performance.

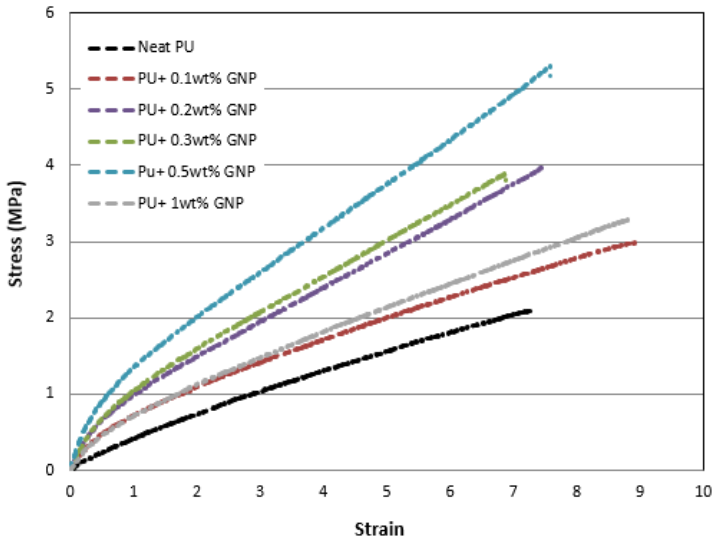

Figure 3-45 Engineering strain-stress of graphene modified PU at various GNP loading at RT and strain rate of 0.05s^{-1}.

Table 3-7 Summary of the tensile properties of the GNP-COOH modified PU.

Table 3-7 Tensile properties of the modified PU with different weight percentage of GNP-COOH.

Specimen Code	**Young's modulus (MPa)**		**UTS (MPa)**		**EL (%)**		**T (kJ/m^3)**	
	Tests	Average	Tests	Average	Tests	Average	Tests	Average
PU+ 0.1 wt% GNP-COOH-RPM8-D18-1	1.95	1.86 ±0.05	29.52	26.41 ±2.71	792	736 ±54	15869	13979 ±1499
PU+ 0.1 wt% GNP-COOH-RPM8-D18-2	1.82		23.91		689		12657	
PU+ 0.1 wt% GNP-COOH-RPM8-D18-3	1.84		24.44		697		12854	
PU+ 0.1 wt% GNP-COOH-RPM8-D18-4	1.89		30.76		829		16244	
PU+ 0.1 wt% GNP-COOH-RPM8-D18-5	1.81		23.41		677		12273	
PU+ 0.2 wt% GNP-COOH-RPM8-D18-1	2.91	2.73 ±0.14	30.35	32.72 ±2.24	645	651 ±33	15761	16468 ±927
PU+ 0.2 wt% GNP-COOH-RPM8-D18-2	2.84		30.04		723		15403	
PU+ 0.2 wt% GNP-COOH-RPM8-D18-3	2.81		35.84		617		17912	
PU+ 0.2 wt% GNP-COOH-RPM8-D18-4	2.53		31.67		638		15678	
PU+ 0.2 wt% GNP-COOH-RPM8-D18-5	2.54		35.7		632		17586	
PU+ 0.3 wt% GNP-COOH-RPM8-D18-1	2.93	2.95 ±0.02	33.51	35.13 ±3.34	580	616 ±28	16678	17361 ±1590
PU+ 0.3 wt% GNP-COOH-RPM8-D18-2	2.95		42.01		589		20696	
PU+ 0.3 wt% GNP-COOH-RPM8-D18-3	2.97		30.39		647		15183	
PU+ 0.3 wt% GNP-COOH-RPM8-D18-4	2.92		34.92		603		17215	
PU+ 0.3 wt% GNP-COOH-RPM8-D18-5	2.98		34.8		661		17037	
PU+ 0.5 wt% GNP-COOH-RPM8-D18-1	3.32	3.72 ±0.25	36	38.60 ±3.58	585	599 ±36	18703	19741 ±1832
PU+ 0.5 wt% GNP-COOH-RPM8-D18-2	4.1		44		659		22858	
PU+ 0.5 wt% GNP-COOH-RPM8-D18-3	3.95		34		550		17460	
PU+ 0.5 wt% GNP-COOH-RPM8-D18-4	3.54		36		568		18134	

PU+ 0.5 wt% GNP-COOH-RPM8-D18-5	3.68		43		635		21550	
PU+ 1 wt% GNP-COOH-RPM8-D18-1	2.09	2.04 ±0.04	32.13	31.34 ±2.03	780	773 ±28	16619	16112 ±1015
PU+ 1 wt% GNP-COOH-RPM8-D18-2	2.01		31.81		775		16274	
PU+ 1 wt% GNP-COOH-RPM8-D18-3	2.09		28.47		738		14896	
PU+ 1 wt% GNP-COOH-RPM8-D18-4	1.96		29.29		746		14838	
PU+ 1 wt% GNP-COOH-RPM8-D18-5	2.05		35.01		828		17933	

Effect of GNP-COOH loading on Young's modulus of PU

Figure 3-46 shows the highest Young's modulus of PU nanocomposite is obtained at 0.5wt% loading of GNP. The Young's modulus is increased by 76% relative to neat PU.

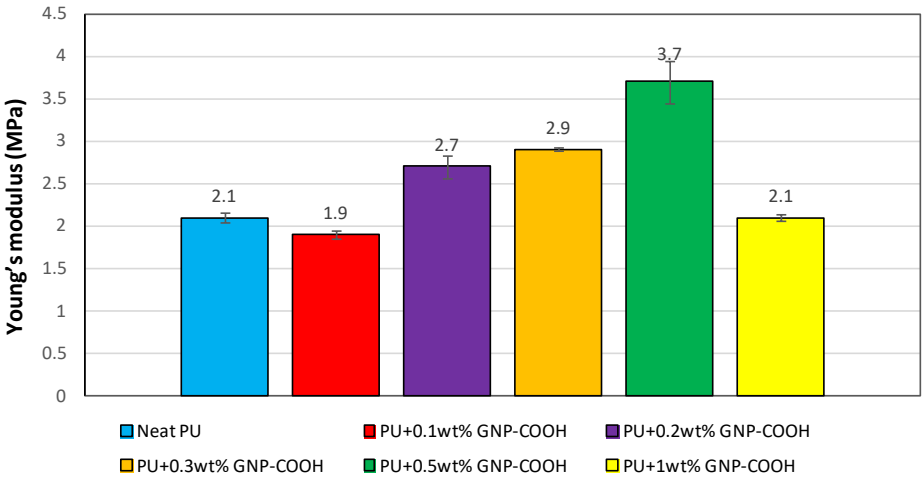

Figure 3-46 Young's modulus of the neat PU, and f-GNP modified PU.

Effect of GNP-COOH loading on elongation at break of PU

Figure 3-47 shows the effect of GNP loading on elongation at break. The highest increase of 11.7% in elongation at break was achieved at 0.1wt% loading of GNP and it was decreased by 9.1% relative to neat PU at loading of 0.5wt% GNP.

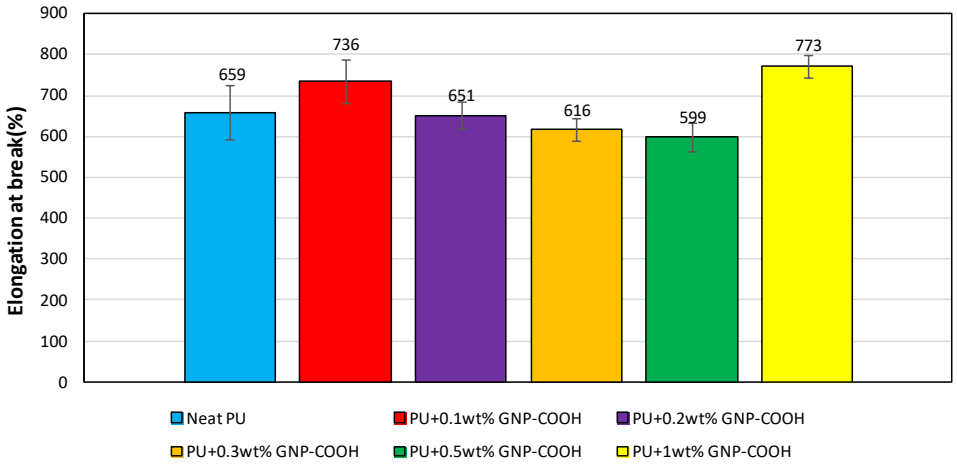

Figure 3-47 Percentage of elongation at break of the neat PU, and f-GNP modified PU.

Effect of GNP-COOH loading on UTS of PU

Ultimate tensile strength is one of the main properties that affect the erosion resistance of a coating. It can be seen from **Figure 3-48** that at 0.5wt% GNP loading to the neat PU the UTS was increased by 76.7% relative to neat PU.

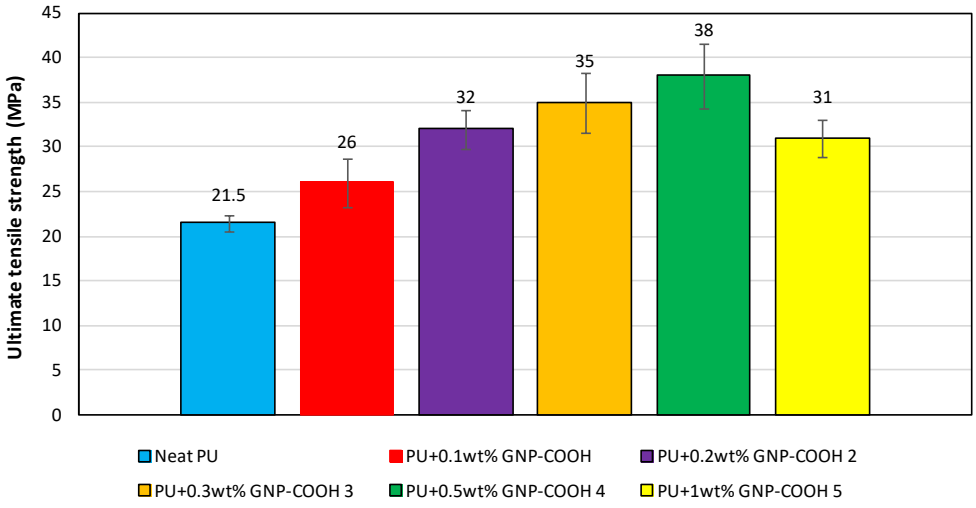

Figure 3-48 Ultimate tensile strength of the neat PU, and f-GNP modified PU.

Effect of GNP-COOH loading on modulus of toughness of PU

The modulus of toughness was also increased by addition of graphene nanoparticles to the neat PU. **Figure 3-49** shows that at 0.5wt% loading of the carboxyl functionalised GNP, the modulus of toughness is increased by 91.6%.

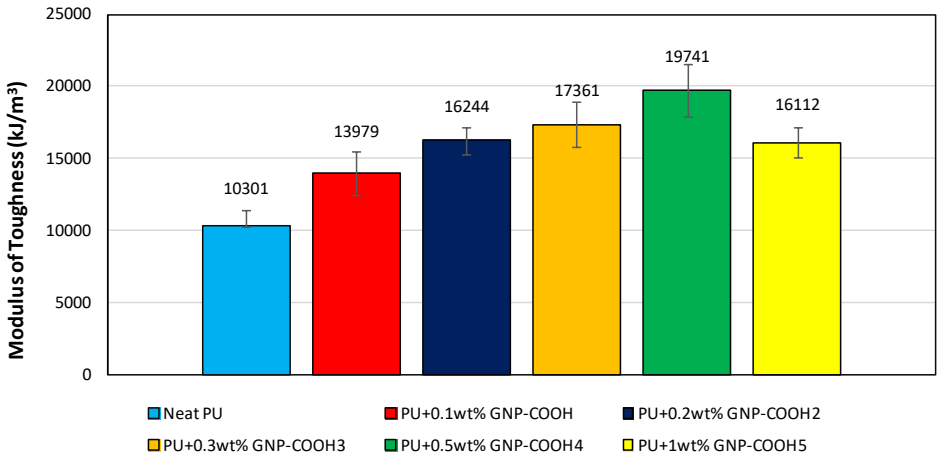

Figure 3-49 Modulus of toughness of the neat PU, and f-GNP modified PU.

3.7.6.5 Analysing the effect of adding hybrid GNP + CNTs on tensile properties of PU

The neat PU was also modified with the mixture of carboxyl functionalised GNP and CNTs. Tensile tests were carried out to analyse the effect of nano-additive materials on the tensile properties of the PU. **Table 3-8** summarise the tensile properties of the hybrid GNP-COOH and CNTs with loading of 0.25wt% GNP-COOH + 0.25wt% CNTs on PU.

Table 3-8 Tensile properties of the modified PU with 0.25wt% GNP-COOH + 0.25wt% CNTs.

Specimen Code	**Young's modulus (MPa)**		**UTS (MPa)**		**EL (%)**		**T (kJ/m³)**	
	Tests	Average	Tests	Average	Tests	Average	Tests	Average
PU+ 0.25wt% GNP-COOH + 0.25wt% CNTs-1	4.2	4.25 ±0.09	23.4	26.28 ±3.19	596	651 ±61	12211	13858 ±1768
PU+ 0.25wt% GNP-COOH + 0.25wt% CNTs-2	4.33		21		544		10818	
PU+ 0.25wt% GNP-COOH + 0.25wt% CNTs-3	4.37		27		685		14843	
PU+ 0.25wt% GNP-COOH + 0.25wt% CNTs-4	4.29		31		730		16243	
PU+ 0.25wt% GNP-COOH + 0.25wt% CNTs-5	4.07		29		698		15173	

Effect of adding hybrid GNP + CNTs on Young's modulus of PU

Figure 3-50 shows the mixture of 0.25wt% GNP-COOH + 0.25wt% CNTs increased the Young's modulus by 104%.

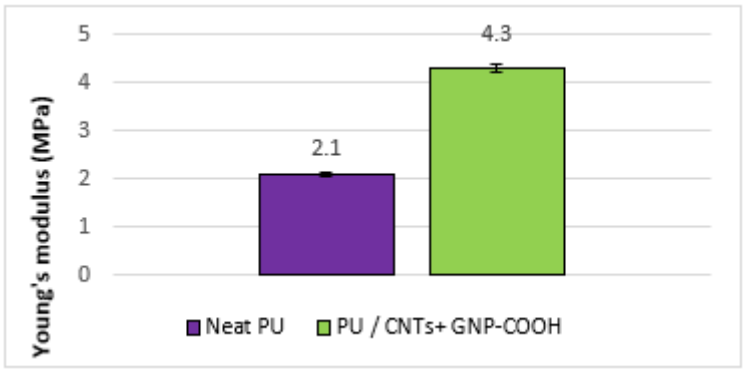

Figure 3-50 Young's modulus of the neat PU and 0.25 wt% GNP-COOH + 0.25 wt% CNTs modified PU.

Effect of adding hybrid GNP + CNTs on elongation at break of PU

The highest percentage of elongation at break is for the pure PU. Adding the 0.25wt% GNP-COOH + 0.25wt% CNTs to the PU decreased the percentage of elongation at break by 1.2 % which is within the experimental variation (**Figure 3-51**).

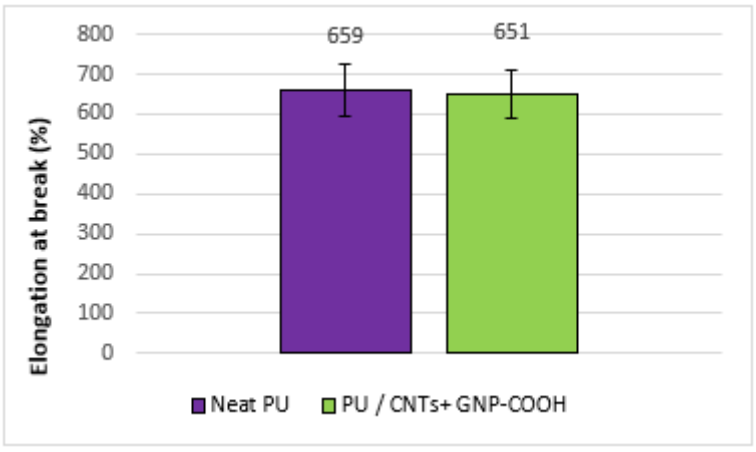

Figure 3-51 Percentage of elongation of the neat PU and 0.25wt% GNP-COOH + 0.25wt% CNTs modified PU.

Effect of adding hybrid GNP + CNTs on UTS of PU

Figure 3-52 shows that adding 0.25wt% GNP-COOH + 0.25wt% CNTs to the neat PU increased the UTS by 17.3%.

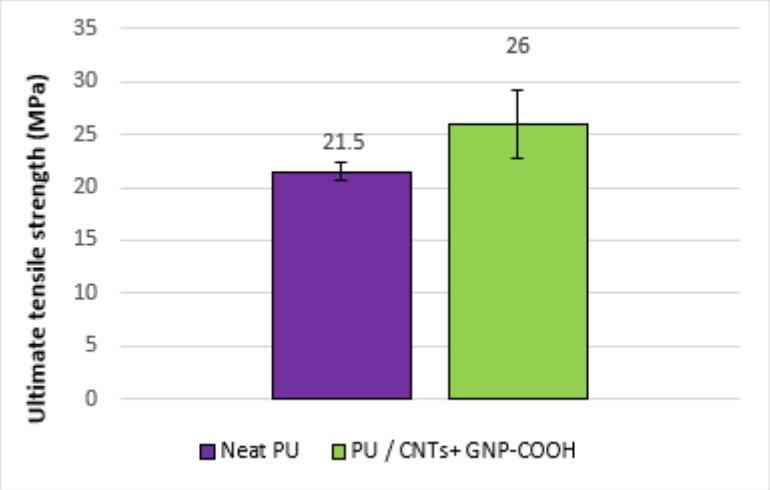

Figure 3-52 Ultimate tensile strength of the neat PU and GNP-COOH + CNTs modified PU.

Effect of adding hybrid GNP + CNTs on modulus of toughness of PU

The results of tensile test show that adding 0.25wt% GNP-COOH + 0.25wt% CNTs to the pure PU increase the modulus of toughness by 34.5% (**Figure 3-53**).

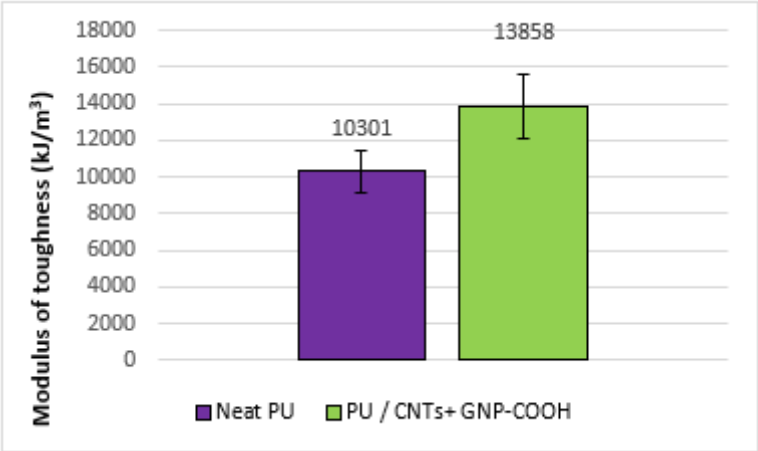

Figure 3-53 Modulus of toughness of the neat PU and GNP-COOH + CNTs modified PU.

3.7.6.6 Analysing the effect of adding different loading of hydrophobic silica-based sol-gel on tensile properties of PU and PU + GNP

The effect of adding hydrophobic silica-based sol-gel to PU and PU+GNP matrices on the materials' tensile mechanical properties was investigated. Four different set of specimens were manufactured:

- 1wt% SG+PU
- 2.5wt% SG+PU
- 1wt% SG+0.5wt% GNP+PU
- 2.5wt% SG+0.5wt% GNP+PU

The results of %EL, UTS, modulus of toughness and Young's modulus are summarised in Table 3-9.

Table 3-9 Tensile properties of modified PU with SG and GNP.

Sample	**%EL**		**UTS (MPa)**		**T (kJ/m^3)**		**E (MPa)**	
	Test	Average	Test	Average	Test	Average	Test	Average
1wt% SG+PU-1	222	254 ±31	21.17	24.11 ±3.39	9668	11773 ±1692	6.03	5.97 ±0.09
1wt% SG+PU-2	280		27.42		12713		6.02	
1wt% SG+PU-3	311		30.03		14135		6.09	
1wt% SG+PU-4	221		20.45		9301		5.82	
1wt% SG+PU-5	236		21.47		13048		5.89	
2.5wt% SG+PU-1	404	405 ±21	10.68	11.18 ±0.49	6060	6574 ±509	2.08	2.29 ±0.10
2.5wt% SG+PU-2	424		11.49		7029		2.35	
2.5wt% SG+PU-3	375		10.6		5994		2.29	
2.5wt% SG+PU-4	386		11.01		6315		2.35	
2.5wt% SG+PU-5	440		12.12		7476		2.41	
1wt% SG+0.5wt% GNP+PU-1	450	540 ±71	65.55	46.54 ±11.48	22996	23054 ±2376	4.22	4.1 ±0.11
1wt% SG+0.5wt% GNP+PU-2	658		46.72		23454		4.03	
1wt% SG+0.5wt% GNP+PU-3	492		32.62		20059		4.13	
1wt% SG+0.5wt% GNP+PU-4	486		31.89		20912		3.89	
1wt% SG+0.5wt% GNP+PU-5	617		55.91		27853		4.23	
2.5wt% SG+0.5wt% GNP+PU-1	186	241 ±40	4.3	4.81 ±0.49	2274	2668 ±444	1.84	1.85 ±0.03
2.5wt% SG+0.5wt% GNP+PU-2	297		5.9		3654		1.91	
2.5wt% SG+0.5wt% GNP+PU-3	219		4.7		2598		1.82	
2.5wt% SG+0.5wt% GNP+PU-4	209		4.7		2493		1.81	
2.5wt% SG+0.5wt% GNP+PU-5	292		4.45		2323		1.89	

Effect of sol-gel loading on Young's modulus of PU and PU +GNP

Figure 3-54 shows the variation in Young's modulus for the PU nanocomposites. The highest Young's modulus was shown by the PU modified with 1wt% SG and the next highest being for the PU modified with 0.5wt% GNP+1wt% SG. It can be seen that increasing the wt% of SG from 1% to 2.5% adversely affected the PU+GNP+SG nanocomposite indicated by a significant reduction in the Young's modulus.

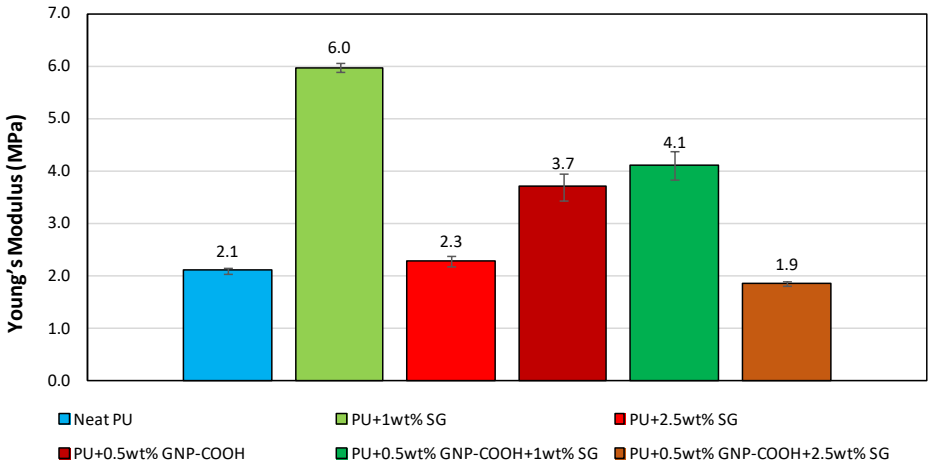

Figure 3-54 Young's modulus of neat PU, PU+SG and PU+GNP+SG.

Effect of sol-gel loading on elongation at break of PU and PU +GNP

The effect of sol-gel loading on elongation at break of neat PU and PU+GNP is shown in **Figure 3-55**. It can be seen that adding the SG to the neat PU decreases the elongation at break. The greatest elongation at break is obtained for the neat PU and the lowest one is for the PU+0.5wt% GNP+2.5wt%SG.

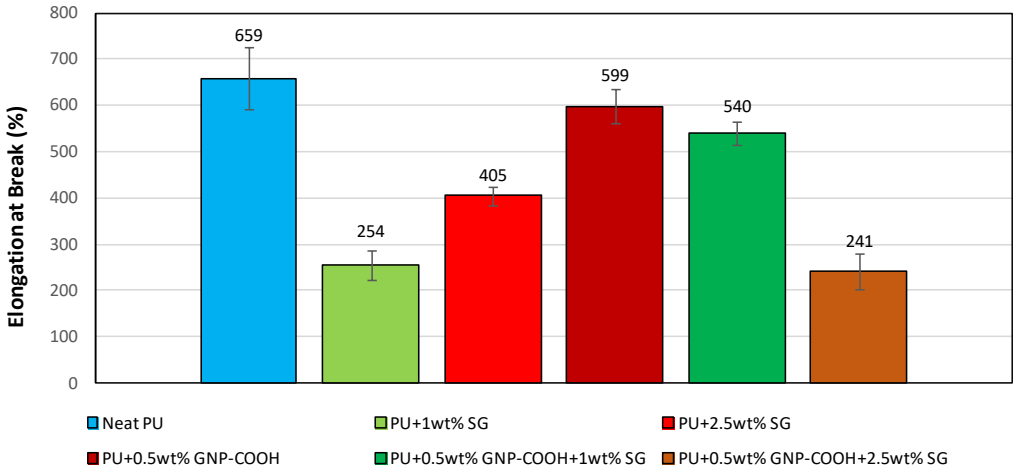

Figure 3-55 Elongation at break of neat PU, PU+SG and PU+GNP+SG.

Effect of sol-gel loading on UTS of PU and PU +GNP

The effect of sol-gel loading on the UTS of neat PU and GNP modified PU is shown in **Figure 3-56**. Addition of 1wt% SG loading to the neat PU and modified PU+GNP resulted in an increase in the UTS of the PU; but by further increasing the SG loading to 2.5wt% the UTS was decreased for both pure PU and modified PU+GNP nanocomposite.

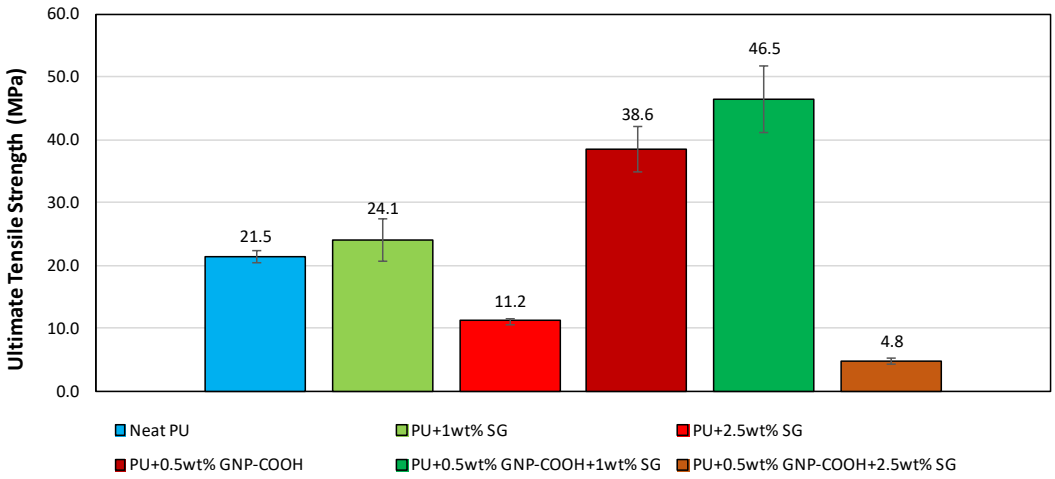

Figure 3-56 Ultimate tensile strength of neat PU, PU+SG and PU+GNP+SG.

Effect of sol-gel loading on modulus of toughness of PU and PU +GNP

The effect of sol-gel loading on the modulus of toughness of neat PU and modified PU+GNP nanocomposite is shown in **Figure 3-57**. At 1wt% SG loading, the modulus of toughness increased for both the neat PU and the PU+GNP nanocomposite. However, by increasing the SG loading to 2.5wt%, the modulus of toughness was decreased for neat PU and the PU+GNP.

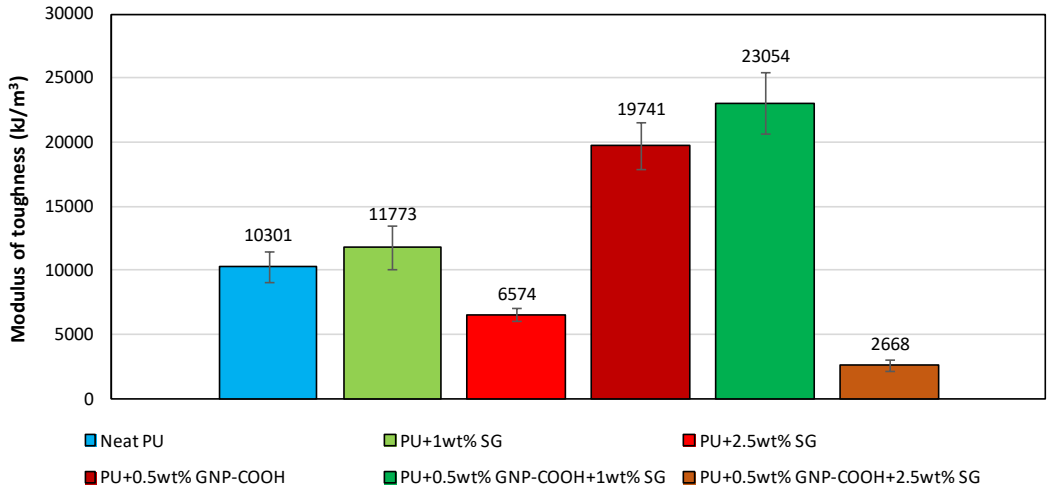

Figure 3-57 Modulus of toughness of neat PU, PU+SG and PU+GNP+SG.

3.7.6.7 Summary of tensile test results

From tensile testing results it was found that by increasing the temperature, the Young's modulus, UTS, elongation at break and modulus of toughness of the neat PU at all strain rate were decreased. In addition, by increasing the strain rate, the Young's modulus, UTS, elongation at break and modulus of toughness at different temperatures were increased. Also optimum mixing procedure of CNPs was established; 8000 rpm for 18 minutes. This mixing procedure resulted in the highest amount of UTS, modulus of toughness and second highest elongation at break and Young's modulus of CNP modified PU. The best mechanical properties of PU are achieved for 0.5wt% carboxyl functionalised GNP loading and a 1wt% SG loading. Young's modulus, UTS, elongation at break and modulus of toughness for pure PU, GNP modified PU, and SG modified PU+GNP are summarised in **Table 3-10**.

Table 3-10 Tensile properties of the neat PU, 0.5wt% GNP modified PU, and 0.5wt% GNP+1wt% SG modified PU.

Properties	**Neat PU**	**PU+GNP**	**PU+GNP+SG**
Young's modulus (MPa)	2.10±0.05	3.7±0.3	4.1±0.1
%EL	659±66	599±36	540±71
UTS (MPa)	21.5±0.9	38.0±3.6	46.5±11.5
Modulus of Toughness (kJ/m^3)	10301±1158	19741±1832	23054±2376

3.7.7 Compression tests results

The compression tests were carried out using Zwick/Roell universal machine fitted with a 25kN load cell. An extensometer was used to eliminate the machine error for recording the displacement of the samples [160]. To connect the extensometer to the machine, a fixture was designed and manufactured as shown in **Figure 3-58**. For the compression tests, the crosshead speed was set at 2.1, 10.5 and 21mm/min (equivalent to strain rate of 0.01, 0.05 and $0.1s^{-1}$) and at each strain rate, uniaxial compression tests were performed at three different temperatures 25°C, 50°C and 70°C using in-situ heating chamber (**Figure 3-58**). For each case three specimens were tested (**Table 3-11 and Figure 3-13**).

Figure 3-58 Universal test machine with special compression test fixture.

The specimens are coded based on strain rate (SR), temperature (T), and sample number (1 to 3). The list of tested specimens is summarised in **Table 3-11**.

Table 3-11 Uniaxial compression test conditions and specimen's numbers.

Temperature	**Strain rate $\dot{\varepsilon}$ (s^{-1})**	**Specimen Code**
25°C	0.01	PU-SR0.01-T25- 1 to 3
		PU/GNP-SR0.01-T25- 1 to 3
		PU/GNP/SG-SR0.01-T25- 1 to 3
	0.05	PU-SR0.05-T25- 1 to 3
		PU/GNP-SR0.05-T25- 1 to 3
		PU/GNP/SG-SR0.05-T25- 1 to 3
	0.1	PU-SR0.1-T25- 1 to 3
		PU/GNP-SR0.1-T25- 1 to 3
		PU/GNP/SG-SR0.1-T25- 1 to 3
50°C	0.01	PU-SR0.01-T50- 1 to 3
		PU/GNP-SR0.01-T50- 1 to 3
		PU/GNP/SG-SR0.01-T50- 1 to 3
	0.05	PU-SR0.05-T50- 1 to 3
		PU/GNP-SR0.05-T50- 1 to 3
		PU/GNP/SG-SR0.05-T50- 1 to 3
	0.1	PU-SR0.1-T50- 1 to 3
		PU/GNP-SR0.1-T50- 1 to 3
		PU/GNP/SG-SR0.1-T50- 1 to 3
70°C	0.01	PU-SR0.01-T70- 1 to3
		PU/GNP-SR0.01-T70- 1 to 3
		PU/GNP/SG-SR0.01-T70- 1 to 3
	0.05	PU-SR0.05-T70- 1 to 3
		PU/GNP-SR0.05-T70- 1 to 3
		PU/GNP/SG-SR0.05-T70- 1 to 3
	0.1	PU-SR0.1-T70- 1 to 3
		PU/GNP-SR0.1-T70- 1 to 3
		PU/GNP/SG-SR0.1-T70- 1 to 3

3.7.7.1 Monotonic compression tests of neat PU, PU+GNP and PU+GNP+SG

Monotonic compression tests were performed on neat PU, PU+GNP and PU+GNP+SG nanocomposites at 25°C, 50°C and 75°C for three different strain rates.

Uniaxial compression tests result for PU, PU+GNP and PU+GNP+SG at 25°C and for three strain rates are shown in **Figure 3-59 (a)**, **Figure 3-59 (c)** and **Figure 3-59 (e)**, respectively. The results indicate that neat PU has minimal strain rate dependency at room temperature, and the mechanical properties are only slightly affected by changing the strain rate. However, at higher temperature, the compressive behaviour of neat PU was affected as shown in **Figure 3-59 (b)**. The PU+GNP has a slight strain rate dependency at room temperature and at higher temperature, the compressive behaviour of PU+GNP was substantially affected as shown in **Figure 3-59 (d)**. Similar to PU, PU+GNP+SG has a slight strain rate dependency at room temperature but it is strongly affected by increasing the temperature as shown in **Figure 3-59(f)**.

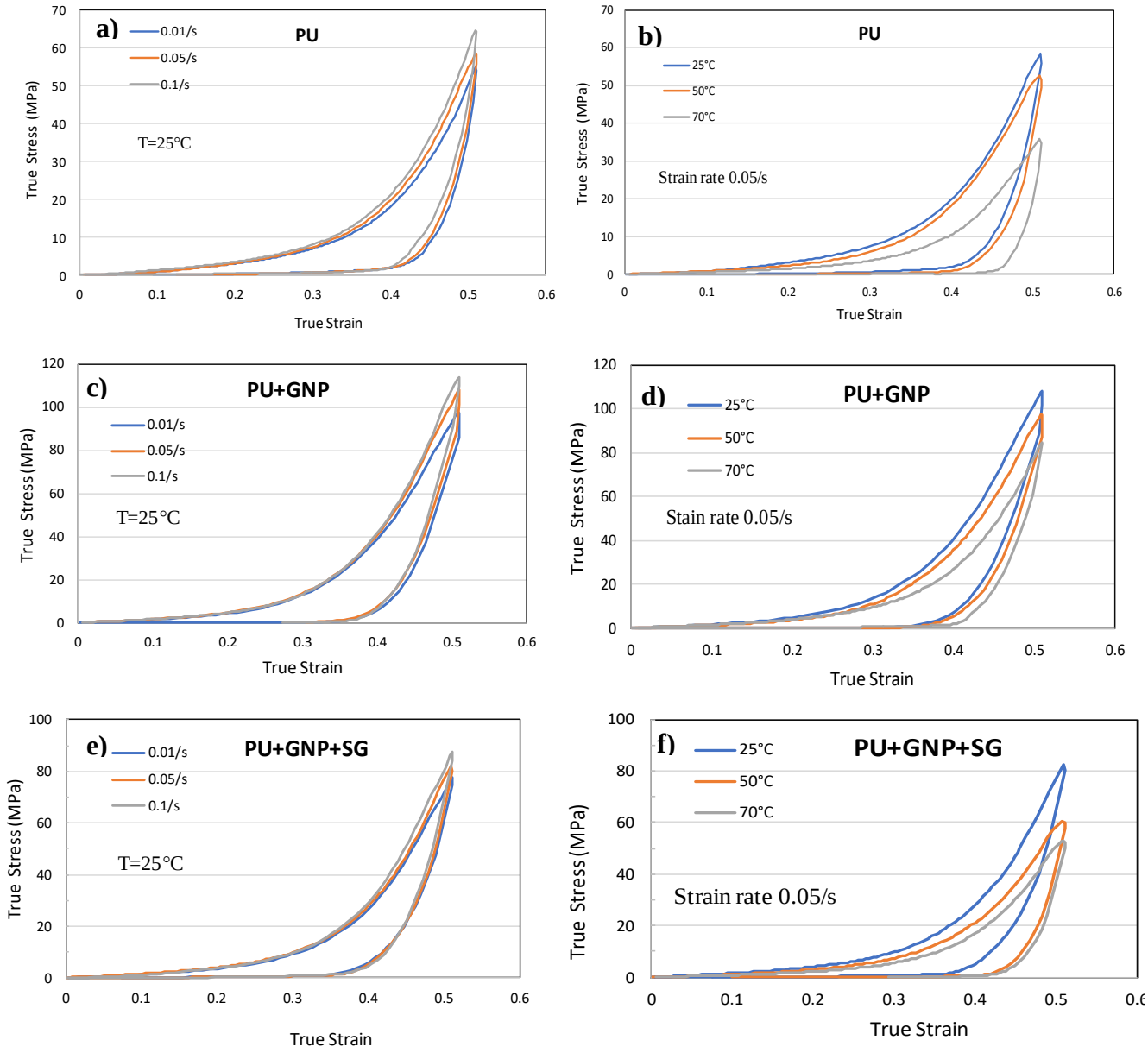

Figure 3-59 True strain-stress at strain rate of 0.01, 0.05 and 0.01s^{-1} at temperature of 25°C, and at strain rate of 0.05s^{-1} at 25°C, 50°C and 70°C for (a, b) neat PU, (c, d) PU+GNP and (e, f) PU+GNP+SG, respectively.

The effects of temperature and strain rate on the values of residual strain (ε^r), compressive strength and energy absorption of neat PU, PU+GNP and PU+GNP+SG in monotonic compressive loading are extracted from **Figure 3-59** are shown in **Figure 3-60**. At a fixed strain rate, an increase in the temperature caused a significant increase in the residual strain for PU. However, the effect of strain rate at the higher temperature of 70°C was less. The change in the compressive strength with increasing strain rate is small and it decreases with increasing temperature. Finally, energy absorption was calculated by measuring the area under the stress-strain curve in the compression test, and as shown in **Figure 3-60** at higher temperature the

energy absorption of neat PU decreases. For PU+GNP material, increasing the temperature at a fixed strain rate; resulted in an increase in residual strain and decreases in the compressive strength and energy absorption. PU+GNP+SG material shows a similar pattern to those seen for PU+GNP material.

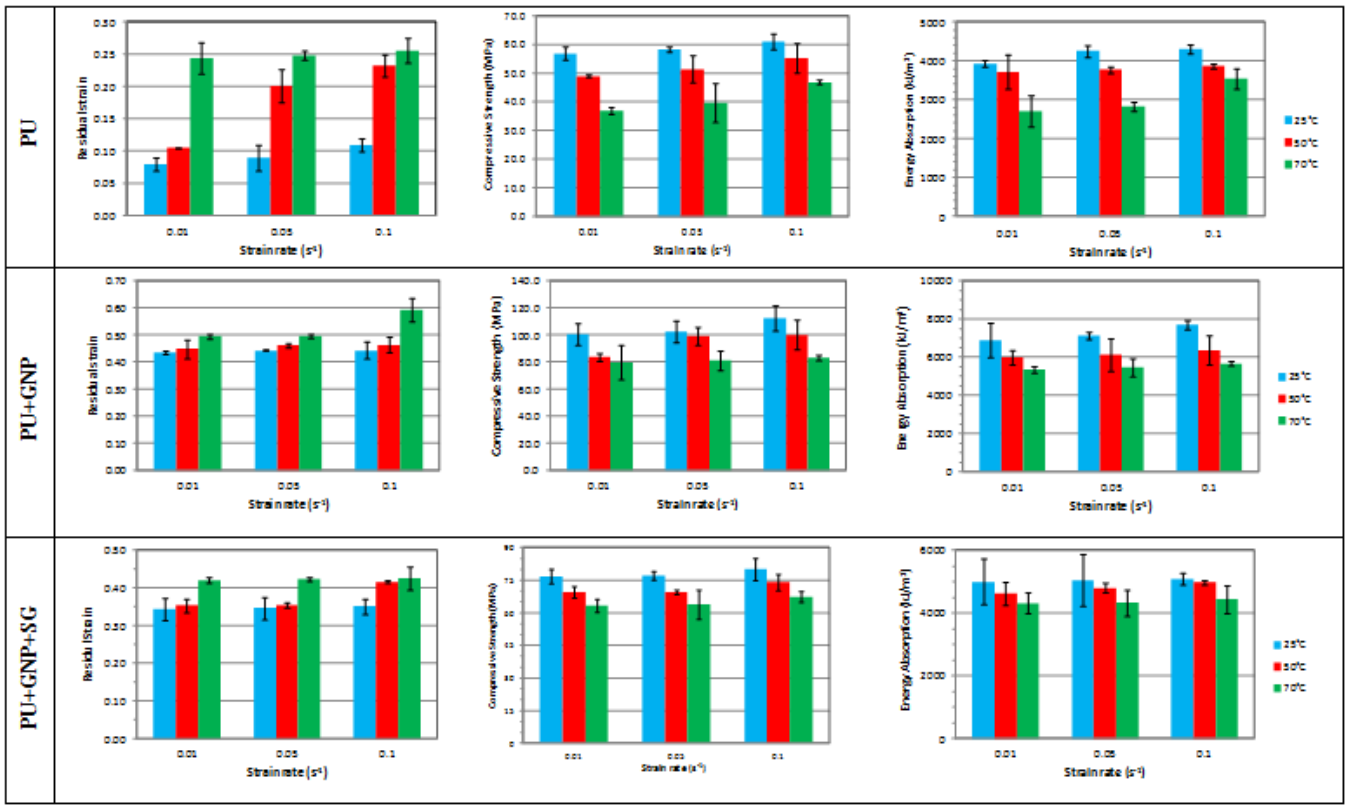

Figure 3-60 Residual strain, compressive strength and energy absorption of the neat PU (top row), PU+GNP (middle row) and PU+GNP+SG (bottom row) versus strain rate at three different temperatures.

3.7.7.2 Cyclic compression test

In this section, the result of true stress-true strain behaviour during cyclic compression loading-unloading tests for maximum strain ε_{max}=0.3 and ε_{max}=0.5 and at strain rate of $\dot{\varepsilon}$ =0.1s^{-1} at 25° are presented. Cyclic compression tests were performed up to five cycles (N=5) for each sample.

The compressive true stress-true strain behaviour of neat PU with ε_{max} = 0.5 and $\dot{\varepsilon}$ = 0.1s^{-1} is shown in **Figure 3-61(a)** and for PU+GNP with ε_{max} = 0.5 and $\dot{\varepsilon}$ = 0.1s^{-1} is shown in **Figure 3-61(b)** and for PU+GNP+SG with ε_{max} = 0.5 and $\dot{\varepsilon}$= 0.1s^{-1} is shown in **Figure 3-61(c)** and with ε_{max} = 0.3 and $\dot{\varepsilon}$= 0.1s^{-1} is shown in **Figure 3-61(d)**.

Residual strain at the end of cycles, compressive strength and energy absorption values for PU, PU+GNP and PU+GNP+SG are extracted from the cyclic stress-strain diagrams, and they are summarised in Table 3-12.

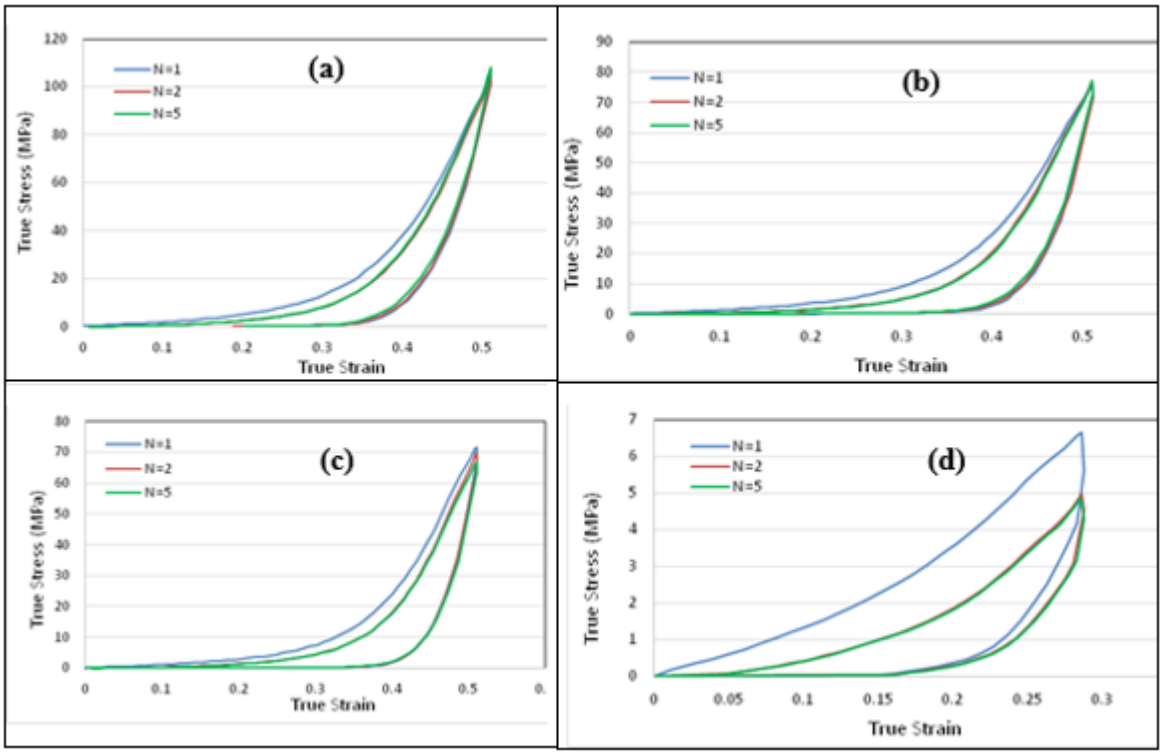

Figure 3-61 True stress-strain results of cyclic compression loading-unloading at $\dot{\boldsymbol{\varepsilon}} = 0.1s^{-1}$ for (a) neat PU at $\varepsilon_{max} = 0.5$, (b) PU+GNP at $\varepsilon_{max} = 0.5$, (c) PU+GNP+SG at $\varepsilon_{max} = 0.5$ and (d) PU+GNP+SG at $\varepsilon_{max} = 0.3$, respectively at RT.

The compressive cyclic loading tests show that the stress-strain curve in the second cycle is far more compliant than that observed in the first cycle, which explains the softening behaviour of all three coating materials after cyclic loading. In addition, the stress-strain behaviours for all three coatings are stabilized after the first cycle. At a maximum strain of 0.5, the stress magnitude reaches a maximum in the first cycle. The unloading paths after a given strain are the same for all coatings and follow the same curve independent of the cycle number, Appendix A.3.

Table 3-12 Results of the cyclic compression test on PU, PU+GNP and PU+GNP+SG at strain rate $\dot{\varepsilon} = 0.1s^{-1}$.

Material	Maximum applied strain	Cycle (N)	Residual Strain ε^r	Compressive Strength (MPa)	Energy Absorption (kJ/m^3)
PU	$\varepsilon_{max} = 0.5$	1	0.341	104.8	6040
		2	0.339	105.2	4167
		5	0.326	107.9	3980
	$\varepsilon_{max} = 0.3$	1	0.205	11.1	708
		2	0.213	9.8	423
		5	0.216	8.6	389
PU+GNP	$\varepsilon_{max} = 0.5$	1	0.385	75.9	5014
		2	0.364	76.2	3594
		5	0.358	77.4	3256
	$\varepsilon_{max} = 0.3$	1	0.224	7.9	333
		2	0.229	6.5	282
		5	0.237	6.2	281
PU+GNP+SG	$\varepsilon_{max} = 0.5$	1	0.392	71.5	4759
		2	0.387	69.7	3310
		5	0.382	66.6	3344
	$\varepsilon_{max} = 0.3$	1	0.236	6.6	572
		2	0.242	5.0	270
		5	0.245	4.9	266

Finally, the energy absorption of neat PU is greater than PU+GNP and PU+GNP+SG for all cyclic compression tests are summarised in **Figure 3-62**. It is noticeable that at the maximum strain, while the maximum stress attained for PU is 107.9 MPa, for PU+GNP it is 77.4 MPa and for PU+GNP+SG it is 71.5 MPa. Hence, PU+GNP+SG was experiencing the least stresses during cyclic compressive loading. In **Chapter 5**, the erosion performance of these three coating under repeated rubber ball impact were investigated and the longevity of PU+GNP+SG was demonstrated which is partly due to experiencing lower compression stress during repeated impact [161]**.**

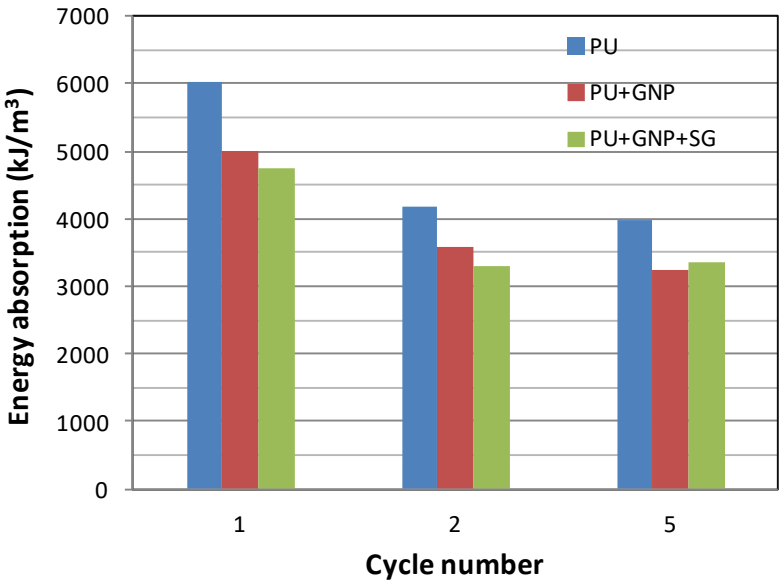

Figure 3-62 Comparison of energy absorption of PU, PU+GNP and PU+GNP+SG at ε_{max} = 0.5 and $\dot{\varepsilon}$ = 0.1 s^{-1} in cyclic compression tests.

3.7.8 Hardness tests results

As can be seen in the **Figure 3-63**, adding 0.5wt% of GNP-COOH increased the hardness of neat PU by 84% and adding 1wt%SG+0.5wt%GNP-COOH increased the hardness of neat PU by85 % from 9.88 to 18.34. This is a good sign of enhancing the rain erosion resistance of the PU; Higher hardness will show higher degree of crosslinking which means higher mechanical stability. This is important to avoid crack initiations in the layer and also crack growth [162].

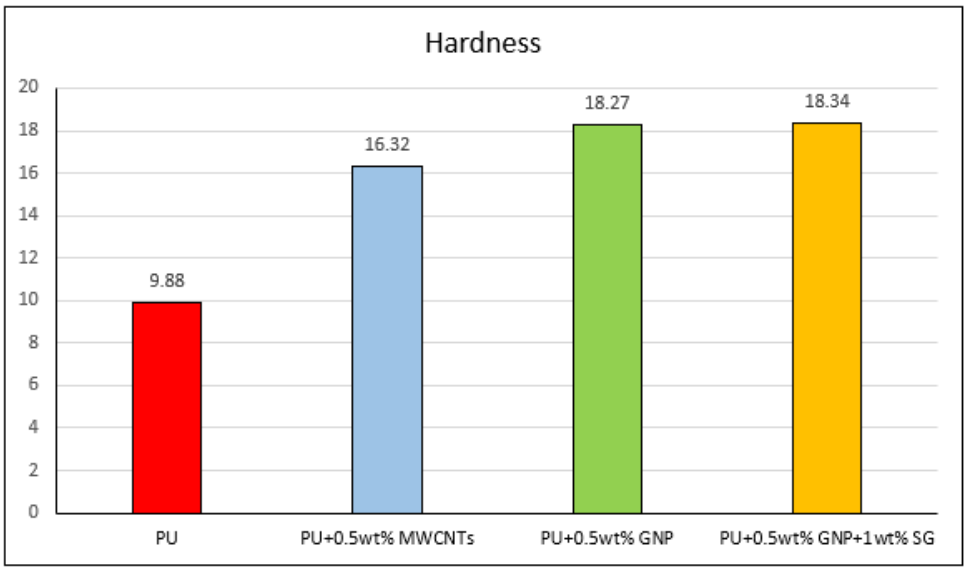

Figure 3-63 Hardness test were carried out using a Durometer 0-100 HA. Samples dimension of 5×5×5mm.

3.7.9 Tearing tests results

The results of the tearing tests on neat PU are shown in **Figure 3-64** (a). All three specimens show similar behaviour during the test. For all three specimens in the first 35mm of elongation, the force was monotonically increased until the start of tearing, then crack growth occurred and the force decreased until the specimens completely tore into two pieces. Between displacements of 35 to 45mm, when crack growth occurred, there are slight differences in the behaviour of the specimens due to difference in the crack paths. The cracks tend to follow different preferred crack directions and they find the lowest resistance path for crack propagation [163]. There were small fluctuations in the force during tearing tests. These variations are not noises from the instrument but rather caused by the stick-slip behaviour observed during fracture in the PU as can be seen in the inset of **Figure 3-64** (a). During stick-slip, the minimum force occurs when the crack extends, and the maximum represents crack arrest. The interval of these fluctuations relates to the morphology and micro mechanism of the polymer material, such as the polymer chain alignment, arrangement and distribution of crystalline [163].

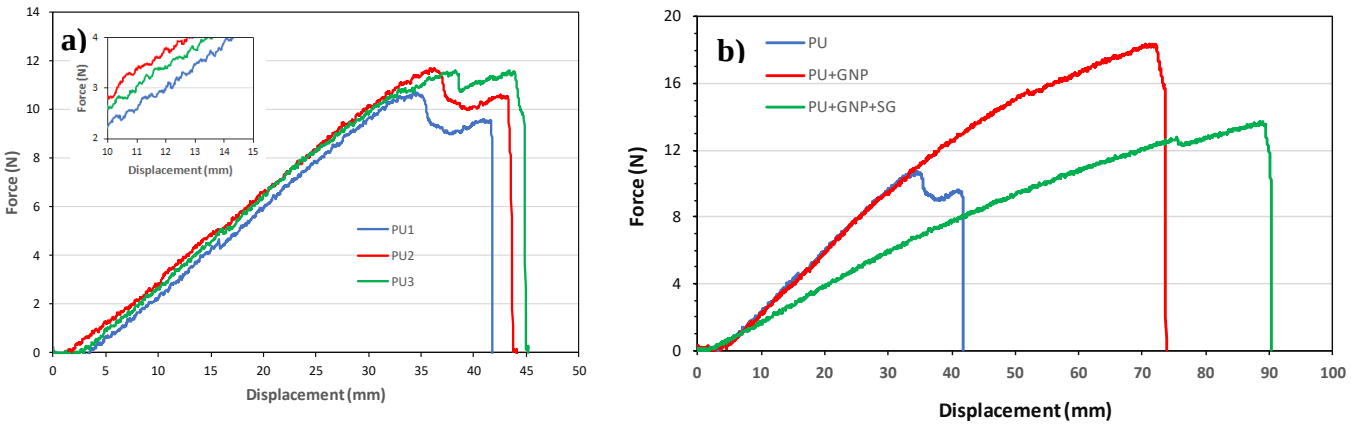

Figure 3-64 Tearing tests results of (a) three neat PU specimens (inset showing stick-slip), and (b) the PU, PU+GNP and PU+GNP+SG materials.

The results of the tearing tests of PU, PU+GNP and PU+GNP+SG are compared in **Figure 3-64(b)**. On average the tearing strength of PU+GNP material is 45% higher and its elongation at break 55% higher than neat PU values. Also on average, the tearing strength of PU+GNP+SG material is 12%, higher than neat PU but 30% less than PU+GNP. PU+GNP+SG elongation at break is 102% higher than neat PU value, and 31% more than for PU+GNP. The tearing energy of PU+GNP nanocomposites is 137% higher than the neat PU and for PU+GNP+SG it is 148% higher than neat PU and 4.4% more than PU+GNP. A summary of the tearing tests results for

the PU and its two nanocomposites together with 95% confidence levels are presented in **Table 3-13**.

Table 3-13 Results of tearing test of neat PU, and PU+GNP and PU+GNP+SG nanocomposites.

Coating material	Ts (kN/m)	Elongation at break (mm)	Tearing Energy (J)
PU	5.81± 0.03	44.3 ± 0.7	0.285 ± 0.016
PU+GNP	8.45± 0.88	68.5 ± 4.2	0.677 ± 0.081
PU+GNP+SG	6.51± 0.26	89.7 ± 5.3	0.707 ± 0.045

3.7.10 Water absorption tests results

To calculate the amount of water absorbed by each sample, after taking the samples out from water, first the surface of them was dried and then a scale was used to weight them, after that the amount of the water absorption per gram of each sample was calculated. To analyse the effects of absorbed water on the mechanical properties of each sample, a tensile test Zwick/Roell machine was used.

3.7.10.1 Water absorption test on neat PU, PU + GNP and PU + GNP + SG

Results of the water absorption tests are shown in **Figure 3-65** and **Table 3-14, Table 3-15** and **Table 3-16**. The amount of the water absorption by each material was calculated per initial weight of the sample and after that the average was taken for each type of material. Also, by looking at the temperature, humidity and PH of the water, it can be said that the environmental condition during the period of experiment was almost steady and no substantial change in the environmental conditions occurred.

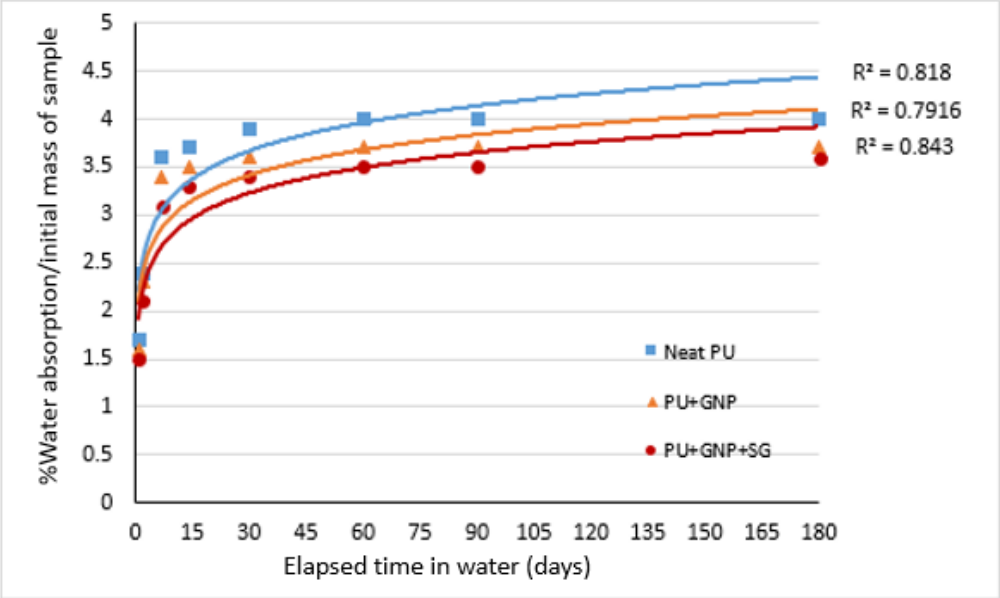

Figure 3-65 Water absorption results for neat PU, PU+GNP and PU+GNP+SG coatings.

Table 3-14 Amount of the absorbed water per gram of the material after 24hrs, 48hrs and 1 week.

Sample	Duration of water immersion												
		24 Hours (T=23.7, H=31.5%, PH=7.42)				48 Hours (T=23, H=35.2%, PH=7.51)				1 Week (T=23.9, H=36.95%, PH=7.38)			
	Initial dry weight (g)	Weight at the end of immersion (g)	WA (g)	WA/ g	%WU	Weight at the end of immersion (g)	WA (g)	WA/ g	%WU	Weight at the end of immersion (g)	WA (g)	WA/ g	%WU
Pure Pu-1	**11.96**	12.15	0.19	0.015	**1.7**	12.26	0.3	0.025	**2.4**	12.38	0.42	0.035	**3.6**
Pure Pu-2	**12.88**	13.12	0.24	0.018		13.17	0.29	0.023		13.32	0.44	0.034	
Pure Pu-3	**12.31**	12.52	0.21	0.017		12.63	0.32	0.025		12.78	0.47	0.038	
PU+GNP-1	**13.12**	13.31	0.19	0.014	**1.6**	13.4	0.28	0.021	**2.3**	13.51	0.39	0.029	**3.4**
PU+GNP-2	**11.90**	12.10	0.20	0.016		12.17	0.27	0.023		12.31	0.41	0.034	
PU+GNP-3	**10.12**	10.32	0.20	0.019		10.4	0.28	0.027		10.51	0.39	0.038	
PU+GNP+ SG-1	**10.43**	10.61	0.18	0.017	**1.5**	10.64	0.21	0.020	**2.1**	10.74	0.31	0.029	**3.1**
PU+GNP+ SG-2	**9.65**	9.82	0.17	0.017		9.9	0.25	0.025		9.94	0.29	0.030	
PU+GNP+ SG-3	**9.85**	9.96	0.11	0.011		10.05	0.2	0.020		10.17	0.32	0.032	

* Water absorption = WA; Water up-take = WU

Table 3-15 Amount of the absorbed water per gram of the material after 2 weeks, 1 month and 2 months.

Sample	Duration of water immersion												
		2 Weeks (T=20.6, H=42.6%, PH=7.52)				1 Month (T=22.8, H=47.6%, PH=7.55)				2 Months (T=23.5, H=40.7%, PH= 7.67)			
	Initial dry weight (g)	Weight at the end of immersion (g)	WA (g)	WA/ g	%WU	Weight at the end of immersion (g)	WA (g)	WA/ g	%WU	Weight at the end of immersion (g)	WA (g)	WA/ g	%WU
Pure Pu-1	**11.96**	12.4	0.44	0.036	**3.7**	12.43	0.47	0.039	**4**	12.43	0.47	0.039	**4**
Pure Pu-2	**12.88**	13.36	0.48	0.037		13.39	0.51	0.040		13.40	0.52	0.040	
Pure Pu-3	**12.31**	12.79	0.48	0.038		12.80	0.49	0.040		12.81	0.5	0.041	
PU+GNP-1	**13.12**	13.51	0.39	0.029	**3.5**	13.53	0.41	0.031	**3.6**	13.54	0.42	0.032	**3.7**
PU+GNP-2	**11.90**	12.35	0.45	0.037		12.35	0.45	0.038		12.35	0.45	0.038	
PU+GNP-3	**10.12**	10.49	0.37	0.036		10.51	0.39	0.038		10.52	0.4	0.040	
PU+GNP+ SG-1	**10.43**	10.66	0.23	0.022	**3.3**	10.68	0.25	0.024	**3.4**	10.68	0.25	0.024	**3.5**
PU+GNP+ SG-2	**9.65**	10.06	0.41	0.042		10.06	0.41	0.042		10.06	0.41	0.042	
PU+GNP+ SG-3	**9.85**	10.21	0.36	0.036		10.22	0.37	0.037		10.24	0.39	0.040	

* Water absorption = WA; Water up-take = WU

Table 3-16 Amount of the absorbed water per gram of the material after 3 months and 6 months.

Sample	Duration of water immersion								
		3 Months (T=24, H=44%, PH=7.78)				6 Months (T=21.8, H=39.1%, PH=7.97)			
	Initial dry weight (g)	Weight at the end of immersion (g)	WA (g)	WA/ g	% WU	Weight at the end of immersion (g)	WA (g)	WA/ g	% WU
Pure Pu-1	**11.96**	12.43	0.47	0.039	**4.0**	12.43	0.47	0.039	**4**
Pure Pu-2	**12.88**	13.40	0.52	0.040		13.40	0.52	0.04	
Pure Pu-3	**12.31**	12.80	0.49	0.040		12.80	0.49	0.041	
PU+GNP-1	**13.12**	13.55	0.43	0.033	**3.7**	13.57	0.45	0.032	**3.7**
PU+GNP-2	**11.90**	12.35	0.45	0.038		12.35	0.45	0.038	
PU+GNP-3	**10.12**	10.52	0.4	0.040		10.52	0.4	0.04	
PU+GNP+ SG-1	**10.43**	10.69	0.26	0.024	**3.5**	10.69	0.26	0.025	**3.6**
PU+GNP+ SG-2	**9.65**	10.07	0.42	0.042		10.06	0.41	0.042	
PU+GNP+ SG-3	**9.85**	10.26	0.41	0.04		10.25	0.4	0.041	

* Water absorption = WA; Water up-take = WU

Figure 3-65 shows that the weight of the samples increased significantly at the beginning and during the first two weeks of immersion in the water. After that the rate of water absorption decreased and the weight of the samples was increased at a lower rate. The water absorption tests results showed that the weight of the pure PU samples were increased by 1.7% after 24 hours and by 0.7% after 48 hours of immersion in the water and it continued to increase until 2 months from the start of the immersion and after that no further noticeable water absorb was recorded. PU+GNP also showed the same behaviour as neat PU and the weight of the samples increased significantly for the first month of immersion and after 2 months the weight did not increase anymore. The results for the PU+GNP+SG samples showed the weight was increased after immersion in the water at the lowest rate relative to neat PU and PU+GNP. This shows that these PU+GP+SG materials are hydrophobic and absorbed the least amount of water relative to the other two coating materials (neat PU and PU+GNP).

3.7.10.2 Effects of water absorption on tensile properties of PU, PU + GNP and PU + GNP + SG

Tensile tests were performed on the dogbone after 24 hrs, 48 hrs, 1 week, 2 weeks, 1 month, 2 months, 3 months and 6 months immersion in water tank. Young's modulus, elongation at break, UTS and modulus of toughness of various specimens are extracted from stress strain diagram. An example of tensile tests results after 24 hrs immersion in water is shown in **Figure 3-66** and the full results are summarised in **Table 3-17**. The tensile test results at other immersion duration are presented in the Appendix **A.4** .

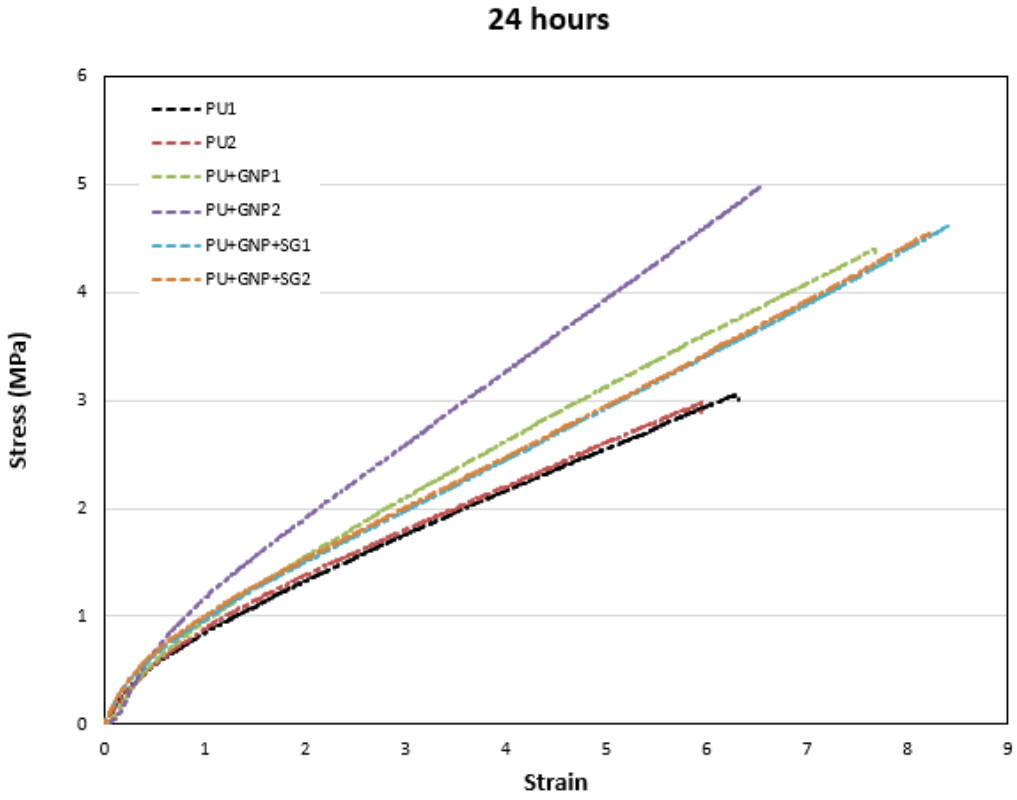

Figure 3-66 Effect of the water absorption on the tensile behaviour of the neat PU and modified PUs.

Table 3-17 shows that for the neat polyurethane, elongation at break decreased after 24hours of immersing into the water by 22.4% from 659 to 511, while for another sample of pure PU after 48 hours of immersing into the water it decrease by only 16.5% which shows that although the water absorption decrease the elongation at break for the pure polyurethane but, the duration of immersing into the water doesn't have significant effect on this properties; even after 6 months of immersing the pure polyurethane into the water elongation at break decrease by only 10% in comparison with the 48 hours of immersing into the water. For PU+GNP and PU+GNP+SG effects of absorbed water on the elongation at break was different, as can be

seen in the table below for the PU+GNP elongation at break increased by 11% after 6 months immersing in water and for PU+GNP+SG increased by 3.5% for the same duration of immersing into the water. By looking at the modulus of toughness it can be seen that for the neat polyurethane for the first month of immersing into the water it starts increasing by 4, 6.7, 6.6, 10.5 and 2.7% respectively after 24h, 48h, 1w, 2w and one month, but after that started to decrease and by passing 6 months of immersing into the water it decreased by 32%. Behaviour of the modulus of toughness for the PU+GNP and PU+GNP+SG also was similar to neat PU which means absorbed water decrease the amount of modulus of toughness by 12.3% for PU+GNP and 34% for PU+GNP+SG after 6 months immersing into the water. Ultimate tensile strength for all three types of material decreased because of absorbed water; for neat PU it decreased by 5.1%, for PU+GNP decreased by 11.6% and for PU+GNP+SG decreased by 39%. Young's modulus also decreased for the PU+GNP by 23% and for the PU+GNP+SG by 32% while increased for the neat PU by 40% after 6 months immersing into the water.

Table 3-17 Results of the tensile tests after water immersion from 24 hrs up to 6 months.

Effects of water absorption on Young's modulus of the coatings

	EL%						T						UTS						E					
	PU		PU+ GNP		PU+ GNP+ SG		PU		PU+ GNP		PU+ GNP+ SG		PU		PU+ GNP		PU+ GNP+ SG		PU		PU+ GNP		PU+ GNP+ SG	
Dry	659		599		540		103 01		197 41		230 54		21.5		38		46		2.1		3.7		4.1	
24 hrs	493	530	**511 ± 18.5**		550	666	**608 ± 58**		685	736	**710 ± 26**		10315	11178	**10746 ± 432**		17738	18961	**18349 ± 612**		20658	21252	**20955 ± 297**	
48 hrs	550	550	**550 ± 0**		493	596	**544 ± 52**		565	646	**605 ± 41**		11849	10152	**11000 ± 849**		16949	18233	**17364 ± 642**		19872	17878	**18875 ±997**	
1 week	546	496	**521 ± 25**		543	486	**514 ± 29**		542	535	**538 ± 3.5**		10873	11102	**10987 ± 115**		16951	16699	**16825 ± 126**		15731	17175	**16453 ± 722**	
2 weeks	546	470	**508 ± 38**		513	644	**578 ± 66**		561	537	**549 ± 12**		1186	10905	**11383 ± 479**		1516	16647	**15907 ± 740**		1790	16248	**17074 ± 827**	
1 month	493	540	**516 ± 24**		606	637	**621 ± 16**		546	567	**556 ± 11**		10702	10461	**10581 ± 121**		16185	17180	**16682 ± 498**		17547	17007	**17277 ± 270**	
2 months	497	503	**500 ± 3**		622	631	**626 ± 5**		566	531	**548 ± 18**		103	10027	**10167 ± 140**		176	16997	**17314 ± 317**		162	16588	**16416 ± 172**	
3 months	483	436	**459 ± 24**		579	646	**612 ± 34**		556	562	**562 ± 3**		10185	9413	**9799 ± 386**		15130	13973	**14551 ± 579**		15148	16643	**15895 ± 748**	
6 months	473	426	**449 ± 24**		516	550	**533 ± 17**		579	585	**559 ± 3**		10397	9679	**10038 ± 359**		17882	16723	**17302 ± 580**		14823	15631	**15227 ± 404**	

20.2	19.1	**19.6 ± 0.6**		31.3	35.7	**33.5 ± 2.2**		31.3	33.4	**32.3 ± 1.1**		1.26	1.56	**1.41 ± 0.2**		2.65	3.42	**3.04 ± 0.4**		2.66	2.97	**2.82 ± 0.2**	
21.4	19.4	**20.5 ± 1**		31.2	35.1	**33.1 ± 1.9**		35.6	34.8	**35.2 ± 0.4**		1.78	1.17	**1.47 ± 0.3**		3.97	2.91	**3.44 ± 0.5**		2.88	2.93	**2.91 ± 0.02**	
21.5	19.3	**19.5 ± 0.2**		36.	34.7	**35.8 ± 1.1**		31.	32.2	**32.0 ± 0.2**		1.2	1.49	**1.38 ± 0.1**		3.9	2.96	**2.95 ± 0.5**		3.4	2.96	**3.19 ± 0.2**	
21.4	19.4	**21.5 ± 0.1**		31.1	33.5	**32.3 ± 1.2**		35.1	31.8	**33.5 ± 1.7**		1.06	1.94	**1.50 ± 0.5**		3.32	2.91	**3.11 ± 0.2**		3.43	2.45	**2.94 ± 0.49**	
21.6	22.1	**21.8 ± 0.3**		32.9	33.5	**33.3 ± 0.3**		31.5	35.1	**33.3 ± 1.8**		1.42	1.96	**1.69 ± 0.3**		3.95	3.33	**3.64 ± 0.3**		2.88	2.61	**2.75 ± 0.14**	
23.7	20.2	**21.9 ± 1.8**		34.5	36.5	**35.5 ± 1**		29.1	35.7	**32.4 ± 3**		1.61	1.46	**1.54 ± 0.1**		3.52	3.45	**3.46 ± 0.06**		2.81	3.13	**2.97 ± 0.16**	
20.1	21.9	**21 .0 ± 0.9**		37.4	37.9	**37.6 ± 0.3**		41.9	43.4	**42.6 ± 0.8**		1.69	1.25	**1.47 ± 0.2**		3.82	3.01	**3.41 ± 0.4**		2.97	2.92	**2.94 ± 0.01**	

Figure 3-67 shows the effects of the water absorption on the Young's modulus. It can be seen that Young's modulus was decreased for all three coating materials, and the highest decrease was for the PU+GNP. After 6 months of immersion in water, the PU+GNP and PU+GNP+SG had approximately the same Young's modulus although the Young's modulus for the neat PU was also decreased significantly.

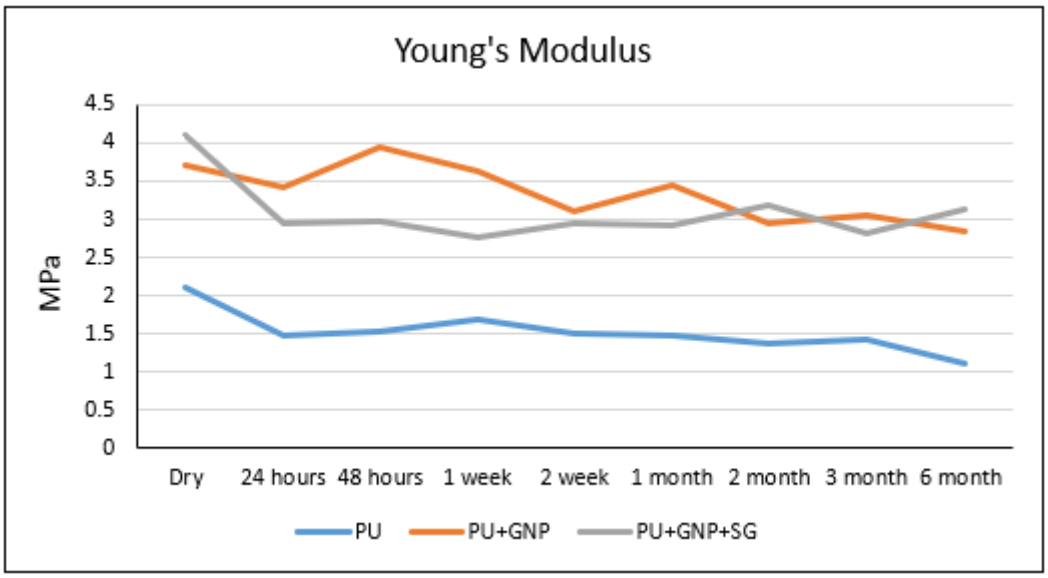

Figure 3-67 Effect of water immersion for 24h, 48h, 1w, 2w, 1m, 2m, 3m and 6 months on the Young's modulus of the neat PU, PU+GNP and PU+GNP+SG.

Effects of water absorption on elongation at break of the coatings

Figure 3-68 shows the effects of water absorption on the elongation at break after 24 hours to 6 months immersion in water. During the immersion, %EL was continuously decreased for neat PU but for PU+GNP and PU+GNP+SG it was initially decreased and then it was remained almost constant.

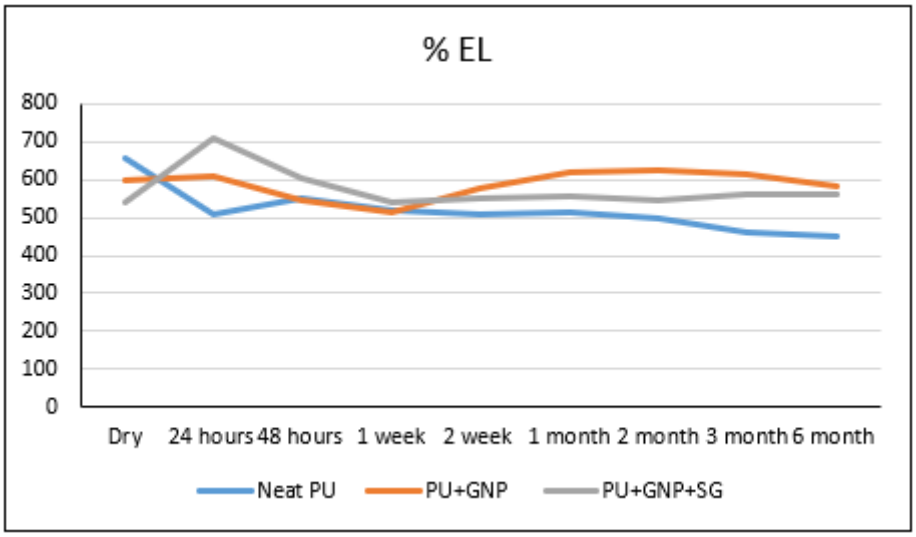

Figure 3-68 Effect of water immersion for 24h, 48h, 1w, 2w, 1m, 2m, 3m and 6 months on the elongation at break of the neat PU, PU+GNP and PU+GNP+SG.

Effects of water absorption on UTS of the coatings

Figure 3-69 shows the effect of water absorption on UTS of the three coating materials. The UTS of PU+GNP+SG was decreased by 30% after 48 hours of immersion in water and after that it remained unchanged. For PU+GNP, the UTS was decreased by 6% then remained almost constant in the next 6 months of immersion. For the neat PU the UTS had similar trend as the modulus of toughness and it was almost remained constant up to 6 months of immersion in the water.

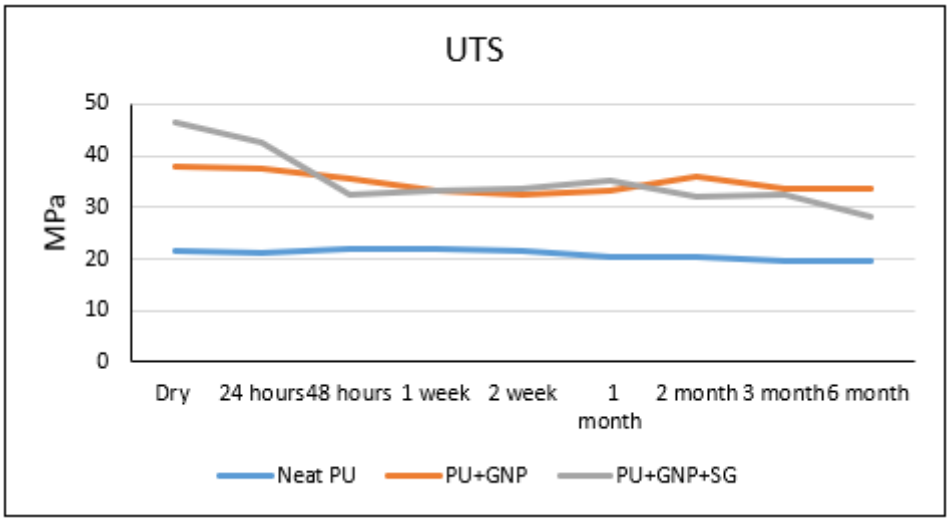

Figure 3-69 Effect of immersing the samples into water for 24h, 48h, 1w, 2w, 1m, 2m, 3m and 6 months on the ultimate tensile strength of the neat PU, PU+GNP and PU+GNP+SG.

Effects of water absorption on modulus of toughness of coatings

Figure 3-70 shows the effect of water uptake on the modulus of toughness of the coatings. The modulus of toughness for PU+GNP and PU+GNP+SG was dramatically decreased in the first

week of immersion in the water. However, after that until the end of the immersion (6 months), there was no significant change on the amount of modulus of toughness for all three coating materials. Also, it can be seen that the absorbed water did not have significant effects on the modulus of toughness of the neat PU.

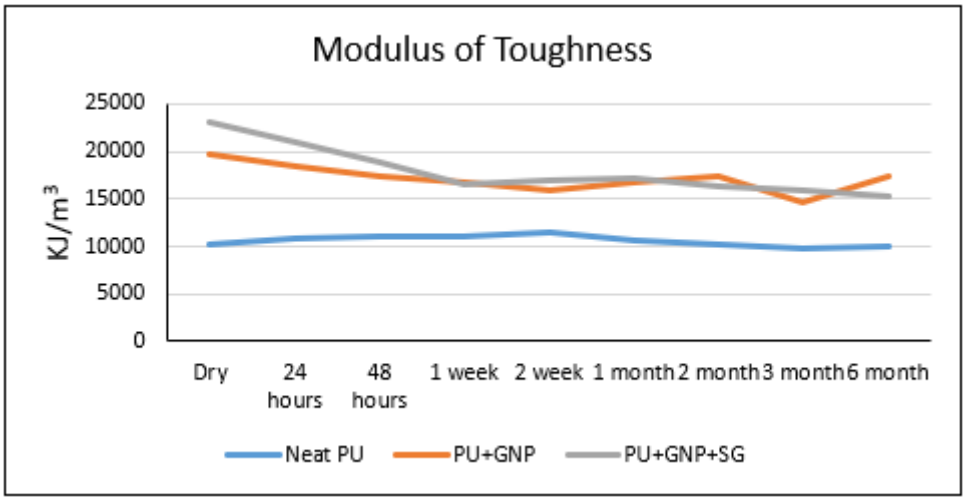

Figure 3-70 Effect of immersing the samples into water for 24h, 48h, 1w, 2w, 1m, 2m, 3m and 6 months on the modulus of toughness of the neat PU, PU+GNP and PU+GNP+SG.

3.7.10.3 Summary of water absorption tests results

In the water absorption tests, all three types of coating materials start absorbing water significantly in the first month of immersion in the water and after two months of immersion, water absorption were not noticeable and the weight of the specimens remained unchanged. The test results showed that water absorption in the neat PU was the highest; while the PU+GNP and PU+GNP+SG had the least water absorption. This is due to increase in hydrophobicity of these coatings by addition of GNP and silica-based sol-gel (SG) to the PU. These tests also showed that after 6 months of water immersion of the neat PU, its elongation at break, modulus of toughness, UTS and Young's modulus were decreased by 32%, 2.5%, 5.1% and 47%, respectively. For the PU+GNP coating, its elongation at break, modulus of toughness, UTS and Young's modulus were decreased by 2.8%, 12.3%, 11.6% and 23%, respectively. Finally, for the PU+GNP+SG coating, its elongation at break, modulus of toughness, UTS and Young's modulus were decreased by 3.5%, 34%, 39% and 23.9%, respectively. These results are summarised in Figure 3-71 to Figure 3-73.

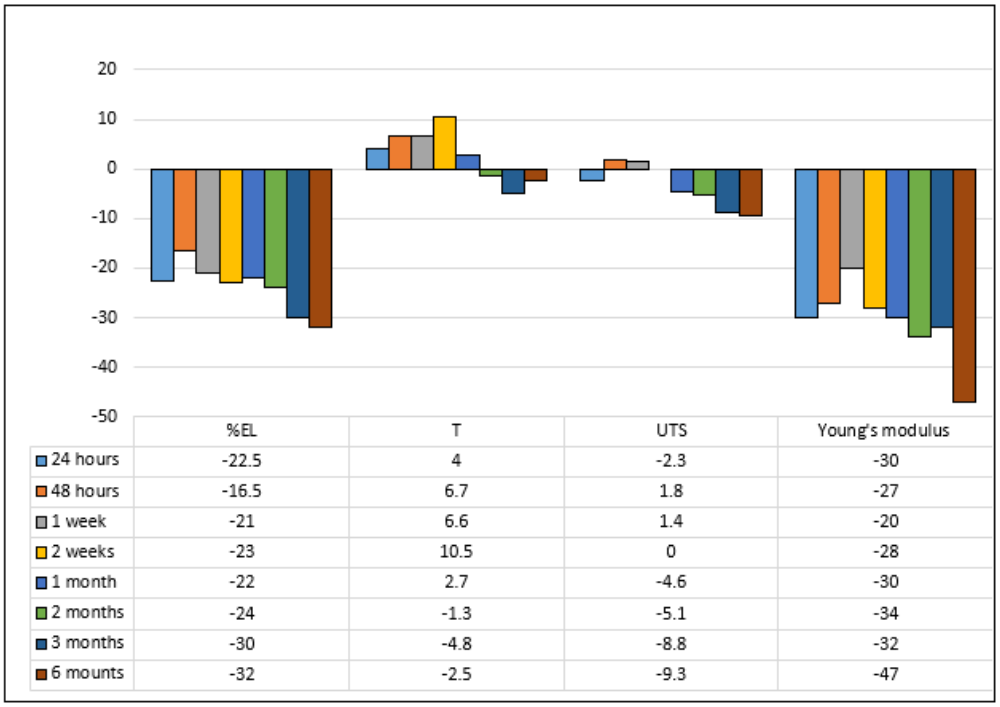

	%EL	T	UTS	Young's modulus
24 hours	-22.5	4	-2.3	-30
48 hours	-16.5	6.7	1.8	-27
1 week	-21	6.6	1.4	-20
2 weeks	-23	10.5	0	-28
1 month	-22	2.7	-4.6	-30
2 months	-24	-1.3	-5.1	-34
3 months	-30	-4.8	-8.8	-32
6 mounts	-32	-2.5	-9.3	-47

Figure 3-71 Variation of the tensile properties of the neat PU after immersing in water from 24h to 6 months.

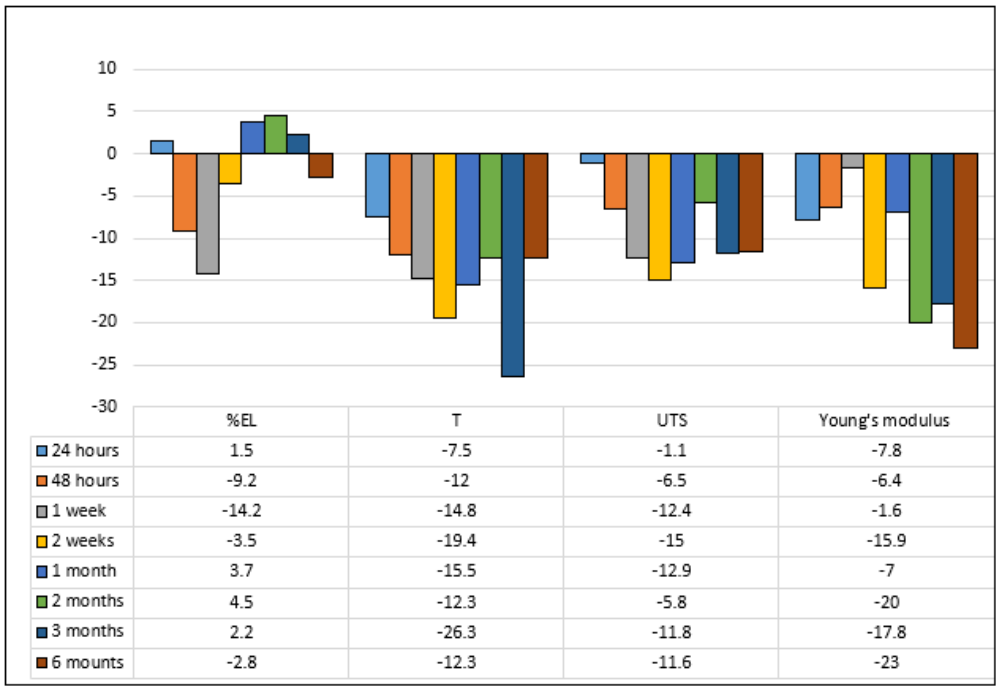

	%EL	T	UTS	Young's modulus
24 hours	1.5	-7.5	-1.1	-7.8
48 hours	-9.2	-12	-6.5	-6.4
1 week	-14.2	-14.8	-12.4	-1.6
2 weeks	-3.5	-19.4	-15	-15.9
1 month	3.7	-15.5	-12.9	-7
2 months	4.5	-12.3	-5.8	-20
3 months	2.2	-26.3	-11.8	-17.8
6 mounts	-2.8	-12.3	-11.6	-23

Figure 3-72 Variation of the tensile properties of the PU+GNP after immersing in water from 24h to 6 months.

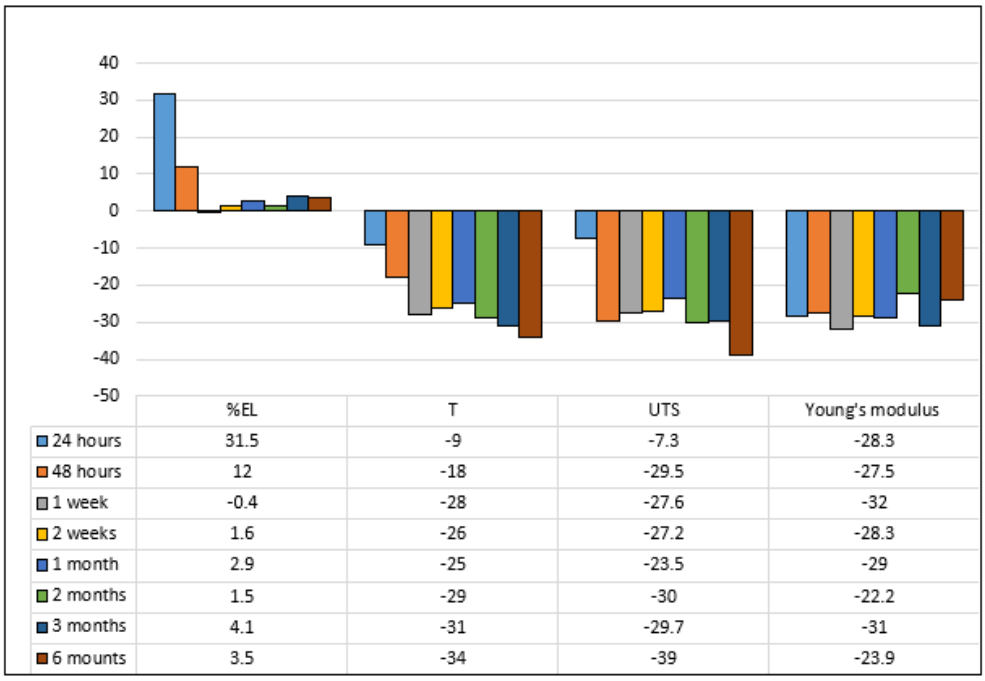

	%EL	T	UTS	Young's modulus
24 hours	31.5	-9	-7.3	-28.3
48 hours	12	-18	-29.5	-27.5
1 week	-0.4	-28	-27.6	-32
2 weeks	1.6	-26	-27.2	-28.3
1 month	2.9	-25	-23.5	-29
2 months	1.5	-29	-30	-22.2
3 months	4.1	-31	-29.7	-31
6 mounts	3.5	-34	-39	-23.9

Figure 3-73 Variation of the tensile properties of the PU+GNP+SG after immersing in water from 24h to 6 months.

Chapter 4 Damping Coefficient, Transmitted and Rebound Energy Measurement

4.1 Introduction

In this chapter drop ball tests were performed for measuring the amount of energy transmitted to the substrate. This has been done by dropping a steel ball on the upper surface of the specimen and recording the voltage from a piezoelectric located at the lower surface of the specimen by an oscilloscope. The results from drop ball tests are analysed by SVD-QR method, and the damping ratio of each material was calculated. At the last section of this chapter resilience tests was performed to analyse the amount of rebound energy by using motion capture system.

Polymers are commonly used for vibration damping and energy absorption [164] because they have better attenuation capability than other materials such as metals and ceramics.

The viscoelastic behaviour of polymers is a key reason why they are used for vibration damping and energy absorption applications. In viscoelastic materials, the elastic elements store energy during deformation and release it in the process of strain recovery [165]. During unloading, some of the energy is recovered while the rest being dissipated in the form of heat. Another property of a vibration damping material is attenuation which can happen through two mechanisms: absorption and scattering of energy. In absorption, sound energy [166] is converted to heat by the elastic motion of particles; in other words, when a material is elastically loaded, it stores energy and when unloaded, some of the mechanical energy is lost and dissipated as heat. Scattering is a result of inhomogeneity in a material such as crystal discontinuities, grain boundaries, inclusions, particles and voids [166]. Scattering causes the energy of the coherent, collimated waves to be converted into incoherent, divergent waves through reflection and refraction [165].

Polyurethane (PU) elastomers is a polymer, which contains the urethane group –NH–CO–O– and they are formed by combining hard (isocyanate) and elastic (polyol) parts, and changing these components creates a range of characteristics for various polyurethane elastomers. Polyurethane elastomers are superior in resistance to abrasion, oxidation, tear, and chemicals (oil, gas). They are also transparent, have good adhesion and are used for vibration-damping applications [167]. The loss angle δ is the phase shift between stress and strain. An equivalent

measure for material loss factor (η) is the loss tangent, defined as $\tan\delta = \eta = \frac{E''}{E'}$, where E' and E'' are the storage modulus, and the loss modulus, respectively. The loss factor is a measure of the energy dissipation capability of the material. It is realized that by adding inorganic fillers to polyurethane, the tan δ increases significantly. For example, adding 10% silica increases the maximum tan δ value of Polyurethane/Poly-ethyl-methacrylate interpenetrating network (PU/PEMA IPNs) from 0.44 to 0.72 [168]. Wang *et al.* [169] also found that adding carbon fibres to PU/EP (epoxy resin) IPNs increases the tan δ from 0.37 to 0.72. One of the weaknesses of polyurethanes is their moderate to low mechanical properties. This weakness arises from the lack of hydrogen bonding between the hard and soft segments and incompatibility between the polar hard segments and nonpolar soft segments. One proposal to overcome this weakness is to introduce carbon nanoparticles to the neat polyurethane [77].

Graphene is an allotrope of carbon, and with one atom thick planar sheets structure of sp^2 bonded carbon atoms packed in a honeycomb like lattice [170]. Graphene has the intrinsic strength of the monolayer membrane of $42N.m^{-1}$, which equates to an intrinsic strength of 130GPa and Young's modulus of 1TPa [171]. However, the strength of the interface is central to the mechanical enhancement of graphene modified polymers rather than of the intrinsic strength of graphene particles. Therefore, the functionalised graphene (f-GNP) which form chemical bonding with the matrix is superior to the pristine graphene for mechanical reinforcement of polymers.

The dispersion of graphene in PU makes noticeable contributions to the enhancement of PU mechanical properties [172]. In this regard, surface treating of nanofillers boost the dispersion of the nanopartciles in PU matrices. In addition, the functionalities located on the surface of nanofillers such as hydroxyl, carboxyl, or amine groups can potentially form chemical bonding with PU matrices resulting in a strong interface between the fillers and the matrix for stress transfer.

The functionalised GNP nanoparticles and polymeric matrices interacts by mechanical interlocking through the wrinkled surface of thin graphene sheets; and chemically by the hydrogen bonding formed between the oxygen functionalities of the GNP and polymeric matrices. It was found hydrogen and covalent bondings are formed between graphite oxide nanoplatelets (GONPs) and PUs which act as a strong interface [173]. It is reported that Young's modulus and hardness of a PU with 4.4wt% GONPs was nearly increased by ~900% and ~327%, respectively, relative to the neat PU due to the covalent interface with the hard segment of the PU [174].

Pokharel *et al.* manufactured polyurethane (PU) nanocomposites by in-situ polymerization using pristine graphene nanoplatelets (GNPs), graphene oxide (GO), and functionalized graphene sheets (FGSs). Tensile testing, dynamic mechanical thermal analysis and the efficacy of functional groups on the graphene were evaluated for the three PU nanocomposites. The PU nanocomposites modified by 2wt% loading of GO or FGS showed significantly higher Young's modulus than that the one modified by GNPs [73]. It is reported the detailed structure of the PU, in terms of the composition and specific chemistry of the hard and soft segments, is probably important for the graphene stabilisation and mechanical properties of the resultant graphene/PU composites [175].

In this study, carbon nanoparticles in the form of functionalised graphene nanoplatelet (f-GNP) alone and in combination with hydrophobic silica base solution (SG) have been added to neat polyurethane to improve the damping coefficient and energy absorption of the resultant nanocomposites for application in protecting the leading-edge of wind turbine blades. First the damping coefficient of neat polyurethane (PU), f-GNP based PU nanocomposite (PU + f-GNP), and f-GNP and hydrophobic silica-based solution PU nanocomposite (PU + f-GNP + SG), together with polytetrafluoroethylene (PTFE), high-density polyethylene (HDPE), ultra-high molecular weight polyethylene (UHMWPE), polyethylene terephthalate (PET), polyvinyl chloride (PVC) and NYLON have been obtained by the drop ball tests under controlled and consistent conditions. Second the attenuation of the various materials has been identified with the SVD-QR method. This experimental modal analysis method has been used to analyse the free response signal of the system during the drop ball test and identify the modal parameters (frequency and damping ratio) of the modes of deformation of the system. Afterwards, resilience tests was performed to analyse the rebound energy of the developed materials.

4.2 Drop Ball Tests

The damping coefficient of neat polyurethane (PU), GNP based PU nanocomposite (PU + GNP), and GNP and hydrophobic silica-based solution PU nanocomposite (PU + GNP + SG), together with polytetrafluoroethylene (PTFE), high-density polyethylene (HDPE), ultra-high molecular weight polyethylene (UHMWPE), polyethylene terephthalate (PET), polyvinyl chloride (PVC) and NYLON have been obtained by the drop ball tests under controlled and consistent conditions.

4.2.1 Manufacturing of samples

For this experiment, in addition to manufacturing neat polyurethane (PU), graphene modified PU (PU + GNP) and graphene/sol-gel modified PU (PU + GNP + SG), other ready-made

selected PTFE, HDPE, UHMWPE, PET, PVC and NYLON polymers were tested in order in to make comparison. The material characteristics that were considered for analysis are $\tan \delta$ and attenuation. Mechanical loss coefficient ($\tan \delta$), is an indication of the effectiveness of a material's damping capabilities. The higher the mechanical loss coefficient, $\tan \delta$, the greater the damping coefficient, the more efficient the material will be in effectively accomplishing energy absorption and dispersal. Attenuation is the decay rate of the wave as it propagates through the material.

Specimens of neat polyurethane, graphene modified PU, and f-GNP+SG modified PU were prepared according to the procedures discussed before.

A cylindrical mould was machined from polyethylene for casting the specimens. There were two options to get the cured samples out of the mould without applying too much stress on them; one method was to manufacture the mould from two symmetric pieces and then bound them together (**Error! Reference source not found.**). The other method was using a milling m achine to cut the mould into two pieces and get the samples out of the mould (**Figure 4-2c**). To get the cured specimens out of the mould, at least two layers of mould release agent were applied on the inner surface of the mould before pouring the materials into it. The first layer of the agent was applied by using paint brush and dried for 1 hour before the second layer was applied (if it was the first time that the mould is being used for making samples, 6 to 7 layers of release agent needed to be applied). Since the polymer hardens quickly, the process of manufacturing the samples needed to be completed within 7 minutes. **Figure 4-2** shows various stages of manufacturing the polyethylene mould and the specimens.

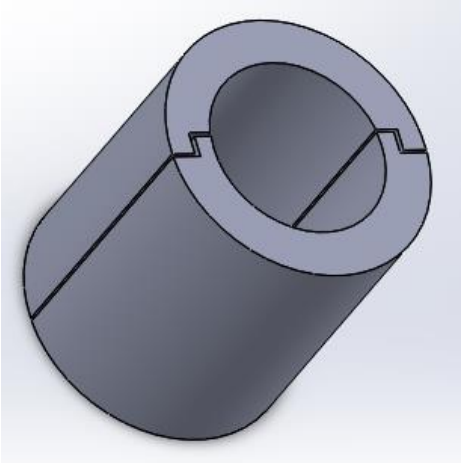

Figure 4-1 Using solid works to design a mould from two symmetric pieces.

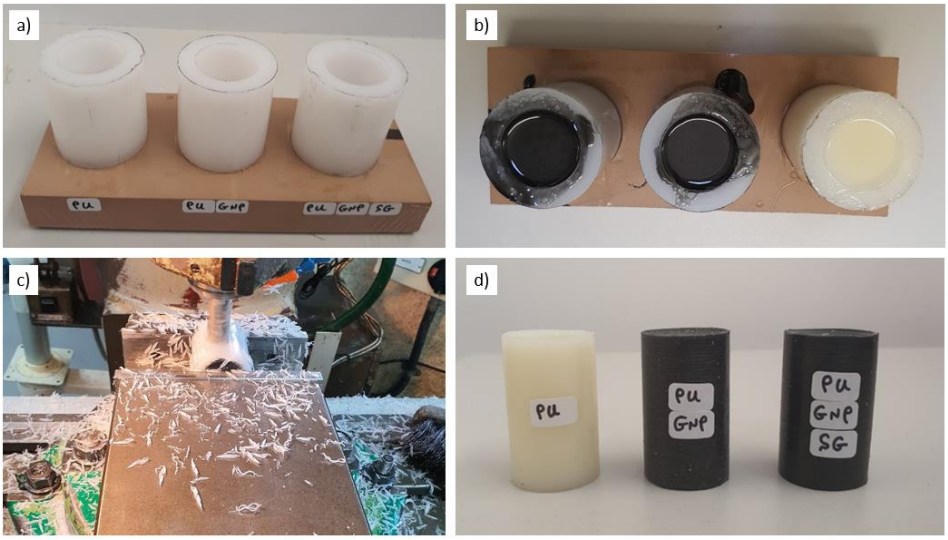

Figure 4-2 a) Manufactured mould for making specimens for drop ball test, b) pouring materials into the mould, c) using a milling machine for demoulding specimens, d) final specimens for testing.

NYLON, HDPE, PTFE, UHMWPE PET and PVC were purchased in 30 mm diameter rods, cut and sanded into 50 mm height specimens. A 15 mm height stainless steel disk was made as the target for the ball drop. The surface condition of the specimens has significant effect on the drop ball test results and the contact surface of the specimens should be very smooth, flat and parallel. To achieve a perfectly smooth surface, 600 grit sand paper was used to sand all specimens. All the specimens that were tested are shown in **Figure 4-3** and their dimensions are summarised in **Table 4-1**.

Table 4-1 Specimen's properties for damping test.

Material	Height (mm)	Diameter (mm)
PU	50.2	31.8
PU + f-GNP	49.8	31.9
PU + f-GNP + SG	49.8	32
NYLON	49.8	32
UHMWPE	50.1	31.9
HDPE	49.8	31.8
PTFE	49.9	31.9
PET	49.9	31.7
PVC	50.1	32

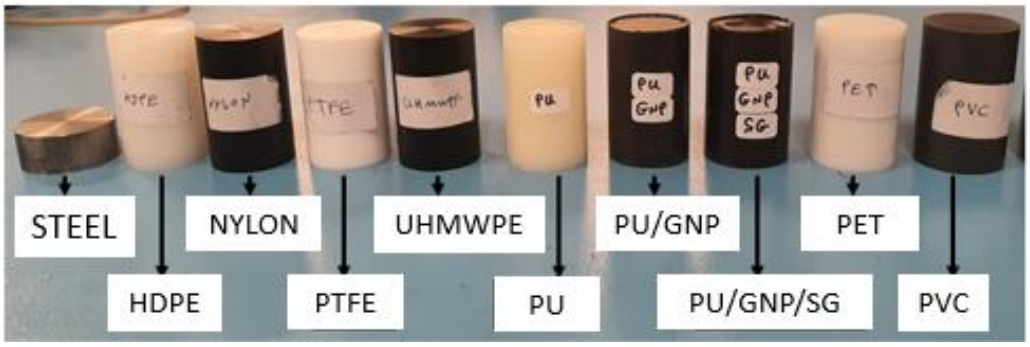

Figure 4-3 Specimens for damping test.

4.2.2 Experimental set up

To eliminate the surface hardness effect of the test specimen, the ball was dropped onto a 15mm stainless steel disk, placed on the top of the specimen. The steel balls used to generate acoustic signals were Chrome steel ball bearings of 3mm diameter and a hardness of HRC 60-67. The stainless-steel disk has hardness up to HRC 40-48. This material is chosen as the target because of its high hardness, thus the steel ball will leave little to no dent on its surface.

As can be seen in **Figure 4-4**, a digital oscilloscope, a piezoelectric sensor, a steel support stand with a screw release clamp and a 3mm diameter steel ball were used to set up the drop ball test. The piezoelectric sensor was placed under the specimen and aligned vertically facing the bottom face of test specimen. The piezoelectric sensor used here is the PCB 333B30 SNLW56739 made by PCB Piezotronics U.S. which is inserted in a UHMWPE casing and laid on a sponge over an HDPE platform (**Figure 4-5**). The sensor was located on the sponge to

eliminate the vibration of the sensor-specimen system on the rigid platform. The acoustic signal is generated by dropping the steel ball onto the target. The input signal travels through the test specimen and the reduced outcome signal is received by the piezoelectric sensor and displayed on a digital oscilloscope. The oscilloscope used here is a TBS-1072-EDU digital oscilloscope made by Tektronix. As can be seen in **Figure 4-5**, the whole system is placed on an HDPE platform to make the setup flat horizontal and also to prevent the steel ball from hitting the floor after bouncing back.

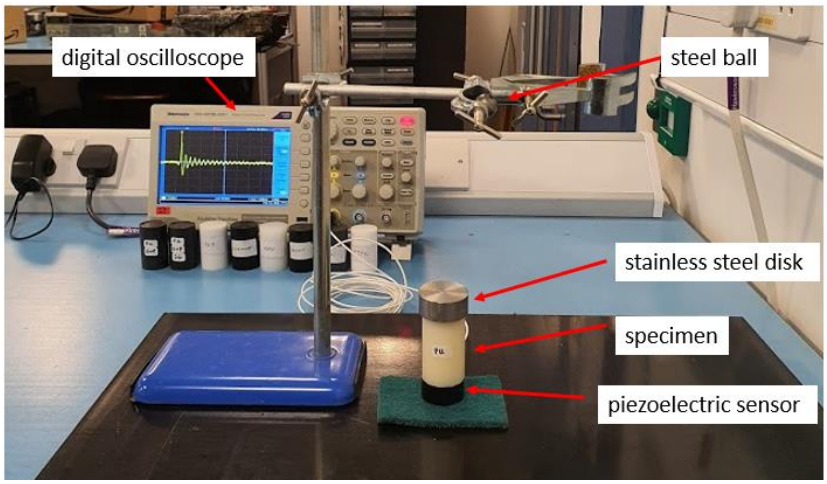

Figure 4-4 Damping test set up.

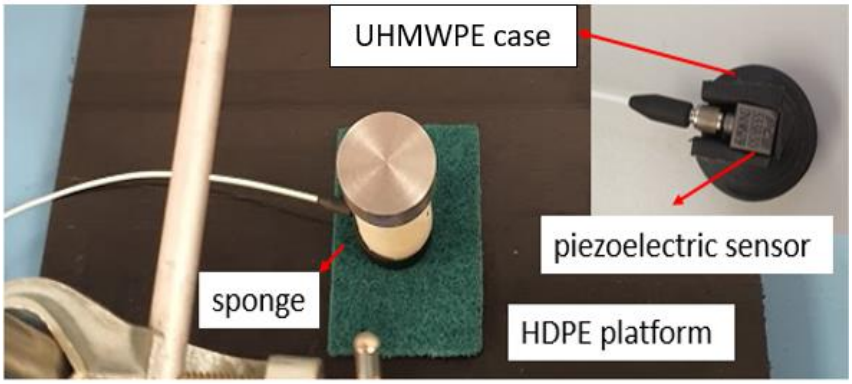

Figure 4-5 Piezoelectric sensor set up for the damping test.

It is known that the impedance mismatch between air and solids is large, that is why there is almost no transmission of ultrasonic waves between the two, so to facilitate the transmission of the ultrasonic signal, the air gap between the specimen and ultrasonic sensor and also between the specimen and stainless-steel target was filled with a couplant.

The choice of the right couplant materials was based on signal transmission capability, the interaction with test specimen along with consistency and the ease of application during

repeated testing. Different couplant materials have different acoustic impedance properties and viscosities which needed to be considered in choosing the right couplant for the test. For this test two types of couplant were initially chosen: petroleum jelly and silicon lubricant. Using petroleum jelly has some disadvantages, for example it was difficult to have a consistent layer thickness for all tests and the different amount of couplant applied each time has a significant effect on the results. Silicon lubricant couplant was ultimately chosen because it is very consistent in application, it leaves a thin layer on the specimen surface, is not too slippery, and the steel target can rest easily on the specimen without sliding off.

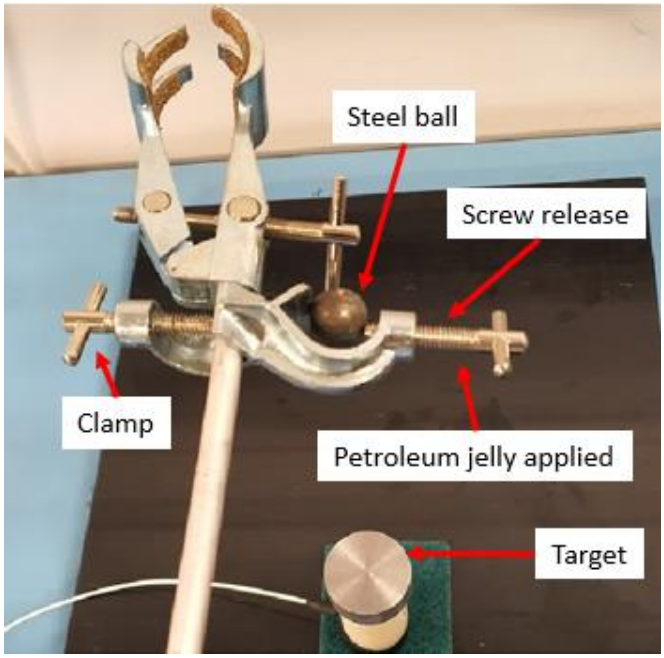

Figure 4-6 Holding the steel ball on the rod with a clamp.

To improve the consistency of the test, the residue couplant on the specimen and sensor were wiped off and reapplied in the same way after each drop test. As can be seen in **Figure 4-6**, the steel ball is held 12cm above the target with a clamp. The ball is dropped by rotating the screw. To ensure consistency of the test, it is important that each time the ball falls on the centre of the target. For that reason, petroleum jelly was applied on the screw to reduce friction. The steel drop-ball is relatively small and so turning the screw should be done gently.

4.2.3 Drop ball tests result

Drop ball tests were performed according to ASTM E976, E2075 and E650. The specimens tested were neat polyurethane (PU), graphene modified PU (PU + f-GNP), graphene and hydrophobic silica base solution modified PU (PU + f-GNP + SG), polytetrafluoroethylene (PTFE), high-density polyethylene (HDPE), ultra-high molecular weight polyethylene fibre (UHMWPE), polyethylene terephthalate (PET), PVC and NYLON. For each specimen, the

drop-ball test was repeated 5 times from a drop height of 12cm above the steel target disc. The maximum voltage of the signal received by the sensor located underneath the specimen was recorded. The lower the voltage, the more the impact signal was attenuated, which indicated a better attenuation capability of the test material. **Table 4-2** shows the test setup specification and **Table 4-3** shows the voltage recorded by the sensor for each drop ball test.

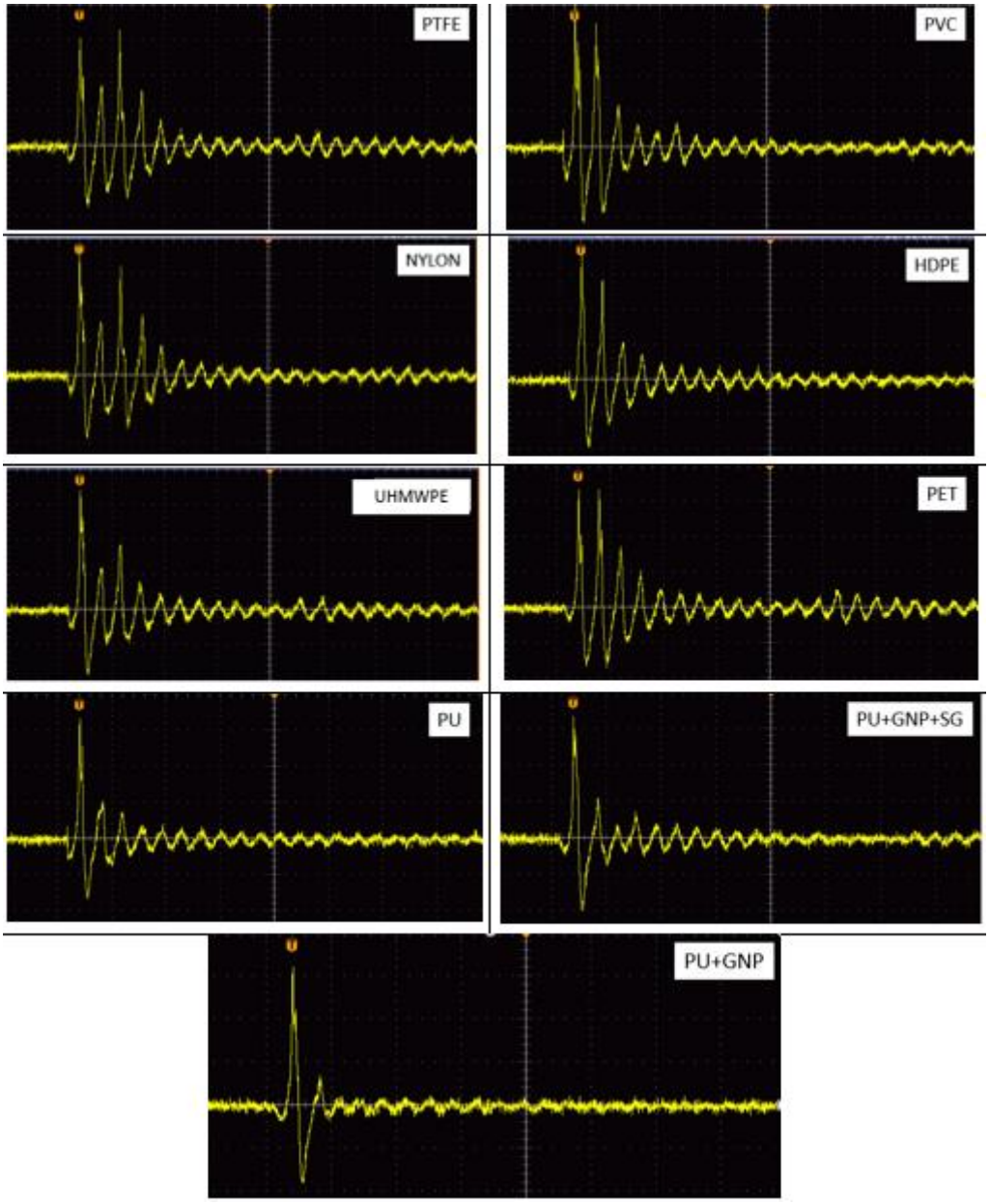

Figure 4-7 Wave signals measured by piezoelectric sensor for different specimen as a result of drop ball test.

Table 4-2 Test setup of the drop ball test.

Oscilloscope display	5mv/div; 10ms/div
Ball size	3mm
Drop height	12cm

Samples of screen shots of the oscilloscope for each specimen are shown in **Figure 4-7**. It can be seen that different materials responded in very different ways to the drop ball impact, generating different wave signals. Studies show that other factors such as the geometry of the specimen, material properties, type of the coupling and test set up also affects the generated wave signals for different materials [165, 166]. When a force is rapidly applied perpendicular to a surface, it will generate a longitudinal wave. This wave will travel through the material. Particles in the vicinity of the wave move parallel to the direction of wave propagation. As a wave propagate through a medium, its intensity decreases, and as the wave travels its intensity will reduce with distance travelled. Since the dropping of the steel ball is consistent for each test, a higher voltage signal indicates less vibration attenuation, and hence a poorer attenuation capability. It can be seen from **Table 4-3** that PTFE shows the highest voltage because of drop ball test and GNP–COOH modified polyurethane (PU + f-GNP) shows the lowest voltage, indicating that graphene modified polyurethane has the highest attenuation. **Table 4-3**, shows that this drop ball test set up is able to generate consistent results which produce waves with less than 1% variation in signal strength.

Table 4-3 Maximum voltage (mV) for the drop ball test from piezoelectric sensor measured by oscilloscope.

	Maximum Voltage (mV)					
Repeat / Specimen	**Test 1**	**Test 2**	**Test 3**	**Test 4**	**Test 5**	**Mean with 95% confidence level (v)**
PU	17.2	17.2	17.4	17.2	17	17.2 ± 0.1
PU + f-GNP	16.8	16.8	16.6	16.6	16.2	16.6 ± 0.2
PU + f-GNP + SG	17.2	16.8	16.8	17	16.6	16.9 ± 0.2
PTFE	22	20.2	22.6	20.2	20.4	21.1 ± 1.2
PVC	21.2	21	20.6	22.2	20.0	21.0 ± 0.6
NYLON	19.6	19.2	19.8	19.4	19.4	19.5 ± 0.2
HDPE	18.8	18.8	18.4	18.2	18.4	18.5 ± 0.2
UHMWPE	17.8	17.8	17.6	17.4	17.6	17.6 ± 0.1
PET	17.2	17.4	17.6	17.2	17.6	17.4 ± 0.2

As a results of this experiment, it can be said that among the PU, PU + f-GNP and PU + f-GNP + SG materials tested in this study, neat polyurethane (PU) has the lowest attenuation (**Figure 4-8**) and which improved by 3.7% by adding 0.5 wt% of GNP – COOH.

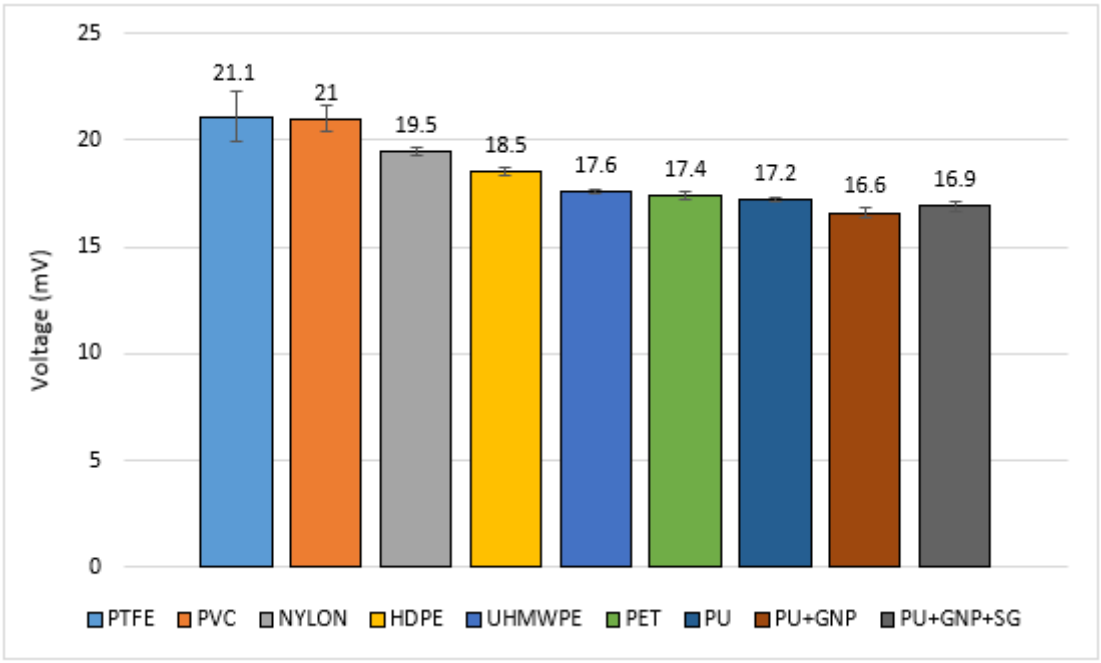

Figure 4-8 Highest voltage recorded by oscilloscope for different specimens as a results of drop ball tests.

The transmitted energy is proportional to piezoelectric voltage, higher voltage corresponds to higher transmitted energy.

4.3 Identification of modal parameters with the SVD-QR method

The objective of the drop ball test is to identify the damping coefficient of the various polymer materials. In order to do this, the modal parameters (frequency and damping ratio) of the main deformation modes of the system (those with highest amplitude and lowest frequency) should be identified. This identification is made by analysing the free response of the system after the drop ball impact. Considering linearity and disregarding higher modes (not relevant for the analysis), this free response is a linear combination of exponentially attenuated harmonic signals as shown in **(Eq. 4.2)**, which is the solution of equation of motion **(Eq.4.1)**. Each of these signals corresponds to a particular deformation mode of the system and has a characteristic frequency and damping ratio.

The EMA (Experimental Modal Analysis) method employed for the signal analysis was the QR Factorization and Singular Value Decomposition (SVD-QR) method [176, 177]. This time-domain method was developed to extract the modal parameters of structural signals of combat aircraft during flutter flight testing carried out at CLAEX (the Spanish Military Flight Test Center). These signals were short, noisy and with close modes, all of which make their analysis difficult.

This method, like most EMA methods, assumes a linear system with viscous damping (proportional to the velocity and opposing motion). It is presumed that the material deformation is elastic and consequently the non-linear effects are negligible. Consequently, the free response of the system can be represented by the following matrix differential equation:

$$[M]\{\ddot{y}\} + [C]\{\dot{y}\} + [K]\{y\} \quad (4.1)$$

where $M, C,$ and K represent the matrices of mass, damping, and stiffness, respectively and $\{y(t)\}$ is the deformation vector [178].

Therefore, $y(t)$, the deformation in one point of the system, can be represented as exponentially damped harmonic function:

$$y(t) = \sum_{i=1}^{n} h_i(t) = \sum_{i=1}^{n} \left\{ A_i \, sin(2\pi f_i t)\, e^{-2\pi \xi_i f_i t} + B_i cos(2\pi f_i t) e^{-2\pi \xi_i f_i t} \right\} \quad (4.2)$$

This equation indicates that the deformation in one point of the system is the result of the addition of n different modes $h_i(t)$ with the associated frequencies f_i and damping ratio ξ_i.

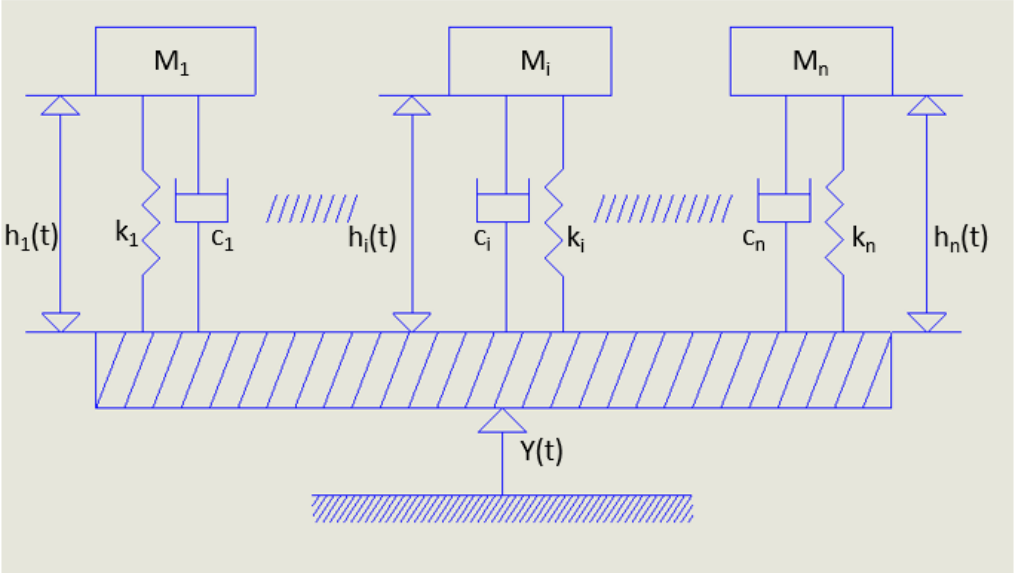

Figure 4-9 Equivalent System

The traditional EMA methods try to adjust (e.g. least squares) the experimental values of the response to the **(Eq. 4.2)** in order to find the 4 values of A_i, B_i, f_i and ξ_i for each of the n modes M_i.

The SVD-QR method takes advantage of a property of linearity of the exponentially damped harmonic functions and consequently of $y(t)$. Assuming that there are n modes and $2n+1$ segment of time of the same length are taken, the response in one period is a linear combination of the responses in the other $2n$ periods.

Assuming that $2p$ samples of the response $y(t)$ has been acquired, $y(t_1), y(t_2), \dots, y(t_{2p})$, a Henkel matrix can be built up:

$$H=\begin{pmatrix} y(t_1) & y(t_2) & \dots & y(t_p) \\ y(t_2) & y(t_3) & \dots & y(t_{p+1}) \\ \vdots & \vdots & \ddots & \vdots \\ y(t_p) & y(t_{p+1}) & \dots & y(t_{2p}) \end{pmatrix} \quad (4.3)$$

Due to the linearity property of $y(t)$ only $2n$ files (or $2n$ columns) are independent, i.e. only $2n$ files are required to represent the whole signal $y(t)$.

As only $2n$ files are necessary, the following step is to select these files and to truncate the matrix H. However, it is paramount to choose the $2n$ files that provide maximum information, i.e. the $2n$ files that are most orthogonal among each other should be selected.

The QR decomposition of the matrix H into a product of an orthogonal matrix Q and an upper triangular matrix R provides a permutation matrix M_p, such that:

$$H \times M_P = Q \times R; \qquad Q^T \times Q = I; \qquad r_{ij} = 0 \; \forall i > j \tag{4.4}$$

$$B = M_p^T \times H \tag{4.5}$$

The files of the matrix H have been reorganised with the permutation matrix M_p in such a way that the $2n$ first files of matrix B provide the maximum of information.

Truncating the matrix B and retaining only the first $2n$ files, the matrix B_t is generated:

$$B_t = \begin{pmatrix} y(t_{s1}) & y(t_{s2}) & \dots & y(t_{sp}) \\ y(t_{u1}) & y(t_{u2}) & \dots & y(t_{up}) \\ \vdots & \vdots & \ddots & \vdots \\ y(t_{o1}) & y(t_{o2}) & \dots & y(t_{op}) \end{pmatrix} \tag{4.6}$$

Since the function of the response $y(t)$ is well known **(Eq. 4.2)**, selecting a frequency f_s and damping ratio ξ_s, a synthetic response can be generated:

$$x(t_K) = \sin(2\pi f_s t_K)\, e^{-2\pi \xi_s f_s t_K} \Leftrightarrow X = [x(t_1) \quad x(t_2) \quad \dots \quad x(t_p)] \Leftrightarrow X^I = \frac{X}{\|X\|} \tag{4.7}$$

The last operation shown in **(Eq. 4.7)** is the division of the components of vector X by its own Euclidean norm, in such a way the norm of vector X^I is one.

Including the vector X^I in the matrix B_t, the extended matrix B_{te} is created:

$$B_{te}(f_s, \xi_s) = \begin{pmatrix} y(t_{s1}) & y(t_{s2}) & \dots & y(t_{sp}) \\ y(t_{u1}) & y(t_{u2}) & \dots & y(t_{up}) \\ \vdots & \vdots & \ddots & \vdots \\ y(t_{o1}) & y(t_{o2}) & \dots & y(t_{op}) \\ x^I(t_1) & x^I(t_2) & \dots & x^I(t_p) \end{pmatrix} \tag{4.8}$$

In the case, in which, the frequency f_s and the damping ratio ξ_s correspond to a mode $h_i(t)$ of the response, the matrix B_{te} will have a rank very close to $2n$. It cannot be exactly $2n$ because the signal $y(t)$ has always some noise. If the parameters do not correspond to those of a mode the rank of matrix B_{te} would be $2n + 1$.

To assess how the rank of the Matrix B_{te} is close to $2n$ or to $2n + 1$, its pseudo-determinant $\psi(f_s, \xi_s)$ is calculated using the SVD (Singular Value Decomposition):

$$B_{te}(f_s,\xi_s) = U \times S \times V^T \Rightarrow S(f_s,\xi_s) = \begin{pmatrix} s_1 & 0 & \dots & 0 \\ 0 & s_2 & \dots & 0 \\ \vdots & \vdots & \ddots & \vdots \\ 0 & 0 & \dots & s_{n+1} \end{pmatrix};\ s_1 \geq s_2 \geq \cdots \geq s_{n+1} \quad (4.9)$$

$$\Psi(f_s,\xi_s) = s_1 \times s_2 \times \dots \times s_{n+1} \quad (4.10)$$

If the ranges of possible values for the modal frequencies and damping ratio of the signal $y(t)$ are known, a search can be performed in such both ranges. In **Figure 4-10** the range of search for frequency is 915 Hz, 920 Hz and 925 Hz, and the range for damping ratio is from 0.005 to 0.055 with increments of 0.005. In total, as shown in **Figure 4-10**, there are 33 sets of frequency and damping ratio.

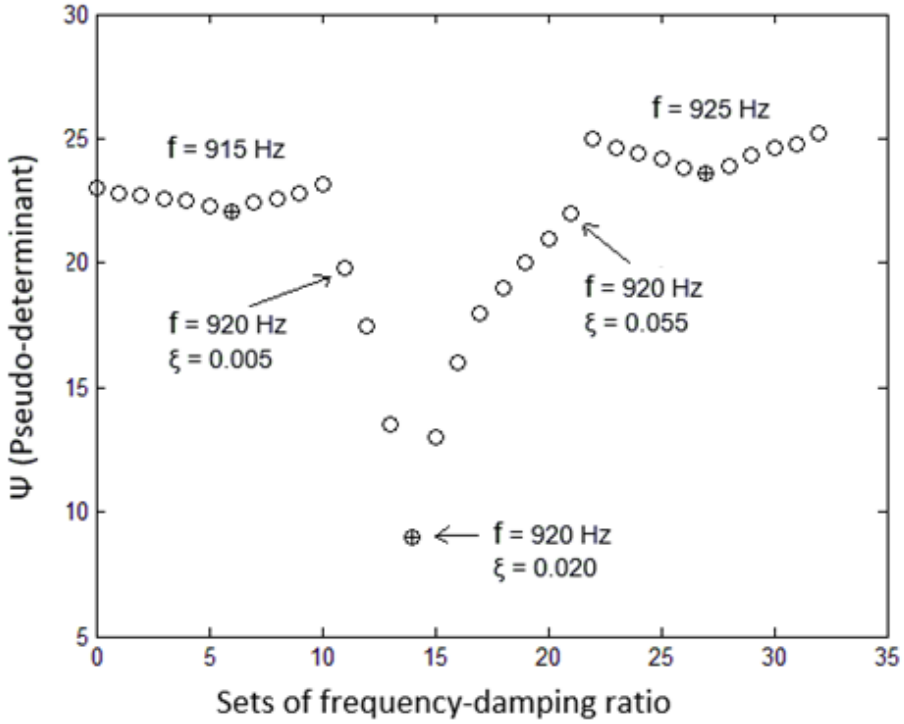

Figure 4-10 Pseudo-determinant for values of frequency and damping ratio.

For each value in the range of frequencies, the pseudo-determinant was calculated. For such a value of frequency, the damping ratio corresponding to the minimum value of pseudo-determinant is chosen. In **Figure 4-10**, for a frequency of 920 Hz, the associated damping ratio is 0.020.

In case the set of frequency and damping ratio resulting in minimum pseudo-determinant, corresponded to a mode and if the signal $y(t)$ were noiseless, the pseudo-determinant would be zero.

Now, a function associating the frequencies in the searching range with a value of pseudo-determinant (and a value of damping ratio) has been generated.

The minimums of this function correspond to frequencies (and associated damping ratios) of the modes of the response $y(t)$.

When the number of modes of the response is unknown (n is not available), it is useful to calculate the parameters for various values of number of modes and compare the results.

On the other hand, special attention must be taken when choosing a segment of signal for the analysis. It is important to ensure that the segment corresponds to a free response and it is not included with contributions corresponding to forced response of the specimen during the impact duration of the ball.

4.3.1 Experimental results of damping coefficient using SVD-QR method

There are three different types of damping: coulomb, which is caused by kinetic friction between sliding dry surfaces; viscous damping which happens when heat is dissipated due to the movement of bodies in a liquid medium; and hysteresis damping is when a solid is deformed and heat is dissipated by internal friction. Hard materials such as metals and ceramics do not show hysteresis damping under a moderate load but soft materials like polymers exhibit large hysteresis [179]. Damping capability is influenced by different factors such as the nature of material, modulus, frequency, temperature and defects [179].

The damping coefficient is a material property that indicates whether a material will bounce back or return energy to a system. For instance, if returning the energy (bounce back) is caused by an unwanted vibration, a high damping coefficient in the material will reduce the response; it will dissipate the energy and reduce the undesired reaction. Materials with high damping coefficients are used in applications of shock absorption, vibration control, and noise reduction. Viscoelastic properties and glass transition temperature are two important factors which influence the vibration damping of polymers [179]. Polyurethanes are attractive for damping applications as they can be modified in order to change their glass transition temperature [180, 181]. For example, increasing the hard segment content of the PU increases the rigidity. The addition of carbon nanoparticles to PU can affect the T_g in two different ways: it can increase the T_g by restricting the molecular motion due to the well-dispersed carbon nanoparticles; or can reduce the T_g by modifying the degree of phase separation (DPS) [182, 66]. It is known that in a PU structure there are two different types of carbonyl groups (C=O), some of them are located at the interfacial zone between hard and soft segments which can be either free or H-

bonded and some of them are located in the hard domain which are H-bounded only. DPS or degree of phase separation can be calculated using below equation:

$$\text{DPS} = \frac{Cb_{C=O}}{Cf_{C=O}+Cb_{C=O}} \quad (4.11)$$

Where C_b is the coefficient of hydrogen bonded urethane and C_f is the free urethane [183].
For example, comparing PU20 containing 20% hard segment + 1wt% f-GNP with PU40 containing 40% hard segment + 1wt% f-GNP showed that PU40 has higher $T_g = 46$ ℃ than PU20 with $T_g = 41$℃ [184]. It should be noted that adding nanomaterials may not increase the glass transition temperature of the PU if the nanomaterials dispersion in the polymeric matrix is poor and not uniform [185].
A mechanical vibrating system is classified according to its damping ratio ξ as: underdamped if $\xi < 1$, critically damped if $\xi = 1$, and overdamped if $\xi > 1$. In all these cases, the response of a system set into motion will eventually decay to zero with time, except when $\xi = 0$ [186].

The damping coefficient is equal to the $\tan\delta$ and to calculate the damping ratio,ξ, this equation can be used:

$$\tan\delta = 1/n\pi \quad (4.12)$$

Where *n* is number of cycles the signal decays $e = 2.718$. The first order damped system amplitude multiplier is $e^{-\xi\omega_n t}$. So when the exponent is -1, it will have a decay magnitude of *e* and therefore,

$$\xi = 1/\omega_n t \quad (4.13)$$

Hence,

$$\tan\delta = 2\xi = \frac{2}{\omega_n t} \quad (4.14)$$

Table 4-4 Damping coefficient, damping ratio and voltage measured by the drop ball test.

Sample	Frequency (200 - 300 Hz)		Frequency (500 - 600 Hz)		Frequency (700 - 1000 Hz)		
	Damping coefficient (tan δ)	**damping ratio (ξ)**	**Damping coefficient (tan δ)**	**damping ratio (ξ)**	**Damping coefficient (tan δ)**	**damping ratio (ξ)**	**Voltage (mV)**
PU	0.0250±0.0017	0.0125	0.0485±0.0073	0.0243	0.0813±0.0041	0.0407	17.2
PU+f-GNP	0.0343±0.0061	0.0172	0.0651±0.0012	0.0326	0.1073±0.0044	0.0535	16.6
PU+f-GNP+SG	0.0305±0.0026	0.0153	0.0622±0.0079	0.0311	0.0848±0.0023	0.0424	16.9
PTFE	0.0210±0.0045	0.0105	0.0290±0.0039	0.0145	0.0348±0.0032	0.0174	21.1
PVC	0.0245±0.0035	0.0123	0.0425±0.0079	0.0213	0.0345±0.0016	0.0173	21
NYLON	0.0240±0.0028	0.0120	0.0525±0.0061	0.0253	0.0350±0.0022	0.0175	19.5
HDPE	0.0235±0.0038	0.0117	0.0505±0.0084	0.0253	0.0388±0.0061	0.0194	18.5
PET	0.0240±0.0037	0.0120	0.0408±0.0121	0.0204	0.0405±0.0081	0.0203	17.4
UHMWPE	0.0245±0.0008	0.0123	0.0415±0.0132	0.0208	0.0435±0.0029	0.0218	17.6

PUs are classified as underdamped materials and their damping ratio typically range from 0.05 to 0.15 [187, 188, 144, 143], e.g. damping coefficient of the PU at 30°C is reported 0.1 [143] and at room temperature and 1000Hz is 0.05 [188]. Damping coefficient (tan δ) and damping ratio (ξ) of the drop ball tests with 95%confidenece level at specified frequencies can be find in **Table 4-4**.

Figure 4-11 shows Pseudo-determinant ψ for different frequency and damping values for all materials tested in this study. Inspection of **Table 4-4** shows that the voltage results decrease as tan δ increase which means that when a material has low damping coefficient it has less ability to dissipate the energy of the system and that is why the sensor records higher voltage as a result of drop ball test. Among all materials tested in this study, GNP–COOH modified polyurethane has the highest damping coefficient and shows the lowest voltage recorded by the sensor indicating it is the best attenuating materials among tested polymers. PTFE and PVC show the highest voltage recorded and the lowest damping coefficients.

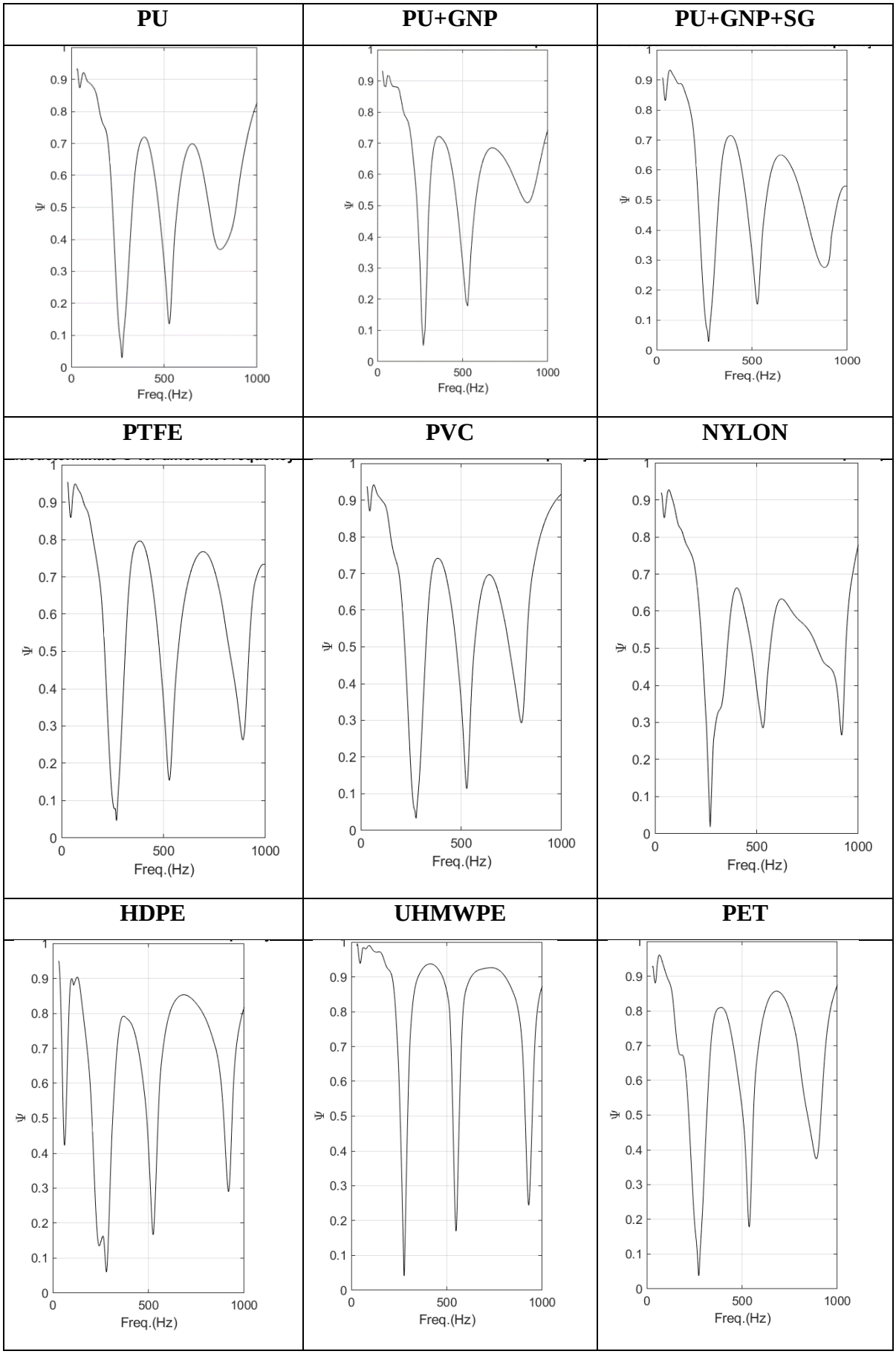

Figure 4-11 Drop ball test results analysis by SVD-QR for all tested materials.

Plots of the damping coefficient versus voltage for frequency range 200-300Hz, 500-700Hz and 700-1000Hz are shown in **Figure 4-12**. From this plot it is evident that the PU and graphene modified PU have higher damping coefficient at higher frequencies, and PU +GNP nanocomposite has 3.14 time increase in damping coefficient at 700-1000Hz relative to its damping coefficient at low frequency range of 200-300Hz. Among PU and nanomodified PU, the highest damping coefficient at all frequency ranges belongs to PU + GNP nanocomposite. Previous work has shown that the graphene increases the damping coefficient and the tortuosity of the neat polyurethane by decreasing the cell size of the PU structure and simultaneously the high aspect ratio and surface area/volume ratio of graphene contribute to the very efficient "stick-slip mechanism" of vibration damping at PU/GNP interfaces, which cause more energy dissipated by interfacial sliding [189].

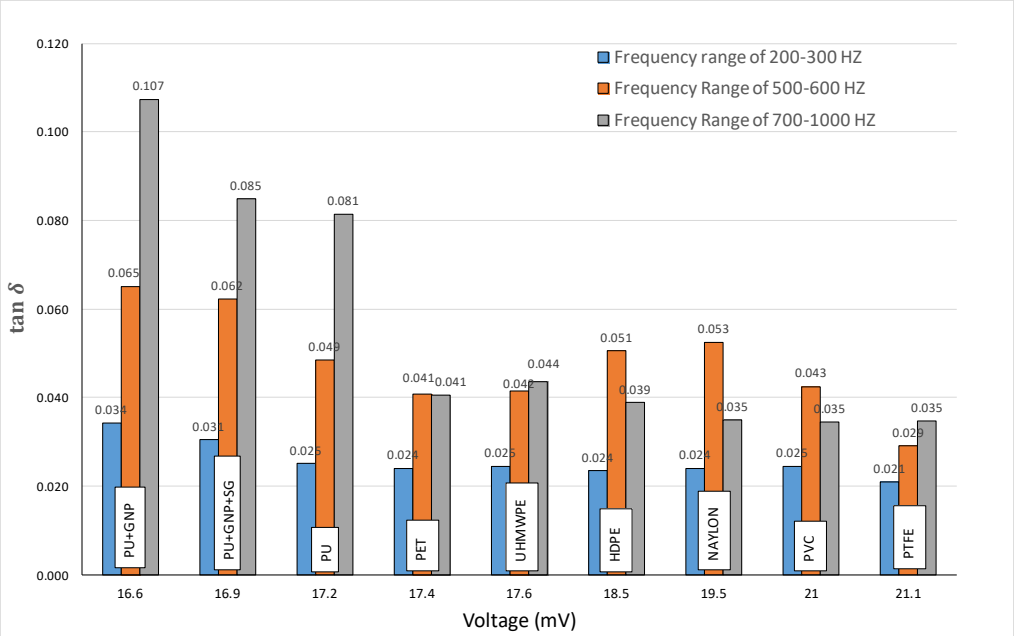

Figure 4-12 Damping coefficient vs. maximum voltage in the frequency range of 200 to 300Hz, 500 to 600 Hz and 700-1000Hz.

Figure 4-13 show variation of damping coefficient ($\tan\delta$) versus frequency for the PU, PU + GNP and PU + GNP + SG. The trend is that at higher frequencies $\tan\delta$ will increase for all three types of polyurethanes. Also, adding f-GNP to PU has significant effect on the amount of increase in $\tan\delta$ for all three frequency ranges but adding GNP + SG to PU had only significant effect on $\tan\delta$ in frequency range of 200-300Hz and 500-600Hz and at high frequency range of 700-1000Hz its effect is diminishing.

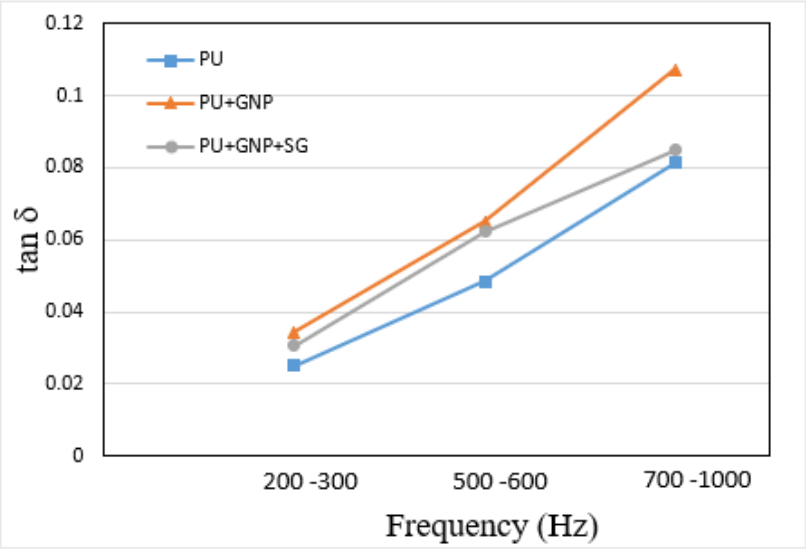

Figure 4-13 $\boldsymbol{tan\,\delta}$ at three frequency ranges for PU, PU+GNP and PU+GNP+SG.

4.4 Summary of damping test

In this study the damping properties of f-GNPs and f-GNP/SG based PU nanocomposites together with untreated PU for three different frequency ranges have been investigated by a drop ball test. The damping properties of HDPE, NYLON, PET, PTFE, and UHMWPE were also measured for comparison.

In drop ball test, the amount of voltage recorded by the piezoelectric sensor is very sensitive to the experimental setup, test specimen preparation and surface condition of the specimen. By keeping the experimental condition stable, and by repeating the test on each specimen five times, reliable results have been obtained. The test results at 95% confidence level show that PTFE and PVC attenuate the least and PU + f-GNP, PU + f-GNP + SG and neat PU attenuate the most. It was shown that graphene modified polyurethane has the highest damping coefficient among all tested materials at all frequency ranges.

The singular value decomposition and QR factorization method has been applied to the analysis of drop ball test data and the frequency and damping of the relevant modes are identified. The results show that by adding GNP–COOH (0.5wt%) to neat polyurethane, the damping coefficient increased by 37.2% for the 200 – 5300Hz range, increased by 34% for the 500 – 600Hz range and increased by 32% for the 700 – 1000Hz range. Adding 1wt% hydrophobic silica-based solution to the GNP–COOH modified polyurethane increases the damping coefficient of the PU by 22% for the 200 – 300Hz range and 28% for the 500 – 600Hz range. However, there is no significant effect on the damping coefficient for 700 – 1000Hz range.

In summary, the carboxyl functionalised graphene nanoplatelets (GNP–COOH) increases the damping coefficient of the neat polyurethane by decreasing the cell size of the PU structure and simultaneously the high aspect ratio and surface area/volume ratio of graphene contribute in very efficient "stick-slip mechanism" of vibration damping at PU/f-GNP interfaces. The developed polyurethane nanocomposite materials have great potential for protecting leading edge erosion of wind turbine.

Comparing the tan δ results measured from DMA tests in Chapter 3 with the ones obtained in this chapter from drop ball tests shows that although these tests were not performed at the same frequency ranges, but consistently the highest tan δ is for PU+GNP samples followed by PU+GNP+SG one and the lowest amount is for pure PU samples.

4.5 Resilience tests

A very common test for measuring the rebound or resilience property of elastomers consists of dropping a metal ball from a known height onto a firmly supported specimen and measuring the rebound height is called a resilience test. Resilience tests are based on the principle of conservation of energy within a closed system. The ball when dropped from a standard height has a total potential energy before being released and this energy transforms into kinetic energy during the free fall. The balls reach to its maximum kinetic energy immediately before impact which, in a perfectly elastic system, would result in the ball rebounding to the starting height. In actuality, at impact some of the kinetic energy is transformed into sound, heat, vibration and deformation energy and the ball rebound to a height less than the original height. The molecular structure and physical properties of various polymers, as well as the construction of the ball, will cause the rebound to differ. PU elastomer coatings have better erosion resistance than most metals owing to their softness and high capability for elastic deformation [190]. In fact, the PU elastic deformation enables the coating absorb the kinetic energy and gradually decelerating the impacting particles with minimal damage to the protected system. The kinetic energy absorbed in the form of elastic strain energy will be released later to rebound the particle from the surface. Hutchings et al. [190] showed that rebound resilience is the most dominant factor affecting the wear resistance of rubber elastomers. Materials with higher rebound resilience (the ratio of energy given up in recovery from deformation to the energy required to produce the deformation, usually expressed in percent) had the higher erosion resistance.

In this section, the effect of modifying PU with GNP and GNP+SG on the resilience behaviour of the PU will be studied.

4.5.1 Resilience tests set up

The apparatus was used for this experiment to perform the resilience tests shown in **Figure 4-14**. This apparatus was manufactured according to the standard D2632–15. Various stages of design and manufacturing are shown in **Figure 4-14**. A plunger is released from a set height and it hits the specimen and the rebound of the plunger was recorded in the experiment. Specification of the plunger can be finding in **Figure 4-15**.

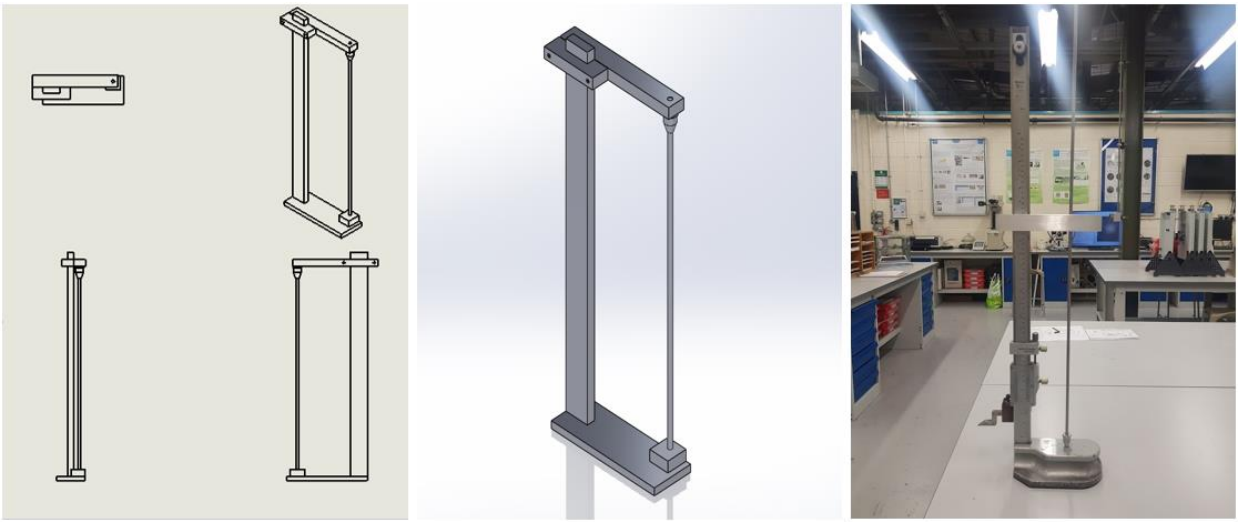

Figure 4-14 Manufacturing the apparatus for vertical rebound test.

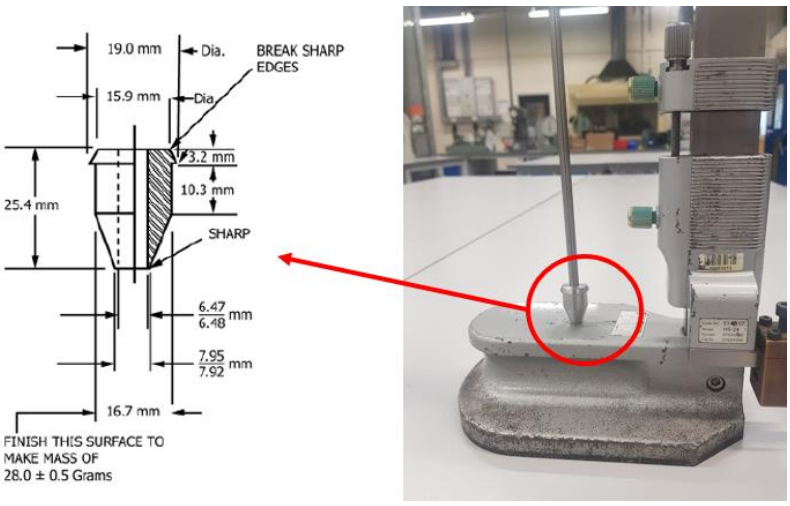

Figure 4-15 Plunger specification according to the Standard D2632.

The tracking of the plunger during its flight from the release to the end of the stationary position after rebound was recorded by a motion capture system (OptiTrack technology). This system includes a motion capture software and sixteen high-speed tracking cameras. Advantages of

this system are offering high precision, independent on external factors such as number of cameras, portable, unlimited range and its capability to capture multiple performances simultaneously. This system is capable of sub-20 µm accuracy in optimal conditions [191]. Manufactured vertical rebound apparatus was placed in the centre of the room which was surrounded by 16 cameras as shown in **Figure 4-16**. Tracking tapes were attached to the plunger so the cameras can detect the position of the plunger in real time during the tests (**Figure 4-17**).

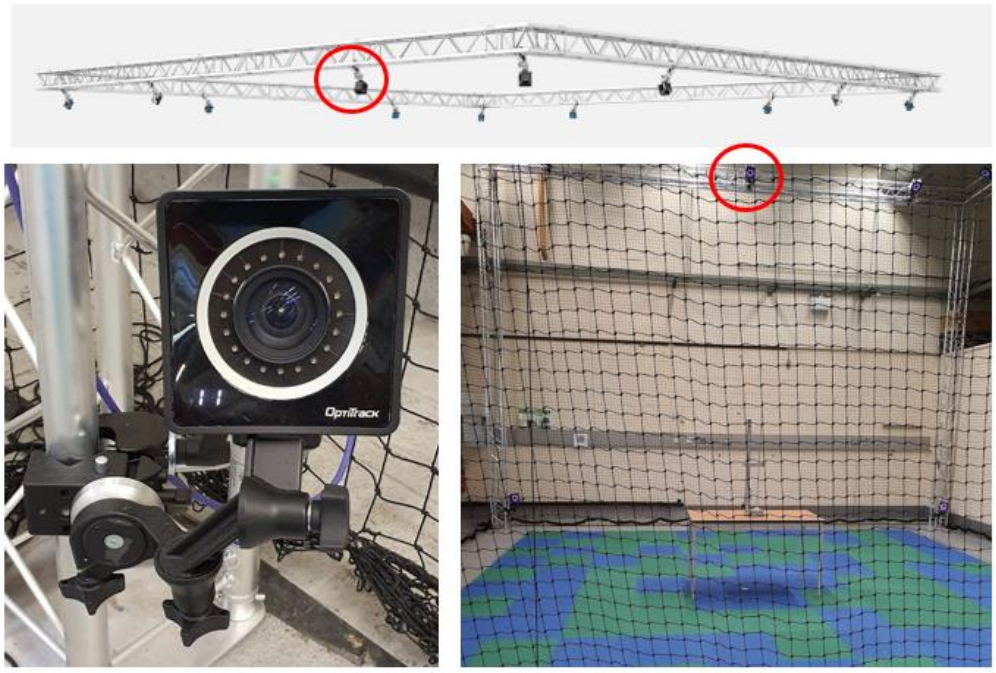

Figure 4-16 Motion capture system (OptiTrack).

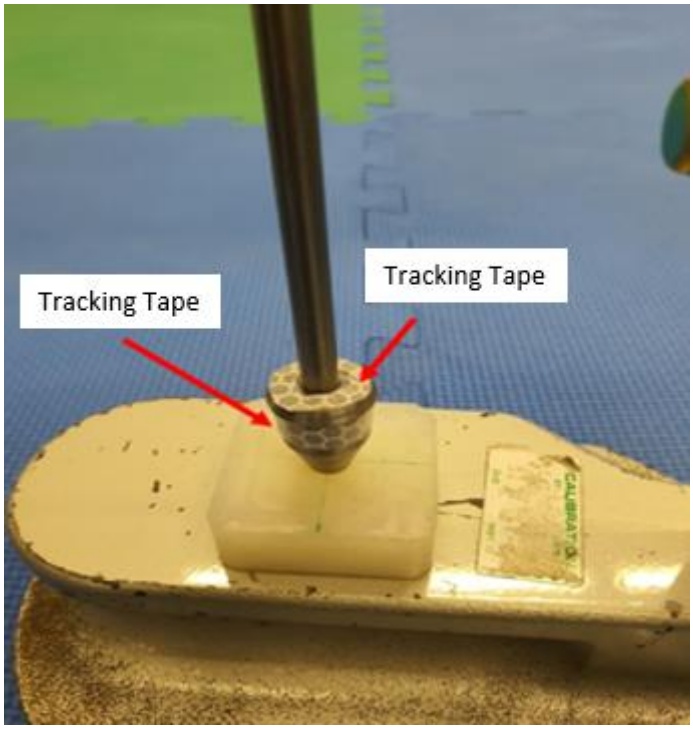

Figure 4-17 Covering plunger with tracking tape.

When the plunger is dropped, the camera starts recording the position of the plunger at each half of the second by using optical motion capture software which called motive, and the signals are recorded by the computer. The recorded data contains the position of the plunger at any time of the flight. Sequence of transferring the data from cameras to computer can be seen in **Figure 4-18**.

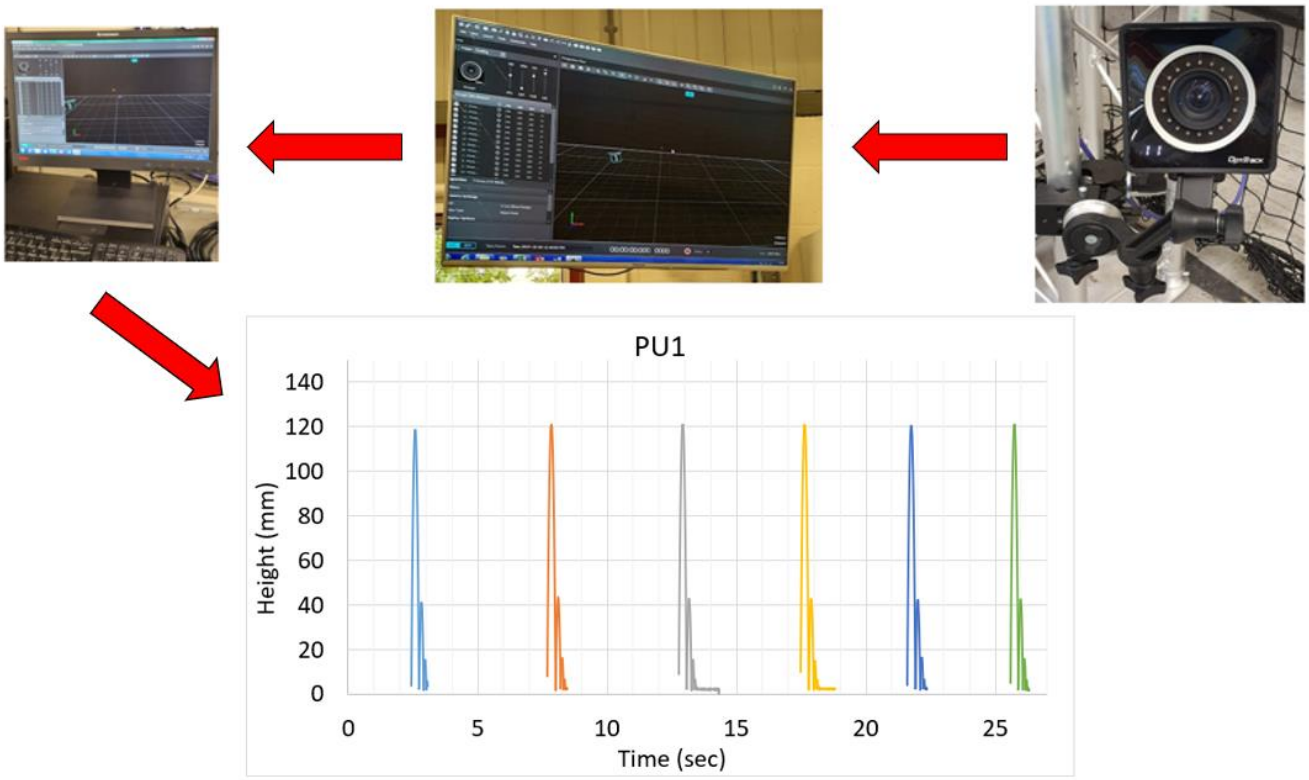

Figure 4-18 Sequence of transferring the data from camera to excel file.

4.5.2 Manufacturing of samples

The resilience tests were conducted according to the standard D2632–15, with cubic specimen with the dimension of 40×40×15mm. Resilience is very sensitive to temperature changes and to depth of penetration of the plunger. Therefore, all the experiments have been conducted in the same environmental condition at room temperature (25°C). The specimens either could be cut from a slab or specifically moulded. The dimensions of the specimen were chosen in a way that the point of plunger impact is at least at a minimum distance of 14mm from the edge of the specimen. In this work the specimens were made by casting in a mould. The mould was designed and manufactured using a milling machine as shown in **Figure 4-19**.

Figure 4-19 Manufacturing of the mould for casting the resilience test specimens.

After manufacturing the mould the PU and modified PU materials were poured in the mould and cured at room temperature (see **Figure 0-20**). The specimens were coded as shown in the **Table** 4-5.

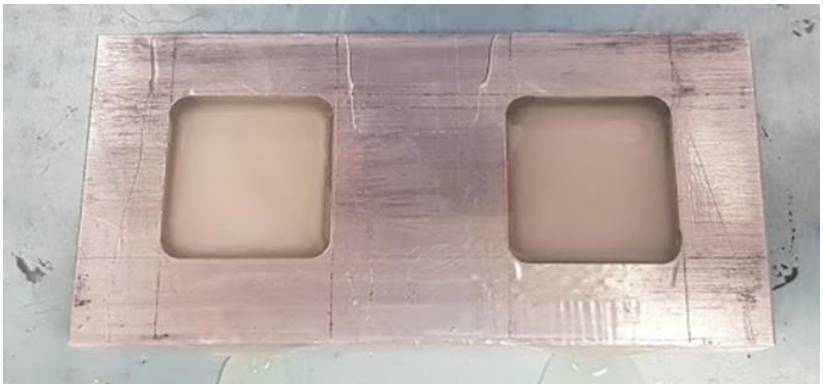

Figure 0-20 Pouring the neat polyurethane into the mould.

Table 4-5 Specimens coding.

Sample	Code
Neat PU	PU1
	PU2
PU+0.5wt% GNP	PU/f-GNP1
	PU/f-GNP2
PU+ 0.5wt% GNP + 1wt% SG	PU/f-GNP/SG1
	PU/f-GNP/SG2

4.5.3 Results of resilience tests

Three different types of coating materials were tested and for each type of material two specimens were manufactured. For each specimen, the test was repeated six times and the average of the rebound height was measured to calculate the transformed energy.

For this experiment the plunger is dropped on the top surface of the specimens from 400mm height. In a fully elastic deformation of the material upon impact, the plunger would rebound to its initial height. Substrates with higher damping characteristic or plastic deformation will dissipate or store small amounts of plunger energy and the plunger will rebound to a reduced height. Eq. (4.15) is used to calculate the energy transformed.

$$\%\ \text{Energy Transformed} = [\frac{h_0 - h_r}{h_0}] \times 100\% \qquad (4.15)$$

Where h_0 is the initial height of the plunger where the ball dropped and h_r is the average rebound height. By assuming that the energy loss during plunger drop to hit the material is negligible (i.e $E_{loss} \approx 0$), the velocity of the plunger just before hitting the material for the first time (v_1) can be found from Eq. (4.16).

$E_2 = E_1 - E_{loss}$

$E_1 = E_2 \rightarrow mgh_0 = \frac{1}{2}mv_1^2$

$$v_1 = \sqrt{2gh_0} \qquad (4.16)$$

The results of the vertical rebound tests are shown in **Figure 4-21** to **Figure 4-23** and they are summarised in **Table 4-6**.

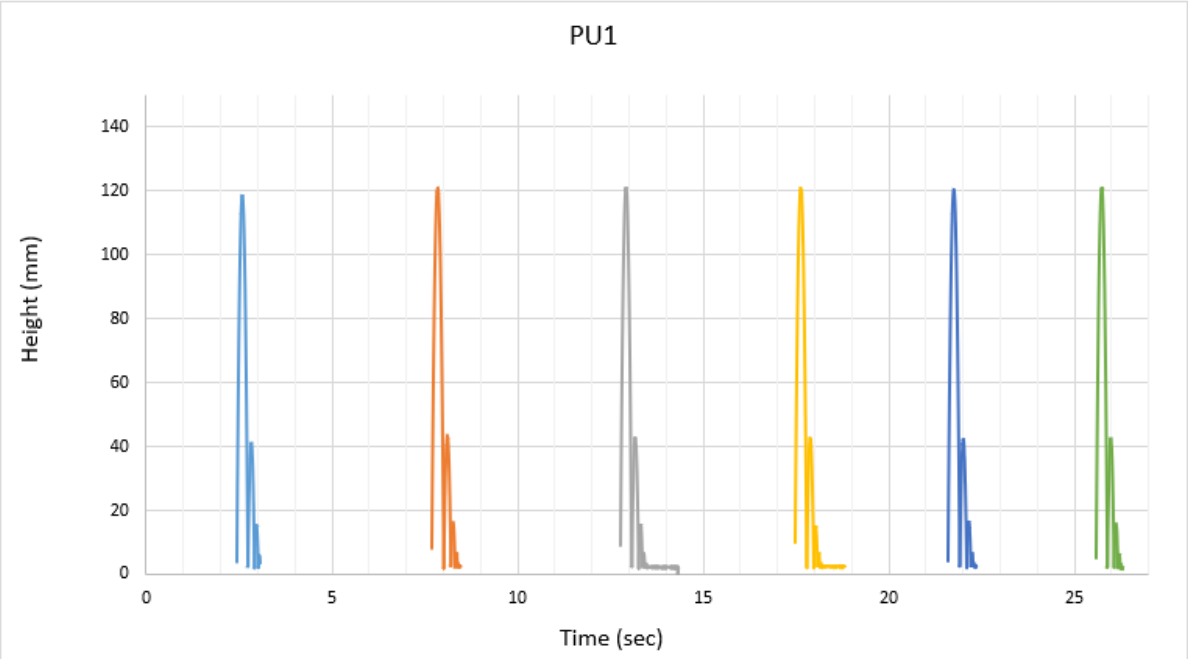

Figure 4-21 Variation of rebound height versus time in the drop ball test on pure PU1 in six attempts.

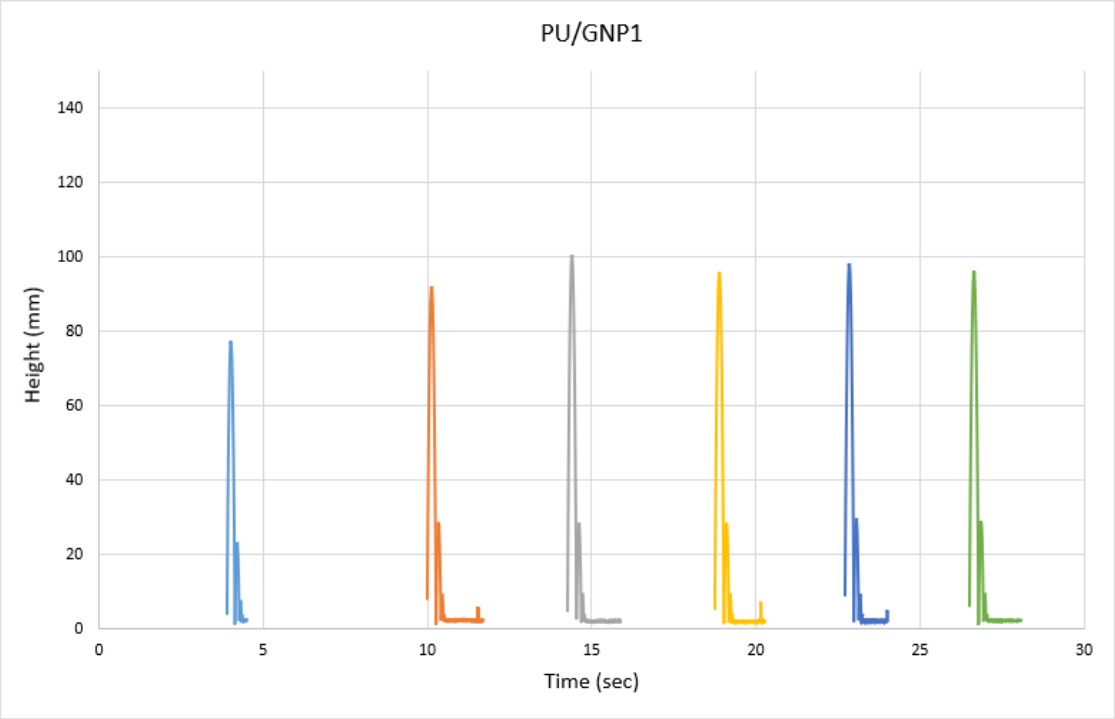

Figure 4-22 Variation of rebound height versus time in the drop ball test on pure PU+GNP1 in six attempts.

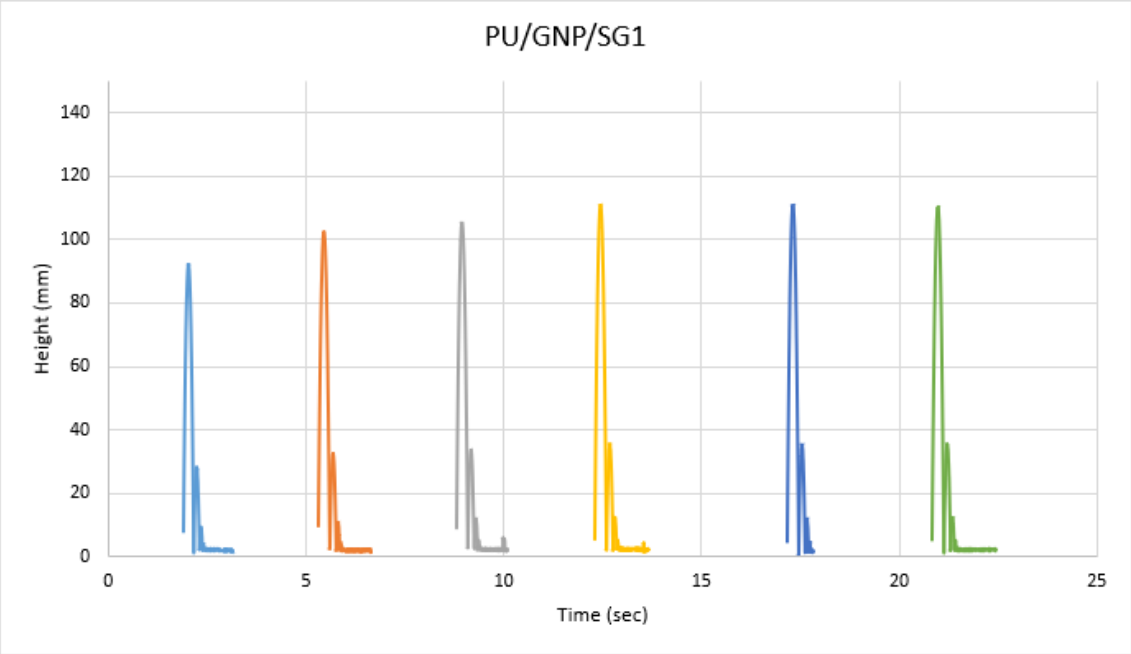

Figure 4-23 Variation of rebound height versus time in the drop ball test on pure PU+GNP+SG1 in six attempts.

Table 4-6 Results of the vertical rebound tests on the neat PU, PU+GNP and PU+GNP+SG.

	Test no.	**1**		**2**		**3**		**4**		**5**		**6**	
PU-1	Cycle	y mm	t s	y mm	t s	y mm	t s	y mm	t s	y mm	t s	y mm	t s
	1	114.9	0.16	119.7	0.15	118.3	0.15	117.6	0.15	116.6	0.16	119	0.16
	2	38.5	0.09	41.8	0.09	40.4	0.09	40.7	0.09	39.5	0.09	40.1	0.09
	3	13.3	0.05	13.5	0.05	13.6	0.06	12.9	0.05	13.3	0.05	13.5	0.05
	(n)	0	3.66	0	2.78	0	2.88	0	3.19	0	3.16	0	3.05
PU-2	1	117.1	0.16	113.5	0.15	117.7	0.15	112.8	0.15	118.5	0.15	115.2	0.15
	2	39.5	0.09	38.7	0.09	38.5	0.09	36.2	0.09	39.8	0.09	36.1	0.08
	3	11.9	0.05	11.5	0.05	12.1	0.05	12.3	0.05	12.1	0.05	11.9	0.05
	(n)	0	2.86	0	2.71	0	2.85	0	2.78	0	2.75	0	2.75
PU+GNP-1	1	84.4	0.125	94.8	0.134	99.2	0.133	94.6	0.14	98.1	0.14	95.4	0.132
	2	21.5	0.071	26.7	0.074	27.2	0.074	27.4	0.075	25.5	0.071	27.5	0.075
	3	6.5	0.03	7.2	0.05	6.7	0.04	6.5	0.04	7.4	0.04	6.9	0.04
	(n)	0	2.11	0	2.43	0	2.48	0	2.58	0	2.51	0	2.58
PU+GNP-2	1	83.9	0.13	86	0.13	84.3	0.13	84.9	0.13	84.1	0.134	87.2	0.135
	2	21.9	0.063	23.5	0.067	22.3	0.067	23.3	0.067	22.8	0.067	24.1	0.068
	3	5.4	0.03	5.6	0.03	5.6	0.03	5.1	0.03	4.9	0.03	5.4	0.03
	(n)	0	2.01	0	2.28	0	1.99	0	1.85	0	1.93	0	2.133
PU+GNP+SG-1	1	90.3	0.14	97.7	0.15	98.4	0.15	109.3	0.15	102.5	0.14	109	0.15
	2	26.9	0.07	33.3	0.08	30.1	0.07	34.4	0.08	34.9	0.07	34.3	0.08
	3	7.2	0.041	10.3	0.05	8.9	0.042	10.6	0.046	9.3	0.076	10.4	0.05
	(n)	0	3.16	0	2.28	0	2.07	0	1.82	0	2.2	0	2.33
PU+GNP+SG-2	1	103.6	0.15	112.1	0.15	112.3	0.15	110.5	0.15	111.8	0.15	112	0.15
	2	30.4	0.08	34.4	0.083	34.2	0.083	34.9	0.088	35.2	0.087	36.8	0.087
	3	9.5	0.054	11.3	0.046	11.5	0.05	12.3	0.05	12.1	0.05	13.5	0.046
	(n)	0	3.092	0	2.5	0	2.01	0	2.38	0	2.7	0	2.89

* n = After n cycles, plunger will not rebound anymore and rest in zero height position (y= 0).

Table 4-6 shows that after the plunger hits the specimen, considerable amount of the kinetic energy was absorbed by specimen. The amount of energy that absorbed by the neat PU is less than the other two modified PU materials. After three rebounds (3rd cycle), 96.85% of energy is transferred to the PU, 98.48% to the PU+GNP and 97.35% to the PU+GNP+SG specimens.

Table 4-7 summarises the rebounding speed of the plunger after hitting the specimens. PU+GNP material has the least rebound speed after the first hit at 41.8 mm/s. The rebound speed of PU and PU+GNP+SG after the first hit are 47.9 mm/s and 45.8 mm/s, respectively. The results shows that more energy was absorbed by the graphene modified PU coating material.

Table 4-7 Energy transformed after the plunge hit the specimens.

Specimen	1	Average		2	Average		Ball rebound (cm)			% Energy Transformed
		y(mm)	t (s)		y(mm)	t (s)	y(mm)	t (s)	V_1 (mm/s)	
Pure PU	Cycle 1	117.7	0.15	Cycle 1	115.8	0.15	116.7±1.13	0.15±0	47.9	70.83
	Cycle 2	40.2	0.09	Cycle 2	38.1	0.09	39.1±0.15	0.09±0	27.7	90.23
	Cycle 3	13.4	0.05	Cycle 3	11.9	0.05	12.6±0.10	0.05±0	15.7	96.85
	n	0	3.12	n	0	2.78	0	2.95±0.24	0.0	100.00
PU+GNP	Cycle 1	92.8	0.13	Cycle 1	85.1	0.13	88.9±0.53	0.13±0	41.8	77.78
	Cycle 2	26	0.07	Cycle 2	23	0.07	24.5±0.21	0.07±0	21.9	93.88
	Cycle 3	6.9	0.04	Cycle 3	5.3	0.03	6.1±0.11	0.03±0.01	10.9	98.48
	n	0	2.45	n	0	2.03	0	2.24±0.29	0.0	100.00
PU+GNP+SG	Cycle 1	103.2	0.15	Cycle 1	110.4	0.15	106.8±0.49	0.15±0	45.8	73.30
	Cycle 2	31.6	0.08	Cycle 2	34.3	0.08	32.9±0.18	0.08±0	25.4	91.78
	Cycle 3	9.5	0.05	Cycle 3	11.7	0.05	10.6±0.15	0.05±0	14.4	97.35
	n	0	2.33	n	0	2.60	0	2.46±0.19	0.0	100.00

* n = After n cycles, plunger will not rebound anymore and rest in zero height position (y= 0).

Figure 4-24, Figure 4-25 and **Figure 4-26** shows the difference between the heights of the plunger after rebound, rebound velocity and also the difference in the amount of the energy transmitted for three different coating materials.

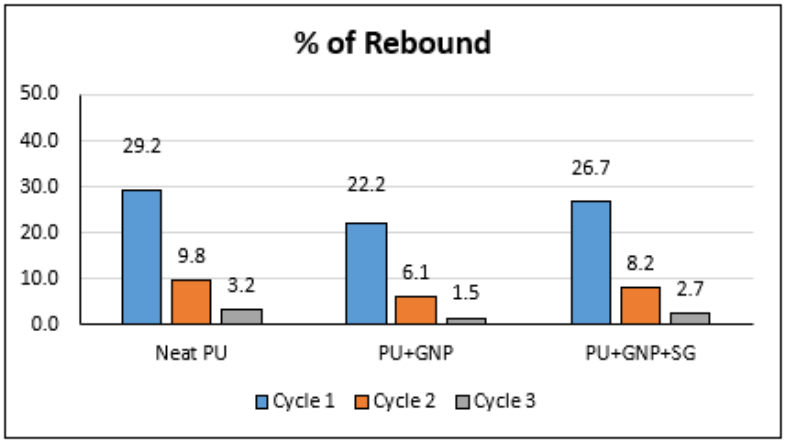

Figure 4-24 Percentage of rebound in the first three cycles for the neat PU, GNP modified PU and GNP/SG modified PU.

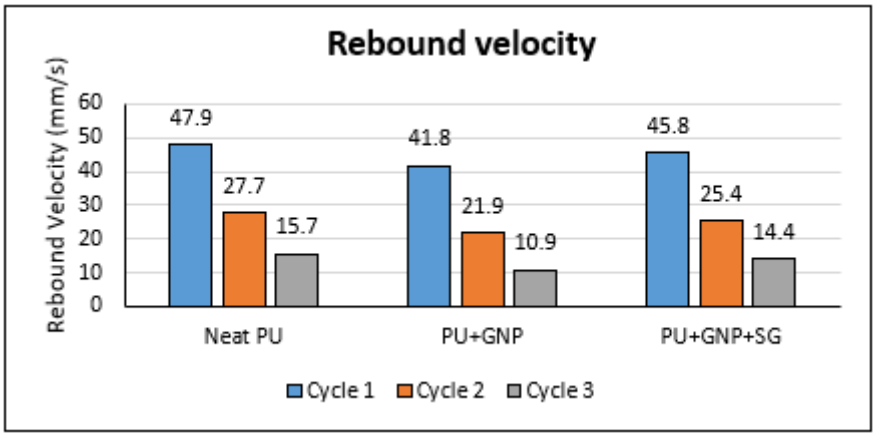

Figure 4-25 Velocity of the plunger rebounding.

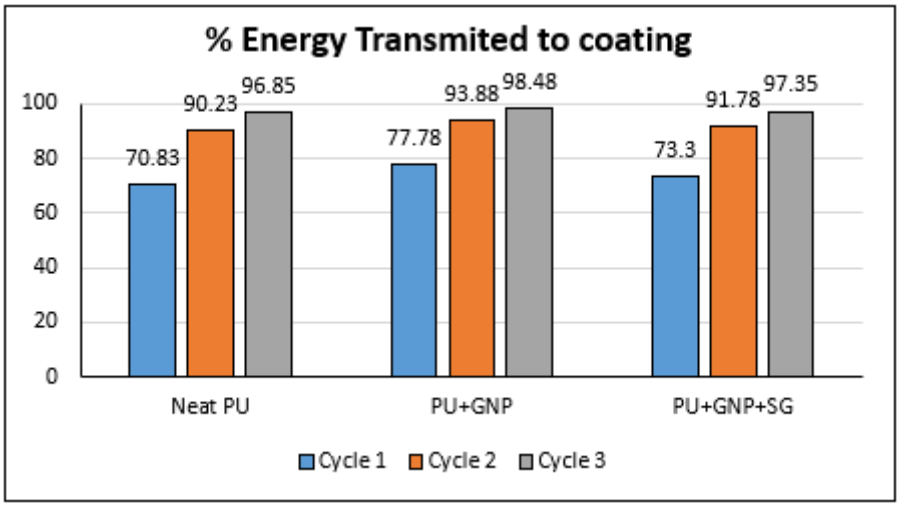

Figure 4-26 Energy transmitted results of the rebound test for neat PU, GNP modified PU and GNP/SG modified PU.

Coefficient of the restitution for three different tested materials was also calculated using Eq. (4.17).

$$\varepsilon = \frac{v_2}{v_1} \tag{4.17}$$

where: v_1 is the impact velocity and v_2 is the rebound velocity

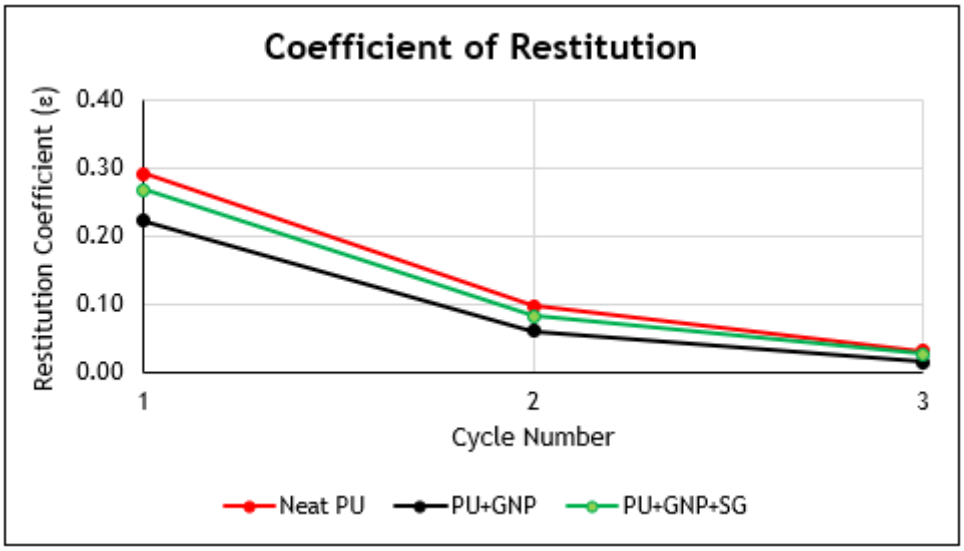

Figure 4-27 Coefficient of restitution for neat PU, GNP modified PU and GNP/SG modified PU

4.5.4 Summary of resilience tests

The resilience tests were used to measured rebound energy according to the ASTM Standard D2632. The results of this test showed that PU+GNP performed better than the other two coating materials in energy absorption (77.8% after first impact). The rebound resilience of PU+GNP can be employed as a parameter representing the ability of this elastomer to absorb higher kinetic energy of the erodent particles upon impact. PU+GNP+SG was second best coating material in energy absorption (73.3% after first impact).

In conclusion, adding the GNP to the pure PU will increase the energy absorption capability of the PU by about 7% and by adding SG to PU+GNP will increase the energy absorption capability of the PU by about 2.5% after the first hit. This is a good sign for developing a rain erosion resistant coating for wind turbine blades as the rain droplets hits the coating in majority of cases only once.

Chapter 5 Erosion Test

5.1 Introduction

In this chapter first, cool down time for pure PU coating was determined and based on that the required interval between shooting of the rubber ball in the Single Point Impact Fatigue Tester (SPIFT) were determined. After that SPIFT tests were performed at two different impact speeds of 150 m/s and 173 m/s. Energy dissipation and the extend of the heat affected are measured using thermographic infrared camera. The time to crack initiation, delamination and material loss are determined. At the end of the SPIFT tests SEM images of cross sections of specimens are obtained to compare the pattern of crack growth in different coating materials.

As mentioned before leading edge will affect the aerodynamic performance of the wind turbine blade by increasing the roughness. It is proved that increasing the roughness will decrease the lift-carve slope and $cl_{,max}$ and increase the drag. The critical height of the leading-edge roughness (LER) is defined as the lower threshold with no influence on the aerodynamic performance [192].

It is proved that in case of keeping the roughness elements constant, increasing the length of the blade will decrease the effect of LER [23].

Hence there are major incentives for protecting the leading edge of blades. Possible solution to overcome leading edge erosion can be grouped as preventing by reducing tip speed [23], repair by placing tapes over eroded area or protecting by covering the leading edge with erosion resistant coating.

Elastomeric materials are currently considered to be amongst the best candidates for LEE protection [162, 193, 194, 39] and polyurethane is one of the best choices. Polyurethane (PU) elastomers have a urethane group -NH-CO-O in their structure. PUs are formed by the reaction of isocyanates [$R-(N=C=O)^n$] with polyols. Control of segmentation through stoichiometry and reaction conditions allows the creation of PU elastomers with superior qualities [195, 196]. In addition, PUs has a high capacity for energy absorption; making them particularly suitable for shock and impact protection, thus PUs are good candidates for leading edge protection. In polyurethane, the hard domains are embedded in a rubbery soft segmented matrix. Depending

on the hard segment content, the morphology of the hard domains changes from one of isolated domains to one of interconnected domains. At room temperature, soft domains are above their glass transition temperature and responsible for rubber-like behaviour while hard domains are below their glassy or melting transition temperature. The latter are the primary contributors to the hysteresis, permanent deformation, high modulus, and tensile strength [150]. A wide range of mechanical properties can be obtained in PUs by varying the molecular weight, ratio and chemical composition of the hard and soft segments.

Rain erosion has two phases, first is a period in which cracks nucleate in the regions that were initially free from observable cracks, followed by a second phase in which cracks grow to the point of failure. When a rain drop hits the surface coating, it generates three different types of waves: shear, compression and Rayleigh [197]. The Rayleigh wave moving along the surface create asperities and then the lateral jet cut these asperities and cause of surface coating tearing. For this reason, developing a coating material with high tear resistance is desirable for highly durable rain erosion coatings.

It is evident that the mechanical, thermal and impact properties of polymers can be significantly improved by the addition of nanoparticles [21]. Nanoparticles tend to intercalate and exfoliate in a polymer under appropriate conditions, increasing substantially the area of interface with the polymer [21]. The strength of the interface and the dispersion of nanoparticles are central to the mechanical enhancement of nanoparticle modified polymers [172, 198]. The strength of interface can be improved by functionalisation of nanoparticles to facilitate chemical bond with the matrix. Surface functional groups such as hydroxyl, carboxyl, or amine groups on the nanofillers can potentially form chemical bonds with the polymer matrices resulting in a stronger interface interaction between the fillers and the matrix. In addition, the nanoparticles (in this case graphene) and polymeric matrices interact by mechanical interlocking through the wrinkled surface of thin graphene sheets.

Testing leading edge erosion of wind turbine blade

There are different approaches of testing wind turbine blade erosion [192, 199, 200, 197]. One of the common ways to investigate the erosion process of wind turbine blades is based on a 3-bladed helicopter principle [23]. Another method is impacting continues water jet, impacting water jet slug, water jet provoked impacting droplets and moving samples through the falling water droplet [161].

Erosion Testing by Single Point Impact Fatigue Tester (SPIFT)

Another method to investigate the LEE of wind turbine blade is single point impact fatigue test (SPIFT), which a rubber ball is used to impact the surface of specimen. Using SPIFT is a way to investigate high strain rate and high strain fatigue properties of the coating material [15]. It is the prevailing assumption that fatigue resulting from droplet impacts is the driving mechanism behind erosion [201, 202, 43], so in this part SPIFT method was used to analyse the rubber ball impact on the surface of the developed coating.

The inspiration for the initial design of the SPIFT came from the work of Prayogo [203], who cited the paper by Adler [48]on hyper-sonic rain erosion. Adler noted that nylon polymer pellets provided better results compared to systems using water jets [204]. Advantage of this method among other methods are, providing repeatable impact position and low cost of experimental equipment and samples. Having repeatable impact position give the ability to develop a finite element models (FEM), which means that by having these results it is possible to compare the type, position and number of stresses and strains calculated in the FEM; also having not so costly equipment to manufacture make the technology much more accessible [161].

As can be seen in the **Figure 5-1** in this set up rubber balls enter the chamber of the system and then loaded into the barrel. This system is able to shot up to five rubber balls per second with velocities up to 170m/s [161]. To accelerate the rubber ball through the barrel compressed air was used; this air pressure gives the ability to control the ball velocity. To record the velocity of the rubber ball, optical speed trap was used which located in front of the testing sample before rubber ball hits the sample. As mentioned before it is possible to have different number of shots in a series with different time interval between the shots which can be defined by a programmable microprocessor. The output from the microprocessor triggers the VALKEN V12 built-in control electronics, which in turn controls the electro-pneumatic valves. This approach retains the built-in safety features, which are released once the lid of the test chamber is closed [161]. As the primary means of damage detection, high-resolution digital video images were captured at a 3.1 Megapixel (2048 × 1534 @10 Hz) with an AM7915MZTL long working distance USB microscope from Dino-lite (Fino-Lite, Vodskov, Denmark). Using a working distance of 120 mm between camera and test specimens, an 18 × 13 mm^2 field of view is obtained, resulting in 13.5 pixels mm^{-2} [205]. Typical tip speeds for wind turbine blade is about 95m/s [206], However, at this speed the duration of the fatigue test become too high. As a result, accelerated impact fatigue test were performed at 150m/s and 173m/s. To use SPIFT setup to analyse the LEE it is needed to provide a loading closer to that of a water droplet. To

achieve this nitrile rubber ball was used in this test instead of hard nylon ball. Conducting this type of fatigue testing on conventional cyclical fatigue setup is not feasible for soft viscoelastic materials like PU. As discussed by Weigel [207] results of the traditional cyclic fatigue tests are often not reproducible on other testing set-ups and repeated droplet impacts at a single point with speed over 100 m/s are almost impossible and impractical to achieve on traditional fatigue testing machines. These problems is overcome by using an aperture in the SPIFT impact fatigue testing device, in order to be able to test the fatigue properties of viscoelastic materials under loadings similar to droplet impacts. The controlled impacts rate of discrete impacts can be used to account for the viscoelastic heating effect, which was shown to dramatically reduce fatigue life. The SPIFT also differs from most conventional RET's in that the impacts are not distributed over the surface but repeated on a single point. This means that damage growth can be evaluated, as the loading history is known [208].

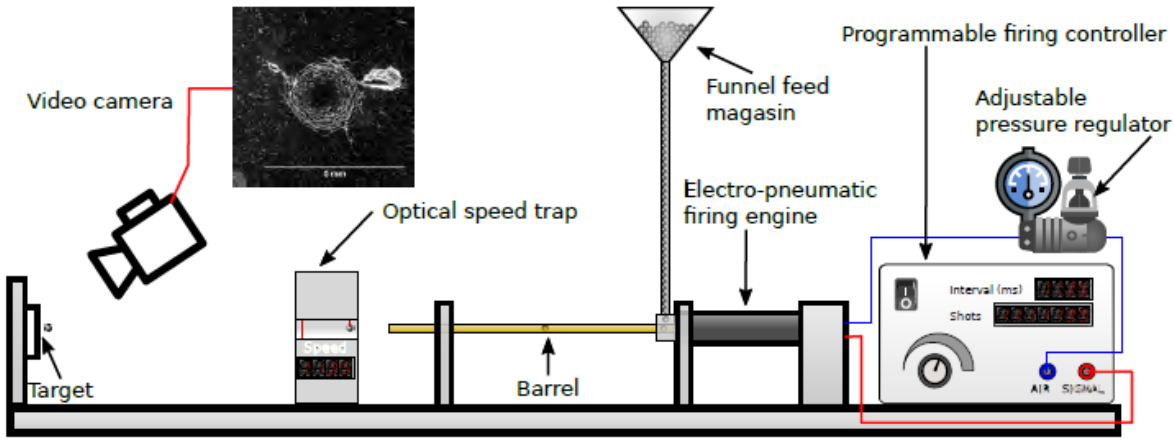

Figure 5-1 The Single Point Impacts Fatigue Tester (SPIFT) erosion testing setup [39].

5.2 Robber ball tests

In this section the results of erosion testing of the new coatings using a single point impact fatigue testing (SPIFT) approach [15]are presented. Thermal effects during blade erosion are discussed.

5.2.1 Manufacturing of fatigue tests specimens

In this part three polyurethane-based coatings were investigated as Leading Edge (LE) protective coatings: pure polyurethane (PU), graphene modified polyurethane (PU + GNP), and graphene + sol gel-modified polyurethane (PU + GNP + SG). A square glass fibre

reinforced laminate with dimensions 40mm × 40mm × 5mm was used as a substrate. An aluminium mould was machined for casting with a 1mm thick layer of the above coatings (see **Figure 5-2**). The film was bonded to the GFRP substrate with 1 mm thick Epoxy DP 110 sublayer. The thickness of the adhesive sublayer is controlled by placing 1mm diameter wires under the top coating. During curing, a 5 kg weight was placed on the top of an aluminium plate on the samples, to make sure that the adhesive is distributed homogeneously all over the GFRP substrate.

(**a**) (**b**)

Figure 5-2. (a) Aluminium mould for casting thin coating film; (b) A finished rain erosion specimen with PU + GNP top coat.

5.3 Experimental set up

5.3.1 Single point impact fatigue tester (SPIFT)

In this experiment two different speeds were used to shoot the rubber ball to the surface of the specimens, at 150m/s and 173 m/s. System was able to fire five balls per second by using high pressure air (HPA) hardball firing system. Nitrile rubber balls which are used in this experiment have well impact resistant properties. There was no visible damage on the balls after repeated use. Properties of the rubber balls can be find in **Table 5-1**.HPA uses electro-pneumatic firing engine to fire the ball with the speed between 60-200m/s, which can be controlled by air pressure and amount of the air released. There are four parameters which affect on the exit speed of the rubber ball, pressure of the compressed air, length of the barrel, size of the nozzle and also mass of the ball.

Table 5-1 Rubber ball properties.

Diameter	6 mm
Shore A hardness	60
Mass	1.43×10^{-4} kg
SD	7.59×10^{-7} kg
Density	1263 kg/m^3

To measure the deformation, incoming and rebound speeds of the ball, a high-speed camera with a speed of 380,000 fps (Phantom v2512 fast, Vision Research, Ltd., Thurmaston, Leicester, UK), was used (Figure 5-3).

In this part of study each specimen impacts to failure for the purpose of analysing the following three parameters:

(i) the number of impacts to initiate the crack.

(ii) the number of impacts to start delamination

(iii) the number of impacts before loss of the coating material starts

Figure 5-3. High speed camera (Phantom v2512 fast) for filming the ball impacts at 380,000 fps [161].

5.3.2 Investigation of thermal effects in erosion

There are key parameters that affect the protective properties of the coating which are, damping properties of the polymer which affect the degree of energy dissipation in the polymer coating after impact of rain droplets, tearing energy, young's modulus which affect the rebound energy, hardness, water absorption and modulus of toughness [209, 197]. Dissipated energy is distributed as thermal energy and deformation of the polymer chain. For analysing energy dissipation mechanism thermographic analysis was carried out during SPIFT. **Figure 5-4**

shows the arrangement of the IR thermography camera in the test setup, the camera (Optris Pi 640) records at 120 Hz with a 0.1 °C temperature resolution.

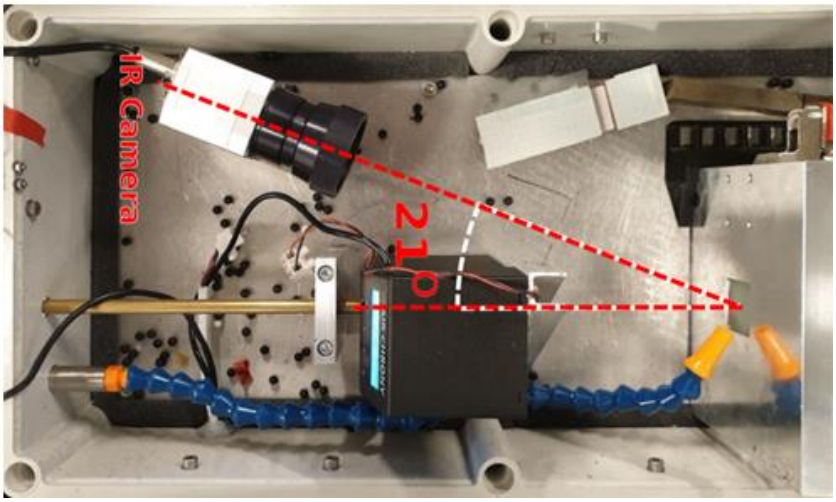

Figure 5-4. The arrangement of the IR camera in test setup [161].

By using IR thermography imaging, it is possible to measure the time taken for the sample to cool down between impacts as a function of impact speed and also it is possible to measure the temperature change as a function of impact speed. This will help to identify differences in damping between coatings. Beside that IR thermography imaging is used to analyse how the absorbed mechanical energy is distributed in the coating.

One of the central features of SPIFT is the ability to control the impact heating phenomenon [50], enabling the determination of a minimum cool downtime to help continuous operation without heat build-up.

To find the time interval between shooting of the balls to reach to the same temperature, the time-temperature graph for the pure polyurethane (PU) is needed and it is assumed the modified PU behave similarly (This decision was taken due to limited time for testing during lock down). **Figure 5-5(a)** shows the average temperature of the measurement area (see **Figure 5-10**), as a function of time. This was used to measure the time needed for the sample to be within 0.2–0.5°C of the initial temperature, before impact. As can be seen in the **Figure 5-5 (a)** there is some temperature increase in the impacts zone during testing, but we allow the impact zone temperature to be lower than 1°C.

Based on these data, a control curve was constructed by fitting an exponential function to the cool-down times as seen in **Figure 5-5(b)**.

$$t(v) = 0.09234\, e^{0.0302v} \qquad (5.1)$$

Where: t is the cool-down time and v is the impact velocity.

By using equation (5.1) the testing time can be minimized, while avoiding the problem of heat accumulation in the sample. The cooling time for impact speed of 150m/s was 8.6 s and for 173m/s was 17.1 s. By decreasing the impact speed, the required number of ball impact to material loss becomes exceedingly high (for PU+GNP+SG becomes 10,000,000 shots at 90 m/s as shown in Figure 5.9 and considering the cooling time between the shots the experiment time becomes exceedingly high), hence the speed for testing is select at 150 m/s and 173 m/s.

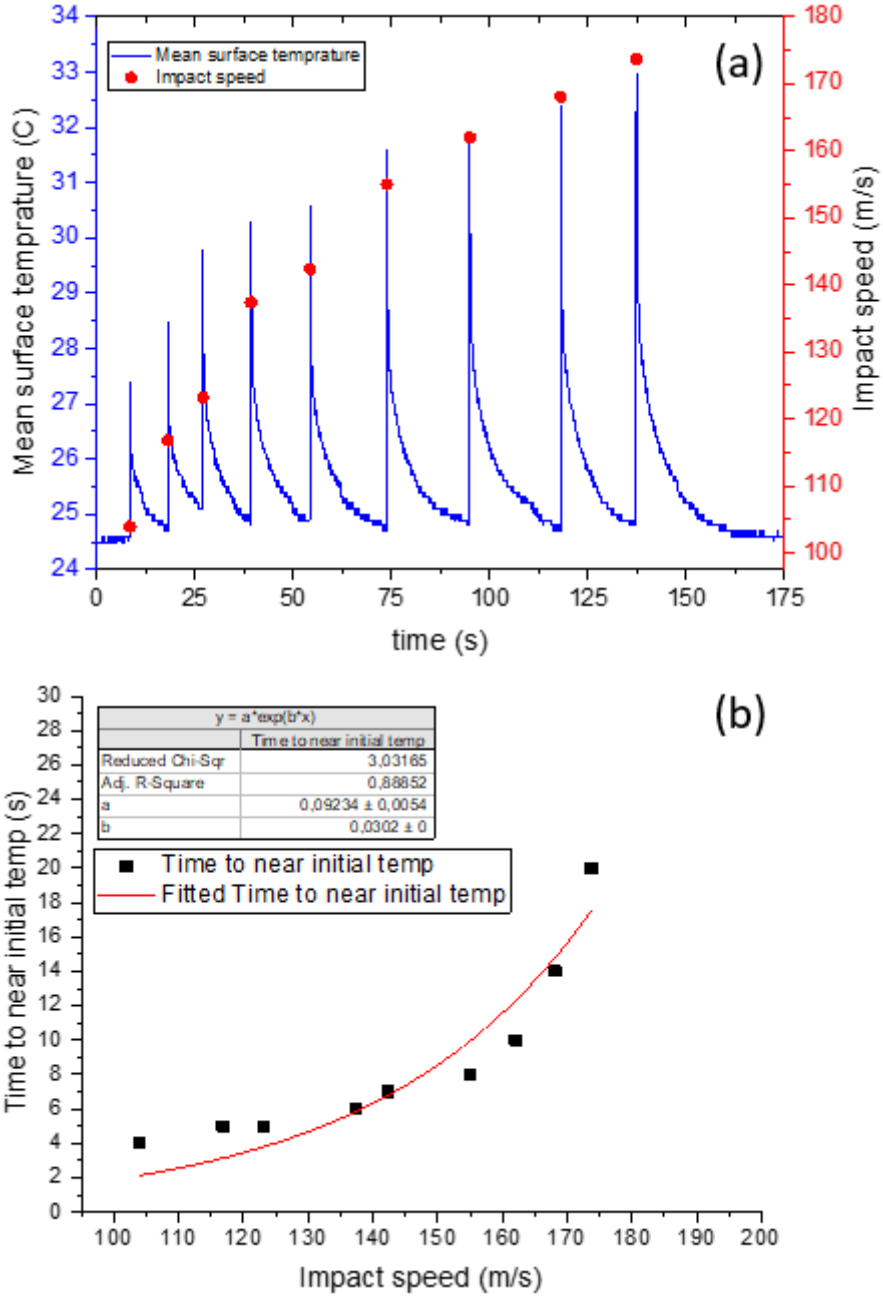

Figure 5-5. (a) Time-temperature variation of the PU coating, the temperature is the average temperature within the impact area shown in blue in Figure 5-10, and on the second y axis, the corresponding impact speed shown in red dots. (b) The measured time needed to be at initial temperature as a function of the impact speed. Data fitted with an exponential curve to construct an empirical function for cool-down time as a function of impact speed [161].

5.3.3 Results of robber ball test

Results of the SPIFT for the impact velocity of 173m/s on three different types of the specimens (PU, PU + GNP and PU + GNP + SG) can be found in **Figure 5-6.** PU+GNP+SG has the best erosion performance. In terms of the number of hits to initiate a crack, the PU + GNP + SG coating is 159% better than neat PU and 70% better than PU + GNP. In terms of number of ball impacts before the start of delamination, the PU + GNP + SG coating is 100% better than neat PU and PU + GNP. In terms of number of ball impacts before` the loss of coating material, the PU + GNP + SG coating is 54% better than neat PU and 39% better than the PU + GNP coating.

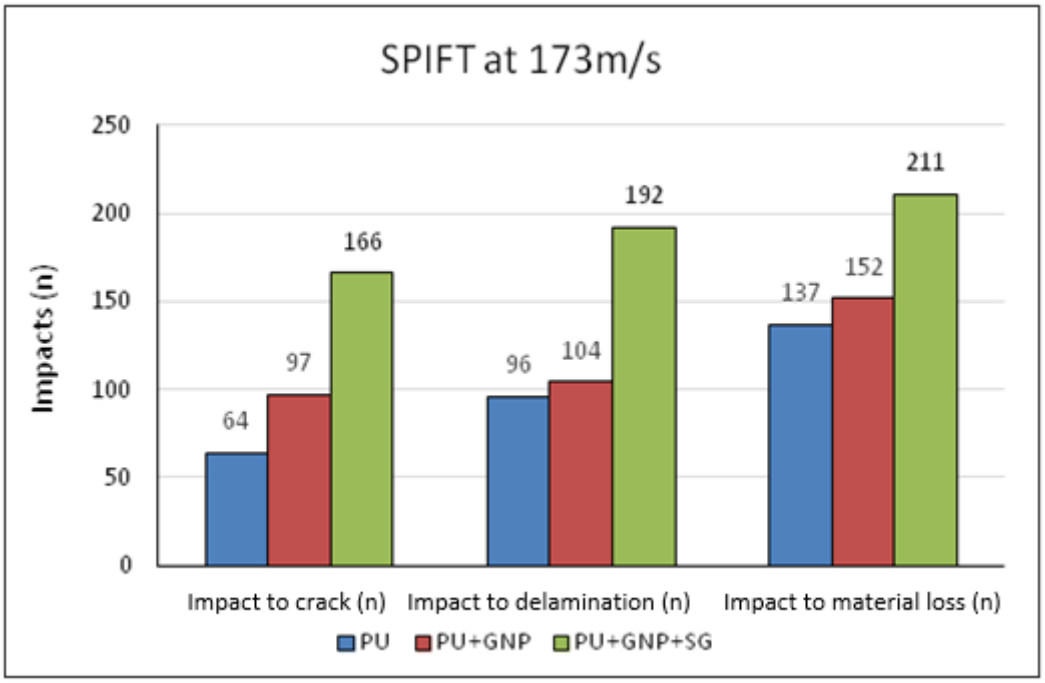

Figure 5-6. SPIFT tests results for PU, PU + GNP, and PU + GNP + SG at 173 m/s.

Figure 5-7 shows images of the extent of damage to the three coatings at various stages of the impact testing. It is clear that the number of impacts to material loss to occur is much longer for the PU + GNP + SG coating than the others.

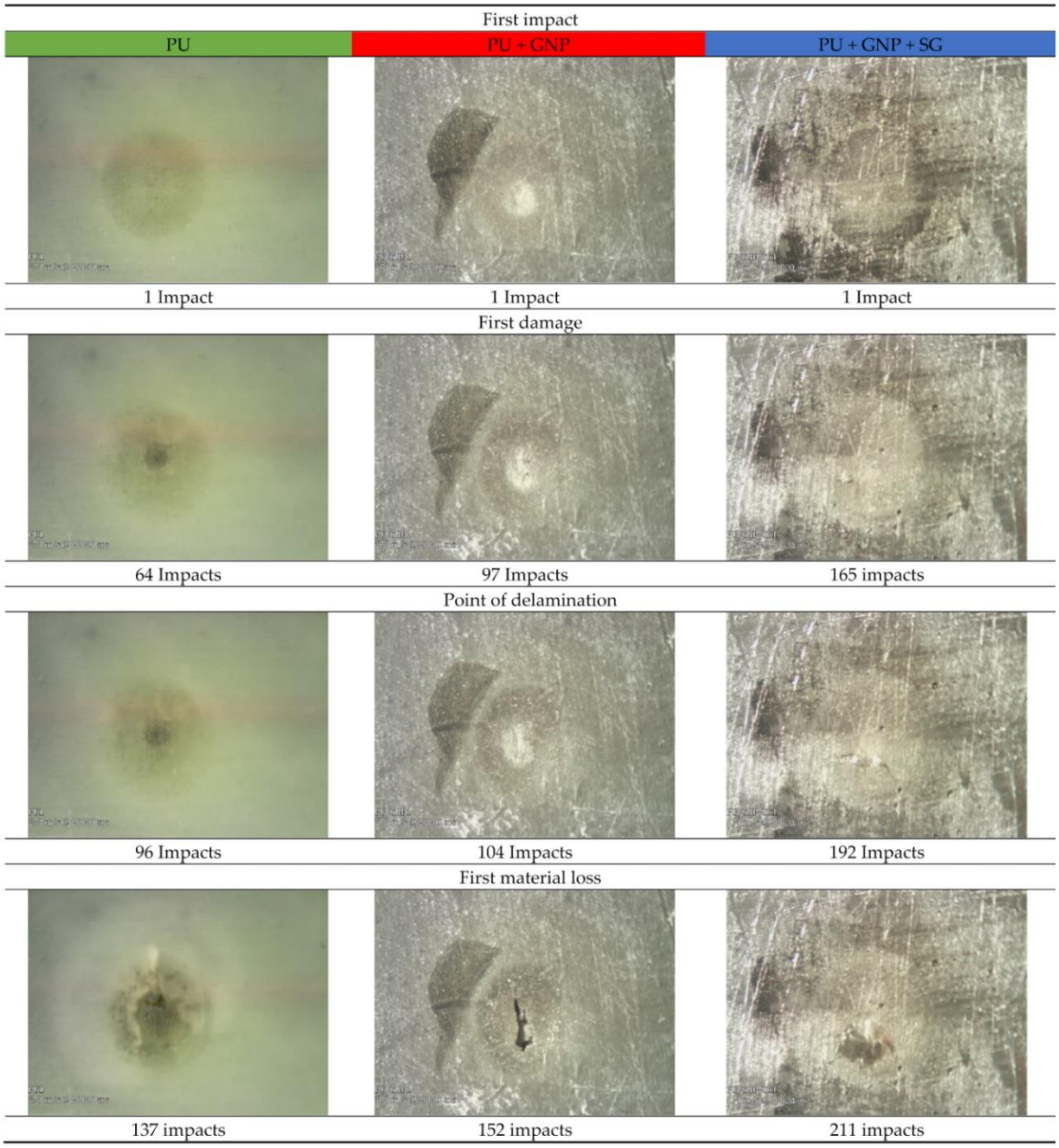

Figure 5-7. The extent of damage to the three coatings at various stages of the ball impact testing, from the 3 different coatings PU, PU + GNP, and PU + GNP + SG. Images are extracted stills during testing, from the DinoLite microscope [161].

The SPIFT test results at 150 m/s are shown in **Figure 5-8.** Again, the results show that at this ball impact velocity, PU + GNP + SG has the best erosion performance. In terms of the number of hits to initiate a crack, the PU + GNP + SG coating is 1248% better than neat PU and 306% better than PU + GNP. In terms of number of ball impacts before the start of delamination the PU + GNP + SG coating is 1682% better than neat PU and 244% better than PU + GNP. Finally, in terms of number of ball impacts before the loss of coating material, the PU + GNP + SG coating is 1063% better than neat PU and 178% better than the PU + GNP coating.

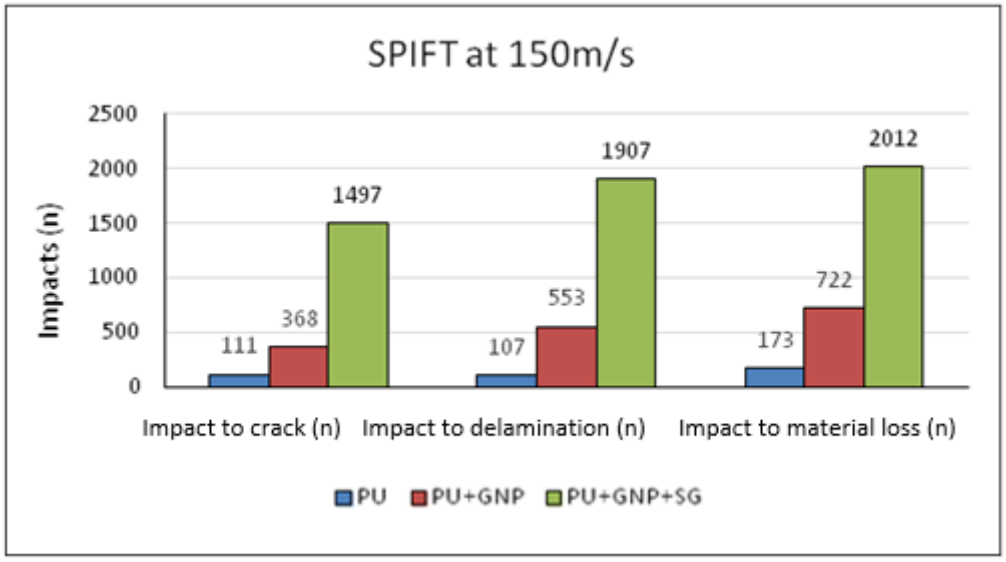

Figure 5-8. Impacts to failure at 150 m/s for PU, PU + GNP, PU + GNP + SG. Each colour represents a single test.

Figure 5-9 shows the impact velocity versus number of impacts before material loss (VN) curves for the speeds of 173 and 150 m/s.

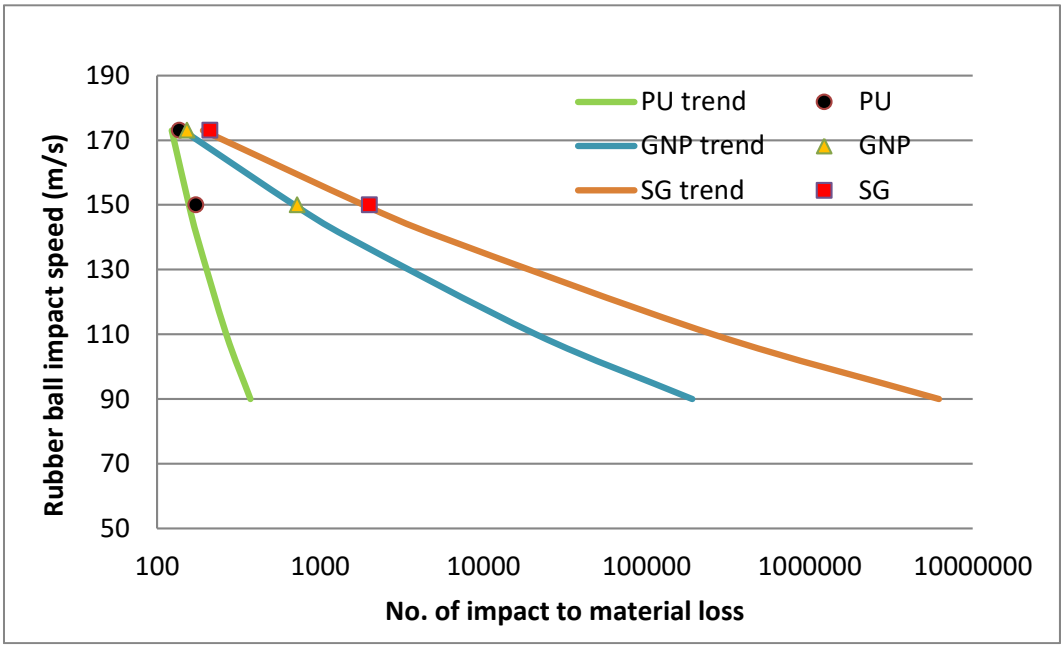

Figure 5-9. VN curves of PU, PU + GNP, and PU + GNP + SG tested at 173 and 150 m/s and fitted by a power curve. Damage was evaluated at the point of material loss. The lines correspond to the following cases: green line (left): PU, red line (middle): PU + GNP; blue line (right): PU + GNP + SG [161].

As it is generally accepted that most materials under a fatigue tend to follow a power law [207], the choice was made to fit a power law curve to data points. This is intended to roughly illustrate the relation between impact speed and coating lifetime.

When fitting a power curve of the form $n(v) = c \times v^m$ to the three coating materials, the following functions were obtained:

$$n_{PU+GNP+SG}(v) = 7.35 \times 10^{37}\ v^{-15.9}$$
$$n_{PU+GNP}(v) = 6 \times 10^{26}\ v^{-11.0} \quad (5.2)$$
$$n_{PU}(v) = 7.85 \times 10^{5}\ v^{-1.7}$$

PU + GNP + SG has a large negative m coefficient, which is a strong indication of good fatigue performance. It is of interest that the angle of the curves is highest for hybrid nanoreinforced coatings, thus, their performance is more sensitive to impact velocity [161]**.**

The experimental studies presented in this section confirm the hypothesis that nanoparticle reinforcement (in particular, GNP+SG) of polyurethane coatings improves the coating anti-erosion performance. Hybrid reinforcement with graphene silica results in 13 times longer lifetime. This has important implications for the development of future anti-erosion coatings.

Combining the Equations (5.1) and (5.2), we can make a rough estimate for the testing time (impact to crack) at 95 m/s (the rated speed for a 15MW turbine [206]). The testing time could be in the order of 3×10^6 impacts; hence about 1500 h of continuous testing is required while for 150 m/s, test time is 4 hours and for 173 m/s, test time is 47 minutes. This illustrates the need for accelerated testing at much higher speed.

5.3.4 Energy dissipation mechanisms and thermal heating: effect of the coating properties

5.3.4.1 Distribution of the temperature and relation to impact models

Thermography analysis was performed in order to analyse the dissipation of thermal component of energy during impact testing. **Figure 5-10** shows thermographs of PU (a), PU + GNP (b) and PU + GNP + SG (c) impacted at similar speeds of approximately 170 m/s, right after impact. As can be seen in the **Figure 5-10**, for all three types of material the hottest and the most deformed regions are whiting the counter line of the contact area of the impact ball, as the temperatures are distributed in a doughnut shape around the centre of the impact. This is in line with many models and observations reported elsewhere [210, 15].

It should be noted that there might be changes in thermal emissivity between the different materials due to the different filler material. Therefore, comparisons of absolute values between the samples might be not totally accurate [161]**.** For lower impact speeds and therefore

temperatures, the general doughnut shape is preserved, but with a lower temperature, and the mean peak temperatures can be found in **Figure 5-5(a)**.

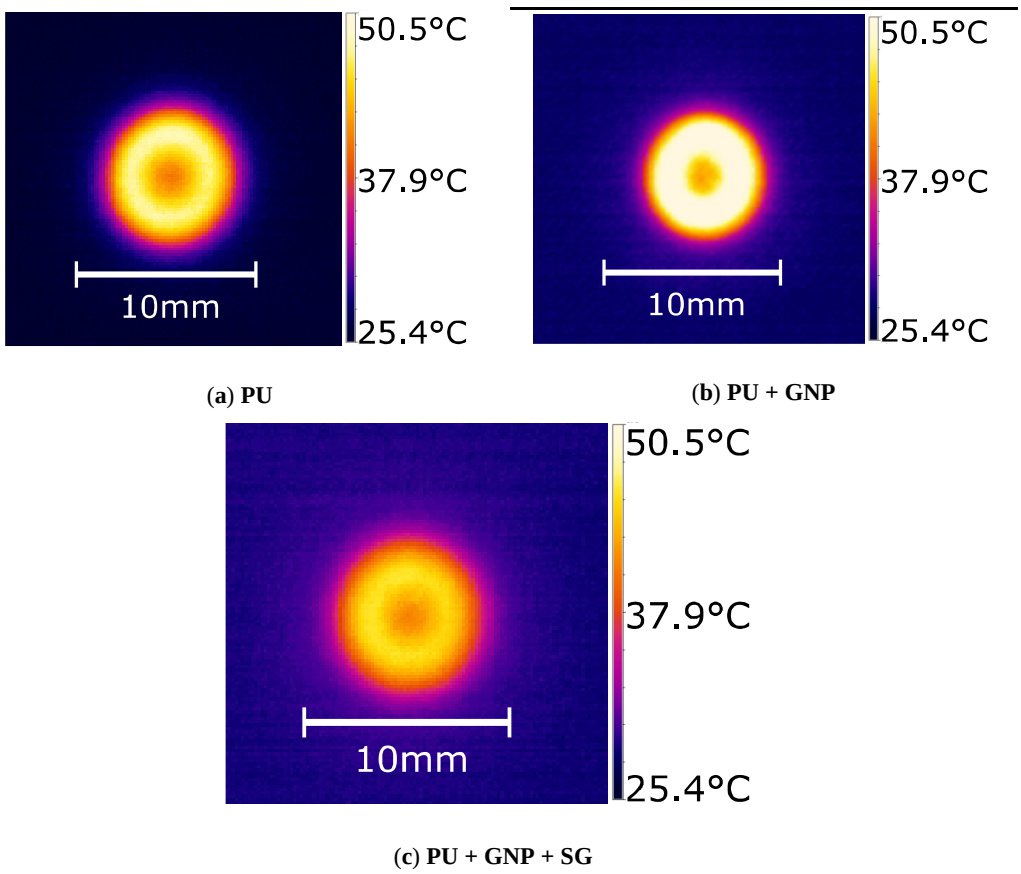

(a) PU **(b) PU + GNP**

(c) PU + GNP + SG

Figure 5-10. Thermographs of (a) PU impacted at 170.9 m/s, (b) PU + GNP impacted at 169.2 m/s, (c) PU + GNP + SG impacted at 170.5 m/s [161].

These data were chosen as they closely match the same impact speed, and the high impact speed gives good thermal contrast.

5.3.4.2 Effect of nano-reinforcement on the change in kinetic energy

Equation (5.3) was used to calculate the changes in kinetic energy of the ball, where v_i is the impact velocity and v_r is the rebound velocity of the ball. These two parameters are measured using recorded high-speed video.

$$\Delta E(v) = \frac{1}{2} m(v_i^2 - v_r^2) \tag{5.3}$$

Figure 5-11 shows the variation of kinetic energy of the rubber ball $\Delta E(v)$ versus impact velocity for each coating material.

The change in $\Delta E(v)$ for all three coatings can be fit with a single power curve,

$$\Delta E(v) = 5 \times 10^{-5} v^{2.0421} \quad (5.4)$$

As can be seen in **Figure 5-11** there is no significant difference between the ΔE values of the three different types of coating. Also, it can be seen that all three coating shows lower ΔE in comparison with the impacting steel target; this can be because of the soft PU coating deformation on impact, which in turn results in less deformation of the nitrile rubber projectile. As nitrile rubber has a very high dampening factor, there is less deformation of the target and more ΔE is conserved during impact. One can assume that the positive effect of nano reinforcement is in its influence on the fatigue properties of polymers.

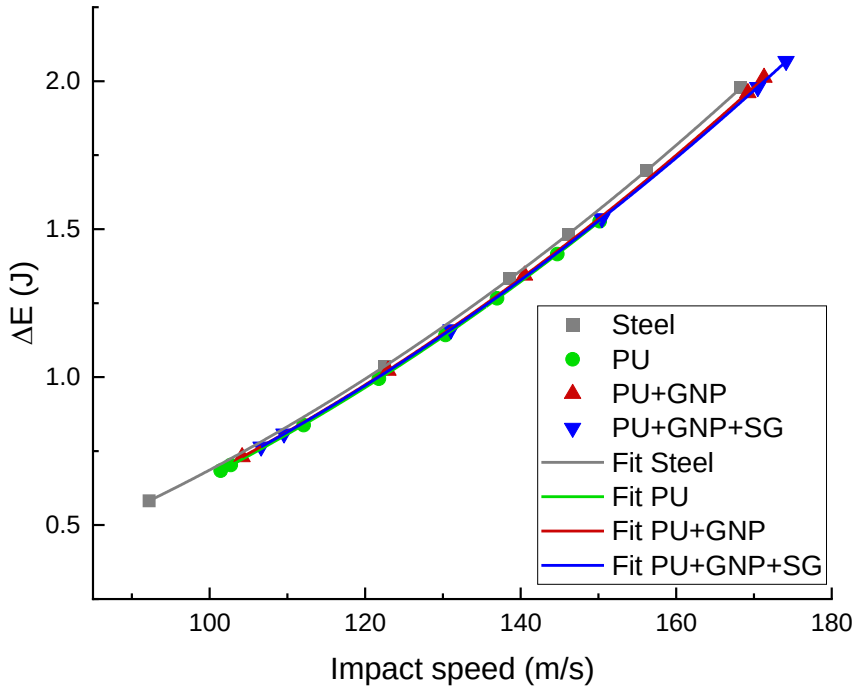

Figure 5-11. Energy loss from ball impactor (ΔE) [161].

5.3.4.3 Microscopic analysis of the influence of coating modifications on the damage mechanisms

In this part of the study three samples were selected after SPIFT to the stage of material loss for scanning microscopy analyses (SEM). The samples were sectioned through the centre of the impact position using a Struers Secotom-50 (Struers Inc., Cleveland, OH, USA) and embedded in epoxy. The cross sections were polished using a Struers RotoPol-22 (Struers Inc., Cleveland, OH, USA) and a RotoForce-4 (Struers Inc., Cleveland, OH, USA) with a 5 N force on each sample and using diamond paste down to 1µm. The polished samples were covered with an approximately 10 nm thick carbon layer using a Bal-Tec SCD 005 sputter coater and afterwards investigated in a Tescan Vega 3 SEM (TESCAN, Brno, Czech

Republic))microscope, where an image of the central crack, with a magnification of 21 times were acquired with a secondary electron detector (**Figure 5-12**).

By looking at **Figure 5-12**, it can be seen that there are cracks in the surface of the coatings PU **Figure 5-12(a)** and PU+GNP **Figure 5-12(b)** while there is no crack on the surface of the coating PU+GNP+SG **Figure 5-12(c)**, these cracks can be seen as a thin white lines in the figure. The number of thin cracks in the coating indicates that the PU is softer than PU + GNP, which again is softer than PU + GNP + SG.

Figure 5-12 (a) shows material loss due to the ball impact and formation of a large crack from the root of the formed cavity to the glue, bonding the PU coating to the GFRP substrate is visible. The crack bent softly to the right.

In **Figure 5-12(b)**, similar material loss was observed except it happened in two places instead of one. Two large cracks were formed at the sharp ends of the cavities that go into the coating material with abrupt changes of direction. Approximately the same amount of material loss can be seen on both images; however, the number of balls impact on these two specimens as explained before are different and for PU + GNP is higher.

At the end of SPIFT tests, the damage resistance of the PU and PU + GNP coatings is more or less the same, but the abrupt changes of crack direction indicate PU + GNP coating is more brittle than the PU coating.

In **Figure 5-12(c)**, no cavity is formed by material loss and a crack propagates in the same manner as the crack in **Figure 5-12(a)**. The number of ball impacts on the PU + GNP + SG specimen is substantially higher than the PU specimen and this indicates that adding SG makes the material more damage tolerant. The failure mechanism is by propagation of a macroscopic crack from top surface to the adhesive bond with GFRP substrate and it follows the same path as the crack in PU coating shown in **Figure 5-12(a)**.

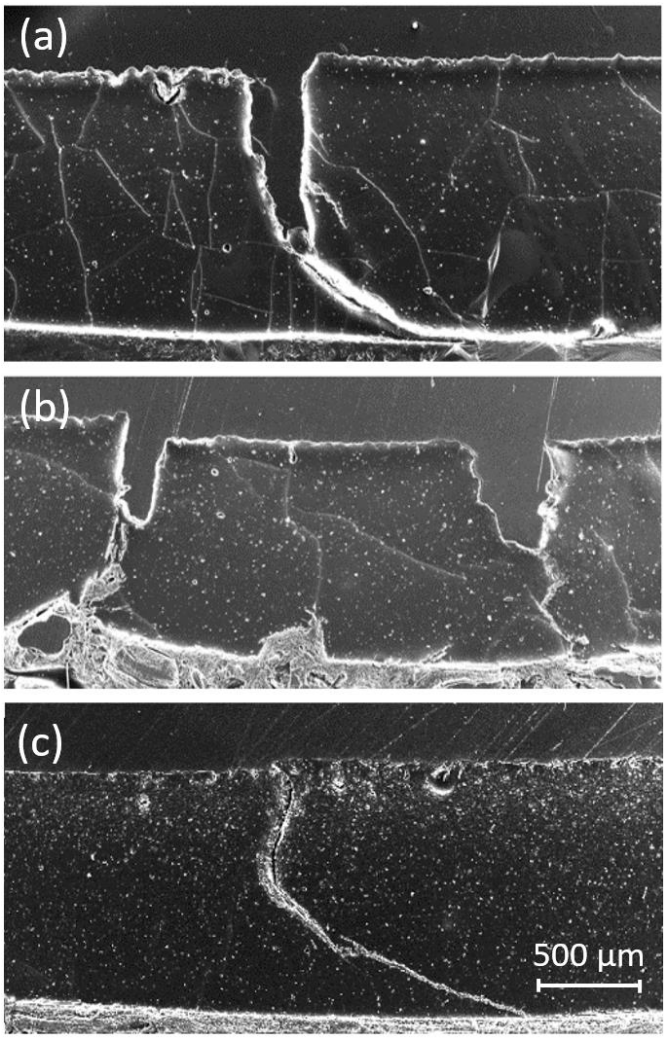

Figure 5-12. SEM micrographs of (a) PU, (b) PU + GNP, and (c) PU + GNP + SG [161].

5.3.5 Impact heating

Figure 5-13 shows the peak temperature change as a function of impact speed for PU, PU + GNP, and PU + GNP + SG. The samples were impacted at speeds between 100–175 m/s and the peak change in temperature ΔT was recorded. **Figure 5-13** shows that pure PU exhibits the largest ΔT values across most of the impact speed range.

In **Figure 5-13**, a linear relationship between the peak impact heating and the impact speed can be seen. Comparing **Figure 5-13** with **Figure 5-8** and **Figure 5-9**, one can see that the coatings with a higher number of impacts before failure correspond to lower peak temperature changes. As a result of this study it can be said that the dependence of temperature change on impact velocity is very different for the three coatings; which means that nanoparticle reinforcement can influence not only local stress wave scattering, but also mechanisms of thermal relaxation of polymers.

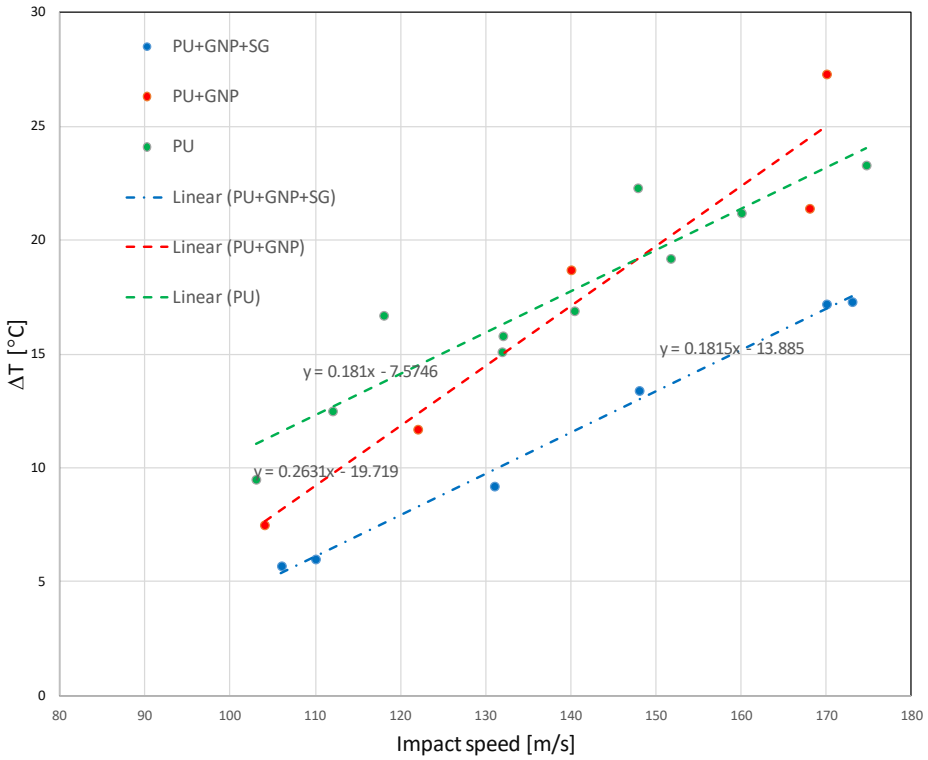

Figure 5-13 Peak ΔT impact heating as a function of impact speed for the three different coatings [161].

5.4 Summary of robber ball test results

An evaluation of novel nanoreinforced polyurethane based coatings for improved leading-edge protection of wind turbine blades is presented in this chapter. Using nanoparticles embedded in the coating to scatter and reflect stress waves arising from rain droplet impacts is proposed. Polyurethane coating samples with graphene and hybrid (graphene/silica) reinforcement have been tested using a Single Point Impact Fatigue Tester (SPIFT) to evaluate their potential erosion resistance. Scanning electron microscopy has been used for analysis of damage after SPIFT testing. The SEM images revealed the PU + GNP + SG is less prone to damage caused by repeated ball impact. It has been demonstrated that the nanoreinforced coatings have significantly greater resistance to erosion. Polyurethane with hybrid GNP + SG nanoparticle reinforced coatings exhibited lifetimes up to 13 time greater than pure polyurethane coatings.

Chapter 6 Conclusions and Future Work

6.1 Conclusions

The main aim of this research was development of nanoengineered rain erosion resistant polyurethane coatings for protection of the leading edge of wind turbine blades. The PU was used as the matrix and it was modified with different CNPs and with silica-based sol-gel to have better mechanical and hydrophobicity performance, these modifications increased the tensile strength of the pure PU by 115%, increased the young's modulus by 95%, increased the modulus of toughness by 123%, increased the tearing energy by 148%, increase the elongation at break by 102% and also reduce the surface energy which results in increasing the water contact angle. By performing the SPIFT rain erosion test it was shown that the developed coatings have substantially improved the lifetime relative to the base pure PU material and the aim of the project was achieved.

Material characterization results from FTIR and FE-SEM show that GNP-COOH and silica-based sol-gel was successfully incorporated in the polyurethane structure and GNP nanoplatelets are making H bonds with PU backbone. Water contact angle measurement showed improvement in hydrophobicity properties of the developed coating material. Mechanical properties such as tensile strength, Young's modulus, modulus of toughness, tearing strength, tearing energy, elongation at break, residual strength, and ultimate compression strength were improved. Impact energy analysis was carried out by performing drop ball test to find the transmitted energy to the substrate. DMA tests and SVD-QR method were used to find the dissipated energy in coating and resilience tests was performed to find the rebound energy for all developed coating materials. All the results will explain in details in following.

6.2 Summary of the results

6.2.1 Summary of the mechanical tests characterisation of developed nanoengineered coatings

FTIR test clearly shows the presence of key functional group of polyurethane at 3250cm^{-1} for N-H, 2950-2800cm^{-1} for C-H and 1700cm^{-1} for carbonyl group; in addition, for PU+GNP+SG it can be seen an additional peak at 800cm^{-1} which is related to Si-O-Si. TGA results showed that weight loss of PU+GNP+SG at temperature of 20 to 280℃ is less than PU and PU+GNP, which prove a better hydrophobicity characteristic of this material due to the introduce of silica to the structure of PU+GNP+SG than the other two material (PU and PU+GNP). Also, weight loss up to 500℃ for all three types of materials shows the decomposition of the urethane bond in polyurethane structure, which was clearly shown in TGA results.

DMA test results showed that adding 0.5wt% graphene to polyurethane will decrease the cell size and increase the cross-link density which results in increasing the damping capacity of the PU+GNP and PU+GNP+SG in compare with pure polyurethane.

Water droplet contact angle test showed that the water CA of pure polyurethane is between 50 to 57 and adding 0.5wt% GNP to PU increased the hydrophobicity of the material, which results in increasing the CA from a range of 50 to 57 to a higher range of 70 to 80. Also adding 1wt% of silica-based SG to the PU+GNP material even increase the CA more (between 105 to 110). It can be said that adding 0.5wt% GNP and 1wt%SG to the pure polyurethane increase the CA by 120% from 50 to 110.

FESEM results showed homogenous dispersion of f-GNP in the PU matrix. By looking at the results of FESEM it can be said that in-situ polymerization technique to produce PU+GNP+SG is one of the most sufficient method which produce even more smoother surface then PU and PU+GNP due to the stronger interactions between the nanoparticles and polymer chains.

In this study tensile test was performed for different purposes. First of all it was done to analyse the tensile properties of pure PU; for this purpose, tensile test was performed on dogbone samples at three different strain rate (crosshead speed) and at three different temperature. Young's modulus, UTS, elongation at break and modulus of toughness were evaluated. Results show that Young's modulus will increase by increasing the strain rate at all three different temperatures (25, 50 and 70℃). The elongation at break is increased by increasing strain rate. At each strain rate by increasing the temperature, elongation at break will decrease. Same

behaviour was observed for UTS and modulus of toughness. The tensile test results showed that properties of PU are strongly dependent on the strain rate and temperature.

The tensile test is also used for optimisation of the mixing parameters of carbon nano-particles in PU. For that reason, 0.5wt% of CNPs was added into PU at three mixing duration (6, 12 and 18 minutes) and at three mixing speed (8000, 12000 and 15000rpm) and then tensile test was performed. Results show that at each mixing speed, by increasing the mixing duration, Young's modulus will decrease; but elongation at break shows different behaviour than Young's modulus and it increased. In addition, at each mixing duration, by increasing the mixing speed, elongation at break decreased. UTS and modulus of toughness showed the same behaviour to elongation at break, which means that increasing the mixing duration at any speed increases the UTS and also modulus of toughness. By analysing the results of this part, the optimum parameters for mixing CNPs in PU was determined: duration of 18 minutes and mixing speed of 8000 rpm, resulted in the highest elongation at break, UTS and modulus of toughness.

The effect of adding 0.1, 0.2, 0.3, 0.5 and 1wt% loading of MWCNTs to PU on tensile properties of the resulting nanocomposites, at mixing speed of 8000 rpm and mixing duration of 18minutes was investigated. It was found that adding 0.5wt% of MWCNTs to pure PU increased the Young's modulus of PU by 203% from 0.99MPa to 3 MPa, the elongation at break almost doubled from 341% to 646%, the UTS increased by 277% from 6.83 MPa to 25.8 MPa and the modulus of toughness increased from 3442 kJ/m3 to 10777 kJ/m^3. From this part of the study it was concluded the optimum loading of MWCNTs is 0.5wt%.

Same experiment as above was done to find the optimum loading of GNP-COOH to PU. Results show that highest amount of Young's modulus (3.7 MPa), UTS (38MPa), modulus of toughness (19741 kJ/m^3) and elongation at break (589%) were achieved at 0.5wt% loading of GNP-COOH.

The effect of adding hybrid GNP-COOH + MWCNTs on tensile properties of PU were also investigated. Results show that Young's modulus increased by 104%, UTS increased by 17.3%, modulus of toughness increased by 34.5% and no significant difference was observed for elongation at break.

The development of erosion resistant coating for LE of wind turbine blade was continued by selecting 0.5wt% loading of GNP-COOH and there will be hydrogen bonding in addition to mechanical interlocking which strengthen the interface of the CNPs with the PU matrixes.

Also, hydrophobicity of the coating is very important. The optimum wt% loading of hydrophobic silica-based sol-gel for adding to PU+GNP was required. For this purpose, 1wt% and 2.5wt% SG was added to PU+GNP and tensile tests were carried out. Results showed that

adding 0.5wt% GNP-COOH + 1wt% SG to PU gave the best tensile properties for the nanocomposite.

After establishing the nonmaterials for reinforcement of PU, uniaxial compression tests were performed to analyse the effect of temperature and strain rate on mechanical properties of developed coatings and the value of residual strain, compressive strength and energy absorption under compression were obtained. Results of uniaxial compression test indicate that mechanical properties of neat PU at room temperature (25℃) are not significantly affected by changing strain rate, although by increasing the temperature this behaviour will change; for other two modified PU, mechanical properties are affected by changing the strain rate at all three different temperatures. Also, it was shown that for neat PU at fixed strain rate, increase in temperature caused a significant increase in residual strain, no obvious change in compressive strength and decrease in energy absorption. For PU+GNP and PU+GNP+SG results were a bit similar but also it shows that increasing the temperature will decrease the compressive strength as well.

Cyclic compression tests were also performed to analyse the stress-strain curve of the materials at different cycles and also analyse the unloading path after a given strain. These tests are very important as the LE coating repeatedly impacted by droplets and goes under cyclic compression. Results of cyclic compression test showed the softening behaviour of all three materials after compression cyclic loading. It was also found that for neat PU the maximum stress attained was higher than modified PUs. This shows that neat PU experiencing the highest stress during cyclic compressive loading. The cyclic compression tests revealed that the maximum stress at maximum strain of 0.5 for PU is 107.9 MPa, for PU + GNP is 77.4 MPa and for PU + GNP + SG is 71.5 MPa.

Tearing test was performed to analyse the elongation at break, tearing strength and tearing energy of the developed materials. Results show that although PU+GNP has highest tearing strength but PU+GNP+SG has highest elongation at break and tearing energy.

Water absorption test was done to analyse the amount of water absorbed by each material after immersing into water and also analyse the effect of absorbed water on tensile properties of materials. Results show that PU and modified PUs absorbed significant amount of water after immersing into water for first 30 days, but after that the rate of water absorption is decreased. After two months of immersion in water, no further water absorption has taken place. Amount of absorbed water by PU+GNP+SG was less than other two materials which shows the hydrophobicity properties of this material due to introduction of the silica-based sol-gel. On the other hand analysing the tensile properties of each material after immersing in water at

specific period of time show that, after 6 months immersing the samples in water, PU+GNP+SG shows the highest amount of elongation at break (24% higher than neat PU), same Young's modulus as PU+GNP but 180% higher than neat PU, 52% higher modulus of toughness and 37% highest UTS than the neat PU. These results show that PU+GNP+SG is more suitable in encountering the adverse effect of exposing to water.

In this study damping test was also performed to analyse the damping properties of developed coatings at different frequency ranges. Results show that adding 0.5wt% GNP-COOH and 1wt% SG to the neat PU will increase the damping coefficient of PU at all frequency ranges. Also; it was found that this modification will increase the energy transmitted and reduce the rebound height and rebound velocity which indicate that these modified materials are able to absorb the impact energy of erodent particles with minimal damage.

6.2.2 Summary of the erosion tests of developed coating

In this part, single point impact fatigue test (SPIFT) was performed to analyse the erosion resistant property of the developed coating, using robber ball.

Results of the erosion test show that developed coating (PU+GNP+SG) exhibit life time 13 times greater than the coating using pure polyurethane (PU). It is shown that at impact velocity of $173\ ^{m}/_{s}$, modified coating (PU+GNP+SG) in terms of number of hits to initiate a crack, 159%, to start of delamination 100% and to begin the loss of coating 54% is better than the unmodified coating (PU). Same experiment was proved that even PU+GNP+SG has better performance than graphene modified polyurethane coating (PU+GNP); at same impact velocity ($173\ ^{m}/_{s}$) modified coating (PU+GNP+SG) in terms of number of hits to initiate a crack, 70%, to start of delamination 100% and to begin the loss of coating 39% is better than the modified coating (PU+GNP).

Also, it is shown that at lower impact velocity of $150\ ms^{-1}$, modified coating (PU+GNP+SG) in terms of number of hits to initiate a crack, 1248%, to start of delamination 1682% and to begin the loss of coating 1063% is better than the unmodified coating (PU). Same experiment was proved that even PU+GNP+SG has better performance than graphene modified polyurethane coating (PU+GNP); at same impact velocity ($150\ ms^{-1}$) modified coating (PU+GNP+SG) in terms of number of hits to initiate a crack, 306%, to start of delamination 244% and to begin the loss of coating 178% is better than the modified coating (PU+GNP).

SEM was done after SPIFT to analyse the damage of the coating and it is shown that developed coating is more damage resistant in compare with unmodified coating.

At the end, it is proved by this study that adding nanoparticle reinforcement to pure polyurethane will scatter the local stress as well as mechanisms thermal relaxation of polymers.

6.3 Future research challenges for enhancement of coatings for rain erosion resistance

The coating developed and tested in this research was a single layer which was bonded to the GFRP substrate with an epoxy adhesive. The coating performance can be improved if multi-layer coating is developed with fine tuning of each layer to optimise the intended protection of the substrate, i.e. leading edge of the turbine. Moreover, in the present work, only Single Point Impact Fatigue Test (SPIFT) using rubber ball has been done and the performance of the coatings were evaluated. In the future work, it is desirable the coating will be tested by water jet erosion machine. The effect of silica-based sol-gel will become clearer in these tests as water will be presented and the coating will be exposed to water during the testing period.

Finite element modelling of the impact of the rubber balls and water droplets on the developed coating is also another area for further research on these coatings. Calculation of stress waves and their effect on the failure of these coating can be investigated.

Finally, the performance of the developed coatings in the real environmental condition and on an industrial scale wind turbine blade for short term and long term performance is required.

References

[1] S. Zhang, K. Dam-Johansen, S. Nørkjær, P. L. Bernad and S. Kiil, "Erosion of wind turbine blade coatings – Design and analysis of jet-based laboratory equipment for performance evaluation," *Progress in Organic Coatings,* vol. 78, pp. 103-115, 2015.

[2] Y. Oka and H. Miyata, "Erosion behaviour of ceramic bulk and coating materials caused by water droplet impingement," *Wear,* vol. 267, no. 11, pp. 1804-1810, 2009.

[3] W. Han, J. Kim and B. Kim, "Effects of contamination and erosion at the leading edge of blade tip airfoils on the annual energy production of wind turbines," *Renewable Energy,* vol. 115, pp. 817-823, 2018.

[4] G. Fiore and M. Selig, "Simulation of Damage Progression on Wind Turbine Blades," in *American Institute of Aeronautics and Astronautics,* California, 2016.

[5] A. Sareen, C. A. Sapre and M. S. Selig, "Effects of leading edge erosion on wind turbine blade performance," *Wind Energy,* vol. 17, no. 10, pp. 1531-1542, 2013.

[6] M. Schramm, H. Rahimi, B. Stoevesandt and K. Tangager, "The Influence of Eroded Blades on Wind Turbine Performance Using Numerical Simulations," *Energies,* vol. 10, no. 9, p. 1420, 2017.

[7] C. Alessio, "Computational analysis of wind-turbine blade rain erosion," *Computers & Fluids,* vol. 141, pp. 175-183, 2016.

[8] S. Zhang, K. Dam-Johansen, P. L. Bernad and S. Kiil, "Rain erosion of wind turbine blade coatings using discrete water jets: Effects of water cushioning, substrate geometry, impact distance, and coating properties," *Wear,* Vols. 328-329, pp. 140-148, 2015.

[9] Sun & Wind Energy, "Eradicating blade damage (Nov. 2014)," 17 Nov 2014. [Online]. Available: http://www.sunwindenergy.com/wind-energy/eradicating-blade-damage. [Accessed 02 01 2019].

[10] L. Rempel, "Rotor blade leading edge erosion real life experiences," *Wind Systems Mag,* Oct. 2012.

[11] A. O'Carroll, M. Hardiman, E. F. Tobin and T. M. Young, "Correlation of the rain erosion performance of polymers to mechanical and surface properties measured using nanoindentation," *Wear,* Vols. 412-413, pp. 38-48, 2018.

[12] B. J. Wilcox, E. B. White and D. C. Maniaci, "Roughness Sensitivity Comparisons of Wind Turbine Blade Sections, Tech. Rep.," Sandia National Laboratories, Oct 2017.

[13] E. K. Kruse, N. N. Sørensen and C. Bak, "A two-dimensional quantitative parametric investigation of simplified surface imperfections on the aerodynamic characteristics of a NACA 633-418 airfoil," *Wind Energy,* vol. 24, no. 4, pp. 310-322, 2021.

[14] R. Kithil, "Lightningsafety.com," National Lightning Safety Institute, 6 2008. [Online]. Available: http://www.lightningsafety.com/nlsi_lhm/wind_blade_damage.pdf. [Accessed 12 1 2018].

[15] A. Fraisse, J. I. Bech, K. K. Borum, V. Fedorov, J. N. F-J, M. McGugan, L. Mishnaevsky and Y. Kusano, "Impact fatigue damage of coated glass fibre reinforced polymer laminate Fraisse," *Renewable Energy,* vol. 126, pp. 1102-1112, 2018.

[16] Y. Kusano, V. Fedorov, M. McGugan, T. L. Andersen and N. F.-J. Johansen, “Impact damage reduction by structured surface geometry,” *Materials Letters,* vol. 221, pp. 296-300, 2018.

[17] P. Panagos, C. Ballabio, P. Borrelli and et al., “Rainfall erosivity in Europe,” *Science of the Total Environment,* vol. 511, pp. 801-814, 2015.

[18] P. Panagos, P. Borrelli, K. Meusburger and et al., “Global rainfall erosivity assessment based on high-temporal resolution rainfall records,” *Scientific Reports,* vol. 7, p. Article number: 4175, 2017.

[19] J. I. Bech, C. B. Hasager and C. Bak, “Extending the life of wind turbine blade leading edges by reducing the tip speed during extreme precipitation events,” *Wind Energ. Sci.,* vol. 3, pp. 729-748, 2018.

[20] B. Amirzadeh, A. Louhghalam, M. Raessi and M. Tootkaboni, “A computational framework for the analysis of rain-induced erosion in wind turbine blades, part I: Stochastic rain texture model and drop impact simulations,” *J. Wind Eng. Ind. Aerodyn.,* vol. 163, pp. 33-43, 2017.

[21] N. Domun, H. Hadavinia, T. Zhang, T. Sainsbury, G. H. Liaghat and S. Vahid, “Improving fracture toughness and strength of epoxy using nanomaterials – A review of current status,” *Nanoscale,* vol. 7, no. 23, p. 10294–10329, 2015.

[22] N. Domun, H. Hadavinia, T. Zhang, G. H. Liaghat, S. Vahid, K. Paton, C. Spacie and T. Sainsbury, “Improving the fracture toughness properties of epoxy using graphene nanoplatelets at low filler content,” *Nanocomposites,* vol. 3, no. 3, pp. 85-96, 2017.

[23] L. Mishnaevsky, C. Hasager, C. Bak, A. Tilg, J. Bech, S. Doagou Rad and S. Fæster, “Leading edge erosion of wind turbine blades: Understanding, prevention and protection,” *Renewable Energy,* vol. 169, pp. 953-969, 2021.

[24] N. Fujisawa, T. Yamagata, K. Hayashi and T. Takano, “Experiments on liquid droplet impingement erosion by high-speed spray,” *Nuclear Engineering and Design,* vol. 250, pp. 101-107, 2012.

[25] N. Fujisawa, T. Yamagata and K. Wada, “Attenuation of wall-thinning rate in deep erosion by liquid droplet impingement,” *Annals of Nuclear Energy,* vol. 88, pp. 151-157, 2016.

[26] N. Fujisawa, T. Yamagata, S. Takano, K. Saito, R. Morita, K. Fujiwara and F. Inada, “The influence of material hardness on liquid droplet impingement erosion,” *Nuclear Engineering and Design,* vol. 288, pp. 27-34, 2015.

[27] N. Fujisawa, T. Yamagata, K. Saito and K. Hayashi, “The effect of liquid film on liquid droplet impingement erosion,” *Nuclear Engineering and Design,* vol. 265, pp. 909-917, 2013.

[28] F. Heymann, “Liquid impingement erosion,” in *Friction, Lubrication, and Wear Technology,* vol. 18, ASM International, 1992, pp. 221 - 231.

[29] Y. Oka, S. Mihara and H. Miyata, “Effective parameters for erosion caused by water droplet impingement and applications to surface treatment technology,” *Wear,* vol. 263, no. 1-6, pp. 386-394, 2007.

[30] A. Hojjati Najafabadi, R. Shoja Razavi, R. Mozaffarinia and H. Rahimi, “A New Approach of Improving Rain Erosion Resistance of Nanocomposite Sol-Gel Coatings by Optimization Process Factors,” *Metallurgical and Materials Transactions A,* vol. 45, no. 5, pp. 2522-2531, 2014.

[31] B. Lee, K. Riu, S. Shin and S. Kwon, “Development of a water droplet erosion model for large steam turbine blades,” *KSME International Journal,* vol. 17, no. 1, pp. 114-121, 2003.

[32] S. DeCorso, “Erosion tests of steam turbine blade materials.,” *American Society for Testing and Materials - Proceedings,* vol. 64, pp. 782-796, 1964.

[33] M. J. Jackson and J. E. Field, “Modelling liquid impact fracture thresholds in brittle materials,” *British Ceramic Transactions,* vol. 99, pp. 1-13, 2000.

[34] M. B. Lesser and J. E. Field, “The Impact of Compressible Liquids,” *Annual Review of Fluid Mechanics,* vol. 15, no. 1, pp. 97-122, 1983.

[35] P. Shipway and K. Gupta, “The potential of WC-Co hardmetals and HVOF sprayed coatings to combat water-droplet erosion,” *Wear,* vol. 271, no. 9-10, pp. 1418-1425, 2011.

[36] J. Zahavi and S. Nadiv, “Indirect damage in composite materials due to raindrop impact,” *Wear,* vol. 72, pp. 305-313, 1981.

[37] M. Jackson and J. Field, “Modelling liquid impact fracture thresholds in brittle materials,” *British Ceramic Transactions,* vol. 99, no. 1, pp. 1-13, 2000.

[38] R. J. Wasley, Stress wave propagation in solids, an introduction., New York: M. Dekker, 1973.

[39] H. Slot, E. Gelinck, C. Rentrop and E. van der Heide, “Leading edge erosion of coated wind turbine blades: Review of coating life models,” *Renewable Energy,* vol. 80, pp. 837-848, 2015.

[40] E. Tobin, T. Young, D. Raps and O. Rohr, “Comparison of liquid impingement results from whirling arm and water-jet rain erosion test facilities,” *Wear,* vol. 271, no. 9-10, pp. 2625-2631, 2011.

[41] E. Tobin, T. Young and D. Raps, “Evaluation and correlation of interlaboratory results from rain erosion test campaign,” in *28th Congress of the International Council of Aeronautical Sciences (ICAS)*, Brisbane, Australia, Sep 2012.

[42] M. A. S. Shohag, E. C. Hammel, D. O. Olawale and O. I. Okoli, “Damage mitigation techniques in wind turbine blades: A review,” *Wind Engineering,* vol. 41, no. 3, pp. 185-210, 2017.

[43] O. Gohardani, “Impact of erosion testing aspects on current and future flight conditions,” *Prog. Aerosp. Sci.,* vol. 47, pp. 280-303, 2011.

[44] R. A. Caruso and M. Antonietti, “Sol−Gel Nanocoating: An Approach to the Preparation of Structured Materials,” *Chemistry of Materials,* vol. 13, no. 10, pp. 3272-3282, 2001.

[45] R. Karmouch and G. G. Ross, “Superhydrophobic wind turbine blade surfaces obtained by a simple deposition of silica nanoparticles embedded in epoxy,” *Applied Surface Science,* vol. 257, no. 3, pp. 665-669, 2010.

[46] C. Peng, S. Xing, Z. Yuan, J. Xiao, C. Wang and J. Zeng, “Preparation and anti-icing of superhydrophobic PVDF coating on a wind turbine blade,” *Applied Surface Science,* vol. 259, pp. 764-768, 2012.

[47] T. Obara, N. Bourne and J. Field, “Liquid-jet impact on liquid and solid surfaces,” *Wear,* Vols. 186-187, pp. 388-394, 1995.

[48] W. F. Adler, “Rain impact retrospective and vision for the future,” *Wear,* Vols. 233-235, pp. 25-38, 1999.

[49] T. Ikohagi, “On Evaluation of LDI Erosion Rate based on Fluid/Solid Coupled Simulation,” in *Eighth International Conference on Flow Dynamics*, Sendai, January 2011.

[50] S. Hattori and M. Kakuichi, “Effect of impact angle on liquid droplet impingement erosion,” *Wear,* Vols. 298-299, pp. 1-7, 2013.

[51] F. J. Heymann, “Conclusions from the ASTM interlaboratory test program with liquid impact erosion facilities,” in *Proc. 5th Int. Conf. Erosion by Liquid and Solid Impact*, Cambridge, UK, Sep. 3-6, 1979.

[52] L. Claire, G. Marie, G. Julien, S. Jean-Michel, R. Jean, M. Marie-Joëlle, R. Stefano and F. Michele, “New architectured hybrid sol-gel coatings for wear and corrosion protection of low-carbon steel,” *Progress in Organic Coatings,* vol. 99, pp. 337-345, 2016.

[53] M. Grundwürmer, O. Nuyken, M. Meyer, J. Wehr and N. Schupp, “Sol–gel derived erosion protection coatings against damage caused by liquid impact,” *Wear,* vol. 263, no. 1-6, pp. 318-329, 2007.

[54] Sharmin.E. and Zafar.F., “Polyurethane: An Introduction,” *Polyurethane,* 2012.

[55] Ashrafizadeh.H., McDonald.A. and Mertiny.P., “Erosive and Abrasive Wear Resistance of Polyurethane Liners,” *Aspects of Polyurethanes,* 2017.

[56] Chattopadhyay.D.K. and Raju.K.V.S.N., “Structural engineering of polyurethane coatings for high performance applications,” *Progress in Polymer Science,* vol. 32, no. 3, pp. 352-418, 2007.

[57] Konieczny.J. and Loos.K., “Green Polyurethanes from Renewable Isocyanates and Biobased White Dextrins,” *Polymers,* vol. 11, no. 2, p. 256, 2019.

[58] Sumer.G.T., Ansari.M., Shanks.R. and Khong.I., “Mechanical Studies on Polyurethane (PU)-Starch Nanocomposites,” Melbourne, 2016.

[59] Godfrey.M., Siederer.O., Zekonyte.J., Barbaros.I. and Wood.R., “The effect of temperature on the erosion of polyurethane coatings for wind turbine leading edge protection,” *Wear,* vol. 476, 2021.

[60] Cizmas.P. and Slattery.J., “Dimensionless correlation for sand erosion of families of polymers,” *Wear,* vol. 262, no. 3-4, pp. 316-319, 2007.

[61] J. Leng and A. Lau, Multifunctinal polymer nanocomposite, Boca Raton: Taylor and Francis group, 2010.

[62] Z. Sh, K. S, D. J. K, B. J and P. L, “Accelerated rain erosion of wind turbine blade coatings,” Technical University of Denmark, Denmark, 2014.

[63] N. DALILI, A. EDRISY and R. CARRIVEAU, “A review of surface engineering issues critical to wind turbine performance,” *Renewable and Sustainable Energy Reviews,* vol. 13, no. 2, pp. 428-438, 2009.

[64] X. P. H, “Polyurethane Nanocomposite Coatings for Aeronautical Applications,” University of Bristol, Bristol , 2010.

[65] E. CORTÉS, F. SÁNCHEZ, A. O’CARROLL, B. MADRAMANY, M. HARDIMAN and T. YOUNG, “On the Material Characterisation of Wind Turbine Blade Coatings: The Effect of Interphase Coating–Laminate Adhesion on Rain Erosion Performance,” *Materials,* vol. 10, no. 10, p. 1146, 2017.

[66] Xia.H and Song.M., “Preparation and characterization of polyurethane–carbon nanotube composites,” *Soft Matter,* vol. 1, no. 5, p. 386, 2005.

[67] M. Malaki, Y. Hashemzadeh and M. Karevan, “ Effect of nano-silica on the mechanical properties of acrylic polyurethane coatings,” *Progress in Organic Coatings,* vol. 101, pp. 477-485, 2016.

[68] Z. S. Petrović, I. Javni, A. Waddon and G. Bánhegyi, “Structure and properties of polyurethane–silica nanocomposites,” *Journal of Applied Polymer Science,* vol. 76, no. 2, pp. 133-151, 2000.

[69] Y.-C. Chung, K. H. Chung, J. W. Choi and B. C. Chun, “Preparation of hybrid polyurethane-silica composites by a lateral sol-gel process using tetraethyl orthosilicate,” *Journal of Composite Materials,* vol. 52, no. 2, pp. 159-168, 2018.

[70] C. Syamsundar, D. Chatterjee, M. Kamaraj and A. K. Maiti, “Erosion characteristics of nanoparticle-reinforced polyurethane coatings on stainless steel substrate,” *J. Mater. Eng. Perform.,* vol. 24, no. 4, pp. 1391-1405, 2015.

[71] D. J. Mills, S. S. Jamali and K. Paprocka, “Investigation into the effect of nano-silica on the protective properties of polyurethane coatings,” *Surface Coating Technology,* vol. 209, pp. 137-142, 2012.

[72] D. Kotnarowska, M. Przerwa and M. Wojtyniak, “Effect of epoxy and polyurethane coating modification with nanofillers on their resistance to erosive wear,” *Vibroengineering ,* vol. 13, pp. 870-875, 2011.

[73] P. Pokharel, B. Pant, K. Pokhrel, H. R. Pant, J. G. Lim, H. Y. Kim and S. Choi, “Effects of functional groups on the graphene sheet for improving the thermomechanical properties of polyurethane nanocomposites,” *Composite Part B,* vol. 78, pp. 192-201, 2015.

[74] A. E. Tarasov, D. V. Anokhin, Y. V. Propad, E. A. Bersenev, S. V. Razorenov, G. V. Garkushin and E. R. Badamshina, “Synergetic effect of fullerene and graphene oxide nanoparticles on mechanical characteristics of cross-linked polyurethanes under static and dynamic loading,” *Journal of Composite Materials,* vol. 53, no. 26-27, pp. 3797-3805, 2019.

[75] U. Tayfun, Y. Kanbur, U. Abacı, H. Y. Güney and E. Bayramlı, “Mechanical, electrical, and melt flow properties of polyurethane elastomer/surface-modified carbon nanotube composites,” *Journal of Composite Materials,* vol. 51, no. 14, pp. 1987-1996, 2017.

[76] S. Guo, C. Zhang, W. Wang, T. Liu, W. C. Tjiu, C. He and W.-D. Zhang, “Preparation and Characterization of Polyurethane/Multiwalled Carbon Nanotube Composites,” *Polymers and Polymer Composites,* vol. 16, pp. 501-507, 2008.

[77] Y. Li, H. Jiao, G. Pan, Q. Wang and T. Wang, “Mechanical and damping properties of carbon nanotube-modified polyisobutylene-based polyurethane composites,” *Journal of Composite Materials,* vol. 50, no. 7, pp. 929-936, 2015.

[78] X. Qiao, R. Chen, H. Zhang, J. Liu, Q. Liu, J. Yu, P. Liu and J. Wan, “Outstanding cavitation erosion resistance of hydrophobic polydimethylsiloxane-based polyurethane coatings,” *Journal of Applied Polymer Science,* vol. 136, no. 25, p. 47668, 2019.

[79] Z. Eivazi Zadeh, A. Solouk, M. Shafieian and M. Haghbin Nazarpak, “Electrospun polyurethane/carbon nanotube composites with different amounts of carbon nanotubes and almost the same fiber diameter for biomedical applications,” *Material Science and Engineering: C,* vol. 118, p. 111403, 2021.

[80] M. H. Moghim and S. M. Zebarjad, “Tensile properties and deformation mechanisms of PU/MWCNTs nanocomposites,” *Polymer Bulletin,* vol. 74, p. 4267–4277, 2017.

[81] M. Alberto, M. Iliut, M. P. Pitchana, J. Behnsen and A. Vijayaraghavan, “High-grip and hard-wearing graphene reinforced polyurethane coatings,” *Composites Part B: Engineering,* vol. 213, p. 108727, 2021.

[82] T. Rihayat, M. Saari, M. H. Mahmood, W. M. Z. W. Yunus, A. R. Suraya, K. Z. H. M. Dahlan and S. M. Sapuan, “Mechanical Characterisation of Polyurethane/Clay Nanocomposites,” *Polymers and Polymer Composites,* vol. 15, no. 8, pp. 647-652, 2007.

[83] Y.-C. Chung, N. D. Khiem and B. C. Chun, “Characterization of a polyurethane copolymer covalently linked to graphite and the influence of graphite on electric conductivity,” *Journal of Composite Materials,* vol. 49, no. 14, pp. 1689-1703, 2014.

[84] B. C. Dave, X. Hu, Y. Devaraj and S. K. Shirshak K. Dhali, “Sol–Gel-Derived Corrosion-Protection Coatings,” *Journal of Sol-Gel Science and Technology,* vol. 32, pp. 143-147, 2004.

[85] H. Huang, B. Orler and G. Wilkes, “Ceramers-hybrid materials incorporating polymeric oligomeric species into inorganic glasses utilizing a sol-gel approach,” *Polymer Bulletin,* vol. 14, no. 6, pp. 557-564, 1985.

[86] H. Schmidt and H. Wolter, “Organically modified ceramics and their applications,” *Journal of Non-Crystalline Solids,* vol. 121, no. 1-3, pp. 428-435, 1990.

[87] K.-H. Haas and H. Wolter, “Synthesis, properties and applications of inorganic–organic copolymers (ORMOCER®s),” *Current Opinion in Solid State and Materials Science,* vol. 4, no. 6, pp. 571-580, 1999.

[88] S. Dash, S. Mishra, S. Patel and B. K. Mishra, “Organically modified silica: Synthesis and applications due to its surface interaction with organic molecules,” *Advances in Colloid and Interface Science,* vol. 140, no. 2, pp. 77-94, 2008.

[89] L. Sowntharya and R. Subasri, “A comparative study of different curing techniques for SiO2–TiO2 hybrid coatings on polycarbonate,” *Ceramics International,* vol. 39, no. 4, pp. 4689-4693, 2013.

[90] R. S. Kalidindi and R. . Subasri, “Sol-gel nanocomposite hard coatings,” in *Anti-Abrasive Nanocoatings: Current and Future Applications*, Elsevier, 2015, pp. 105-136.

[91] T. Olding, M. Sayer and D. Barrow, “Ceramic sol–gel composite coatings for electrical insulation,” *Thin Solid Films,* vol. 398–399, pp. 581-586, 2001.

[92] “Introduction to sol-gel,” 2006. [Online]. Available: http://www.ceramics.mmat.ubc.ca/introduction.html. [Accessed 1 11 2017].

[93] V. Gavalas, R. Andrews, D. Bhattacharyya and L. Bachas, “Carbon Nanotube Sol−Gel Composite Materials,” *Nano Letters,* vol. 1, no. 12, pp. 719-721, 2001.

[94] J. D. Maeztu, P. J. Rivero, C. Berlanga, D. M. Bastidas, J. F. Palacio and R. Rodriguez, “Effect of graphene oxide and fluorinated polymeric chains incorporated in a multilayered sol-gel nanocoating for the design of corrosion resistant and hydrophobic surfaces,” *Applied Surface Science,* vol. 419, pp. 138-149, 2017.

[95] S. Attia, J. Wang and J. Shen, “Review on sol-Gel Derived Coatings: Process, Techniques and Optical Applications,” *Journal of Materials Science and Technology,* vol. 18, no. 3, pp. 211-218, 2002.

[96] G. Kickelbick, Hybrid Materials: Synthesis, Characterization, and Applications, USA: Willey-VCH, 2007.

[97] K. Sugiyama, S. Nakahama, S. Hattori and K. Nakano, “Slurry wear and cavitation erosion of thermal-sprayed cermets,” *Wear,* vol. 258, no. 5-6, pp. 768-775, 2005.

[98] D. Meyerhofer, “Characteristics of resist films produced by spinning,” *Journal of Applied Physics* , vol. 49, p. 3993, 1978.

[99] W. Dou, P. Wang, D. Zhang and J. Yu, “An efficient way to prepare hydrophobic antireflective SiO2 film by sol–gel method,” *Materials Letters,* vol. 167, pp. 69-72, 2016.

[100] S. Amiri and A. Rahimi, “Hybrid nanocomposite coating by sol–gel method: a review,” *Iranian Polymer Journal,* vol. 25, no. 6, pp. 559-577, 2016.

[101] M. Goosey, “A short introduction to graphene and its potential interconnect applications,” *Circuit World,* vol. 38, no. 2, pp. 83-86, 2012.

[102] R. Maria-Hormigos, B. Jurado-Sanchez and L. Vazquez, “Carbon Allotrope Nanomaterials Based Catalytic Micromotors,” *Chemistry of Materials,* vol. 28, no. 24, pp. 8962-8970, 2016.

[103] S. Iijima and T. Ichihashi, “Single-shell carbon nanotubes of 1-nm diameter,” *Nature ,* vol. 363, pp. 603-605, 1993.

[104] S. Iijima, “Helical microtubules of graphitic carbon,” *Nature,* vol. 9, no. 6348, pp. 56-58, 1991.

[105] A. Eatemadi, H. Daraee, H. Karimkhanloo, M. Kouhi, N. Zarghami, A. Akbarzadeh, M. Abasi, Y. Hanifehpour and S. Joo, “Carbon nanotubes: properties, synthesis, purification, and medical applications,” *Nanoscale Research Letters,* vol. 9, no. 1, p. 393, 2014.

[106] M. Aegerter, “Characterization of the mechanical properties of sol-gel coatings,” in *Sol-Gel Science and Technology,* Springer, Cham, 2017, pp. 1-19.

[107] H. Dai, “Carbon Nanotubes: Synthesis, Integration, and Properties,” *Accounts of Chemical Research,* vol. 35, no. 12, pp. 1035-1044, 2002.

[108] M. Dresselhaus, G. Dresselhaus and R. C. Saito, “Physics of carbon nanotubes,” vol. 33, no. 7, pp. 883-891, 1995.

[109] S. Kushch and N. Kuyunko, “Fullerene black: Structure, properties and possible applications,” *Russian Journal of General Chemistry,* vol. 81, no. 2, pp. 345-353, 2011.

[110] A. Castro Neto, F. Guinea, N. Peres, K. Novoselov and A. Geim, “The electronic properties of graphene,” *Reviews of Modern Physics,* vol. 81, no. 1, pp. 109-162, 2009.

[111] S. Chatterjee, F. A. Nuesch and B. T. T. Chu, “Comparing carbon nanotubes and graphene nanoplatelets as reinforcements in polyamide 12 composites,” *Nanotechnology,* vol. 22, no. 27, p. 275714, 2011.

[112] I. D. Rosca, F. Watari, M. Uo and T. Akasaka, “Oxidation of multiwalled carbon nanotubes by nitric acid,” *Carbon,* vol. 43, no. 15, pp. 3124-3131, 2005.

[113] A. Alam, C. Wana and T. McNally, “Surface amination of carbon nanoparticles for modification of epoxy resins: plasma-treatment vs. wet-chemistry approach,” *European Polymer Journal,* vol. 87, pp. 422-448, 2017.

[114] X.-Z. Tang, W. Li, Z.-Z. Yu, M. A. Rafiee, J. Rafiee, F. Yavari and N. Koratkar, “Enhanced thermal stability in graphene oxide covalently functionalized with 2-amino-4,6-didodecylamino-1,3,5-triazine,” *Carbon ,* vol. 49, no. 4, pp. 1258-1265, 2011.

[115] Q. Zhang, J. Wu, L. Gao, T. Liu, W. Zhong, G. Sui, G. Zheng, W. Fang and X. Yang, “Dispersion stability of functionalized MWCNT in the epoxy-amine system and its effects on mechanical and interfacial properties of carbon fiber composites,” *Materials & Design,* vol. 94, pp. 392-402, 2016.

[116] K. A. Wepasnick, B. A. Smith, K. E. Schrote, H. K. Wilson, S. R. Diegelmann and D. H. Fairbrother, “Surface and structural characterization of multi-walled carbon nanotubes following different oxidative treatments,” *Carbon,* vol. 49, no. 1, pp. 24-36, 2011.

[117] B. Smith, K. Wepasnick, K. E. Schrote, H. Cho, W. P. Ball and D. H. Fairbrother, “Influence of Surface Oxides on the Colloidal Stability of Multi-Walled Carbon Nanotubes: A Structure−Property Relationship,” *Langmuir,* vol. 25, no. 17, pp. 9767-9776, 2009.

[118] N. Domun, K. Paton, H. Hadavinia, T. Sainsbury, T. Zhang and H. Mohamud, "Enhancement of Fracture Toughness of Epoxy Nanocomposites by Combining Nanotubes and Nanosheets as Fillers," *Materials,* vol. 10, no. 12, p. 1179, 2017.

[119] H. Hiura, T. W. Ebbesen and K. Tanigaki, "Opening and purification of carbon nanotubes in high yields," *Advanced Materials,* vol. 7, no. 3, pp. 275-276, 1995.

[120] N. Blanchard, R. Hatton and S. Silva, "Tuning the work function of surface oxidised multi-wall carbon nanotubes via cation exchange," *Chemical Physics Letters,* vol. 434, no. 1-3, pp. 92-95, 2007.

[121] N. Montakhab, S. Sadegh Hassani, A. Rashidi and H. Arabi, "Synthesis and charactrization of SiO2-CNT hybrid using sol-gel method," in *Ultrafine Grained and Nanostructured Materials*, Tehran, 2011.

[122] Y. Peng and H. Liu, "Effects of Oxidation by Hydrogen Peroxide on the Structures of Multiwalled Carbon Nanotubes," *Industrial & Engineering Chemistry Research,* vol. 45, no. 19, pp. 6483-6488, 2006.

[123] K. J. Ziegler, Z. Gu, J. Shaver, Z. Chen, E. L. Flor, D. J. Schmidt, C. Chan, R. H. Hauge and R. E. Smalley, "Cutting single-walled carbon nanotubes," *Nanotechnology,* vol. 16, no. 7, pp. 539-544, 2005.

[124] J. Shen, W. Huang, L. Wu, Y. Hu and M. Ye, "Study on amino-functionalized multiwalled carbon nanotubes," *Materials Science and Engineering: A,* vol. 464, no. 1-2, pp. 151-156, 2007.

[125] W. Wu, C. Wan and Y. Zhang, "Graphene oxide as a covalent-crosslinking agent for EVM-g-PA6 thermoplastic elastomeric nanocomposites," *RSC Advances ,* vol. 5, no. 49, p. 39042–39051, 2015.

[126] W. Zhao, M. Fang, F. Wu, H. Wu, L. Wang and C. G., "Preparation of graphene by exfoliation of graphite using wet ball milling," *Journal of Materials Chemistry,* vol. 20, no. 28, pp. 5817-581, 2010.

[127] N. Pierard, A. Fonseca, Z. Konya, I. Willems, G. Van Tendeloo and J. B. Nagy, "Production of short carbon nanotubes with open tips by ball milling," *Chemical Physics Letters,* vol. 335, no. 1-2, pp. 1-8, 2001.

[128] I.-Y. Jeon, H.-J. Choi, S.-M. Jung, J.-M. Seo, M.-J. Kim, L. Dai and J.-B. Baek, "Large-scale production of edge-selectively functionalized graphene nanoplatelets via ball milling and their use as metal-free electrocatalysts for oxygen reduction reaction," *Journal of the American Chemical Society,* vol. 135, no. 4, pp. 1386-1393, 2013.

[129] R. d'Agostino, P. Favia, C. Oehr and M. Wertheimer, "Low-temperature plasma processing of materials: past, present, and future," *Plasma Processes and Polymers,* vol. 2, no. 1, pp. 7-15, 2005.

[130] T. Desmet, R. Morent, N. D. Geyter, C. Leys, E. Schacht and P. Dubruel, "Nonthermal plasma technology as a versatile strategy for polymeric biomaterials surface modification: a review," *Biomacromolecules ,* vol. 10, no. 9, pp. 2351-2378, 2009.

[131] V. Georgakilas, M. Otyepka, A. B. Bourlinos, V. Chandra, N. Kim, K. C. Kemp, P. Hobza, R. Zboril and K. S. Kim, "Functionalization of Graphene: Covalent and Non-Covalent Approaches, Derivatives and Applications," *Chemical Reviews,* vol. 112, no. 11, pp. 6156-6214, 2012.

[132] J. Park and M. Yan, "Covalent functionalization of graphene with reactive intermediates," *Accounts of Chemical Research,* vol. 46, no. 1, pp. 181-189, 2013.

[133] A. Sinitskii, A. Dimiev, D. A. Corley, A. A. Fursina, D. V. Kosynkin and J. M. Tour, "Kinetics of Diazonium Functionalization of Chemically Converted Graphene Nanoribbons," *ACS Nano,* vol. 4, no. 4, pp. 1949-1954, 2010.

[134] W. Zan, “Chemical functionalization of graphene by carbene cycloaddition: A density functional theory study,” *Applied Surface Science,* vol. 311, pp. 377-383, 2014.

[135] T. A. Strom, E. P. Dillon, C. E. Hamilton and A. R. Barron, “Nitrene addition to exfoliated graphene: a one-step route to highly functionalized graphene,” *Chemical Communications,* vol. 46, no. 23, p. 4097, 2010.

[136] S. Vadukumpully, J. Gupta, Y. Zhang, G. Q. Xu and S. Valiyaveettil, “Functionalization of surfactant wrapped graphenenanosheets with alkylazides for enhanced dispersibility,” *Nanoscale,* vol. 3, no. 1, pp. 303-308, 2011.

[137] H. M. Chong, S. J. Hinder and A. C. Taylor, “Graphene nanoplatelet-modified epoxy: effect of aspect ratio and surface functionality on mechanical properties and toughening mechanisms,” *J Mater Sci,* vol. 51, pp. 8764-8790, 2016.

[138] Leverette.C., Wills.C., Perkins.M. and Jacobs.S., “Structural Analysis of Nanofilms Using FTIR Spectroscopy. An Introduction to the Spectroscopic Analysis of Nanostructures for Undergraduate Students,” *Journal of Chemical Education,* vol. 86, no. 6, p. 719, 2009.

[139] Shankar.S.N., “Characterization of polyurethane at multiple scales for erosion mechanisms under sand particle impact,” A&M University, Texas, 2010.

[140] Agilent, “FTIR Spectroscopy FAQs,” Agilent, [Online]. Available: https://www.agilent.com/en/support/molecular-spectroscopy/ftir-spectroscopy/ftir-spectroscopy-basics-faqs. [Accessed 26 12 2021].

[141] Le.V., Ngo.C., Le.Q., Ngo.T., Nguyen.D. and Vu.M., “Surface modification and functionalization of carbon nanotube with some organic compounds,” *Advances in Natural Sciences: Nanoscience and Nanotechnology,* vol. 4, no. 3, 2013.

[142] Ghobashy.. and Abdeen., “Radiation Crosslinking of Polyurethanes: Characterization by FTIR, TGA, SEM, XRD, and Raman Spectroscopy,” *Journal of Polymers,* pp. 1-9, 2016.

[143] Chang.J., Tian.B., Li.L. and Zheng.Y., “Microstructure and Damping Property of Polyurethane Composites Hybridized with Ultraviolet Absorbents,” *Advances in Materials Science and Engineering,* pp. 1-9, 2018.

[144] Razmara.M., Saidpour.S.H. and Arunchalam.S., “DMA Investigation on Polyurethane (PUR),” in *International Conference on Fascinating Advancement in Mechanical Engineering (FAME2008)*, 2018.

[145] A. Olad, F. Rezvani and R. Nosrati, “Preparation and characterization of polyurethane based self-cleaning and antibacterial coating containing silver ion exchanged montmorillonite/TiO2 nanocomposite,” *Research on Chemical Intermediates,* vol. 44, no. 3, pp. 1711-1727, 2017.

[146] S. Lee and C. Park, “Influence of alkaline treatment on surface roughness and wetting properties of hydrophobized silk fabrics,” *Textile Research Journal,* vol. 88, no. 7, pp. 777-789, 2017.

[147] Q. Dou, C. Wang, C. Cheng, W. Han, P. Thüne and W. Ming, “PDMS-Modified Polyurethane Films with Low Water Contact Angle Hysteresis,” *Macromolecular Chemistry and Physics,* vol. 207, no. 23, pp. 2170-2179, 2006.

[148] K. Chang, Y. Wang, K. Peng, H. Tsai, J. Chen, C. Huang, K. Ho and W. Lien, “Preparation of silica aerogel/polyurethane composites for the application of thermal insulation,” *Journal of Polymer Research,* vol. 21, no. 1, 2014.

[149] Y. Ibrahim, V. S. Wadi, M. Ouda, V. Naddeo, F. Banat and S. W. Hasan, “Highly selective heavy metal ions membranes combining sulfonated polyethersulfone and self-assembled manganese oxide nanosheets

on positively functionalized graphene oxide nanosheets," *Chem. Eng. J.,* vol. 428, no. 15, p. 131267, 2022.

[150] H. Qi and M. Boyce, "Stress–strain behavior of thermoplastic polyurethanes," *Mechanics of Materials,* vol. 37, no. 8, pp. 817-839, 2005.

[151] W. Cherng, "Influence of Material Surface Hardness and Particle Size on the Erosion of DC 11 Tool Steel," China Institute of Technology.

[152] ISO 34-1 2015 Standard, "Rubber, vulcanized or thermoplastic-Determination of tear strength-part 1:Trouser, angle and crescent test pieces".

[153] R. P. Institute, "A Novel Laboratory Dispersive and Distributive MiniMixer and Applications," University of Bradford, Bradford, 2009.

[154] P. R. Pinto, L. C. Mendes, M. L. Dias and C. Azuma, "Synthesis of acrylic-modified sol-gel silica," *Colloid Polym. Sci,* vol. 284, pp. 529-535, 2006.

[155] A. Dashtkar, N. J. Johansen, L. Mishnaevsky Jr., N. A. Williams, W. Shadi, V. Wadi, A. Silvello and H. Hadavinia, "Graphene/sol gel modified polyurethane coating for wind turbine blade leading edge protection: Properties and performance," *Polymers and Polymer Composites,* vol. 30, pp. 1-18, 2022.

[156] Trovati.G., Sanches.E., Neto.S., Mascarenhas.Y. and Chierice.G., "Characterization of polyurethane resins by FTIR, TGA, and XRD," *Journal of Applied Polymer Science,* vol. 115, no. 1, pp. 263-268, 2010.

[157] Crawford.D. and Escarsega.J., "Dynamic mechanical analysis of novel polyurethane coating for military applications," *Thermochimica Acta,* Vols. 357-358, pp. 161-168, 2000.

[158] Z. Wu, H. Wang, X. Tian, M. Xue, X. Ding, X. Ye and Z. Cui, "Surface and mechanical properties of hydrophobic silica contained hybrid films of waterborne polyurethane and fluorinated polymethacrylate," *Polymers,* vol. 55, p. 187–194, 2014.

[159] M. Khani, D. Woo, E. Mumpower and B. Benicewicz, "Poly(alkyl methacrylate)-grafted silica nanoparticles in polyethylene nanocomposites," *Polymers,* vol. 109, p. 339–34, 2017.

[160] B. Radomir and F. Martin, "Loading and unloading curve of Foam material based on compression test," *Mechanical Engineering ,* vol. 69, no. 3, pp. 3-8, 2019.

[161] N. Frost-Jensen Johansen, L. Mishnaevsky, A. Dashtkar, N. Williams, S. Fæster, A. Silvello, A. Cano and H. Hadavinia, "Nanoengineered Graphene-Reinforced Coating for Leading Edge Protection of Wind Turbine Blades," *Coatings,* vol. 11, no. 9, p. 1104, 2021.

[162] A. Dashtkar, H. Hadavinia, M. Sahinkaya, S. Williams, F. Ismail and M. Turner, "Rain erosion-resistant coatings for wind turbine blades: A review," *Polymers and Polymer Composites,* vol. 27, no. 8, pp. 443-475, 2019.

[163] E. Andreasson, N. Mehmood and S. Kao-Walter, "Trouser tear tests of two thin polymer films," in *13th Int. Conf. Fract. ,* Beijing, 2013.

[164] N. Liu, G. Song, J. Yi and Y. Xu, "Damping analysis of polyurethane/polyacrylate interpenetrating polymer network composites filled with graphite particles," *Polymer Composites,* vol. 34, no. 2, pp. 288-292, 2013.

[165] Y. Zhang, "Measuring Acoustic Attenuation of Polymer Materials Using Drop Ball," Embry-Riddle Aeronautical University , Florida , 2013.

[166] D. Ensminger and L. Bond, Ultrasonics Fundamentals, Technologies, and Applications, CRC Press, 2011.

[167] M. Nakamura, Y. Aoki, G. Enna, K. Oguro and H. Wada, "Polyurethane damping material," *Journal of Elastomers & Plastics,* vol. 47, no. 6, pp. 515-522, 2014.

[168] T. Trakulsujaritchok and D. Hourston, "Damping characteristics and mechanical properties of silica filled PUR/PEMA simultaneous interpenetrating polymer networks," *European Polymer Journal,* vol. 42, no. 11, pp. 2968-2976, 2006.

[169] T. Wang, S. Chen, Q. Wang and X. Pei, "Damping analysis of polyurethane/epoxy graft interpenetrating polymer network composites filled with short carbon fiber and micro hollow glass bead," *Materials & Design,* vol. 31, no. 8, pp. 3810-3815, 2010.

[170] P. Pötschke, A. R. Bhattacharyya, A. Janke and H. Goering, "Melt mixing of polycarbonate/multi-wall carbon nanotube composites," *Composite Interfaces* , vol. 10, no. 4-5, pp. 389-404, 2003.

[171] C. Lee, X. D. Wei, J. W. Kysar and J. Hone, "Measurement of the elastic properties and intrinsic strength of monolayer graphene," *Science,* vol. 321, no. 5885, pp. 385-388, 2008.

[172] X. Wang, Y. Hu, L. Song, H. Yang, W. Xing and H. Lu, "In situ polymerization of graphene nanosheets and polyurethane with enhanced mechanical and thermal properties," *Journal of Materials Chemistry,* vol. 21, p. 4222, 2011.

[173] M. Song and D. Cai, "Polyurethane Nanocomposites by In-situ Polymerization Approach and Their Properties," in *In-Situ Synthesis of Polymer Nanocomposites,* Wiley, 2011, pp. 169-220.

[174] D. Cai, K. Kamal Yusoh and M. Song, "The mechanical properties and morphology of a graphite oxide nanoplatelet/polyurethane composite," *Nanotechnology,* vol. 20, no. 8, p. 085712, 2009.

[175] U. Khan, P. May, A. O'Neill and J. N. Coleman, "Development of stiff, strong, yet tough composites by the addition of solvent exfoliated graphene to polyurethane," *Carbon* , vol. 48, no. 14, pp. 4035-4041, 2010.

[176] J. Barros-Rodriguez, R. F. Le Roux, J. Lopez-Diez and R. Martinez-Val, "Frequency and damping identification in flutter flight testing using singular value decomposition and QR factorization," *Proc IMechE Part G: J Aerospace Engineering,* vol. 229, no. 3, p. 323–332, 2015.

[177] J. Barros-Rodriguez, M. F. Fructuoso, R. F. Le Roux, S. S. Prieto and O. R. Polo, "Unveiling modal parameters with forced response using SVD and QR during flutter flight testing," *Proc IMechE Part G: J Aerospace Engineering,* vol. 232, no. 1, pp. 68-76, 2018.

[178] H. Sönnerlind, "Comsol," 14 03 2019. [Online]. Available: https://uk.comsol.com/blogs/damping-in-structural-dynamics-theory-and-sources/. [Accessed 12 05 2020].

[179] V. Geethamma, R. Asaletha, N. Kalarikkal and S. Thomas, "Vibration and sound damping in polymers," *Resonance,* vol. 19, no. 9, pp. 821-833, 2014.

[180] K. Yoon, J. Kim and D. Bang, "Damping properties and transmission loss of polyurethane. II. PU layer and copolymer effect," *Fibers and Polymers,* vol. 4, no. 2, pp. 49-53, 2003.

[181] M. Song, D. J. Hourston and F. U. Schafer, "Correlation between mechanical damping and interphase content in interpenetrating polymer networks," *Journal of Applied Polymer Science,* vol. 81, no. 10, pp. 2439-2442, 2001.

[182] A. Pei, J. Malho, J. Ruokolainen, Q. Zhou and L. Berglund, “Strong Nanocomposite Reinforcement Effects in Polyurethane Elastomer with Low Volume Fraction of Cellulose Nanocrystals,” *Macromolecules,* vol. 44, no. 11, pp. 4422-4427, 2011.

[183] M. Bernal, I. Molenberg, S. Estravis, M. Rodriguez-Perez, I. Huynen, M. Lopez-Manchado and R. Verdejo, “Comparing the effect of carbon-based nanofillers on the physical properties of flexible polyurethane foams,” *Journal of Materials Science,* vol. 47, no. 15, pp. 5673-5679, 2012.

[184] M. Strankowski, “Effect of Variation of Hard Segment Content and Graphene-Based Nanofiller Concentration on Morphological, Thermal, and Mechanical Properties of Polyurethane Nanocomposites,” *International Journal of Polymer Science,* pp. 1-20, 2018.

[185] J. González-Irún Rodríguez, P. Carreira, A. García-Diez, D. Hui and R. Artiaga, “Nanofiller effect on the glass transition of a polyurethane,” *Thermal Analysis and Calorimetry,* vol. 87, no. 1, pp. 45-47, 2007.

[186] P. Macioce, “Viscoelastic Damping 101,” *Sound and Vibration,* vol. 37, no. 4, pp. 8-10, 2003.

[187] N. Ahmad, “A Methodology For Developing High Damping Materials With Application of Noise Reduction of Railway Track,” University of Southamppton, 2009.

[188] K. Lee, J. Choi, S. Kim, B. Lee, J. Hwang and B. Lee, “Damping and mechanical properties of composite composed of polyurethane matrix and preplaced aggregates,” *Construction and Building Materials,* vol. 145, pp. 68-75, 2017.

[189] J. Mun Kim, D. Hoon Kim, J. Kim, J. Wook Lee and W. Nyon Kim, “Effect of Graphene on the Sound Damping Properties of Flexible Polyurethane Foams,” *Macromolecular Research,* vol. 25, no. 2, pp. 190-196, 2017.

[190] I. Hutchings, D. Deuchar and A. Muhr, “Erosion of unfilled elastomers by solid particle impact,” *Materials Science,* p. 4071–4076, 1987.

[191] S. M, “optiTrack application,” OptiTrack , 2022. [Online]. Available: https://www.optitrack.com/applications/robotics/. [Accessed 01 06 2022].

[192] L. Mishnaevsky, S. Fæster, L. Mikkelsen, Y. Kusano and J. Bech, “Micromechanisms of leading edge erosion of wind turbine blades: X-ray tomography analysis and computational studies,” *Wind Energy,* vol. 23, no. 3, pp. 547-562, 2019.

[193] M. H. Keegan, D. H. Nash and M. M. Stack, “On erosion issues associated with the leading edge of wind turbine blades,” *Journal of Physics D: Applied Physics,* vol. 46, no. 38, p. 383001, 2013.

[194] R. Herring, K. Dyer, F. Martin and C. Ward, “The increasing importance of leading edge erosion and a review of existing protection solutions,” *Renewable and Sustainable Energy Reviews,* vol. 115, p. 109382, 2019.

[195] K. Kojio, S. Nozaki, A. Takahara and S. Yamasaki, “Influence of chemical structure of hard segments on physical properties of polyurethane elastomers: a review,” *Journal of Polymer Research,* vol. 27, p. 140, 2020.

[196] I. Yilg, E. Yilg and G. L. Garth L. Wilkes, “Critical parameters in designing segmented polyurethanes and their effect on morphology and properties: A comprehensive review,” *Polymer,* vol. 58, pp. A1-A36, 2015.

[197] L. Mishnaevsky Jr, “Toolbox for optimizing anti-erosion protective coatings of wind turbine blades: Overview of mechanisms and technical solutions,” *Wind Energy,* vol. 22, no. 11, pp. 1636-1653, 2019.

[198] A. Dashtkar, H. Hadavinia, J. Barros-Rodriguez, N. A. Williams, M. Turner and S. Vahid, "Quantifying damping coefficient and attenuation at different frequencies for graphene modified polyurethane by drop ball test," *Polymer Testing,* p. 107267, 2021.

[199] S. Fæster, N. Johansen, L. Mishnaevsky, Y. Kusano, J. Bech and M. Madsen, "Rain erosion of wind turbine blades and the effect of air bubbles in the coatings," *Wind Energy,* vol. 24, no. 10, pp. 1071-1082, 2021.

[200] L. Mishnaevsky, "Repair of wind turbine blades: Review of methods and related computational mechanics problems," *Renewable Energy,* vol. 140, pp. 828-839, 2019.

[201] M. Elhadi Ibrahim and M. Medraj, "Water Droplet Erosion of Wind Turbine Blades: Mechanics, Testing, Modeling and Future Perspectives," *Materials,* vol. 13, no. 1, p. 157, 2019.

[202] G. Springer, "Erosion by Liquid Impact," Scripta Publishing Co, Dallas, TX, USA, 1976.

[203] G. Prayogo, H. Homma, T. P. Soemardi and A. S. Danardono, "Impact Fatigue Damage of GFRP Materials Due to Repeated Raindrop Collisions," *Transactions of the Indian Institute of Metals,* vol. 64, no. 4-5, pp. 501-506.

[204] M. Graham, J. Carlyle and T. Menna, "Facility for high-speed particle impact testing," *Review of Scientific Instruments,* vol. 46, no. 9, pp. 1221-1225, 1975.

[205] N. Johansen, " Test Methods for Evaluating Rain Erosion Performance of Wind Turbine Blade Leading Edge Protection Systems," Technical University of Denmark, Lyngby, Denmark, 2020.

[206] E. Gaertner, J. Rinker, L. Sethuraman, F. Zahle, B. Anderson, G. Barter, N. Abbas, F. Meng, P. Bortolotti, W. Skrzypinski and G. Scott, "IEA Wind TCP Task 37: Definition of the IEA 15-Megawatt Offshore Reference Wind Turbine," pp. 1-44, 2020.

[207] W. Weigel, "Advanced Rotor Blade Erosion Protection System," Defense Technical Information Center, Fort Belvoir, VA, USA, 1996.

[208] S. Rad and L. J. Mishnaevsky, " Leading edge erosion of wind turbine blades: Computational modelling of multiaxial fatigue.," *Wind Energy,* vol. 23, pp. 1766-1752, 2020.

[209] L. Mishnaevsky and J. Sütterlin, "Micromechanical model of surface erosion of polyurethane coatings on wind turbine blades," *Polymer Degradation and Stability,* vol. 166, pp. 283-289, 2019.

[210] W. Adler, "Liquid drop collisions on deformable media.," 1977.

[211] Liu.Z., Bai.G., Huang.Y., Ma.Y., Du.F., Li.F., Guo.T. and Chen.Y., "Reflection and absorption contributions to the electromagnetic interference shielding of single-walled carbon nanotube/polyurethane composites," *Carbon,* vol. 45, no. 4, pp. 821-827, 2007.

[212] D. E. Bornside, C. W. Macosko and L. E. Scriven, "Spin Coating of a PMMA/Chlorobenzene Solution," *J. Electrochem. Soc.,* vol. 138, no. 1, pp. 317-320, 1991.

[213] Chipara.M., "Carbon Nanotubes and Their Polymer-Based Composites in Space Environment," in *AiAA Conference and exhabition* , California, 2009.

[214] L. Meyer, S. Jayaram and E. Cherney, "Thermal conductivity of filled silicone rubber and its relationship to erosion resistance in the inclined plane test," *Transactions on Dielectrics and Electrical Insulation,* vol. 11, no. 4, pp. 620-630, 2004.

Appendix A

A.1 Engineering stress- strain graphs of neat PU at different strain rate and different temperature

Engineering stress- strain tensile tests result of neat BAYTEC+DESMODUR polyurethane at different strain rate (Figure A1.1) and at different temperature (Figure A1.2).

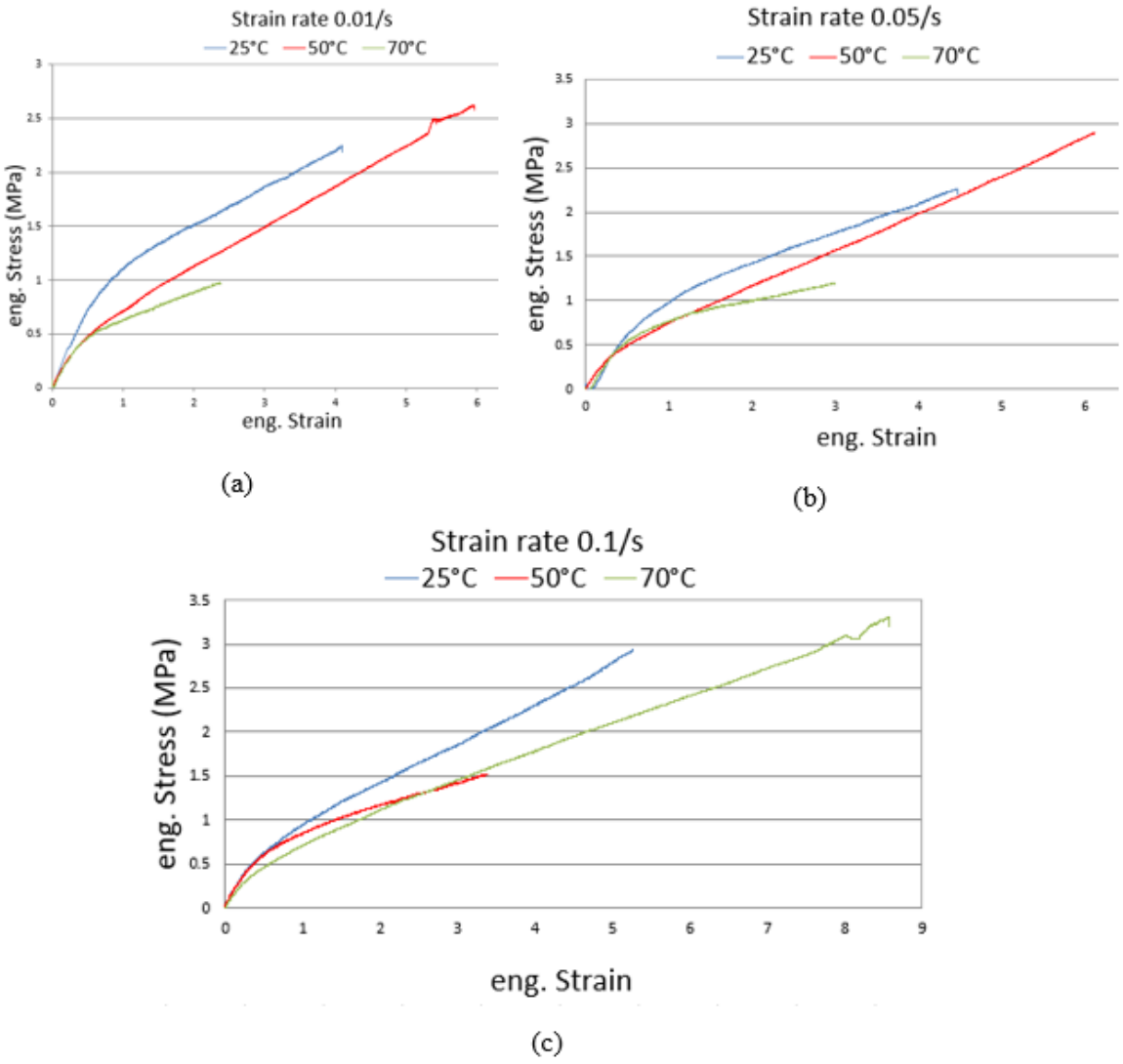

Figure A1.1 Engineering strain-stress for pure PU at different strain rate.

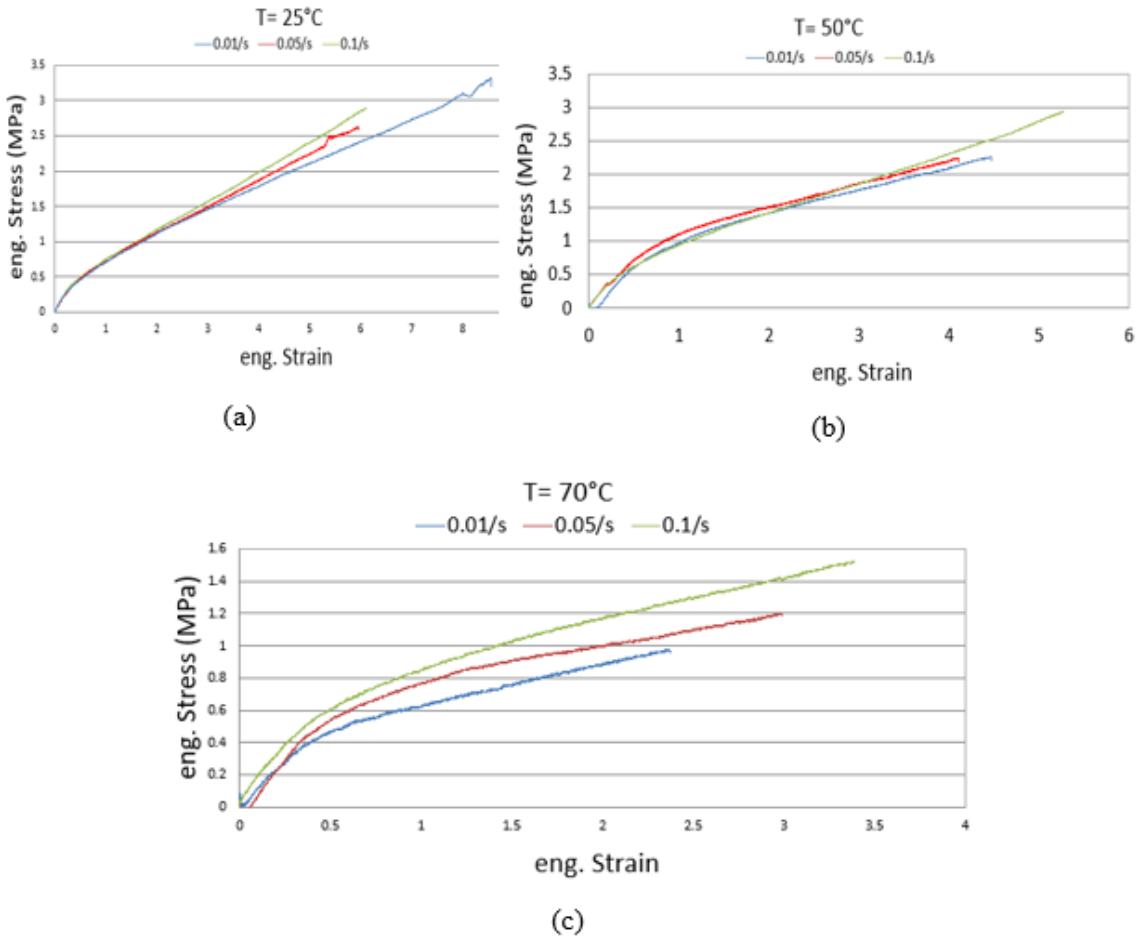

Figure A1.2 Engineering strain-stress for pure PU at different temperature.

A.2 Engineering stress- strain graphs of PU+MWCNTs at different strain rate and different temperature

Engineering stress- strain tensile tests result of BAYTEC+DESMODUR polyurethane + 0.5wt% MWCNT at different mixing speed (Figure A2.1) and at different mixing time (Figure A2.2).

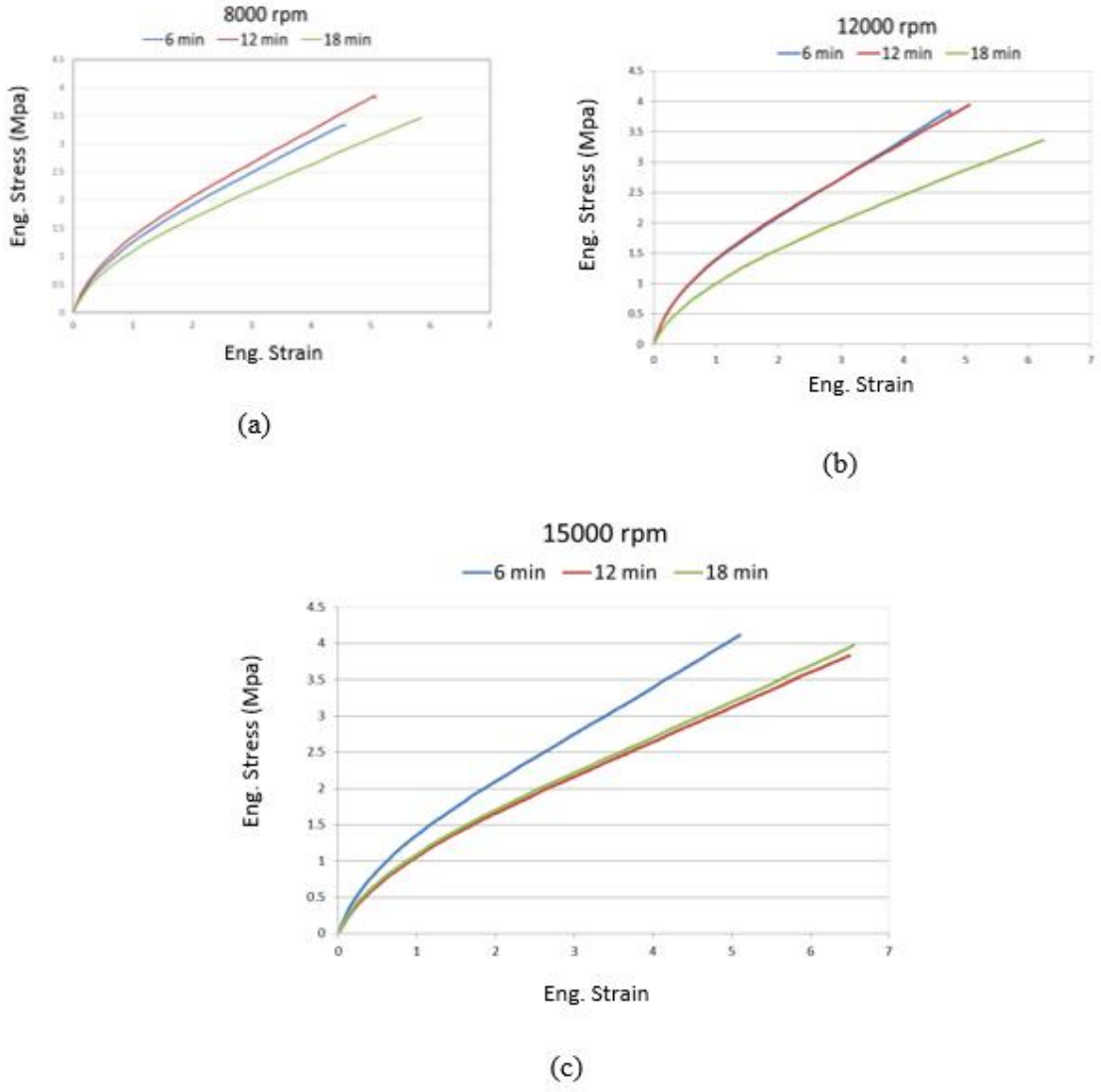

Figure A2.1 Engineering strain-stress for PU+0.5 wt% MWCNTs at different mixing speed.

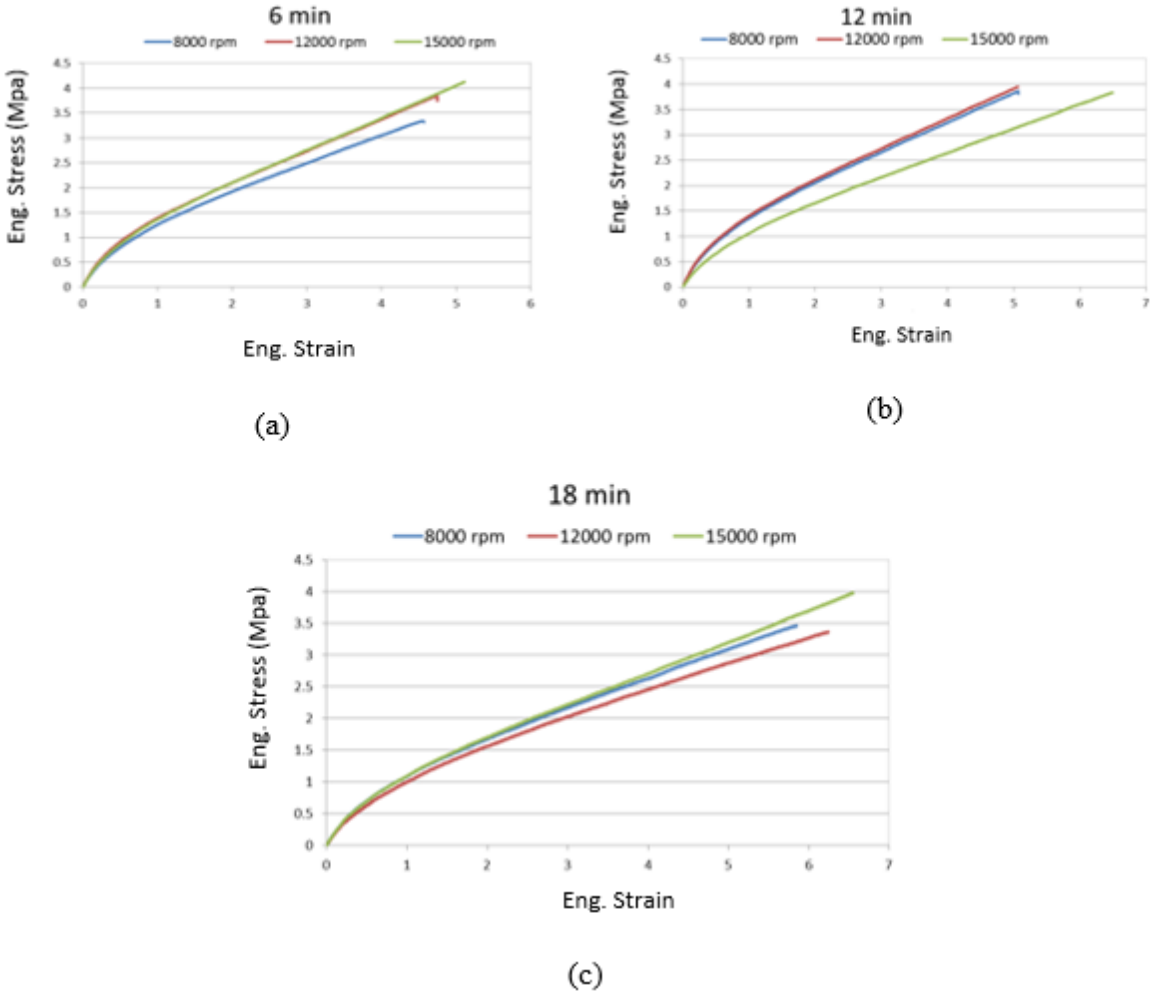

Figure A2.2 Engineering strain-stress for PU+0.5 wt% MWCNTs at different mixing time.

A.3 True stress-true strain graphs of neat PU at different strain rate and different temperature during loading and unloading

True stress-true strain tensile tests result of BAYTEC+DESMODUR polyurethane during a loading-unloading cycle at different temperature and strain rate (Figure A3.1).

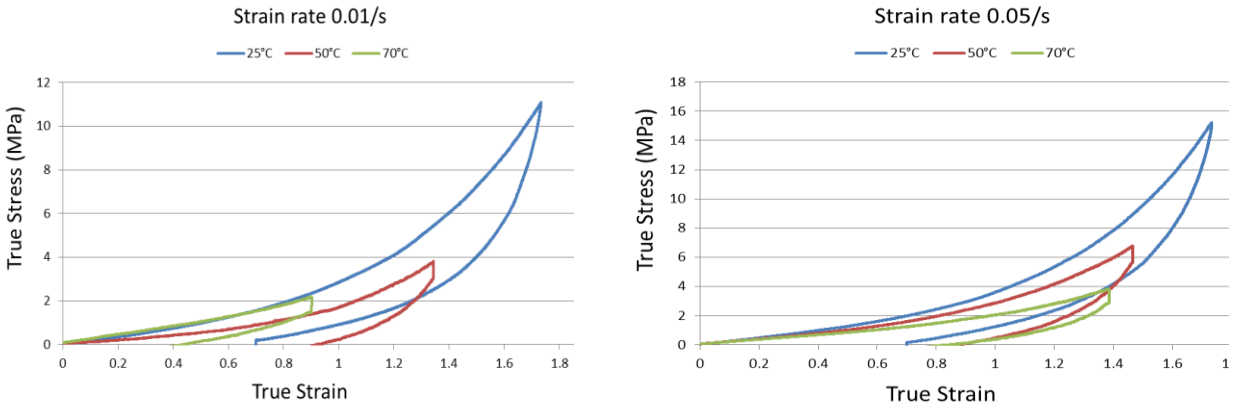

(a)

(b)

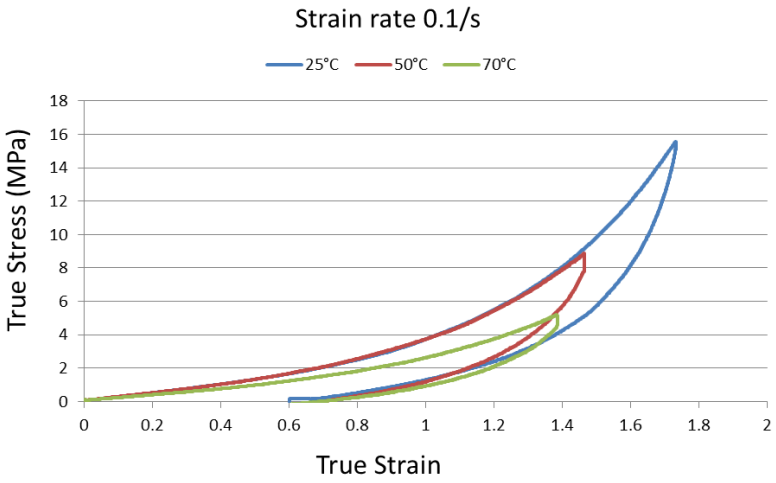

(c)

Figure A3.1 True strain-stress for pure PU at different strain rate.

A.4 Stress-strain graphs of the specimens after immersing in water for different time period

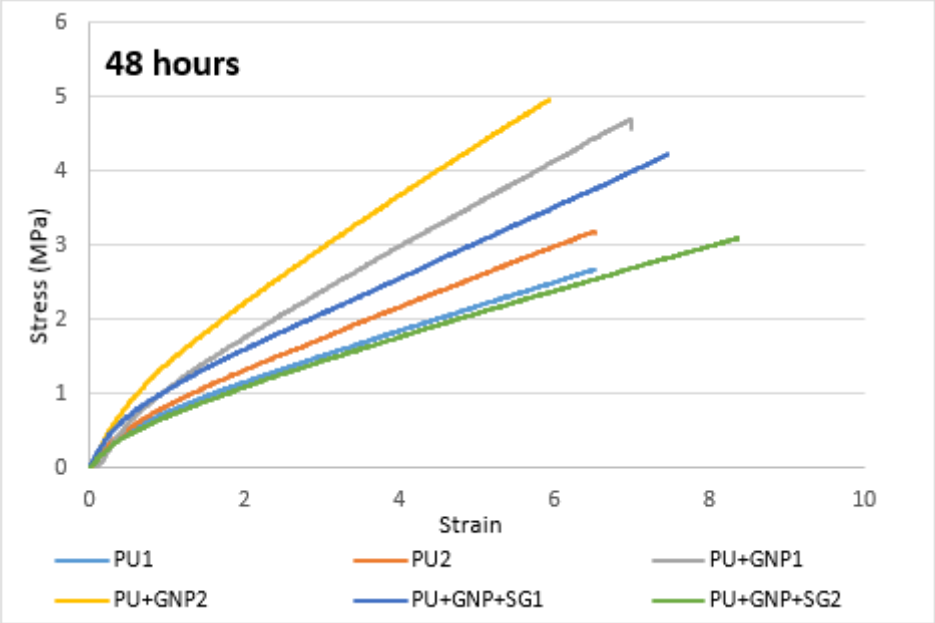

Figure A4.1 Stress-strain diagram after 48 hrs immersing in water.

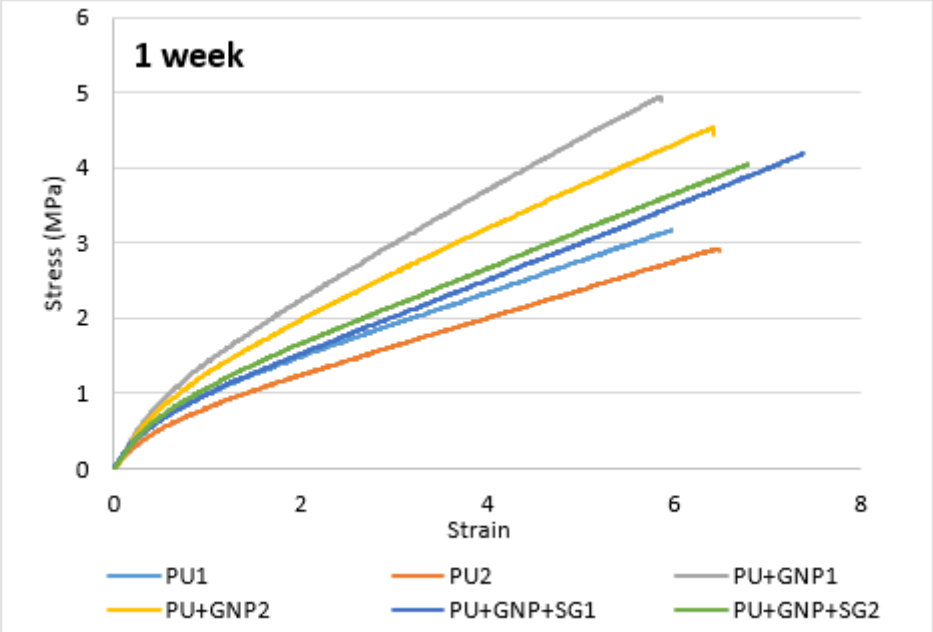

Figure A4.2 Stress-strain diagram after 1week immersing in water.

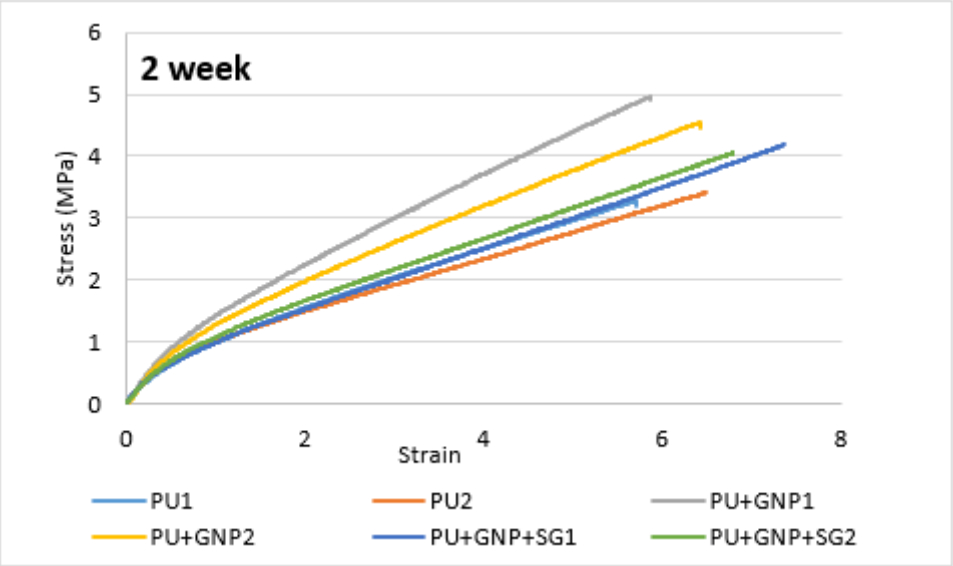

Figure A4.3 Stress-strain diagram after 2 weeks immersing in water.

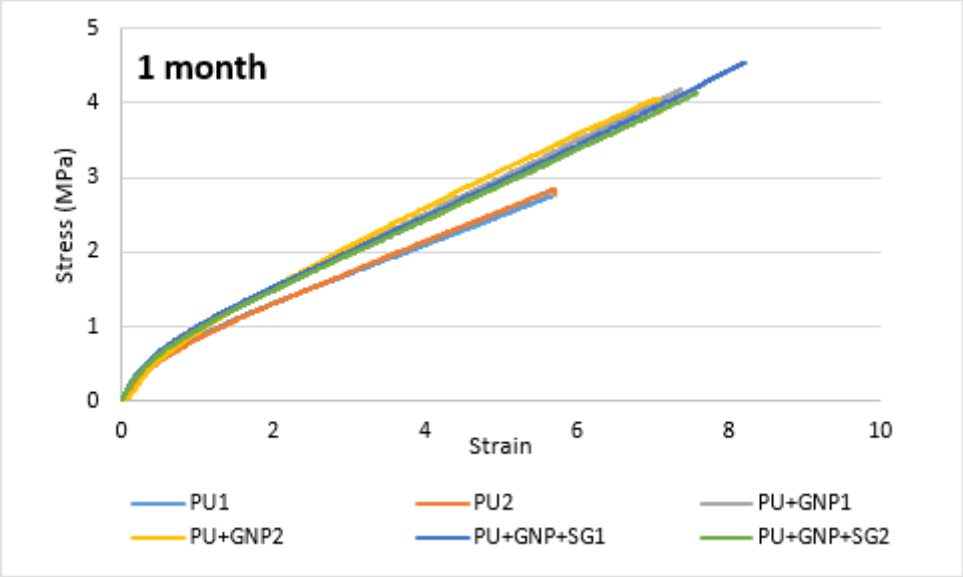

Figure A4.4 Stress-strain diagram after 1 month immersing in water.

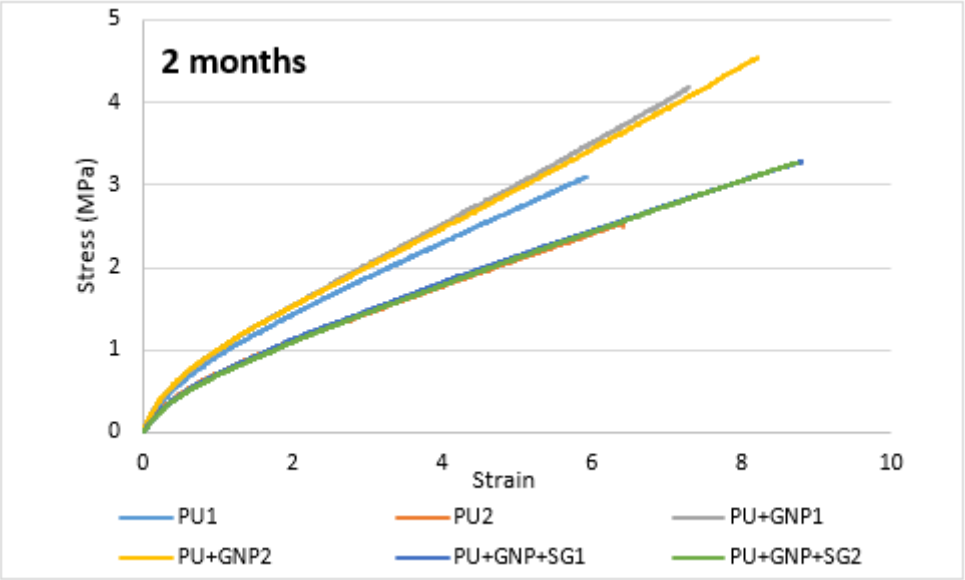

Figure A4.5 Stress-strain diagram after 2 months immersing in water.

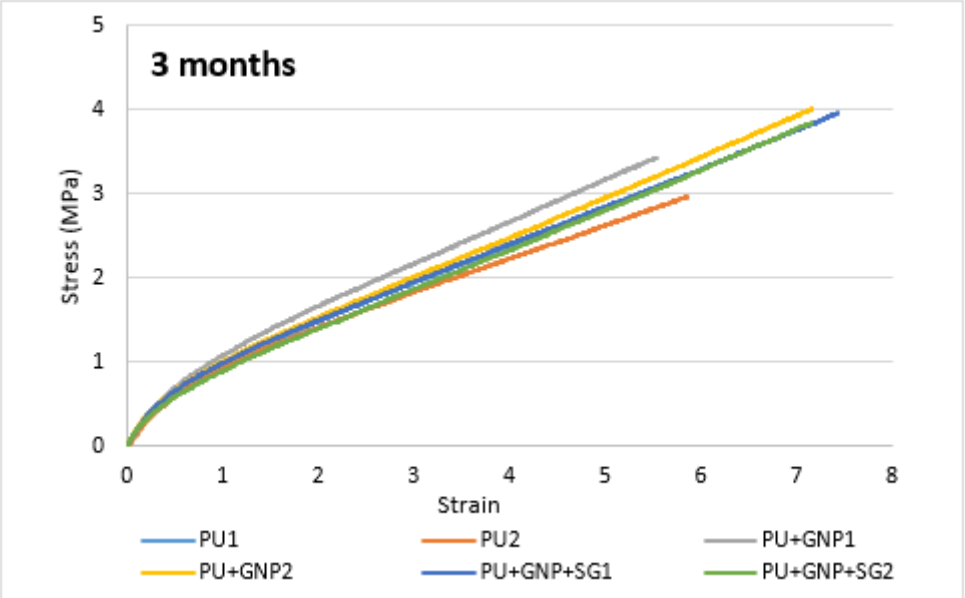

Figure A4.6 Stress-strain diagram after 3 months immersing in water.

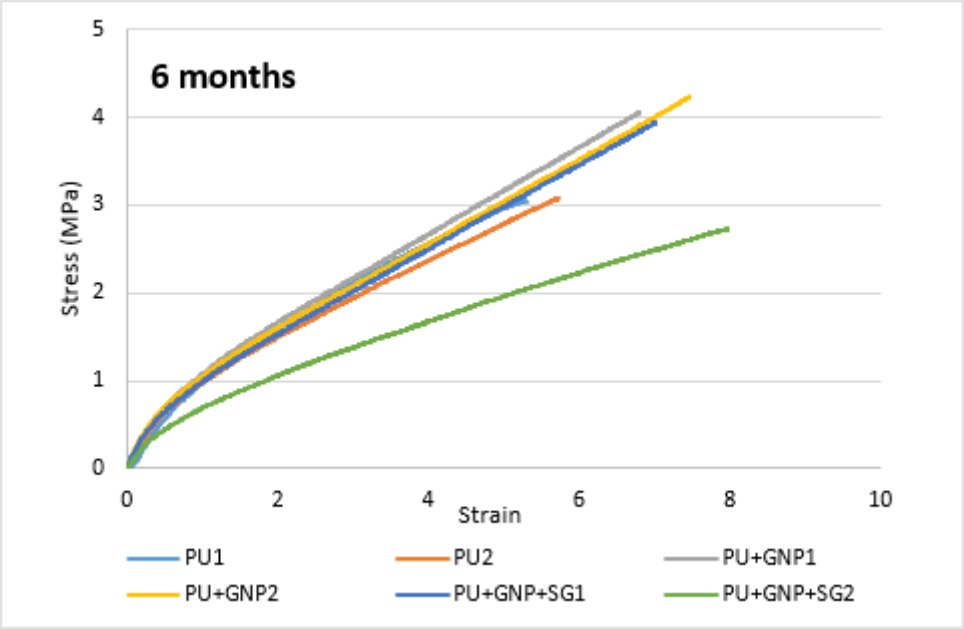

Figure A4.7 Stress-strain graph after 6 months immersing in water.